الف ۔ اللہ چنبے دی بوٹی مَن وچ مُرشد لائی ہو

نفی اَثبات دا پانی مِلیس ہر رَگے ہر جائی ہو

اندر بوٹی مُشک مچایا جاں پُھلاں پر آئی ہو

چِر جُگ جیوے مُرشد باہُو جَیں بوٹی مَن لائی ہو

Bulleh Shah
(1680-1758)

Search for the Single Top Quarks Produced in s-channel via Electroweak Interactions at $\sqrt{s} = 1.96$ at the Tevatron

Shabnam Jabeen

2006

Search for the Single Top Quarks Produced in s-channel via Electroweak Interactions at $\sqrt{s} = 1.96$ at the Tevatron

by

Shabnam Jabeen

Submitted to the Department of Physics and Astronomy and the Faculty of the Graduate School of the University of Kansas in partial fulfillment of the requirements for the degree of Doctor of Philosophy

_____

chair, chair title

_____

_____

_____

_____

Date Submitted: _____

Search for the Single Top Quarks Produced in s-channel via

Electroweak Interactions at $\sqrt{s} = 1.96$ at the Tevatron

Copyright ©2006

by

Shabnam Jabeen

To my parents

and

To Anwar

Acknowledgments

Earth's crammed with Heaven, and every common bush afire with God

Elizabeth Barrett Browning

Abstract

We present a search for single top quarks produced in the s-channel electroweak production mode. The search is performed in the electron+jets decay channels, with one or more secondary-vertex tagged jets to indicate the presence of a b-jet and hence improving the signal:background ratio. Separation between signal and background is further enhanced by the use of Feed Forward Neural Networks. 360 pb^{-1} of Run II data used for this analysis was delivered by the Tevatron, and collected by DØ between August, 2002 and August, 2004. The resulting 95% confidence level upper limit is 4 pb.

Contents

5

List of Figures

9

11

13

List of Tables

Chapter 1

Theoretical Background I: Standard Model

....how progress leads to confusion leads to progress

and on and on without respite.

Abraham Pais

Although the history of physics is full of interesting happenings, the period from the middle of the 20th century onwards is particularly exciting, both in theory and in experiment. Both, theory and experiment, like two very active children trying to get on a wall, sometimes the first pulled the second up and at other times the second pulled the first up, contributed significantly to our understanding of the universe around us.

There was also a lot of progress in the development of detectors, linear accelerators, and colliders. With that development came the "gold rush " of new particles and acompanying advances in the particle physics theory. By 1980 not only were the concepts of quantum chromodynamics and the electroweak forces theoretically solid but a good number of their predictions had been tested. In this chapter I will try to capture major developments of that period which show a beautiful and fascinating interplay of theory and

experiment.

Elementary particle physics is the study of the ultimate constituents of matter and their interactions. Every observed phenomenon in nature is a manifestation of apparently different interactions or fields between particles and each field has its distinct characteristics. Our current understanding of these interactions is embodied in what is called the "Standard Model (SM)" [1, 2, 3, 4]. At the time of this writing [1], there are believed to be four forces or four types of interactions: electromagnetic, strong, weak, and gravitational. The Standard Model combines the first three of these.

Elementary particles are the point-like constituents of matter with no known substructure up to the present limits of $10^{-18} - 10^{-19} m$. There are two types of elementary particles known as matter particles and the intermediate interaction particles. The first ones are fermions of spin $s = \frac{1}{2}$ and are classified into leptons and quarks. Second ones are, the photon, γ, which is the exchanged particle in the electromagnetic interactions; the eight gluons g_α; $\alpha = 1, ..8$, which mediate the strong interactions among quarks, and the three weak bosons, $W^\pm$, Z, which are the corresponding intermediate bosons of the weak interactions. These are all bosons with spin $s = 1$. The known leptons are: the electron, e^-, the muon, μ^-, and the τ^- with electric charge $Q = -1$ (all charges are given in units of the elementary charge e); and the corresponding neutrinos ν_e, ν_μ and ν_τ with $Q = 0$. The known quarks are of six different flavors: u, d, s, c, b and t and have fractional charge $Q = \frac{2}{3}, -\frac{1}{3}$, $-\frac{1}{3}, \frac{2}{3}, -\frac{1}{3}$ and $\frac{2}{3}$ respectively.

The quarks have an additional quantum number, the color, which for them can be of three types, generically denoted as q_i, $i = 1, 2, 3$. Since quarks are only "seen" as part of other experimentally observed matter particles, the hadrons, know that color is not seen in nature and therefore the elementary

---

[1] I always wanted to write a sentence like that ☺

2

quarks must be confined into the. These colorless composite particles are classified into baryons and mesons. The baryons are fermions made of three quarks, qqq, as for instance the proton, p (uud), and the neutron, n (ddu). The mesons are bosons made of one quark and one antiquark as for instance the pions, π^+ $(u\bar{d})$, and π^- $(d\bar{u})$.

A brief summary of quarks and leptons is give in Table (1.1), and gauge bosons in Table (1.2).

QUARKS: $S = 1/2$				LEPTONS: $S = 1/2$			
$Q = 2/3$	m	$Q = -1/3$	m	Q=-1	m	Q=0	m
u_i	$(2\text{--}8)10^{-3}$	d_i	$(5\text{--}15)10^{-3}$	e	5.11×10^{-4}	ν_e	$< 1.5 \times 10^{-8}$
c_i	$1.0\text{--}1.6$	s_i	$0.1\text{--}0.3$	μ	0.10566	ν_μ	$< 1.7 \times 10^{-4}$
t_i	173.8 ± 5.0	b_i	$4.1\text{--}4.5$	τ	1.7770	ν_τ	$< 1.8 \times 10^{-2}$

Table 1.1: Elementary particles of the SM: $S(\hbar)$ is spin, $Q(e)$ is electric charge, and $m(\text{GeV}/c^2)$ is mass. Numerical subscripts indicate the distinct color states of quarks.

GAUGE BOSONS: $S = 1$	
quanta	m
$g_1 \cdots g_8$	$<$ a few $\times 10^{-3}$
γ	$< 6 \times 10^{-25}$
$W^\pm, Z^0$	$80.39 \pm 0.06, 91.187 \pm 0.002$

Table 1.2: Gauge bosons of the SM: $S(\hbar)$ is spin, $m(\text{GeV}/c^2)$ is mass. Numerical subscripts indicate the distinct color states of gluons.

The mathematical framework used to formulate different interactions between these particles is called *quantum field theory (QFT)*. Quantum field theory is a combination of quantum mechanics and special relativity. Here

interaction at a distance is described in terms of the exchange of particles (quanta of fields) associated with the particular type of interaction.

Many attempts have been made to try to understand the relation between different fundamental fields. It is widely believed that four known fundamental interactions are different aspects of a single interaction which manifests itself at some extremely high energy. This symmetry is assumed to be broken at much lower energies, resulting in experimentally observed differences between different interactions.

You might have noticed from the previous paragraphs that the existence of symmetries plays a crucial role in particle physics. In fact, symmetries and particle physics have a very interesting relationship - symmetries give rise to particles and conserved currents but, as we shall see, in order to give those particle masses we have to break these symmetries. So, before going into more details , let's have a look at *symmetries*.

We say that there exists a symmetry S of the system when the Hamiltonian of this system, H, is invariant, i.e., $SHS^\dagger = H$.

There are two main types of symmetries:

Discrete Symmetries, where parameters can take just discrete values. In particle physics, among the most relevant ones are the transformations of: Parity P, Charge Conjugation C and Time Reversal T. All interactions in QFT must be invariant under the total transformation given by the three of them C, P, and T, irrespective of their order (CPT Theorem).

Continuous Symmetries, where parameters take continuous values. The

typical examples are *space-time symmetries*, and *internal symmetries* . Space-time symmetries rotate or move a particle in real space and time. Internal symmetries transform one particle to another with different internal quantum numbers but having the same mass. In other words, particles obeying an internal symmetry are degenerate. Common examples are , the proton $|p>$, the neutron $|n>$, and the pions, $|\pi^+>$, $|\pi^->$ and $|\pi^0>$, which make isospin multiplets. But, since, neither the proton and neutron nor the three pions have exactly the same mass, the isospin symmetry is not an exact symmetry of the strong interactions.

There are two distinct classes of internal symmetries:

Global symmetries, where the continuous parameters of the transformation *do not* depend on the space-time coordinates, and

Local (Gauge) symmetries, where the continuous parameters of the transformation *do* depend on the space-time coordinates .

If the Hamiltonian (or the Lagrangian) of a physical system has a global symmetry, there must be a current and the associated charge that are conserved (Noether's Theorem for Global Symmetries). For example, the $U(1)$ symmetries are global rotations by a given phase. For instance: $\Psi \rightarrow e^{i\alpha}\Psi$, rotates the field Ψ by a phase α and it is the same for all space-time points, i.e. it is a global phase. If we extend this global phase transformation to a local phase transformation and want to keep the theory invariant under these transformations at the same time, we will have to introduce new vector boson fields in order to keep the new Lagrangian $U(1)$ invariant or *gauge invariant*. These new fields are called the *gauge fields*, which interact with the Ψ field in a gauge invariant manner. The number of gauge fields and the particular form of these gauge invariant interactions depend on the symmetry group. The

5

number of associated gauge boson fields is equal to the number of generators of the symmetry group.

The local version of the previous example, $\Psi \rightarrow e^{i\alpha(x)}\Psi$ with the phase α being a function of the space-time point x ($\equiv x_\mu$), has one associated gauge boson field. This simplest case of $U(1)$ has just one generator and correspondingly one gauge field which is the exchanged boson particle and acts as the mediator of the corresponding interaction. Other examples are: $SU(2)$ with three generators and the corresponding three gauge bosons and $SU(3)$ with eight generators and the corresponding eight gauge bosons. The generic case of $SU(N)$ has $N^2 - 1$ generators and correspondingly the same number of gauge bosons.

The above gauge principle is a very important aspect of particle physics and has played a crucial role in the building of the Standard Model. The quantum field theories which are based on the existence of some gauge symmetry are called "gauge theories". The gauge theory based on the above mentioned $U(1)$ is quantum electrodynamics (QED), the gauge theory based on $SU(3)$ is quantum chromodynamics (QCD), the one based on the composed group $SU(2) \times U(1)$ is the so-called electroweak theory. Finally, the Standard Model is the gauge theory based on the total gauge symmetry of the fundamental interactions in particle physics, $SU(3) \times SU(2) \times U(1)$.

Let's have a closer look at these gauge theories.

1.1 Quantum Electrodynamics (QED)

QED is the most successful gauge theory in particle physics and has been tested up to an extremely high level of precision. The underlying global $U(1)$

invariance of the Lagrangian implies the conservation of the electromagnetic current, and the electromagnetic charge, e

All electromagnetic phenomenon are basically $ff\gamma$ interactions , as shown in Fig. 1.1, where f can be any charged fermion and γ is the mediating particle called the photon. The photon is a neutral vector boson with spin 1.
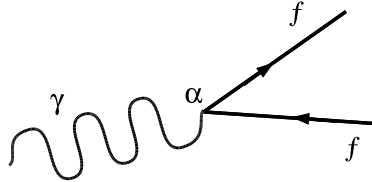
Figure 1.1: QED interaction vertex.

The coupling strength of QED is given by the fine structure constant α_e which has a value of approximately $\frac{1}{137}$. The value of the coupling strength being much less than 1 is a blessing because this is what enables us to use perturbation theory. Here every next order term contributes less than the previous term and so, most of the time, just calculating the leading order process gives us a reasonably accurate result. It turns out that when different processes, at higher orders in QED, are calculated the integrals appearing in the amplitude of these processes become divergent. Especially the processes with loops are logarithmically divergent at large momentum transfer q, in the manner of:

$$\int^\infty \frac{1}{q^4} q^3 dq = ln(q)|^\infty = \infty.$$

It was known (since the 1930's) that the higher order corrections to the theory were infinite. However, in 1947, first results on the Lamb shift[2] were

---

[2]The Lamb shift, named after Willis Lamb, is a small difference in energy between two energy levels $2s_{1/2}$ and $2p_{1/2}$ of the hydrogen atom. Classically, these two energy levels should have the same energy. This particular difference is a one-loop effect of quantum electrodynamics.

presented. These results suggested that the quantum corrections (which could explain these results) were not infinite after all.

This led to a long battle against infinities which was finally won, and today we can say that there exists a procedure that can take care of these infinities. It is called "renormalization". No theory is usable unless it is renormalizable.

There is a very complicated theorem which states that three and only three renormalizations suffice to each order: charge, mass and wave function renormalization. The wave function renormalization does not manifest itself directly in terms of physical parameters. Thus, the charge and mass are what we call "phenomenological parameters", physical quantities that are not predicted by the theory.

One procedure for renormalization involves introducing a cutoff term, say, $C(M)$, where the cutoff mass M is then taken to infinity latter. The term $C(M)$ is defined such that the integral can be divided into a finite term which is independent of M and a term involving M which goes to infinity as $M \rightarrow \infty$, and this term can be absorbed into the mass and coupling constants.

$$m' = m + \delta m, \qquad g' = g + \delta g$$

Where δm, $\delta g \rightarrow \infty$ as $M \rightarrow \infty$. Here, m and g are the "bare" mass and couplimg constant and m' and g', interestingly enough, turn out to be the mass and coupling constant that we measure physically. Thus, in QED, the vacuum behaves like a dielectric and the "vacuum polarization" partially screens the charge and reduces its field. If you get too close (less than the Compton length $\lambda_c = h/mc = 2.43 \times 10^{-10}$), the effective charge increases. The actual charge of the electron, which is what we measure experimentally, is the fully screened effective charge.

There are other finite, M independent terms which also contribute to mass m and coupling g .These terms are functions of the initial momentum trans-

ferred and this is what makes masses and couplings "run" with energy. In the case of QED this dependence is very small but, as we shall see later, in the case of QCD this is what gives rise to something called "asymptotic freedom".

Today, all results obtained in QED are based on the presumed validity of a perturbative power series expansion in α_e. The theoretical studies of order α_e^2 began in 1948 with evaluation of corrections to the electron's magnetic moment. By 1980s, calculations had been pushed to order α_e^4, yielding, for example, agreement with the experimental value for the electron's magnetic moment to 10 significant digits. Today this precision has been pushed to 12 significant digits. This is the highest level of precision reached anywhere in the field of particles and ranks among the highest achievements of twentieth-century physics [6].

1.2 Quantum Chromodynamics (QCD)

In 1968, the first round of experiments at SLAC discovered that in high energy $e - p$ scattering more electrons are scattered at large angles than expected. Like the outcome of Rutherford's experiments, this could only be understood if nucleons were made of almost free particles, which we now know as quarks. QCD is the gauge theory for strong interactions between these quarks and has provided plenty of successful predictions so far [7].

As electromagnetic charge is conserved in QED, the quantity that is conserved in QCD is called "color". The gauge symmetry group that is generated by these color transformations is $SU(3)_C$. Here C refers to colors and 3 refers to the three possible color states of the quarks. The counterparts of the photon in QED are the gluons which mediate the strong force between quarks and there are 8 of them.

The building of the QCD $SU(3)_C$ invariant Lagrangian is done by following the same steps as in the QED case. There is one difference though, the gluons themselves carry charge (color) and so they can interact with other gluons.

Since, so far things are not much different from QED, you would think, let's just repeat the QED steps and we will have a theory for quarks cooked up in no time. Well, not exactly - there is another important difference and that is: the strength of the strong force is greater than 1, which means we can not use perturbation theory. But if not perturbation theory then what? This is the question that plagued QCD for a long time until it was found that the coupling constant is not a constant at all but depends on the distance between interacting particles. At very small distances (that is, at very high energies), this "running" coupling constant becomes small and so perturbation theory <u>can</u> be used in the high energy regime.

Experimentally, values of α_s are found to be small [8], which is a very strong proof of the running of α_s, because such a relatively feeble strong force could not provide hadrons with the observed tight binding.

The fact that at small distances (a distance less than the size of a proton or pion) the coupling strength becomes very small, is called *asymptotic freedom*. The consequence of this is that quarks bound inside a proton or a neutron can be considered as "almost free". In the case of QCD, as in the case of QED, the effective charge is also reduced by the screening of charges from vacuum polarization. But what makes QCD coupling behave differently is the fact that here vacuum polarization also includes gluon-gluon vertices and these have an opposite effect – thus a decrease in effective coupling as one moves closer to the charge (in other words, as one goes to higher energies) [1].

Another thing peculiar about QCD – no observable particle carries color. In other words quarks seem to be *confined* in colorless packets of two (mesons)

or three (baryons).

In an ideal case we would like to use our theory to find out about the structure and properties of the particles and interactions involved. But in the case of QCD this is not possible because of unresolved difficulties in non-perturbative regimes of QCD (where α_s starts to become closer to 1). So we divide our problem into two regions: small distances, and large distances. At short distances, one can calculate a particular interaction between partons. To approximate the total cross section for an interaction involving a proton, say, then, one must sum over the possible parton interactions, weighing each by its probability, $F(x, Q^2)$, to find a parton with momentum fraction x in the proton.

Predictions of quantum chromodynamics have been tested in many measurements including lepton-hadron scattering and hadron-hadron scattering. For example, measured quark and gluon densities in the proton, inclusive jet production, dijet production, and production of photons and W and Z bosons occurring in hadron collisions are very well described by this theory. The production of heavy quark pairs, such as $t\bar{t}$, which is sensitive not only to perturbative processes but also to the effects due to multiple gluon radiation from the scattering quarks, within the limited statistics of current data samples, is also in good agreement with QCD predictions.

1.3 Weak Interactions

The existence of new interactions of weak strength were proposed to explain the experimental data indicating long lifetimes in the decays of known particles, for instance, $n \to pe^-\overline{\nu}_e$ ($\tau_n = 920\ sec$) and $\mu^- \to e^-\overline{\nu}_e\nu_\mu$ ($\tau_\mu = 2.2\times10^{-6}\ sec$). These are much longer lifetimes than the typical decays mediated by strong

or electromagnetic interactions [3].

Between 1930 and 1970 a number of weak interaction theories were presented and confronted with the experimental data, and in the end, were either refined or rejected in order to be compatible with the experimental observations. All this phenomenology of weak interactions, together with the gauge theories led finally to the formulation of the *electroweak theory*, i.e. the gauge theory of electroweak interactions.

The first theory of electroweak interactions was given by *Fermi*, who, in 1934, proposed the four-fermion interactions theory [10] in order to describe the neutron β-decay $n \to pe^-\overline{\nu}_e$,

$$\mathcal{L}_F = -\frac{G_F}{\sqrt{2}} \left[\overline{p}(x)\gamma_\lambda n(x)\right] \left[\overline{e}(x)\gamma^\lambda \nu_e(x)\right] + h.c.$$

where the fermion field operators are denoted by their particle names and,

$$G_F = 1.167 \times 10^{-5} \; GeV^{-2}$$

is the so-called *Fermi constant* which provides the effective dimensionful coupling of the weak interactions.

The above Fermi Lagrangian assumes a vector structure, as in the electromagnetic case, and postulates that the two currents are contracted at the same space-time point x, as shown in Fig. 1.2.

In 1956, the observation of kaon decays in two different final states with opposite parities[4], led Lee and Yang to suggest the non-conservation of parity in the weak interactions responsible for these decays[5] Could be seen by analyzing the decays of Co nuclei $^{60}Co \to^{60} Ni^* \; e^- \; \overline{\nu}_e$ which proceed via neutron decay $n \to pe^-\overline{\nu}_e$. [12].

---

[3]The typical decay times for processes mediated by strong interactions are about $10^{-23}sec$ and by electromagnetic interactions are $10^{-16}sec$.

[4]$K^+ \to \pi^+\pi^0$ and $K^+ \to \pi^+\pi^+\pi^-$

[5]Parity violation was discovered by Wu and collaborators in 1957 [11]

Fermi theory gives reasonable results at low energies but it fails at high energies. Also, due to the above vector structure of the weak currents, the Fermi Lagrangian does not explain the observed parity violation in weak interactions.

After the discovery of parity violation in weak interactions, Feynman and Gell-Mann in 1958 proposed the $V - A$ theory which incorporated the success of the Fermi theory and solved the question of parity non-conservation by postulating a $V - A$ (Vector - Axial) form for the charged weak current instead of V (Vector) alone. The effective current-current interactions are, like in the Fermi theory, contracted at the same space-time point.

The $V - A$ theory also describes the weak interactions at low energies reasonably well. But unfortunately, like Fermi theory, $V - A$ theory is also non-renormalizable. In addition, it could not explain the decays involving the strange[6] Particles.

In 1961, Lee and Yang [13] proposed another theory of weak interactions which assumed that these interactions were mediated by the exchange of massive vector bosons with spin, $s = 1$. First, the existence of intermediate charged vector bosons $W^{\pm}$ for the charged weak interactions was proposed and later Glashow added the intermediate neutral vector boson Z for the neutral weak interactions [14].

The prediction of neutral currents in 1961 was established experimentally 12 years later, in neutrino-hadron scattering by the Gargamelle collaboration at CERN [15]. It was a great success of the intermediate vector boson theory theory, which was later incorporated into the construction of the Standard Model of electroweak interactions.

But this theory is not free of problems either. It does not include the vector bosons self-interactions and, more importantly, it is non-renormalizable. Only

---

[6]These particles are produced via the strong force but decay via the weak force.

at low energies, i.e. below the M_W threshold, is the intermediate vector boson theory a well behaved effective theory of the weak interactions.
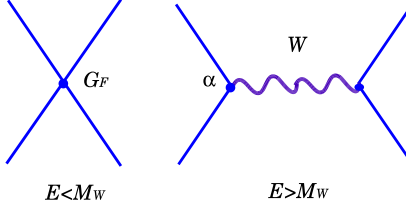
Figure 1.2: At energies less than the W mass, the effective theory of weak interactions is the Fermi theory in which two currents are contracted at the same space-time point (left) and at energies above the W mass, the spontaneously-broken $SU(2)_L \times U(1)_Y$ gauge theory is the effective theory.

1.4   Standard Model of Particle Physics

The Standard Model of electroweak interactions is a gauge theory based on the gauge symmetry of the electroweak interactions $SU(2)_L \times U(1)_Y$ and the intermediate vector bosons, γ, $W^\pm$ and Z are the four associated gauge bosons.

The proposal of the symmetry group for the electroweak theory was given by Glashow in 1961 [14]. His motivation was to unify weak and electromagnetic interactions into one symmetry group. The predictions included the existence of four physical vector boson eigenstates, $W^\pm$, Z, and γ. The electroweak theory, commonly called the Glashow-Weinberg-Salam model, was formulated by Weinberg in 1967 and by Salam in 1968, who incorporated Glashow's idea of unification [16].

The group symmetry of the electromagnetic interactions, $U(1)_{em}$[7], appears

---

[7]the generator of U(1)em is given by $Q = Y/2 + I_3$, where Y is the generator of $U(1)_Y$ (called the hypercharge), and I_3 is one of the SU(2) generators (a component of weak isospin, which is different from strong isospin discussed earlier).

in the SM as a subgroup of $SU(2)_L \times U(1)_Y$ and it is in this sense that the weak and electromagnetic interactions are said to be unified. The gauge boson masses, M_W and M_Z, are generated by the spontaneous breaking of the above electroweak symmetry.

This theory, combined with the theory of the strong force is what is known as the Standard Model of particle physics.

Key Ingredients

The key ingredients used in the building of the Standard Model are:

The *spontaneous symmetry breaking* of local (gauge) symmetries, needed for the breaking of the electroweak symmetry $SU(2)_L \times U(1)_Y$. The procedure for this spontaneous breakdown of gauge symmetries is referred to as the *Higgs Mechanism* [17].

Goldstone Theorem This theorem states the existence of massless spinless particles as an implication of spontaneous symmetry breaking of global symmetries.

Finally, *renormalizability* of gauge theories with and without spontaneous symmetry breaking, the important proof of which was provided by *'t Hooft* in 1971 [18].

Other important ingredients of the SM are: *fermion family replication, quark mixing* and *CP violation.*

Standard Model Lagrangian

The SM Lagrangian can be written as:

$$\mathcal{L}_{SM} = \mathcal{L}_{Gauge} + \mathcal{L}_{Matter} + \mathcal{L}_{Higgs} + \mathcal{L}_{Yukawa}$$

The first part contains the kinetic energy of the gauge fields and their self interactions. The next piece is the matter Lagrangian. This piece contains the kinetic energy of the fermions and their interactions with the gauge fields. Mass terms for the gauge bosons and the fermions are forbidden by the gauge symmetries, the last two terms are needed to provide mass to the gauge bosons and fermions. Yukawa interactions between the fermions and the Higgs bosons are responsible for fermion masses. The Higgs Lagrangian term ($\mathcal{L}_{Higgs}$), contains the kinetic energy of the Higgs field, its gauge interactions, and the Higgs potential.

$$\mathcal{L}_{Higgs} = (D^\mu \phi)^\dagger (D_\mu \phi) + \mu^2 \phi^\dagger \phi - \lambda (\phi^\dagger \phi)^2$$

The coefficient of the quadratic term, μ^2, is the only dimensionful parameter in the Standard Model. The sign of this term is chosen such that the Higgs field has a nonzero vacuum-expectation value on the circle of minima in Higgs-field space given by,

$$\phi^0 = \mu/\sqrt{(2\lambda)} \equiv v/\sqrt{2}$$

The dimensionful parameter μ is replaced by the dimensionful parameter v. This nonzero vacuum-expectation value, acquired by the Higgs field, breaks the electroweak symmetry and generates masses for the gauge bosons.

The tree level predictions for the first generation masses in the Standard Model are:

$$\begin{aligned} M_W &= \frac{gv}{2} \; ; \; M_Z = \frac{\sqrt{g^2 + g'^2}\,v}{2} \\ M_H &= \sqrt{2}\mu \\ m_e &= \lambda_e \frac{v}{\sqrt{2}} \; ; \; m_u = \lambda_u \frac{v}{\sqrt{2}} \; ; \; m_d = \lambda_d \frac{v}{\sqrt{2}} \; ; \ldots \end{aligned}$$

v is determined experimentally from μ-decay [8], and turns out to be,

$$v = (\sqrt{2}G_F)^{-\frac{1}{2}} = 246 \; GeV$$

By definition, *weak eigenstates* are the members of the weak isospin doublets that transform into each other through interaction with the W boson. What we see in the detector, however, are not *weak eigenstates* but *mass eigenstates*, which are states of definite mass created by the interaction with Higgs bosons. For the three generations of quarks, the members of the $SU(2)$ doublet are the mixture of different massive fields.

All the mixing is expressed in terms of a (3×3) unitary matrix V operating on the quarks d, s and b:

$$\begin{pmatrix} d \\ s \\ b \end{pmatrix}_{\text{Weak}} \equiv \begin{pmatrix} V_{ud} & V_{us} & V_{ub} \\ V_{cd} & V_{cs} & V_{cb} \\ V_{td} & V_{ts} & V_{tb} \end{pmatrix} \begin{pmatrix} d \\ s \\ b \end{pmatrix}_{\text{Mass}}$$

The matrix V is known as the Cabibbo–Kobayashi–Maskawa matrix (CKM). The nine matrix elements V_{ij} can be expressed in terms of three mixing angles and one phase.

The Fermionic Sector

The fermionic sector of quarks and leptons is organized in three families with identical properties except for mass. The particles in each family are:

$$1^{st} \text{ family:} \begin{pmatrix} \nu_e \\ e^- \end{pmatrix}_L, \; e^-_R, \begin{pmatrix} u \\ d \end{pmatrix}_L, \; u_R, \; d_R$$

---

[8] by identifying the predictions of the partial width $\Gamma(\mu \to \nu_\mu \bar{\nu}_e e)$ in the SM to low energies $(q^2 << M_W^2)$ and in the V-A theory one gets,

$$\frac{G_F}{\sqrt{2}} = \frac{g^2}{8M_W^2} = \frac{1}{2v^2},$$

$$2^{nd} \text{ family: } \begin{pmatrix} \nu_\mu \\ \mu^- \end{pmatrix}_L, \ \mu_R^-, \ \begin{pmatrix} c \\ s \end{pmatrix}_L, \ c_R, \ s_R$$

$$3^{rd} \text{ family: } \begin{pmatrix} \nu_\tau \\ \tau^- \end{pmatrix}_L, \ \tau_R^-, \ \begin{pmatrix} t \\ b \end{pmatrix}_L, \ t_R, \ b_R$$

Where "L" is for left handed and "R" is for right handed fields which are defined by means of the chirality operator γ_5 as,

$$e_L^- = \tfrac{1}{2}(1 - \gamma_5)e^-; \ e_R^- = \tfrac{1}{2}(1 + \gamma_5)e^-$$

and they transform as doublets and singlets of $SU(2)_L$ respectively.

The Gauge Sector

The gauge sector of the SM is composed of eight gluons which are the gauge bosons of $SU(3)_C$ and the γ, $W^\pm$ and Z particles which are the four gauge bosons of $SU(2)_L \times U(1)_Y$.

The gluons are massless, electrically neutral and carry color quantum numbers. There are eight gluons since they come in eight different colors. The consequence of the gluons being *colorful* is that they interact not only with the quarks but also with themselves. The weak bosons, $W^\pm$ and Z are massive particles and are also self-interacting. The $W^\pm$ are charged with $Q = \pm 1$ respectively and the Z is electrically neutral. The photon γ is a massless, chargeless and non-self-interacting particle.

The electromagnetic interaction has infinite range as it corresponds to an interaction mediated by a massless gauge boson. The short range of the weak interactions of about $10^{-16} cm$ corresponds to the exchange of a massive gauge particle with a mass of the order of $M_V \sim 100 \, GeV$. Finally, the strong interaction's range is not infinite, even though it involves the exchange of a massless gluon, but is finite due to the property of confinement. The short

18

range of the strong interactions of about $10^{-13}cm$ corresponds to the typical size of the lightest hadrons.

1.4.1 Experimental Verification of SM

The Standard Model is one of the most tested theories in the world. Especially, in the last 20 years, the experimental study of this model has made enormous progress. Large collider detectors collected data on *ee*, *ep* and *pp* collision processes[9] and using the data recorded at these experiments, electroweak predictions have been tested up to per-mille precision [19]. The material discussed in this section is mainly based on the reference [20].

Masses and couplings in the Standard Model, as with any renormalizable theory, are free parameters which are not determined by the theory. Hence experimental input of these parameters is needed in order to calculate the other quantities. Some of the Standard Model parameters, for example, α_e, G_F, and m_Z, are very precisely known. From these input parameters one computes the radiative corrections to a sufficient precision to match the accuracy of the experimental data. From these theoretical predictions one can derive constraints on some other observables which are less accurately known (e.g. the masses of light fermions m_f, top mass m_t, and $\alpha_s(m_Z)$) or largely unknown (e.g. the Higgs mass).

By inserting the experimental values of α, G_F and θ_w into the theoretical expressions for masses one gets the tree level values for the gauge boson masses,

$$M_W^{\text{tree}} = 78 \ GeV \ ; \ M_Z^{\text{tree}} = 89 \ GeV.$$

The discovery of the $W^{\pm}$ and Z gauge bosons in 1983 at the CERN SpS collider [21] led to the definitive confirmation of the validity of the SM. The

---

[9]SLD at SLAC, ALEPH, DELPHI, L3 and OPAL at LEP. $D\emptyset$ and CDF at the Tevatron.

measured masses were surprisingly close to the SM tree level predictions,

$$M_W^{\text{SpS}} = (81 \pm 2)\ GeV \ ; \ M_Z^{\text{SpS}} = (93 \pm 3)\ GeV.$$

The present experimental values, given in Table 1.3, are even more precise.

The $W^\pm$ and Z gauge bosons can decay either into quarks or into leptons within the Standard Model. The dominant decays are clearly into quarks due to the extra color factor, N_C, which is not present in the case of leptonic decays. The tree level predictions for the partial widths in the approximation of neglecting the fermion masses are the following,

$$\Gamma(W^+ \to e^+ \nu_e) = \frac{G_F M_W^3}{6\sqrt{2}\pi} = 0.232\ GeV$$

$$\Gamma(W^+ \to u_i \bar{d}_j) = \frac{G_F M_W^3}{6\sqrt{2}\pi} N_C |V_{ij}|^2 = 0.232\ N_C |V_{ij}|^2\ GeV$$

$$\Gamma(Z \to f\bar{f}) = \frac{G_F M_Z^3}{6\sqrt{2}\pi} \kappa_f (g_{Vf}^2 + g_{Af}^2) = 0.3318\kappa_f (g_{Vf}^2 + g_{Af}^2)\ GeV$$

where, V_{ij} are the CKM matrix elements and,

$$\kappa_f = 1\ ,\ f = l, \nu\ ;\ \kappa_f = N_C\ ,\ f = q\ ;\ g_{Vf} = T_3^f - 2Q^f sin\theta_w^2\ ;\ g_{Af} = T_3^f$$

Top Quark Physics

The top mass m_t, like other fermion masses, is not predicted in the Standard Model. Instead, the Standard Model provides, via the Higgs mechanism, the tree level relation,

$$m_t = \lambda_t \frac{v}{\sqrt{2}} = \lambda_t \left(\frac{1}{2\sqrt{2}G_F} \right)^{\frac{1}{2}}$$

Observable	Measurement	SM fit
m_{Z} [GeV]	91.1875 ± 0.0021	91.1873
Γ_{Z} [GeV]	2.4952 ± 0.0023	2.4965
$\sin^2 \theta_{\text{eff}}^{\text{lept}}$ ($Q_{\text{FB}}^{\text{had}}$)	0.2324 ± 0.0012	0.23140
m_{W} [GeV]	80.425 ± 0.034	80.398
Γ_{W} [GeV]	2.133 ± 0.069	2.094
m_{t} [GeV] ($p\overline{p}$ [22])	178.0 ± 4.3	178.1
$\Delta\alpha_{\text{had}}^{(5)}(m_{\text{Z}}^2)$ [23]	0.02761 ± 0.00036	0.02768

Table 1.3: A brief summary of electroweak precision measurements at high Q^2 [19].

which gives m_t in terms of the top Yukawa coupling λ_t. But, λ_t, like the other fermion Yukawa couplings, is also an unknown parameter in the Standard Model.

The long expected discovery of the top quark, finally occurred in 1994 at the $p\overline{p}$ Tevatron collider at Fermilab [24]. The present experimental value of the top mass as provided by the two Tevatron experiments is given in ref. [22]. It is remarkable that the top mass is so much larger than the rest of the fermion masses. For this top mass value, the corresponding Yukawa coupling λ_t comes out to be ~ 1. There is no answer within the Standard Model to the question of why the top quark is so heavy.

The dominent decay of the top quark is, by far, into a W gauge boson and a bottom quark. The Standard Model tree level prediction for the partial width, in the approximation of neglecting the b quark mass (m_b), is

$$\Gamma(t \rightarrow W^+ b) = \frac{G_F m_t^3}{8\pi\sqrt{2}} |V_{tb}|^2 \left(1 - \frac{M_W^2}{m_t^2}\right) \left(1 + 2\frac{M_W^2}{m_t^2}\right) \sim 2 \; GeV.$$
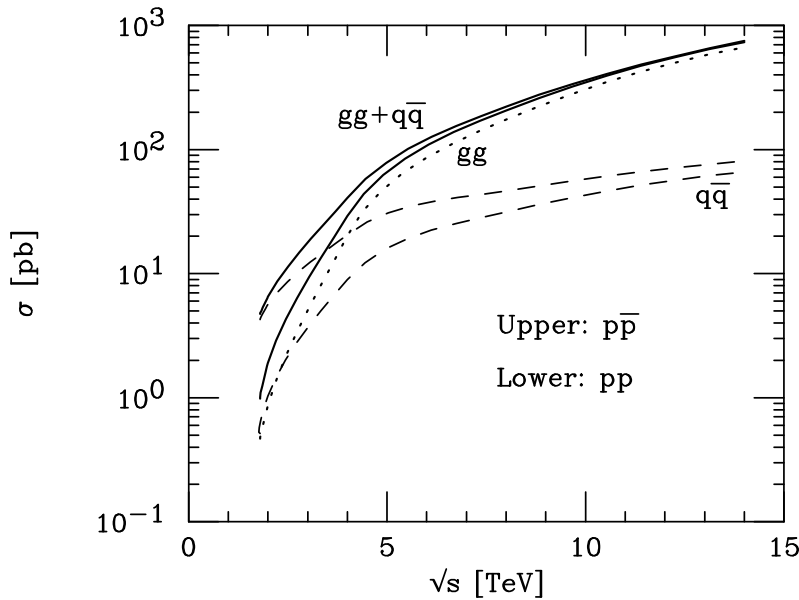
Figure 1.3: $t\bar{t}$ production at hadron colliders

There is no experimental measurement of the total or partial width yet.

Given the large top mass value, at present, it can only be produced at the Tevatron collider. The future hadron collider LHC at CERN will provide additional interesting information on top quark physics. The cross-section for $t\bar{t}$ production at the Tevatron ($\sqrt{s} = 2TeV$) and LHC ($\sqrt{s} = 14TeV$) from the various possible channels is shown in Fig. 1.3.

To summarize, the couplings of quarks and leptons to the weak gauge bosons $W^{\pm}$ and Z are indeed precisely those predicted by the gauge symmetry. The accuracy of a few per-mille for these tests implies that, not only the tree level, but also the structure of quantum corrections has been verified. The triple gauge vertices γW^+W^- and ZW^+W^- have also been found, with a lesser accuracy, to be in agreement with the specific predictions of the Standard Model.

1.5 Beyond The Standard Model

The Standard Model, as beautiful and as successful as it is, is not free of problems. If we look at the experimental data, on the whole the Standard Model performs rather well, and it is fair to say that there is no clear indication for new physics but still there are some issues:

- There are a large number of independent parameters which must be determined experimentally.

- The origin of symmetry breaking is not explained within the Standard Model. The expectation is that there exists another more complete theory to which the Standard Model is an approximation.

- The origin of CP violation is not understood either. A hint that some other source of CP violation may be needed, perhaps manifested only at higher energies, comes from the observed predominance of matter over anti-matter in the universe.

- The fermion masses and the elements of the CKM matrix (including a CP violating phase) are governed by Yukawa couplings of fermions to the Higgs fields. The observed hierarchies among quark fermion masses and mixing parameters are also unexplainable.

All these issues strongly indicate that this model provides an incomplete description of the elementary structure of nature. And then, of course, the Standard Model is incomplete in the sense that it includes only three of the four forces.

At present, there are countless models for new physics, which promise to solve all or some of the above issues. The main candidates are:

Compositeness There is something more fundamental than quarks and leptons. The Standard Model is a good approximation to nature only at energies small compared with the inverse scale of compositeness Λ. In this theory, the observed scale of electroweak symmetry breking, v ($\sim \frac{1}{4}$ TeV), might emerge naturally in connection with the compositeness scale.

Technicolor Here, to replace the Higgs field, a new gauge interaction called technicolor, is postulated, which is strongly coupled at the electroweak symmetry breaking scale. At this scale fermions with technicolor charge, condense, spontaneously breaking both a chiral symmetry and the electroweak gauge symmetry. This is a model with no light scalar particle, but with strong W, Z couplings in the TeV regime, predicting a large number of new composite particles with TeV masses.

Supersymmetry The hierarchy problem can be solved by extending the symmetry of the theory to one that relates bosons to fermions, known as supersymmetry. This requires doubling the number of spin degrees of freedom for matter and gauge particles: for every fermion f there is a complex scalar partner $\tilde{f}$ with the same internal quantum numbers, and for every gauge boson V there is a spin-$\frac{1}{2}$ partner $\tilde{V}$.

One of the most interesting and attractive aspects of supersymmetry is the unification of gauge couplings. When the coupling evolution is calculated using only the content of the Standard Model, unification is not precisely achieved at a single point. Exact unification can be achieved with the particle content of the minimal supersymmetric extension of the Standard Model if superpartner masses lie in a range between 100 GeV and 10 TeV, as shown in Fig. 1.4.

Coupling unification, if true, provides evidence that, above the scale of unification, physics is described by a more fundamental theory.
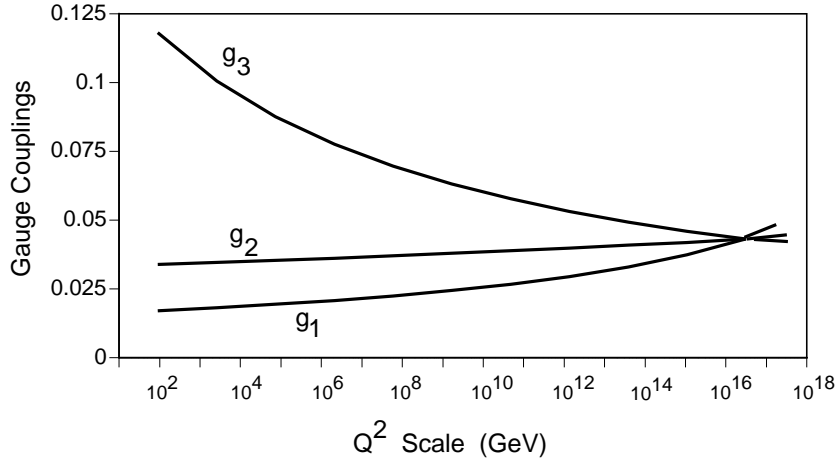
Figure 1.4: Gauge couplings g_1, g_2, g_3 as a function of q^2 in the context of the minimal supersymmetric model, showing unification around 10^{16} GeV.

Superstrings theory is, at present, the only candidate for a quantum theory of gravity. In this case the Standard Model is part of a larger theory which is expected to include a rich spectrum of new particles at higher energies.

With the start of Run II of the Tevatron collider at Fermilab, and of the Large Hadron Collider (LHC) in the near future, we are on the verge of another exciting period in the history of particle physics. Whatever the new theory is, these future experiments can constrain any possible extensions of the Standard Model. It is equally possible that we will discover something completely unanticipated which may lead us to a more fundamental description of nature (Amen! ☺).

25

Chapter 2

Theoretical Background II: Electroweak Production of Top Quark

An invasion of armies can be resisted,
but not an idea whose time has come.
Victor Hugo

2.1 Top Quark

As we have seen from the last chapter, even though, as discovered by the Tevatron CDF and DØ collaborations [24], the top quark is the heaviest elementary particle found so far, it is predicted to be a point like particle in the Standard Model. The relatively large mass of the top quark (~ 175 GeV) is of the order of the electroweak symmetry breaking scale v $(= (\sqrt{2}G_F)^{-1/2} = 246\text{GeV})$, and the top Yukawa coupling λ_t $(= 2^{3/4}G_F^{1/2}m_t)$ is numerically very close to unity and one expects that a study of top quark physics might reveal details of the electroweak symmetry breaking mechanism.

An important consequence of the top quark being so heavy is that it decays long before it can hadronize. The top quark decay width, Γ_t, has been theoretically calculated in the Standard Model to second order in QCD [25] and to first order in electroweak [26] (EW) corrections, and is found to be ~ 2 GeV. This means that the top decay lifetime τ_t ($\approx 0.4 \times 10^{-24}$ s) is much smaller than the typical time for formation of QCD bound states $\tau_{QCD} \approx 3 \times 10^{-24}$ s).

This property of the top quark makes it a very clean source of fundamental information. In particular, the momentum and spin information carried by the top quark is expected to be passed on to its decay products directly, without being distorted by the hadronization process. For example, angular distributions of the top quark decay products are mainly determined by the momentum and spin state of the top quark itself and are not smeared out by hadronization effects [27].

Figure 2.1: Feynman diagrams for ttbar pair production: Left, $q\bar{q} \rightarrow t\bar{t}$, the main mode of production (85%) at the Tevatron; right, $gg \rightarrow t\bar{t}$, the main mode of production (90%) at the LHC.

The unusual properties of the top quark makes it very interesting. It has been argued [28, 29] that new physics might lead to measurable deviations from the Standard Model values that are first manifested in the top sector. There are different models of the electroweak symmetry breaking mechanism which will induce different interactions among the top quark and the W and Z bosons. Therefore, hopefully through studying the top quark system one

may eventually learn about the symmetry breaking sector of the electroweak theory, and the possible existance of any new physics.

2.2 Single Top Quark

Top quarks detected at the Tevatron have been produced in pairs via the strong QCD interactions, as is shown in Fig. 2.1. However, the Standard Model predicts that top quarks should also be produced through electroweak interactions. The very fact that electroweak interactions are involved, makes single top study very interesting because it provides a direct window to the electroweak symmetry breaking sector of the Standard Model. Single top production mechanisms and the related physics of top quark properties have been the subject of many studies [30].

There are three main processes for single top production at hadron colliders.

- The s-channel W^* production: $qq' \to W^* \to t\bar{b}$.

- The t-channel W-exchange mode: $bq \to tq'$ (sometimes referred to as W-gluon fusion [1]).

- The tW production. The tW mode occurs when a b quark radiates a W, as shown in Fig 2.2. This mode may be important at the Large Hadron Collider at CERN (LHC), but this process has a negligible cross section at the Tevatron [31] because the gluon parton density is small and we have a massive W boson and top quark in the final state. We will not discuss this mode in any more detail in the rest of the sections of this chapter.

Each of these processes may be characterized by the virtuality of Q_W^2, the four-momentum squared of the participating W boson. The process $q\bar{q} \to t\bar{b}$

---

[1]The main diagram contributing to this process involves a gluon fusion with a W via a b quark to make a top, hence the name.
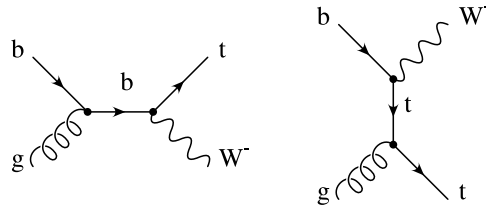
Figure 2.2: Feynman diagrams for $gb \to tW$ process.

probes the top quark with a time-like W boson $(Q^2 > (m_t + m_b)^2)$, while the W-gluon-fusion process involves a space-like W boson $(Q^2 < 0)$.

These three sub-processes have very different kinematics and experimental signatures, and as we shall discuss later, are sensitive to different types of new physics in the top quark sector. Thus these processes provide complimentary information about the properties of the top quark. We discuss the s-channel and t-channel production modes in more detail below.

2.2.1 s-channel Production

The s-channel (W^*) mode of production shown in Fig. 2.3 occurs when a quark and an anti-quark fuse into a virtual W boson, which then splits into a t and $\bar{b}$ quark. For the s-channel, the 2→2 process, as shown in Fig. 2.3, dominates the total cross section. We refer to the s-channel process as "tb," which includes both $t\bar{b}$ and $\bar{t}b$.
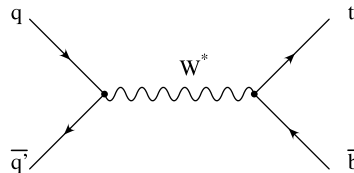
Figure 2.3: Feynman diagram for $q\bar{q} \to W^* \to t\bar{b}$ at the leading order.

29

The total cross section for the W^* production sub-process (σ_{W^*}) has been studied at next-to-leading-order (NLO) in QCD corrections [32], by including NLO corrections to both the $q\bar{q}'$ initial state and the $t\bar{b}$ final state. Detailed studies of the kinematics of this process at leading order (LO) exist in the literature [33, 34, 35], as well as more realistic studies in which the effects of soft gluons on the kinematics have been re-summed [36].

$p\bar{p}\rightarrow t\bar{b}+X$, has a predicted rate at the Tevatron Run II of about 44% of the t-channel rate. Although the process should be observable at the LHC, it has a cross section about 25 times smaller there than the t-channel one, and will therefore be easier to study at the Tevatron.

This sub-process is an attractive mode for studying top quark properties, because the initial state partons are quarks with relatively large momentum fraction x, and thus the parton densities are well understood. In fact, this process may provide the best measurement of the magnitude of the Cabbibo-Kobayashi-Maskawa matrix element V_{tb} [37] (see Sec. 2.3). On the other hand, this mode suffers from a smaller cross section than the W-gluon fusion mode, and a larger percentage dependence on the mass of the top quark [36].

2.2.2 t-channel Production

This process is also called W-gluon fusion and is shown in Fig 2.4. In this case a b quark, coming from gluon splitting, fuses with a W^+ boson, producing a top quark. The presence of this gluon in the t-channel makes things relatively complicated because the gluon distribution function is not well-known.

The W-gluon fusion mode has also been studied at NLO in QCD [38]. Fig 2.4 shows the two most important diagrams contributing to t-channel production. Combining these two diagrams is a little tricky because the treatment
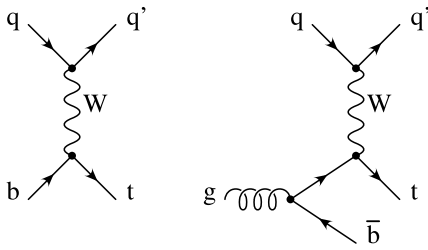
Figure 2.4: Representative Feynman diagrams for the W-gluon fusion mode of single-top production. Here left diagram is representative of 2→2 process and right diagram is representative of 2→3 process.

of the b quark as a parton must be done carefully. Since the LO calculation of the t-channel rate already includes, through the b PDF, the region of the gluon splitting diagram where the b quark becomes collinear with the initial gluon, this part should be properly subtracted out to avoid double counting [35, 39].

Fig 2.5 shows that there are two different diagrams for the 2→3 process for t-channel production, and it also shows how they destructively interfere with each other. The diagram containing $g{\rightarrow}t\bar{t}$ is not always shown when discussing single top quark production, but is always present for the t-channel.

It is found that the total rate of the $2 \rightarrow 3$ W-gluon fusion process is about 25% less than the $2 \rightarrow 2$ event rate for $m_{top} = 180$ GeV, regardless of the energy or the type (*i.e.*, pp or $p\bar{p}$) of the machine [51].

The t-channel production mode has the advantage of a larger cross section (σ_{Wg}) and a smaller percentage dependence on top mass than the s-channel (W^*) process. This mode is also of interest because within the Standard Model, it provides a way to directly probe the partial width of the top quark, $\Gamma(t \rightarrow W^+b)$, through the effective-$W$ approximation [41], valid at energies much larger than the W mass, in which the W boson is treated as a parton within the proton. For details see [37].
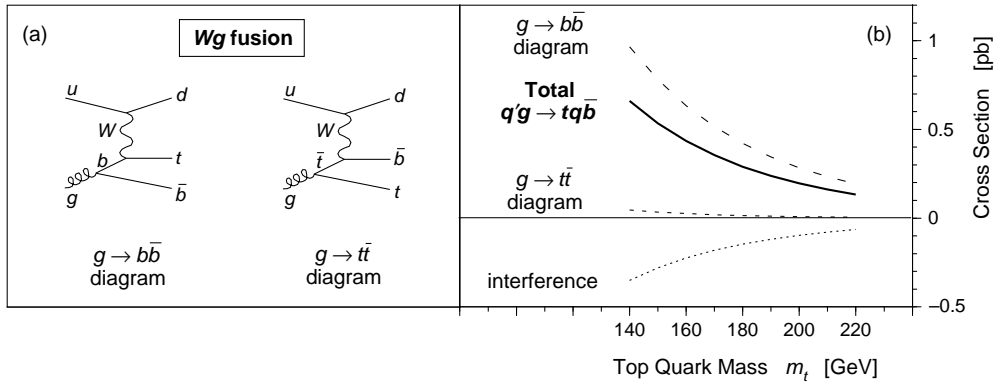
Figure 2.5: At $\sqrt{s} = 1.8$ TeV, (a) Feynman diagrams for t-channel W-gluon fusion ($q'g{\to}tq\bar{b}$). (b) t-channel cross section for the 2$\to$3 process versus top quark mass, showing the contributions from each of the Feynman diagrams in (a), and the large destructive interference between the two processes [31]

.

The major drawback of the W-gluon fusion mode is that it suffers from a larger theoretical uncertainty due to the uncertainty in the b quark parton density.

2.2.3   NLO Calculations of Single Top Production

The next to leading order (NLO) production rates at the Tevatron Run II ($\sqrt{s} = 1.96$ TeV) for the s- and t-channel single top modes have been calculated in Refs. [31, 50, 51, 52]. Results for cross sections are shown in Table 2.1.

The NLO rates at the Tevatron Run II ($\sqrt{s} = 1.96$ TeV) for the s- and t-channel single top modes have been calculated in Refs. [50, 51, 52]. The cross sections and the errors for the cross sections are shown in Table 2.1.
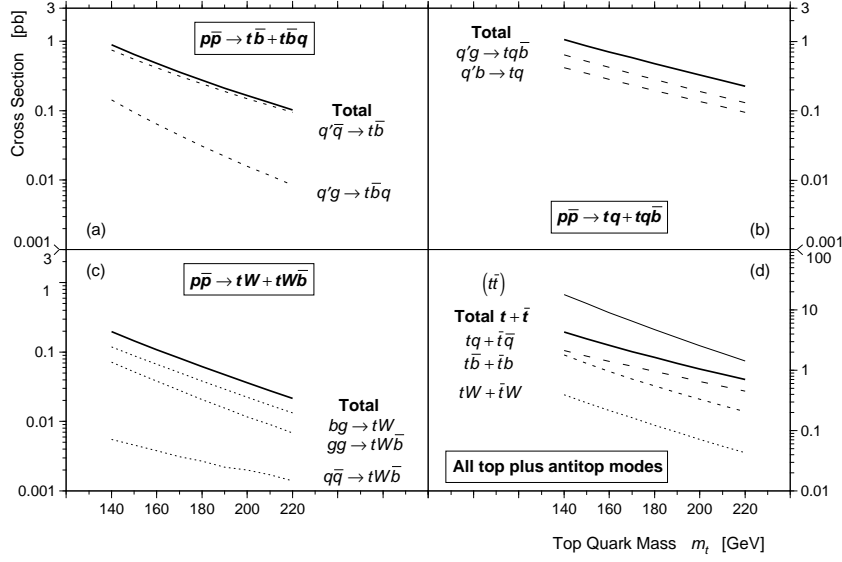
Figure 2.6: Single top quark cross sections at the Tevatron with $\sqrt{s} = 1.8$ TeV, versus top quark mass: (a) s-channel production $p\bar{p} \to t\bar{b} + t\bar{b}q$; (b) t-channel production $p\bar{p} \to tq + tq\bar{b}$; (c) $p\bar{p} \to tW + tW\bar{b}$; and (d) the total single top and anti-top cross section $p\bar{p} \to t + \bar{t} + X$. The resummed next-to-leading order (NLO) $t\bar{t}$ cross section of Ref. [43] is shown as the uppermost line in (d), for comparison with single top production (at leading order) [44].

Process	Cross Section [pb]
s-channel (tb)	$0.88^{+0.07}_{-0.06}$
t-channel (tqb)	$1.98^{+0.23}_{-0.18}$
tW-production	0.093 ± 0.024

Table 2.1: Total cross sections for single top quark production at $\sqrt{s} = 1.96$ TeV with $m_t = 175$ GeV.

Errors include components for the choice of scale and for the uncertainties on the parton distribution functions, but not for the top quark mass uncertainty. Fig 2.6 shows the leading order (LO) single top cross sections as a function

33

of the top quark mass. This figure is from a leading-order calculation, not a NLO one. The Feynman diagrams included in this calculation do not include those with loops although all other types are included.

Since the s-channel cross-section calculation does not rely on the gluon parton density functions, the errors due to the pdf uncertainty are significantly lower than those for Wg-fusion. The error in the cross section due to an assumed 2 GeV error in the top mass is higher for s-channel than for t-channel, but this is outweighed by the advantage in the other sources of error.

The approximate breakdown of uncertainties from different components mentioned above is: $\sim \pm 5\%$ from scale in the b quark distribution function and from the strong coupling; $\sim \pm 10\%$ from PDF's, especially gluon distribution functions; $\sim \pm 5\%$ from the top quark mass.

2.3 Physics with Single Top

Although the cross section for single top is smaller than that for top pair production, as we shall see in later sections, it is important to pursue this study because single top production can be used to study and to measure top quark properties that are not accessible through $t\bar{t}$ pair production studies alone.

The three single top production processes contain the vertex of the Standard Model $(t - W - b)$, as shown in Fig. 2.7, and thus are sensitive to any possible modification of this vertex from physics beyond the Standard Model, and to the Cabibbo-Kobayashi-Maskawa (CKM) parameter V_{tb}. In the sections below we will give an overview of the information that we can extract from single top within the Standard Model and the kind of new physics one could expect beyond the Standard Model.
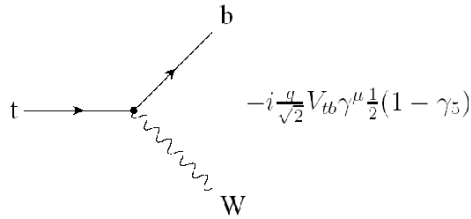
Figure 2.7: $t - W - b$ vertex that appears in single top production.

2.3.1 Within the Standard Model

Within the Standard Model, the single top production cross section is proportional to the quark-mixing matrix element V_{tb}, providing a probe of the charged-current weak interaction connecting top to the down-type quarks. Also because of the weak interaction, single top quarks are produced with nearly 100% polarization, which serves as a test of the $V - A$ structure. We will now study these effects in more detail.

CKM Matrix Element V_{tb}

There are several ways to obtain indirect information on V_{tb}. One way would be to look at $t\bar{t}$ production which contains two $t - W - b$ vertices in its decay. Although this is the dominant mechanism for producing top quarks at the Tevatron and LHC, it cannot be used to make a direct measurement of V_{tb}.

Within the Standard Model framework V_{tb} is known very precisely, but indirectly [54], from the unitarity of the CKM matrix,

$$|V_{ub}|^2 + |V_{cb}|^2 + |V_{tb}|^2 = 1 \qquad \Rightarrow \qquad 0.9990 \leq |V_{tb}| \leq 0.9993.$$

Measurements from $t\bar{t}$ can provide a ratio of matrix elements:

$$\frac{B(t \to Wb)}{B(t \to Wq)} = \frac{|V_{tb}|^2}{|V_{td}|^2 + |V_{ts}|^2 + |V_{tb}|^2} \tag{2.1}$$

where we have already assumed that there exist only three generations (i.e the CKM matrix is unitary). Thus we can constrain V_{tb}. In fact, top quark pair production at the Tevatron has been used with this assumption to measure the above ratio to be [42]:

$$\frac{|V_{tb}|^2}{|V_{td}|^2 + |V_{ts}|^2 + |V_{tb}|^2} = 0.94^{+0.31}_{-0.24} \tag{2.2}$$

But what if there exist more than three generations? Well, in that case $|V_{tb}|$ becomes virtually unconstrained [54]:

$$0.08 \leq |V_{tb}| \leq 0.9993,$$

and the only information that Eq. 2.2 gives us is that,

$$|V_{tb}| \gg |V_{ts}|, |V_{td}|$$

V_{tb} can also be constrained by comparing precision electroweak measurements to loop corrections containing the $t - W - b$ vertex, but again, this is just a constraint, not a direct measurement. Within the Standard Model, a measurement of the single top cross section allows direct extraction of the Cabibbo-Kobayashi-Maskawa (CKM) matrix element $|V_{tb}|^2$. The CKM matrix element V_{tb} appears in the leading-order (LO) Feynman diagrams for t-channel production, s-channel production, and Wt-associated production (Fig. 2.7).

By measuring the rate of single top processes and combining this information with the value of the $t \to Wb$ branching ratio and top mass measurements, the absolute value of V_{tb} can be extracted.

Here, as previously discussed, since both production modes probe the top-quark charged current in different regions of Q^2 and have different advantages

for measuring V_{tb}, both of these modes should be pursued in order to get independent measurements of V_{tb}. Taking into account the uncertainties in the NLO cross section calculations, it is expected that V_{tb} will be measured to ($\pm 12\%$) via the s-channel process in Run II. This is comparable to the accuracy achieved via the t-channel, which has a smaller statistical uncertainty, but a larger theoretical uncertainty [37].

Polarization

The single top quark is produced through a left-handed interaction and therefore it is expected to be highly polarized. Because of the very small decay width, no hadronization occurs and spin correlations are directly passed on to the final decay products. Hence, single top quark production offers an opportunity to observe the polarization of top quarks.

It has been shown [55] that the top quark spin in each event follows the direction of the down-type quark momentum in the top quark rest frame. This is the direction of the initial $\bar{d}$-quark for the s-channel, and mostly the direction of the final d-quark for t-channel single top production. The above result follows directly from the properties of the polarized top decays when single top production is considered as a top quark decay going "backwards in time [56]." The differential decay width of a polarized top quark to a bottom quark and two leptons or two light quarks (from W boson) is given by a very simple formula in the Standard Model:

$$\frac{1}{\Gamma} \frac{d\Gamma}{d \cos \theta^*_{fp}} = \frac{1}{2}(1 + K_f \cos \theta^*_{fp}),$$

where θ^*_{fp} is the angle between the momentum direction of one of the final fermions f in the top rest frame and the direction of the top quark polarization vector. The coefficients K_f are equal to 1 for the down-type fermions l^+, d and s quarks, and to -0.31 for the up-type fermions ν_l, u and c quarks [57].

This means that the angle between the d-quark direction in the production processes and the charged lepton (or d, s-quark) direction from the top decay in the top rest frame is the best variable to observe maximal top spin correlations between single top production and subsequent decay. The NLO corrections do not change this property significantly. NLO corrections to the lepton factor K_l are very small, $-0.0015\alpha_s$ [58] and for the quark factor $K_{d,s}$ they are about -6% [59].

Charged Current Couplings

Finally, measurements of the charged-current couplings of the top quark may probe any nonstandard structure of the couplings and therefore provide hints of new physics [28, 29, 60]. Especially any deviation in the $(V-A)$ structure of the Wtb coupling would lead to a violation of the spin correlation properties [31].

2.3.2 Beyond the Standard Model

In the case of physics beyond the Standard Model, both s-channel and t-channel production are important in direct searches for supersymmetry and CP violation [61, 62, 63, 64, 65, 66, 67, 68, 69]. Both channels also contribute a significant background to all signals that include $W + $ jets with, or without, b tags. These backgrounds appear in a number of Higgs search channels, and other new physics, such as supersymmetry searches [70, 71, 72].

It is found that models that extend the Standard Model often predict large corrections to s-channel or t-channel production, but not to both [48].

Anything that produces an anomalous coupling [48, 73, 74, 75, 76, 77, 78, 79, 80], or flavor changing neutral currents [48, 81], between the top quark and any other quark, affects t-channel production, but only slightly

changes the s-channel production. On the other hand, any process that allows a new intermediate particle, such as strong dynamics [82, 83, 84, 85], a charged top-pion [48, 86, 87], Kaluza-Klein modes of the W [88], or a W' boson [48, 82, 89, 90, 91], would enhance s-channel production, but is highly mass suppressed in t-channel production [37].

Non-SM Resonances

One possible form of new physics in single top quark production is a resonance coupled to the top quark. Generically, W', a heavy vector boson with charge $Q = +1$ can affect the rate of single top production (in either $s-$ or t-channel processes) by contributing additional diagrams in which the W' is exchanged, such as those shown in Fig. 2.8.

Because the initial and final states are the same for both the W exchange and W' exchange diagrams, they can interfere at the amplitude level and thus the effect of the W' could either raise or lower the single top cross sections, depending on the relative sign of the couplings between the W and the fermions, and the W' and the fermions.

It is expected that the two modes of single top production will show a very different sensitivity to the presence of a W'. The s-channel (W^*) process can show a large sensitivity. Because of the time-like momentum, the exchanged W' can be close to on-shell, providing an enhancement from the W' propagator in the s-channel matrix element.

On the other hand, the t channel process requires a space-like momentum for the W' boson, and thus can never experience this type of resonant propagator enhancement. The additional t-channel diagram containing the W' will be suppressed by $1/M^2_{W'}$. In fact, s-channel single-top-quark production has been found to be the most sensitive probe of high-mass charged vector W'
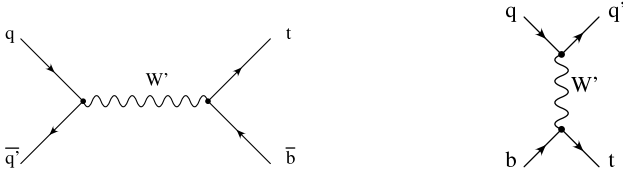
Figure 2.8: Feynman diagram showing how an additional heavy charged vector particle (W') can contribute to the s-channel process(Left) and t-channel process (right) of single top production.

bosons [92] at the Tevatron [93] and LHC [94].

Other types of heavy resonances can also be added to the Standard Model, such as those found in supersymmetry. But these are unlikely to affect s-channel ot t-channel cross sections in a large way, though they could modify the top's decay width and branching ratios. For example, a charged Higgs, $H^{\pm}$ could modify the top width by allowing decays such as $t \rightarrow H^+ b$, but would not affect the $s-$channel or $t-$channel rates because the Higgs couples very weakly to the light fermions.

Flavor Changing Neutral Currents (FCNC)

It is also possible that the top quark couples differently to light particles from what is predicted by the Standard Model [95, 96, 97, 98, 99]. For example a flavor-changing neutral current (FCNC) could couple the top to the charm quark and the Z boson (Fig. 2.9). This form of new physics will allow new decay modes for the top quark, and thus will modify the top quark's full decay width, $\Gamma(t \rightarrow X)$, and will cause its branching ratio $BR(t \rightarrow bW^+)$ to deviate from the Standard Model prediction of $\sim 100\%$, by allowing new decay modes such as $t \rightarrow Zc$.

Since, for the Standard Model t-channel production mechanism, the distri-
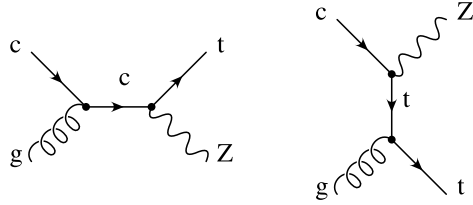
Figure 2.9: Feynman diagrams indicating how an anomalous Z-t-c vertex can produce the additional mode of single top production, $gc \to tZ$

bution of charm quarks in the proton is larger than the distribution of bottom quarks (Fig.2.4), this contribution may be visible even if the FCNC Z-t-c vertex coupling strength is not large.
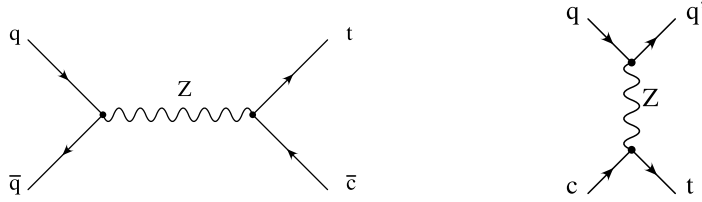
Figure 2.10: Representative Feynman diagrams showing how an anomalous Z-t-c vertex can contribute to the s-channel (left) and t-channel process (right) of single top production.

It is also possible for this FCNC vertex to modify the rate of $s-$channel and t-channel single top production through diagrams such as those shown in Fig. 2.10.

New physics can also appear in a form which may directly modify the W-t-b vertex. In this case, all three modes of single top production will show effects from the modification, as will the top's total decay width $\Gamma(t \to X)$, though the branching ratio $BR(t \to bW^+)$ will remain close to the Standard Model value of $\sim 100\%$. It would again be possible to use the W-gluon fusion mode to directly probe the top's partial width $\Gamma(t \to W^+ b)$. In this case, one could examine the s-channel production and W-gluon fusion rates separately in order

to probe the dependence of the modified vertex on Q^2, the momentum of the W boson, in the time-like and space-like regions, respectively. With enough statistics, the tW^- production mode could also be helpful in this regard, since this process is not sensitive to additional resonances, or to FCNC interactions.
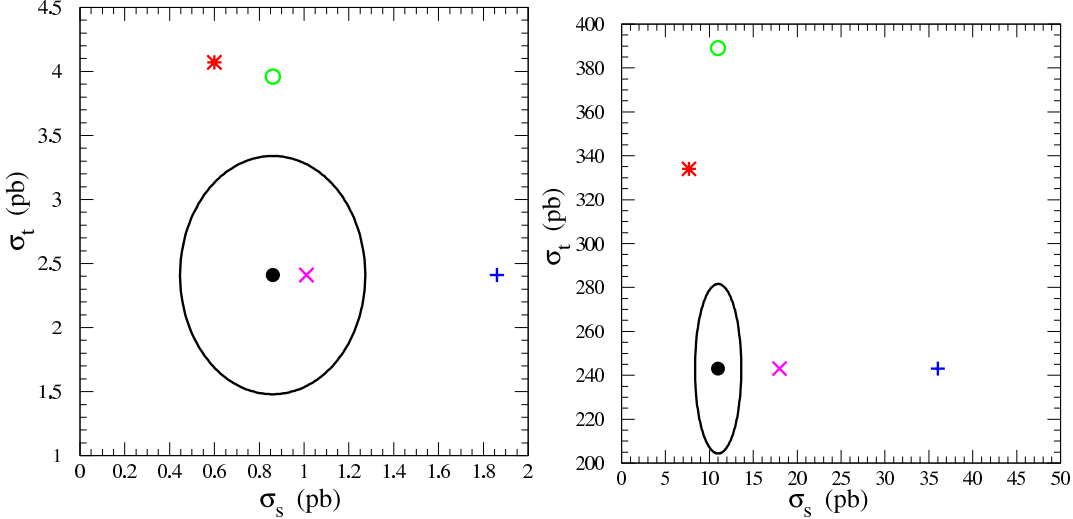
Figure 2.11: Left: The location of the $m_t = 175$ GeV SM point (the solid circle) in the σ_{W^*}-σ_{Wg} plane. The curve represents a 3σ deviation from this point. Also plotted are the results for the top-flavor model with $M_{Z'} = 1$ TeV and $\sin^2 \phi = 0.05$ (the X) and the FCNC Z-t-c vertex with $\kappa_{tc}^Z = 1$ (the open circle), a model with a charged top-pion ($m_\pi = 250$ GeV) (the +), and a four quark generation scenario with $|V_{ts}| = 0.55$ and $|V_{tb}| = 0.835$ (the asterisk). All cross sections sum the t and $\bar{t}$ rates; Right: Same for the LHC [37].

In order to see the effects of these different modes of new physics, a useful thing to look at would be the correlation of the two cross sections, σ_{W_s} and σ_{W_t}, in a two dimensional plane, as shown in Fig 2.11.

2.4 Single Top at the Tevatron

It has been shown [33, 35, 39, 100] that because of the difference in kinematics, it is possible to statistically disentangle the two sub-processes from each other, and from the Standard Model backgrounds expected in the Tevatron Run II.

The final state fermions from the top decay have relatively high transverse momenta and central pseudorapidities. Since the s-channel process involves the decay of a heavy virtual object, the $\bar{b}$ quark produced with the top quark is also at high transverse momentum and central pseudorapidity. On the other hand, the light quark in the t-channel appears at lower transverse momentum and at more forward pseudorapidities because it is produced when an initial state parton emits a virtual W boson. The $\bar{b}$ quark from t-channel initial state radiation appears typically at very low p_T and also at high pseudorapidities and is thus often not reconstructed experimentally.

Fig. 2.12 shows the transverse momenta (p_T) and pseudorapidities (η) for the partons of the s-channel and t-channel single top processes, after decay of the top quark and the W boson.

2.4.1 Signatures in the Detector

Combining the s- and t-channel cross sections, the total single-top production rate is about 40% of that of $t\bar{t}$, at both the Tevatron and the LHC. To observe single top is more difficult than observing $t\bar{t}$ pair production, not only because of the smaller production rate but more importantly because of the smaller multiplicity of final particles (leptons or jets) and the lower production threshold. As a result, signal to background ratios are far smaller for single top compared with top pair production. Therefore, extracting the signal from the backgrounds is significantly more complicated in a single top search.

43
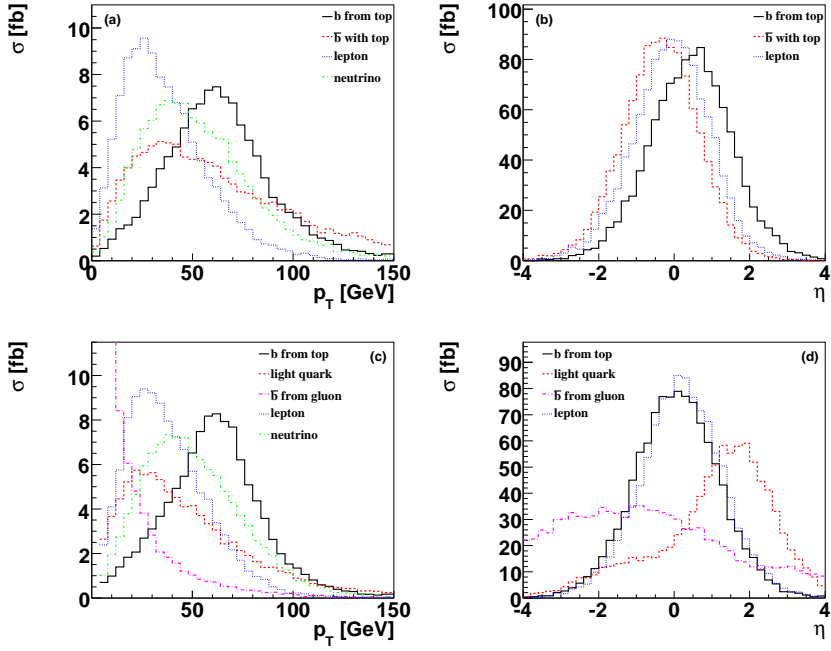
Figure 2.12: Distributions of transverse momenta (a,c) and pseu-
dorapidity (b,d) for the final-state partons in s-channel (a,b) and
t-channel (c,d) single top quark events. The histograms only in-
clude the final state of t, not $\bar{t}$ [101].

In both the production modes that we have discussed so far, at least one
W boson and one b jet are present in the final state. Although the branching
ratio of W to jets is much larger ($\sim 70\%$) than W's decay to any of the leptons
($\sim 10\%$), the W's decay to jets is a very difficult mode to detect in hadron
colliders because of the enormous QCD background. Hence our best bet is
to focus on the leptonic W-decay sub-channels. The final-state signatures of
a single top quark event, therefore, are characterized by a high-p_T centrally
produced isolated lepton (e or μ) and missing transverse energy ($\not{E}_T$) from a
neutrino from the decay of the W boson from the top quark decay, together
with two or three jets. One of these jets comes from a high-p_T central b quark

44
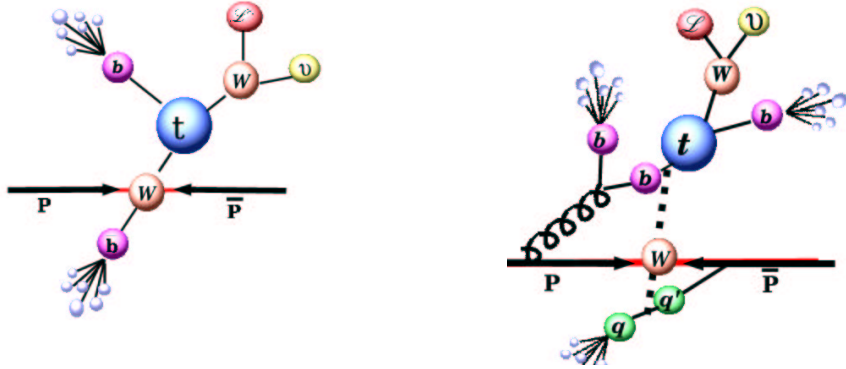
Figure 2.13: Drawings showing event signatures in the detectors:
Left, for s-channel; Right, for t-channel.

from the top quark decay (Fig. 2.13).

2.4.2 Backgrounds to Single Top Signals

Processes that can share this final state include W+jets events, $t\bar{t}$, $b\bar{b}$, multijet
events with a jet misidentified as a lepton, and some smaller contributions
from Z+jets and diboson events.

- *W+jets* events form the dominant part of the background. The cross
  section for $W+$ 2jets is over 1000 pb [102, 103] with a $Wb\bar{b}$ contribution of
  about 1%. The representative diagrams for W+jets and $Wb\bar{b}$ production
  are shown in the Fig. 2.14. W+jets, where jets are from light quarks,
  is kinematically different and is somewhat easier to deal with, especially
  after b-tagging. $Wb\bar{b}$, on the other hand, forms an irreducible background.

- *tt̄ pair production* NNLO cross section = 6.77±0.42 pb, for $m_t = 175$ GeV,
  $Q^2 = m_t^2$ has a larger multiplicity of final state particles than single top
  events, as shown in the Fig. 2.15. However, when some of the jets or
  a lepton are missed, the kinematics of the remaining particles are very
  similar to those of the signal. Here two different modes are important.

45
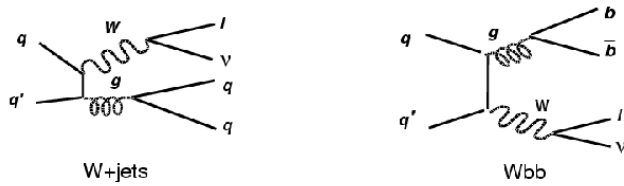
Figure 2.14: The representative diagrams for W+jets (left) and Wbb (right) production.

$t\bar{t} \to l + jets$, where the W from one top quark decays leptonically and other decays hadronically, and $t\bar{t} \to ll + jets$, where both W's from the tops decay leptonically.
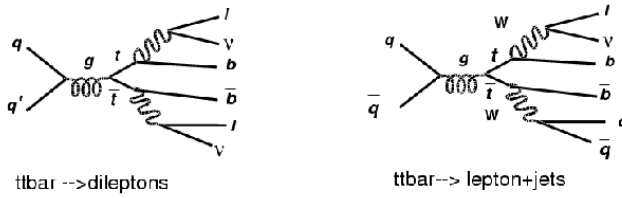
Figure 2.15: The representative diagrams for $t\bar{t}$ pair production: $t\bar{t} \to l + jets$ (right) and $t\bar{t} \to ll + jets$ (left).
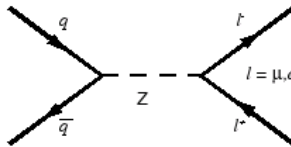
Figure 2.16: The representative diagram for the Drell-Yan process.

- $b\bar{b}$ production (resummed NLO cross section $= 58\,\mu$b, for $\sqrt{s} = 1.8$ TeV [105]) contributes to the background when one of the b's decays semileptonically and the electron or muon is mistaken for one from a W boson decay. In

46

the muon channel, $b\bar{b}$ events form a background when the muon travels wide of its jet and is reconstructed as an isolated muon, or when the jet is not reconstructed. This background in the electron channel is very small.

- *Multijet* events form a background in the electron channel when a jet is misidentified as an electron. The probability of such misidentification is rather small, about 10^{-4}, but the ≥ 2 jet cross section is so large that the overall contribution is significant.

WW production   **WZ production**

Figure 2.17: The representative diagrams for diboson production.

- *Z/Drell-Yan+jets* production [2] can mimic the single top signals in two ways. There are two isolated leptons (e^+e^- or $\mu^+\mu^-$) in the final state, as shown in Fig. 2.16, but if one is not reconstructed, then this results in missing transverse energy, which reconstructs as a W boson when combined with the other lepton. The second way that Z/DY+jets events create a background is when there are two muons in the final state. One accidentally overlaps a jet and is thereby identified as a tagging muon from a semileptonic b decay.

- *WW, WZ, ZZ* processes are the electroweak part of the W+jets and Z+jets backgrounds. Fig. 2.17 shows representative diagrams for diboson production. The cross sections are a few picobarns each. This electroweak

---

[2]The Drell-Yan process is an electromagnetic effect in which a quark and antiquark annihilate to give a lepton pair.

47

part of the W+jets and Z+jets processes has different kinematics than the W+(QCD) jets part.

Fig. 2.18 shows a graphical repersentation of the relative contributions of the main single top backgrounds. As you can see, the single top signal is almost invisible among all the backgrounds. The challenge is to understand very precisely the rate and kinematics of all processes, especially $W + jets$. Only with such understanding, and with enough data, we will be able to observe single top.
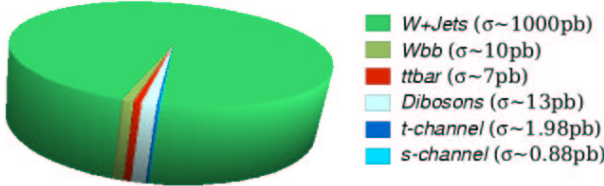
Figure 2.18: A pie chart showing relative proportions of these background and signal processes for single top . The production rates are shown here before any cuts.

2.5 Status of Single Top Searches

In Run I, the accumulated statistics of about 90 pb^{-1} was not enough to observe single top production, and the first limits on the cross sections were presented by both the DØ [106, 107] and the CDF [108] collaborations. At the 95% confidence level, the DØ limit on the s-channel was 17 pb and the CDF limit was 18 pb. At the same confidence level, the limit on the t-channel production cross section was 22 pb by DØ and 13 pb by CDF. CDF also published a combined limit of 14 pb.

	Limit on Cross Section [pb]at 95% C.L.			
	DØ		CDF	
	Run I	Run II	Run I	Run II
$s - channel$	< 17 pb	< 6.4 pb	< 18 pb	< 13.6 pb
$t - channel$	< 22 pb	< 5.0 pb	< 13 pb	< 10.1 pb
$s + t$	—	—	< 14 pb	< 17.8 pb

Table 2.2: Limits on single top production cross section set by DØ [101] and CDF [110].
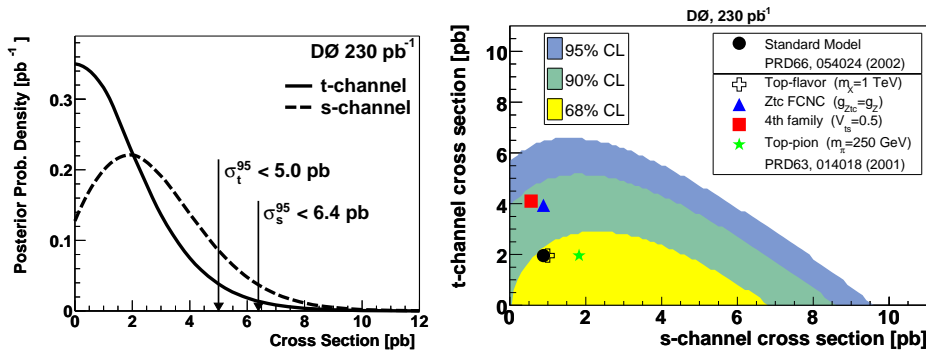
Figure 2.19: Left: The observed posterior probability density for the s-channel and the t-channel searches, as a function of the single top quark cross section; Right: Exclusion contours at 68%, 90%, and 95% confidence level on the observed posterior density distribution as a function of both the s-channel and t-channel cross sections. Several representative non-standard model contributions from Ref. [48] are also shown [101, 109].

For Run II the search is on. Both the DØ and the CDF collaborations have gone through first rounds of analyses and have set limits on the cross section (Table.2.2). We (DØ) published our first Run II results [101], with about 230 pb^{-1} of data, using neural networks to separate signal from overwhelming background. As you can see from the Table 2.2 that these limits are lot

more stringent than any previous analysis. The observed posterior probability densities as a function of the s-channel and t-channel cross section are shown in Fig. 2.19. Also contours of observed posterior density in the σ_s versus σ_t plane are shown. To illustrate the sensitivity of this analysis to different contributions, the expected SM cross section as well as several representative non-SM contributions are also shown.

The analysis presented in this thesis is a step further in this direction. We are using about 360 pb^{-1} of data with improved Neural Network analysis.

Chapter 3

Experimental Setup: the Tevatron and the DØ Detector

The strongest arguments prove nothing so long as the conclusions are not verified by experience. Experimental science is the queen of sciences and the goal of all speculation.

Roger Bacon

3.1 Accelerating the Particles

To find new particles and to explore properties of the known subatomic particles, physicists accelerate particles to the highest possible energies, smash them together and then examine the debris of the collision. Particle accelerators are giant machines that may expand to miles. These giant tools of particle physics can accelerate particles to speeds very close to the speed of light.

Until the mid-fifties of the last century, cosmic rays were the best source of the elementary particle studies. The flux of cosmic ray protons with energies

in a few GeV range is something like one per cm^2 per minute per steradian. Comparing it with the 6×10^{30} protons per cm^2 per sec produced at CERN, where W and Z bosons were produced for the first time, one can imagine where we would stand if accelerators were not discovered!
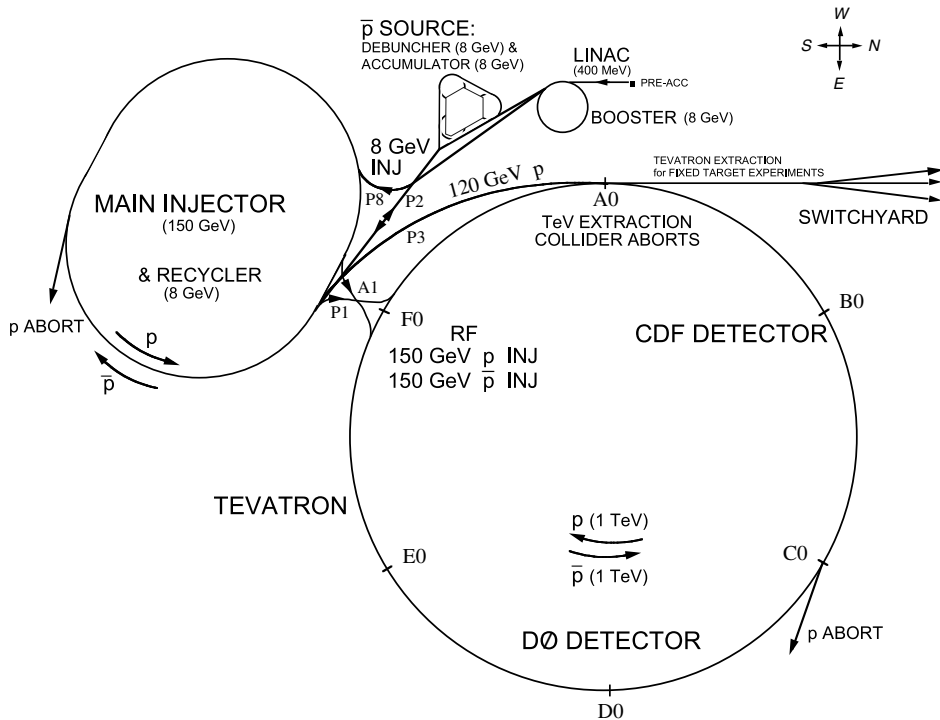
Figure 3.1: Fermilab's Accelerator Complex.

The analysis presented in this thesis used data collected from the collisions of proton and antiproton beams accelerated by the Tevatron accelerator at Fermilab near Chicago (USA). The Tevatron, the world's first superconducting synchrotron, started working as a proton-antiproton collider in 1985. At present, the Tevatron is the world's highest energy accelerator. The oppositely traveling beams of protons and antiprotons, with the center of mass energy of

1.96 TeV, collide at two different points on the the ring, where two 5,000-ton detectors, CDF and DØ, track and record the subatomic particles that emerge from these collisions. In late 1997, the laboratory ended Tevatron Run I, in order to make major improvements to the accelerator complex and the two big collider detectors.

The upgraded Tevatron complex [111], shown in Fig. 3.1, consists of five major accelerators and storage rings linked together. The main parts are:

The Proton Source - consists of the hydrogen ion source, the 750 keV Cockroft- Walton voltage multiplier, the 400 MeV Linac and the Booster Synchrotron which accelerates protons up to 8 GeV.

The Antiproton Source - to produce antiprotons, 120 GeV protons are produced in the main injector and are made to collide with a nickel target. These collisions, among other things, produce many antiprotons. The antiproton source consists of the antiproton production target, debuncher storage ring, accumulator storage ring and recycler storage ring, all operating at 8 GeV energy. So the final product here is 8 GeV $\bar{p}$'s.

The Main Injector Synchrotron - accelerates the incoming 8 GeV protons and antiprotons to 150 GeV.

The Tevatron - accelerates 150 GeV protons and antiprotons to almost 1000 GeV (1 TeV).

The main injector and recycler are physically located in the same tunnel enclosure and each has a two mile circumference, one half that of the four mile circumference of the Tevatron's superconducting magnet ring. The Tevatron complex has the design capability to operate in several modes for physics research, including 1 TeV × 1 TeV colliding protons and antiprotons, 1 TeV proton beam on a fixed target, 120 GeV protons (from the Main Injector) on

a fixed target, and 8 GeV protons on a fixed target.

The proton and antiproton beams consist of 36 equally spaced bunches circulating in the Tevatron tunnel. The two beams circulate in the opposite directions. The bunch spacing is 396 ns. The main Tevatron parameters for Run II are summarized in Table 3.1.

The information on a specific interaction, produced when particle beams collide, is contained in a number called the *cross section (σ)*. Cross sections can be measured experimentally and calculated from theory. It is, basically, the probability that a particular fundamental interaction will take place in the collision. The number of events of a particular kind expected to be produced per second is given by:

$$\text{Number of events per second} = \mathcal{L} \times \sigma,$$

where $\mathcal{L}$ is the luminosity of the colliding beam. Luminosity is a performance measure of colliding beams that is independent of any specific fundamental particle interaction. It contains the information of the incoming particle flux, the number of incoming particles per second, and the number of target particles per unit area, which is the colliding, or target beam.

$$\mathcal{L} = \frac{B N_p N_{\bar{p}}}{\beta \epsilon}$$

Where B is the number of bunches per beam, N_p ($N_{\bar{p}}$) is the number of protons (antiprotons) in a bunch, ϵ is the emittance (95% of the beam area), and β is the effective beam overlap area of the two bunches when they collide.

A commonly used number is *integrated luminosity* which is given by

$$\text{Integrated Luminosity} = \int \mathcal{L} \, \text{dt} \, ,$$

and is the luminosity, integrated over the total time a high energy particle physics experiment has run. Integrated Luminosity, when multiplied by the cross section, gives the number of events of that kind that the experiment

Energy per Beam	980 GeV
Number of Bunches per Beam	36
Bunches Spacing	396 ns
Protons per Bunch	2.7×10^{11}
Antiprotons per Bunch	7.5×10^{10}
Antiprotons Stacking	2×10^{11} per hour
Total Antiprotons	1.98×10^{12}
Typical Instantaneous Luminosity	2.0×10^{32} $cm^{-2}s^{-1}$
Typical Integrated luminosity	41.0 pb^{-1} per week
Interactions per Crossing	5.8 - 2.0

Table 3.1: Tevatron running conditions for Run II [112]

should have seen, which means, the physics productivity of an accelerator depends on the maximum luminosity that it can give and how long it can run at that luminosity.

In the last 4 years, since the Tevatron started its Run II, about 1000 pb^{-1} of usable data has been recorded by $D\emptyset$, as shown in the Fig. 3.2, and more than 4 fb^{-1} of data are expected to be recorded during Run II.

3.2 Interaction of Particles with Matter

When beams of protons and antiprotons collide at a point in space and time, at nearly the speed of light, protons and antiprotons burst into showers of secondary particles with different energies, emitted at different angles and momenta.

The detector, basically, has to perform two tasks. The first task is to look at the different particles that are coming from a collision, and record differ-
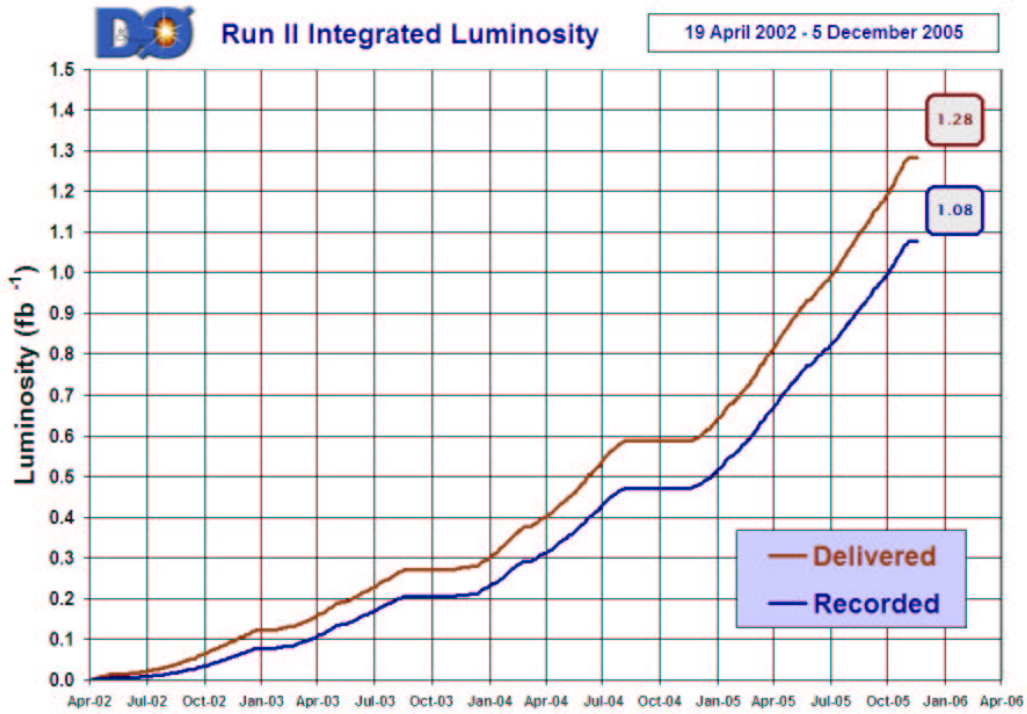
Figure 3.2: Integrated Luminosity: Recorded and Reconstructed
at DØ

ent signatures that different particles make in different parts of the detector
or to measure the time and location of interaction, the vector momenta P_i,
and charge of these emitted particles. The detector's second task is to decide
which of the millions of collisions that occur each second are worth recording.
Because it would be impossible to save them all. A combination of hardware
and software is used to *trigger* the recording of a particular event of interest
depending upon the different signatures that it makes in different parts of the
detector, thus keeping only the most interesting collisions in detail for later
analysis.

In the light of above requirements, to understand the working of the DØ
detector, remaining sections of this chapter have been divided in to three parts:

- How different particles behave when they pass through matter, which, in turn, explains the necessity of having ,

- Different parts of our detector, and finally,

- How to keep only the interesting events out of the millions of events that are being produced every second.

An event is analyzed by looking at its long lived products like electrons, photons, muons, hadronic particles and neutrinos. These particles interact in different ways with the material they pass through, and this difference in behavior is what is used to detect a certain particle and to differentiate it from others. Below we briefly discuss the interactions of different particles with matter. For more details see Ref. [8].

Electrons and Photons

High energy electrons passing through matter lose energy primarily through bremsstrahlung. The emitted photons produce electron-positron pairs, which in turn emit photons. The resulting shower of electrons and photons grows until the energy of the electrons falls below the critical energy,

$$E_c = \frac{800}{Z + 1.2} \text{ MeV}$$

where Z is the atomic number of the medium. Below the critical energy, energy loss is primarily by ionization. The mean distance over which an electron loses all but $1/e$ of its energy is called the radiation length X_0. A fit to the data gives [8],

$$X_0 = \frac{716.4A}{Z(Z+1)\ln(287/\sqrt{Z})} \text{ g cm}^{-2}$$

57

where A is the atomic mass of the medium in $\mathrm{g\,mol^{-1}}$.

Photons interacting with matter produce electron-positron pairs, and hence an electromagnetic shower. Thus, in the detctor, an electron appears as a charged track plus an electromagnetic shower, and a photon, being chargeless, appears as an electromagnetic shower only.
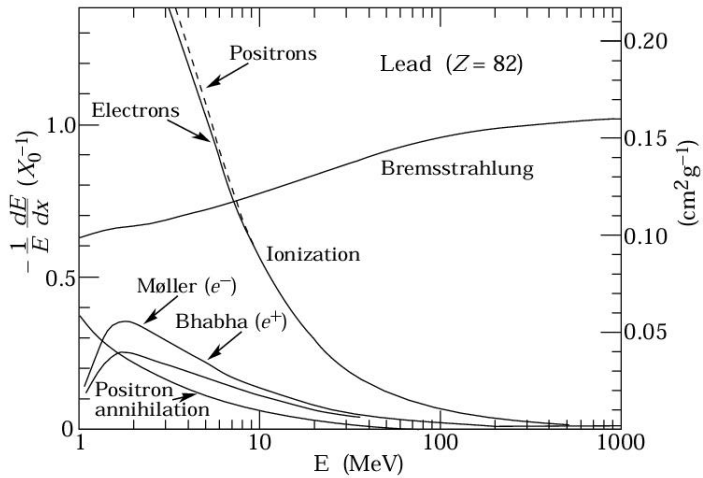
Figure 3.3: Fractional energy loss per radiation length in lead as a function of electron or positron energy [8].

Muons

Muons, because they are much heavier than electrons, interact through bremsstrahlung at a much lower rate than electrons. Their energy loss is primarily through ionization. Fig. 3.4 shows the energy loss of muons for various energy regimes. We see that for the energy range of $\sim$ GeV, muons at the Tevatron are minimum ionizing particles, also called MIP's. They deposit only minimal energy in the central detector and, like neutrinos, can pass through several meters of thick material without leaving (almost) any traces. Thus, in

the detector, a muon will appear as charged track that penetrates most of the material of the detector.
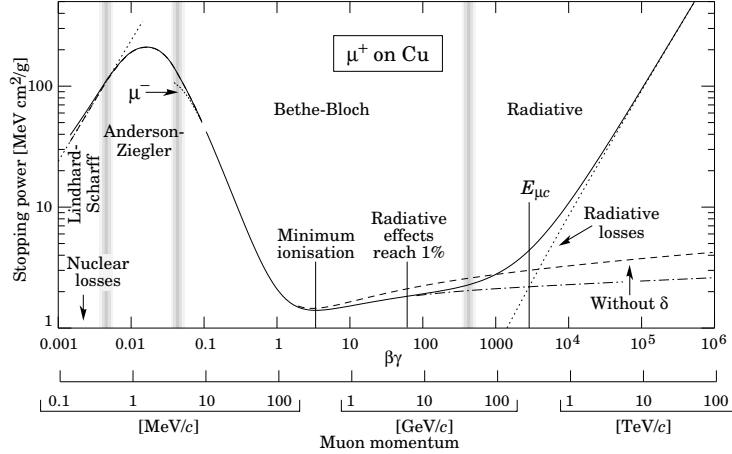
Figure 3.4: Energy loss through ionization of muons in various energy regimes [8].

Hadronic Particles

Low-energy hadrons lose energy in matter primarily by electromagnetic ionization and atomic excitation. At high energies, hadronic interactions result in the production of secondary (less massive) hadrons, e.g. pions. These interactions often result in a hadronic shower or cascade of secondary particles.

The characteristic length scale for strong interactions is the nuclear interaction length, which is dependent on the material density and atomic mass and is roughly independent of energy:

$$\lambda_I \approx 35 \ A^{1/3} \ \mathrm{g \ cm^{-2}}$$

This interaction length is longer than the radiation length, allowing hadrons to penetrate further into material than electrons and photons, before showering.

59

A significant fraction of the energy of the initial hadron escapes the hadronic cascade in the form of neutral pions, which produce a secondary cascade. A smaller fraction results in invisible energy loss through the unbinding of nuclei by spallation, non-ionizing collisions and uncaptured energy of neutrinos.

Neutrinos

As uncharged leptons, neutrinos interact only weakly via W and Z boson exchange, making their energy loss negligible and their direct detection practically impossible at DØ. However, their presence can be inferred from transverse momentum conservation requirements.

3.3   DØ Detector

The DØ detector is a general purpose detector, which makes use of many detection technologies at the same time, and therefore, consists of many individual sub-detectors. These individual sub-detectors can mainly be divided into two categories - ones that let a particle pass but keep track of its direction and momentum, and others that simply capture them and measure the energy lost by these particles. Here we give a brief account of the major parts of the DØ detector based on the material in Ref. [113]. For details see Refs. [114, 115, 116, 117, 118, 119].

In the detector description and the data analysis, we use a right-handed coordinate system in which the z-axis is along the proton beam direction and the y-axis is upward, as shown in Fig. 3.5. The x-axis then points toward the center of the accelerator ring. The angles ϕ and θ are the azimuthal and polar angles, respectively, with $\theta = 0$ along the proton beam direction. The r coordinate denotes the perpendicular distance from the z axis.
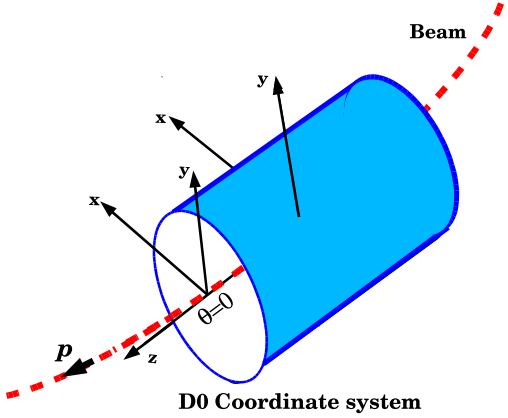
Figure 3.5: The DØ coordinate system.

An important thing to note here is that, since some particles escape down the beam pipe and the initial momentum of the interacting partons is not known, the quantities of interest tend to be momentum, energy and missing energy in the direction perpendicular to the beam axis — i.e. transverse momentum (p_T), transverse energy (E_T), and missing transverse energy $(\not{E}_T)$.

Another quantity of great interest in hadron collision experiments is the rapidity y,

$$y \equiv tanh^{-1}\beta_z = \frac{1}{2}\ln\{\frac{E+p_z}{E-p_z}\} = \ln\{\frac{E+p_z}{m_T}\}$$

where $\beta_z(= v_z/c = p_z/E)$ is the relativistic longitudinal velocity, p_z is the longitudinal momentum and m_T is the transverse mass of the particle ($m_T^2 = m^2 + p_T^2$). The good thing about this quantity is that it is additive under longitudinal Lorentz boost. In hadron collision experiments, the center of mass of the parton-parton scattering is generally boosted along the longitudinal direction with respect to the incoming hadrons. Therefore, it is convenient to discuss the longitudinal distributions of final state particles in terms of rapidity, which transforms simply under a longitudinal boost [8, 122].

In the non-relativistic limit $(v \ll c)$, the rapidity y reduces to longitudinal
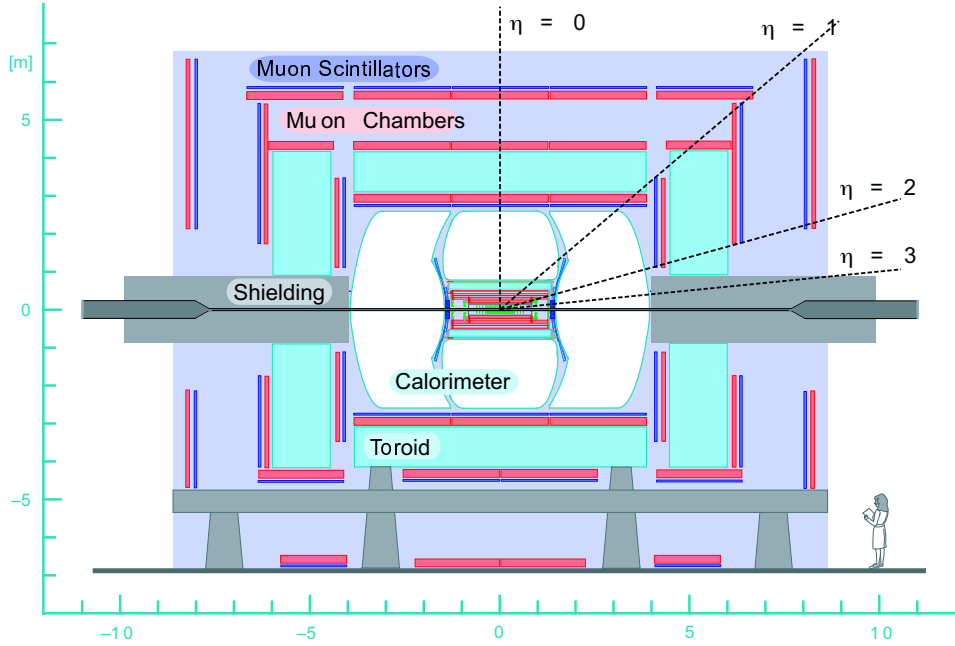
Figure 3.6: X-section view of the DØ Detector [121]

velocity v_z. In the case of large velocities, i.e $m \ll p$, the rapidity can be approximated as "pseudorapidity", given by,

$$\eta = -\ln\{\tan(\frac{\theta}{2})\}$$

Pseudorapidity η is the quantity normally used in high energy experiments instead of rapidity y.

A cross section of the DØ detector is shown in Fig. 3.6. There are four individual detectors that are used for tracking, shown in Fig. 3.7. These are immersed in a strong magnetic field (from a solenoid which provides a nearly uniform 2T magnetic field parallel to the beam axis) that makes the path of charged particles curve. The tracks of higher-energy particles curve less than those of low-energy particles. We can measure the momentum of the particles

62
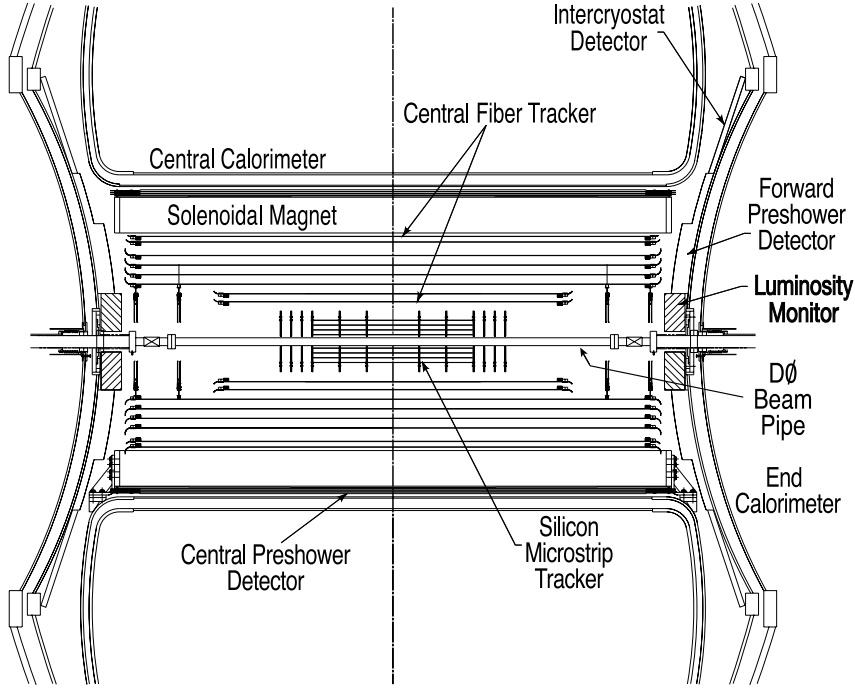
Figure 3.7: X-section view of the dzero Detector, showing different parts of the tracker [113].

by looking at the curvature of the particle tracks in the magnetic field,

$$R = p/qB$$

where R is the radius of curvature, B is the magnetic field, m and v are the mass and the velocity of the particle, respectively.

Ouside the tracker is the calorimeter which measures the energy of electrons, photons and hadrons. The outermost part is the muon detector.

3.3.1 Silicon Microstrip Tracker (SMT)

The silicon microstrip tracker (SMT) is the sub-detector that is closest to the beam pipe. It makes the precision measurements of track positions that are crucial for the accurate measurement of impact parameters and the

63
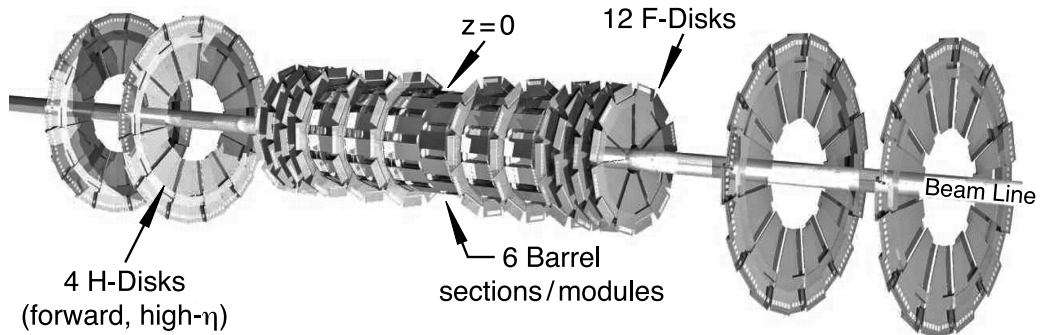
Figure 3.8: Disk and Barrel design of the Silicon microstrip tracker. [123]

identification of primary and secondary vertices. The SMT consists of 3.0 m^2 of silicon.
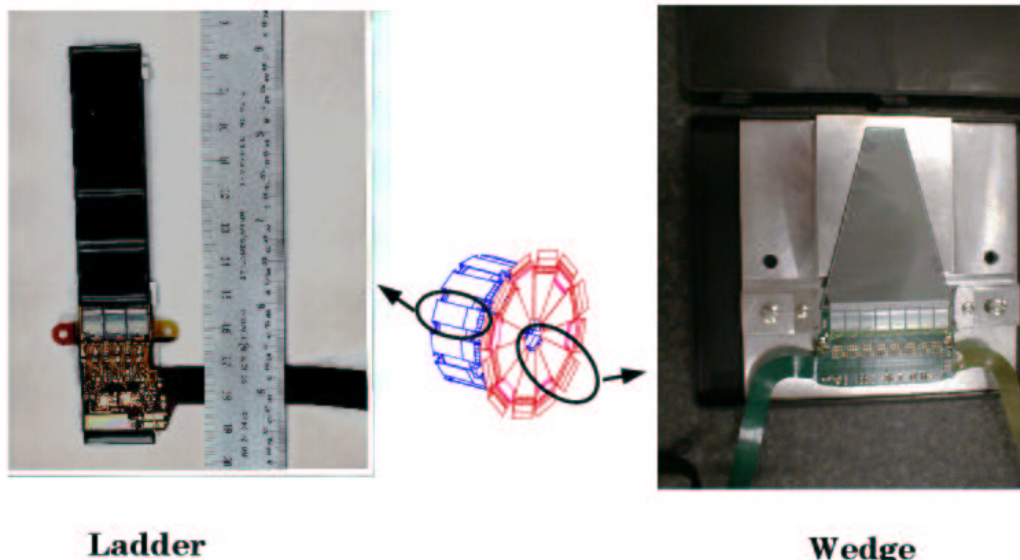
Ladder   **Wedge**

Figure 3.9: Individual Ladder and Wedge detectors [123].

The design of the SMT is shown in Fig 3.8. Here silicon modules installed in the barrels are called "ladders." Layers 1 and 2 have twelve ladders each; layers 3 and 4 have twenty-four ladders each, for a total of 432 ladders. Each barrel is capped at high $|z|$ with a disk of twelve double-sided wedge detectors, called an "F-disk." In the far forward and backward regions, two large-diameter disks, "H-disks," provide tracking at high $|\eta|$. Barrel and wedge detectors are shown in Fig. 3.9 . There are 912 readout modules, with 792,576 channels.

The barrel detectors measure primarily the $r - \phi$ coordinate and the disk detectors measure $r - z$ as well as $r - \phi$ coordinates. Thus vertices for high η particles are reconstructed in three dimensions by the disks. The vertices of particles at small values of η are measured in the barrels and central fiber tracker.
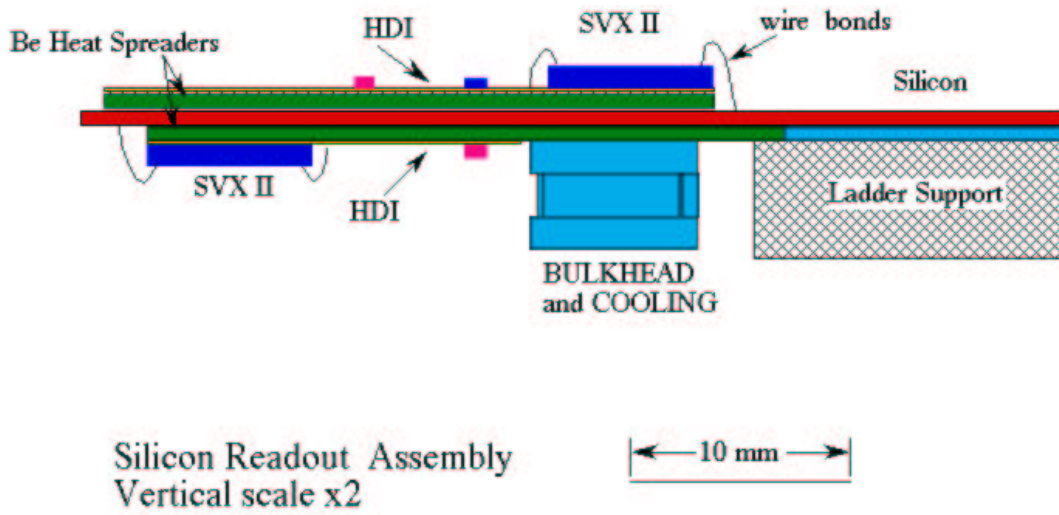
Figure 3.10: Readout chain for the Silicon microstrip tracker.

The SMT detector is made of wafers of n-type silicon and strips of p-type and n^+-type silicon strips. When charged particles pass through 300 μm of n-type wafers, they produce pairs of electrons and holes. The ionized charge

is collected by p-type or n^+-type strips.These provide for measurement of the position of the ionization in one dimension. The wafers have p-type strips parallel to the beam axis; many have n^+-type strips on the reverse side, placed at $2°$ or $90°$ for measurement in two dimensions.

Fig. 3.10 shows the SMT readout chain. The charges accumulated in the silicon strips are collected into arrays of capacitors by the SVXII read out chip, which holds the information from an event while a trigger decision is made. If the event is triggered, the charges are digitized and sent to the data acquisition system. The SVXII sequencer provides timing and control signals for eight chains of SVXII chips.

The silicon temperature is maintained below $5°$ C. The coolant is a water/30% ethylene glycol mixture supplied at $-10°$ C.

3.3.2   Central Fiber Tracker (CFT)

Outside the silicon tracker are the 8 concentric cylindrical layers of the central fiber tracker with radii ranging from 20 cm to 51 cm. Each layer consists of 2 doublets of fibers, thus making a total of 16 layers of fibers, as shown in Fig. 3.11. Eight of these sixteen layers are parallel to the beam, providing excellent resolution in ϕ and are called axial layers. The other eight, stereo layers, are placed at alternating angles of $\approx \pm 3°$ relative to the beam axis, which provides a measurement of the z position with less precision. The scintillating fibers were made into ribbons consisting of 256 fibers in two layers of 128 fibers each.

The scintillating fibers, including cladding, are 835 μm in diameter. They are optically connected to clear fiber waveguides of identical diameter. The scintillating fiber contains fluorescent dyes. The CFT uses about 200 km of
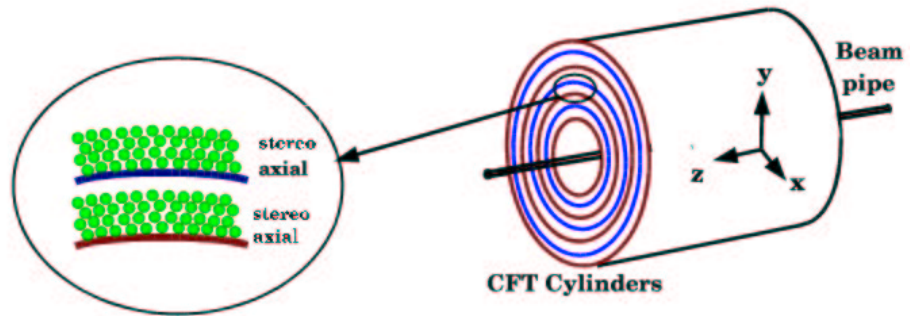
Figure 3.11: Schematic diagram of The CFT cylinders and axial and stereo layers.

scintillating fiber and 800 km of clear fiber.

Light production, caused by the passage of a charged particle through the fibers, is a multistep process which involves three types of materials.

- The base core material is doped with the organic fluorescent dye. The excitations in the base core material are rapidly transferred to the fluorescent dye.

- The fluorescence material has a rapid fluorescence decay (a few nanoseconds) and a short emission wavelength (≈ 340 nm). The mean free path of the emitted light is only a few hundred microns in the base core material.

- The wave-shifter dye is added to get the light out of the detector. It absorbs the 340 nm radiation from the fluorescent dye and re-emits it at 530 nm which is well-transmitted in the base core material.

Fig. 3.12 shows the readout chain for the CFT. Passage of a charged particle through one of the fibers produces light. We observe this light from only one end of each scintillating fiber. The opposite end is mirrored with an aluminum coating that provides a reflectivity of 85 to 90%. Light then, through the clear wave guides, reaches the visible light photon counters (VLPC's) housed in the

67
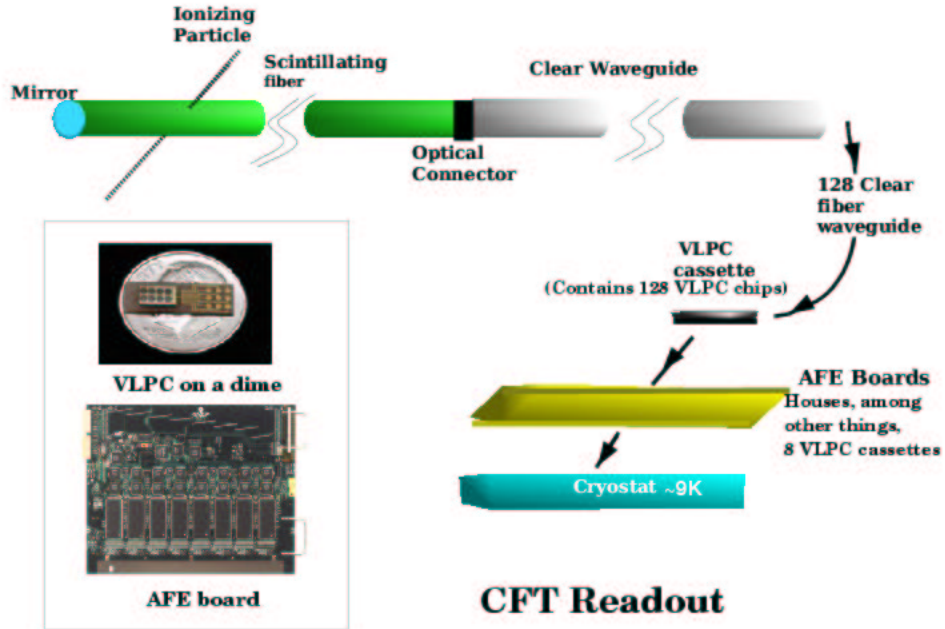
Figure 3.12: Readout chain for the Central Fiber Tracker. The
VLPC and AFE board photographs are from Ref. [124].

VLPC cassettes. VLPCs are silicon avalanche photo-detectors which convert
light into electrical signals. VLPC's are capable of detecting single photons
and provide fast response, excellent quantum efficiency ($\geq 75\%$), high gain
(17,000 to 65,000), low gain dispersion and the capability of functioning in a
high background environment. The only problem, being silicon based, is that
they require a low operating temperature of about 9 K

Each VLPC cassette consists of a cassette body housing eight modules.
Each module is composed of a 128-fiber bundle. Each VLPC, thus, provides
1024 (128 $\times$ 8 fibers) individual pixels of light-sensitive detector. The 128-
fiber bundle terminates at the top (warm) end in an optical connector, and

68

at the bottom (cold) end in sixteen groups of eight fibers. The fibers accept light from the clear fiber waveguides which are connected to the warm-end optical connectors at the top of the cassette and pipe the light to the VLPC's mounted in the cold-end assemblies.

From the VLPC's, the electrical signals are sent to the preamplifiers on the analog front end boards (AFE's) which are mounted on the cassette body. In addition to preamplifiers, the AFE's also provide trigger discrimination, temperature control, and bias-voltage control electronics. The temperature sensors and heaters are employed to control the temperature of the VLPC's to within 0.1 K.

On the AFE, the SVXII chip provides for the integration of the charge signals from the VLPC's, a pipeline for storing the signals while the trigger is formed, and digitization of the signals and sparsification of the digitized data for readout. Because the signals from the AFE are also needed for the trigger system, another chip, the SIFT chip, is used. Each SIFT chip has eighteen channels. The SIFT chips receive the signals from the VLPC's before the SVXII. For each channel, the SIFT has a preamplifier, which integrates the incoming charge, and switched capacitors, which are used to split the amplified signal and send it along two paths: one, to the SVXII, for later digitization and readout, the other to present the signal to a discriminator which fires if the charge exceeds a preset threshold (typically 10 to 15 fC).

For tracks traversing the detector at normal incidence, the thickness of each cylinder can be broken down as follows: 0.52% of a radiation length for the scintillating fibers, 0.32% for the carbon fiber support cylinder, 0.13% for the glue used to make ribbons out of fibers, and 0.17% for the glue used to attach the ribbons to the support cylinders.

The small-diameter scintillating fibers used in the CFT coupled with the
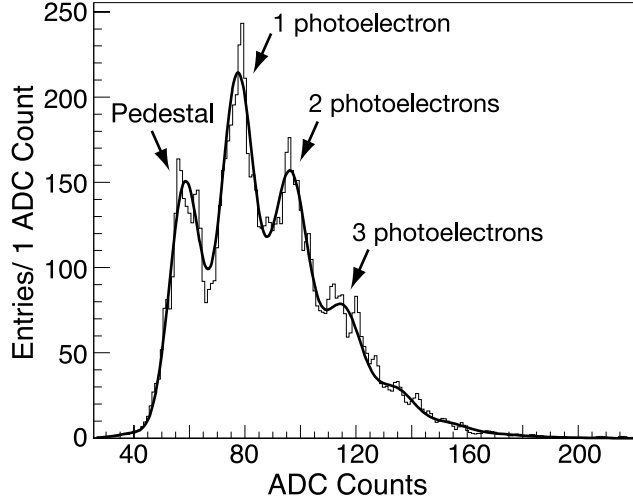
Figure 3.13: A typical LED spectrum for a single VLPC for an axial CFT fiber. The solid histogram is the data; the smooth curve is the fit [113].

long waveguides, necessary to direct the signals to the platform, cause the signals generated by the VLPC's to be small ($\approx$10 photoelectrons incident upon the VLPCs). To assure acceptable efficiency for triggers and tracking, the individual channel thresholds must therefore be set between 1.5 and 2 photoelectrons (pe). To maintain a low and stable threshold and to be able to distinguish individual photo-peaks during calibration, the analog signal must be digitized with a noise of less than 0.4 pe or about 2 fC. In fact, the front end electronics are able to achieve or exceed all requirements.

A typical LED spectrum for a single VLPC for an axial CFT fiber is shown in Fig. 3.13. Every channel is fit automatically and the parameters of the fit are extracted and used for monitoring. Typically, more than 97% of the axial channels are fit successfully. The mean pedestal width from fits to LED calibration spectra for all axial fibers is 0.24 pe or 1.6 fC and discriminator thresholds have similar noise and offsets of less than 2 fC so that it is possible to set the discriminator thresholds below 10 fC for most channels. For an

70

Central field	2.0 T
Operating current	4820 A
Integrated field homogeneity	$\pm 5.0 \times 10^{-3}$
Stored energy	5.6 MJ
Inductance	0.48 H
Cold mass	≈ 1500 kg
Thickness	0.9 X_0
Cooldown time	≤ 120 hours
Magnet charging time	≤ 30 minutes
Fast discharge time constant	≤ 15 seconds
Slow discharge time constant	≤ 330 seconds

Table 3.2: Main parameters of the solenoid used in the DØ detector [113].

instantaneous luminosity of 2×10^{32} cm^{-2}s^{-1}, the fiber-doublet hit efficiency is above 98%.

3.3.3 The magnet

Both the silicon tracker and central fiber tracker are surrounded by a superconducting solenoidal magnet. The magnet for the DØ detector was added for Run II and, therefore, is designed to optimize the momentum resolution, $\delta p_T / p_T$, and tracking pattern recognition within the constraints imposed by the existing detector. The main parameters of the magnet are given in Table 3.2

3.3.4 Preshower Detectors

Between the solenoid and the calorimeter there are two more scintillating fiber based detectors, the central preshower (CPS) and forward preshower (FPS) detectors. Both preshower detectors are made from interlocking trian-
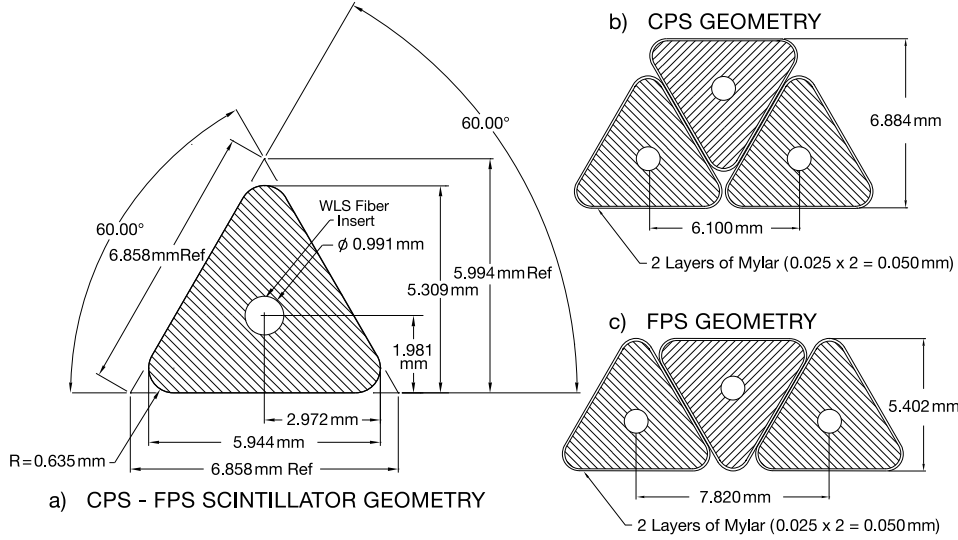
Figure 3.14: Cross section and layout geometry of the CPS and FPS scintilator strips [113].

gular strips of scintillator, as shown in Fig. 3.14. Because of this shape of strips, there is no dead space between strips and most tracks traverse more than one strip, allowing improved position measurement. At the center of each triangular strip is a wavelength-shifting (WLS) fiber which collects and carries the light to the edge of the detector. At the readout end, fibers are grouped into bunches of sixteen and potted into connectors for transition to clear light-guide fibers. Light is transmitted via the clear fibers to a VLPC for readout. The CFT and the central and forward preshower detectors use the same front-end electronics to process the signals from the VLPCs.

The CPS consists of three concentric cylindrical, one axial and two stereo, layers of triangular scintillator strips and is located in the 5 cm gap between the solenoid and the central calorimeter. Between the solenoid and the CPS is a lead radiator approximately 1 radiation-length (X_0) thick.

The two FPS detectors are each mounted on the spherical heads of the end calorimeter cryostats. Each detector is made from two layers, at different z,

of a double layer of scintillator strips, separated by a $2X_0$-thick lead-stainless-steel absorber.

The upstream layers are known as the minimum ionizing particle, or MIP, layers while the downstream layers, those behind the absorber, are called the shower layers. All charged particles passing through the detector will register a minimum ionizing hit in the MIP layer, allowing measurement of the location (in η, ϕ, and z) of the track.

3.3.5 The Calorimeter

Up to this point we have been using detectors that keep track of the particles produced in a given collision, without disturbing them in any way (except, of course, bending them in the magnetic field). These detectors were designed to trace the trajectories of the incoming particles, measure their momentum and charge, and reconstruct their vertices. The other important information that we need is the energy of these particles. Also, since the tracker is good for only charged particles, we need some kind of detector which can detect neutral particles too. The calorimeters are what we use to provide this information.

The DØ calorimeter is used for the identification of electrons, photons, jets and muons and to establish the transverse energy balance in an event.

The main parts of the DØ calorimeter are shown in Fig. 3.15. The central calorimeter (CC) extends in pseudorapidity to roughly $|\eta| = 1.1$, and the two end (forward) calorimeters, ECN (north) and ECS (south), extend coverage to $|\eta| \approx 4$. The active medium for all of the calorimeters is liquid argon and each of the three calorimeters (CC, ECN, and ECS) is located within a cryostat that maintains the temperature at approximately 80 K.

Each calorimeter system is divided into three sections, as shown in Fig. 3.16.

Electromagnetic calorimeter - designed to measure precisely the energy of
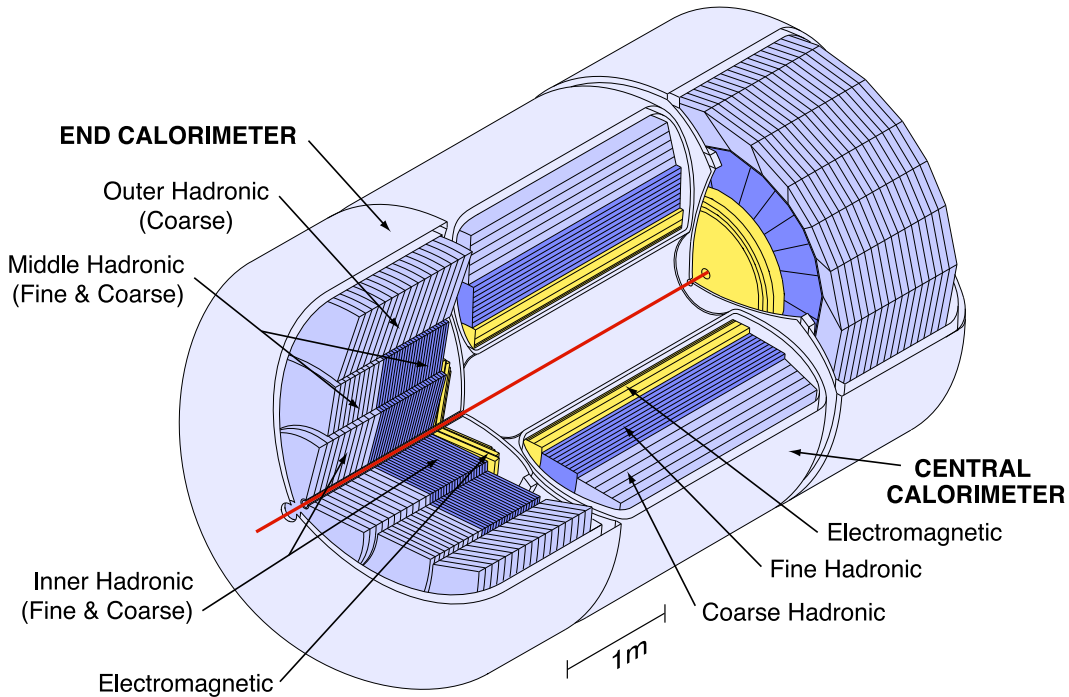
Figure 3.15: An Isometric view of the DØ central and two end calorimeter detectors, showing the organization of the calorimeter cells [113].

the electromagnetic particles. It contains in total 65.6 mm of uranium, which represents more than 20 radiation lengths ($X_0^{Ur} \approx 3.2$mm) to capture the overwhelming fraction of the electromagnetic energy. The electromagnetic calorimeter is further divided into four layers; the third layer is placed where the shower is expected to reach its maximum and the cells measure $\eta \times \phi = 0.05 \times 0.05$, to provide improved spatial resolution.

Fine Hadronic calorimeter - to capture hadronic particles. As the nuclear interaction length is much larger than the radiation length, ($\lambda_I^{Ur} \approx 10.5$cm $\approx 30X_0$), hadronic particles typically deposit most of their energy in the outer section of the calorimeter, which contains $\approx 6.4\lambda_I$ of uranium and copper. The fine hadronic calorimeter has 3 (4) layers of cells in the central (forward)

η=0.0   0.2   0.4   0.6   0.8   1.0
                                    1.2
                                    1.4
                                    1.6
                                    1.8
                                    2.0
                                    2.2
                                    2.4
                                    2.6
                                    3.2
                                    4.1
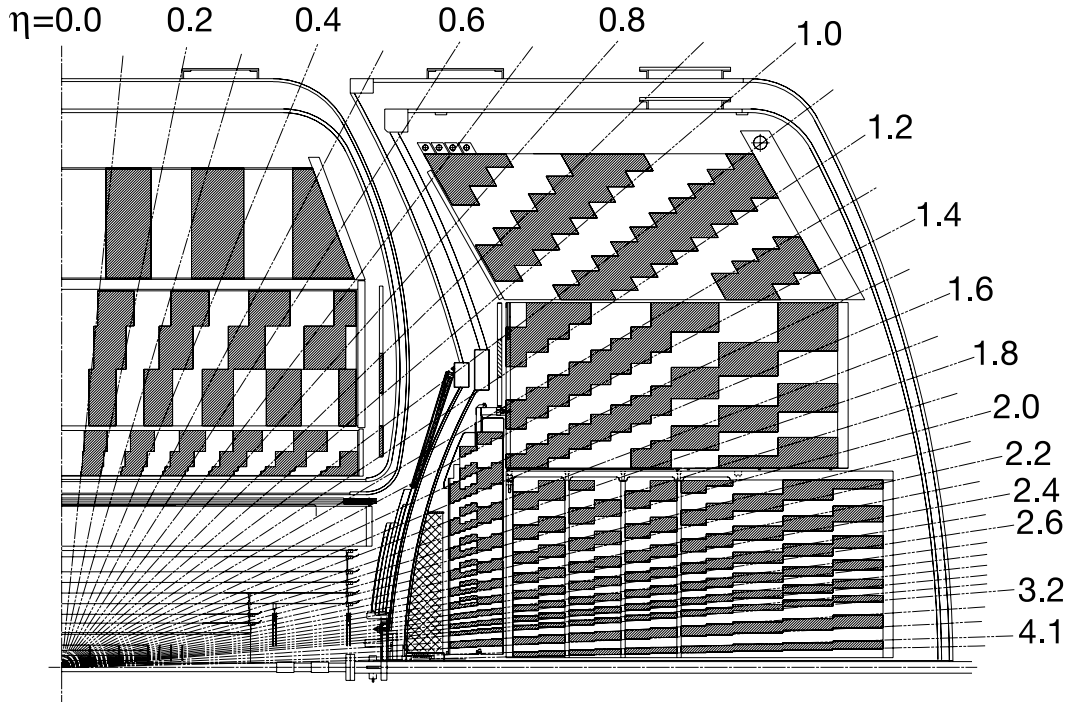
Figure 3.16: Schematic view of a quarter of the DØ calorimeter showing the transverse and longitudinal segmentation pattern. The shading pattern indicates groups of cells ganged together for single readout. The rays indicate pseudorapidity intervals from the center of the detector [113].

region.

Coarse Hadronic calorimeter - provides the final stopping power. Coarse hadronic modules are ganged into one or three layers.

The basic unit used for detection, a calorimeter cell, is shown in Fig. 3.17. Each cell contains absorber plates of depleted uranium (or copper), the active liquid argon and a copper readout pad for collecting the ionization. The surface of the pad is held at high voltage to function as an anode; the ionization of the

active material creates an image charge in the readout pad. When a particle enters a cell it first passes through absorber plates, producing electromagnetic and hadronic showers. The surviving fraction of the shower energy is sampled through ionization in active layers.
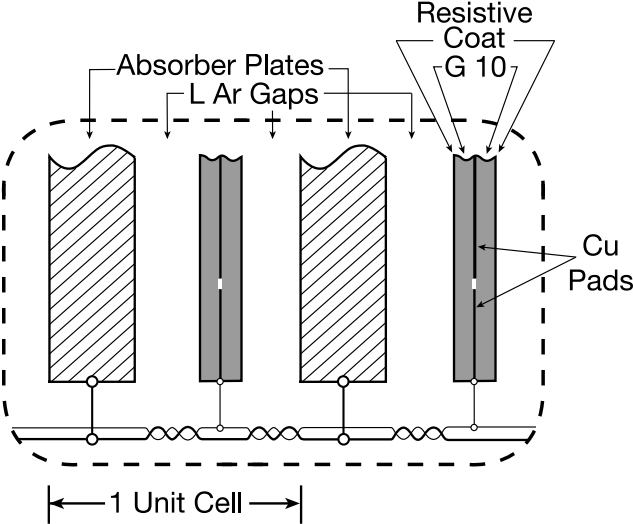
Figure 3.17: Schematic view of the unit cell for the calorimeter [113].

The energy of the particle is determined by adding up the signals from each cell. We can distinguish between different types of particles such as pions and electrons by noting the positions of the cells in which they deposit their energies. It is here that we can detect the neutral particles that left no trace in the tracking detector.

The calorimeter cells are arranged and sized such that each covers roughly an area of $\eta \times \phi = 0.1 \times 0.1$.

The transverse sizes of the readout cells are comparable to the transverse sizes of showers: 1–2 cm for EM showers and about 10 cm for hadronic showers. The scale in η and ϕ is set by the typical size of parton jets, $\Delta R = \sqrt{\Delta\eta^2 + \Delta\phi^2} \approx 0.5$. Segmentation finer than this is useful in prob-

76

ing the shapes of jets. Longitudinal subdivisions are useful since longitudinal shower profiles help distinguish electrons and hadrons.

There are 55,296 read out channels. The readout is accomplished in three stages.

1. In the first stage, the signals from the uranium-liquid argon detector are transported to charge preamplifiers located on the cryostats.

2. In the second stage, the signals from the preamplifiers are transported to the signal shaping and analog storage circuits (baseline subtracter boards or BLSs) located underneath the cryostats. The BLSs hold the signal for about 4 μs until the trigger is available, and provide baseline subtraction to remove any low frequency noise or pileup present in the signal. In addition, faster shaped analog sums of the signals are picked off to provide prompt inputs to the calorimeter trigger system for both the Level 1 and Level 2 trigger decisions.

3. The precision signals from the BLSs are sent over 130 m to analog-to-digital converters (ADC), and then enter the data acquisition system for the Level 3 trigger decision and storage to tape.

3.3.6 The Muon Chamber

Since muons do not undergo hadronic interactions but only lose energy by ionization, they are the only charged particles that can pass through the several meters of highly dense material present in the calorimeter. To detect these particles we have the muon detector which wraps around all the other detectors.

The detector, shown in Fig. 3.18, consists of following parts:

Toroidal Magnets Improve the momentum resolution for high momentum muons and allows for cleaner matching with central detector tracks. They also
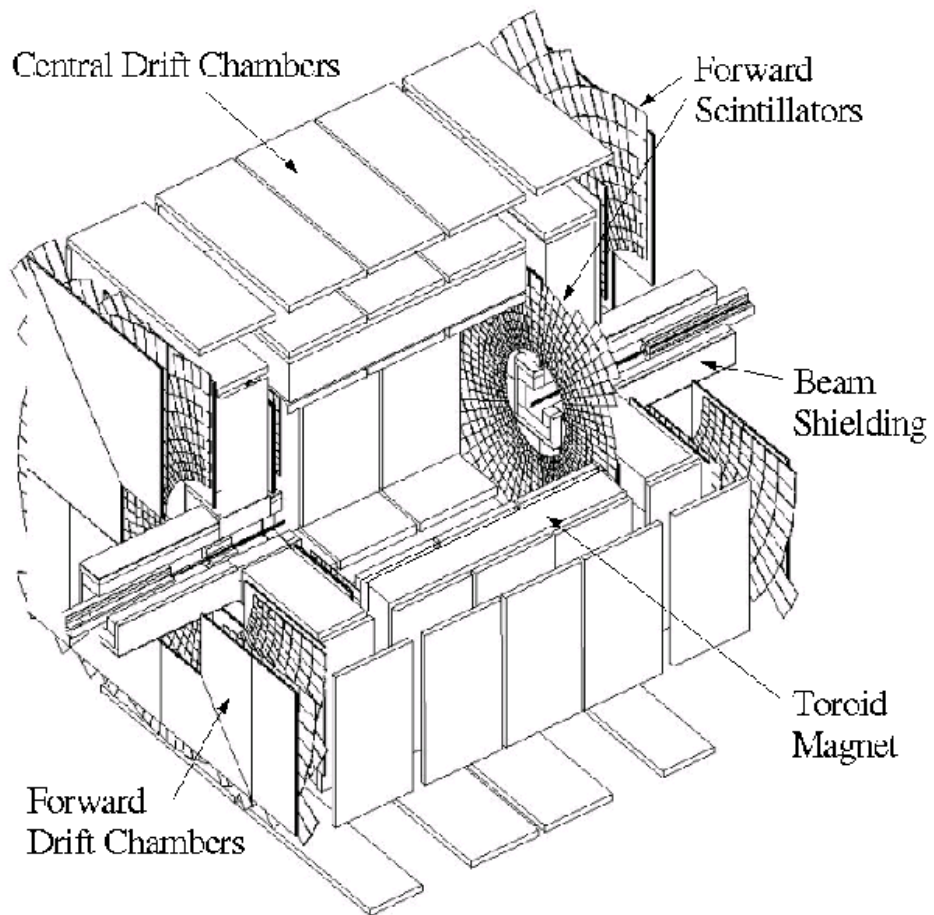
Figure 3.18: A cut-away view of the muon system.

help in rejection of π/K decays.

Proportional Drift Tubes (PDTs) The PDTs provide tracking coverage for $|\eta| \leq 1.0$ with an expected resolution of around 0.5 mm.

Mini Drift Tubes (MDTs) The forward muon tracking system uses planes of mini drift tubes and extends the muon detection to $|\eta| = 2.0$. The design of the forward muon system is made of individual tubes with 8 cells of 1 cm x 1 cm cross section, each holding one wire.

Scintillation counters Scintillator counters are installed both in the central and forward regions. These are used for triggering, cosmic ray veto, beam related muon rejection and track reconstruction.
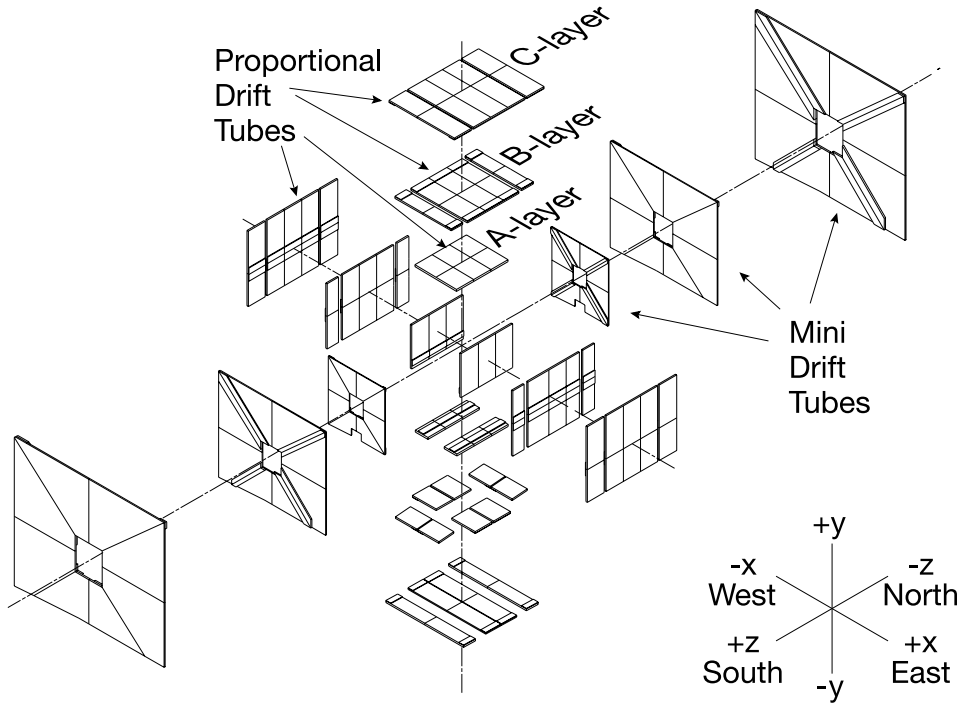
Figure 3.19: Exploded view of the muon drift tubes [113].

Each of the last three systems has three layers called A, B, and C with A being the innermost layer, as shown in Fig. 3.19. To measure the muon momentum a toroid magnet is placed between the layers A and B.

The detector thickness is in the range of 5-9 interaction lengths in the calorimeter, and in the range of 7-9 interaction lengths in the iron. The most probable value for the energy loss of a muon in the calorimeter is 1.6 GeV and

about 1.7 GeV in the iron. The momentum measurement is corrected for this energy loss.

3.3.7 Forward proton detector

The forward proton detector (FPD) measures protons and antiprotons scattered at small angles (on the order of 1 mrad) that do not impinge upon the main DØ detector. During Run I, such diffractive events were tagged using a rapidity gap (the absence of particles in a region of the detector), however a forward particle detector is necessary for access to the full kinematics of the scattered particle [113].

3.3.8 Luminosity Monitor (LM)

The primary purpose of the luminosity monitor (LM) is to determine the Tevatron luminosity at the DØ interaction region. This is a very important task as the precision of a cross section determination depends on the precision of the luminosity measurement. This is accomplished by detecting inelastic $p\bar{p}$ collisions with a dedicated detector. The LM also serves to measure beam halo rates and to make a fast measurement of the z coordinate of the interaction vertex.

The LM detector consists of two arrays of 24 plastic scintillation counters with photomultiplier tube (PMT) readout, located at $z = \pm 140$cm as shown in Fig. 3.20. The arrays are located in front of the end calorimeters and occupy the radial region between the beam pipe and the forward preshower detector. The counters are 15 cm long and cover the pseudorapidity range $2.7 < |\eta| < 4.4$.

Collision products will arrive at each set of scintillators roughly in coincidence, while beam halo products passing through the detector will appear distinctly separated.
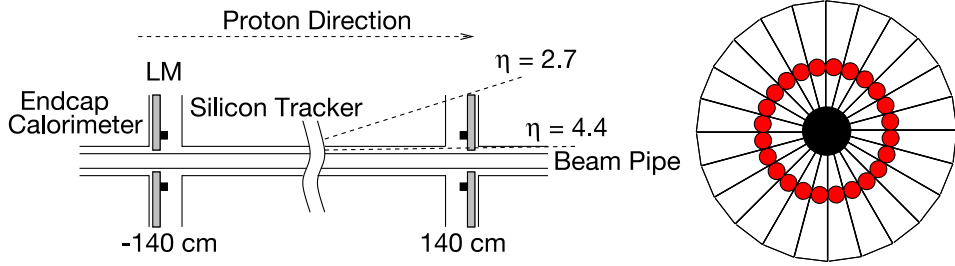
Figure 3.20: Schematic drawing showings LM. Left: the location of the LM detectors; Right: the geometry of the LM counters and the locations of the PMTs (solid red dots) [113].

The luminosity is determined from:

$$\mathcal{L} = \frac{fN}{\sigma}$$

where, f is the beam crossing frequency, σ is the effective cross section for the luminosity monitor, and N is the average number of inelastic collisions per beam crossing measured by the luminosity monitor. Since N is typically greater than one, it is important to account for multiple $p\bar{p}$ collisions in a single beam crossing. This is done by counting the fraction of the beam crossings with no collisions and using Poisson statistics to determine N.

3.3.9 Trigger

The rate of events being produced in the detector is extremely high (many millions per sec). Although, all the detectors we have described so far have very fast readouts, they are still not fast enough to read all the events taking place inside the detector and even if they could read all the events, there is not enough disk space to save them all. Also, most of the events produced in the detector are not interesting anyway, and we would like to get rid of them from the beginning. All these things lead to the necessity of having an efficient trigger system. The simple layout of the DØ trigger system consists of three

levels, as shown in Fig. 3.21. Each succeeding level examines fewer events but in greater detail and with more complexity.

The first level consists of hardware components, the second level uses both software and hardware, and the third level, which does a full event reconstruction, is based on software only.
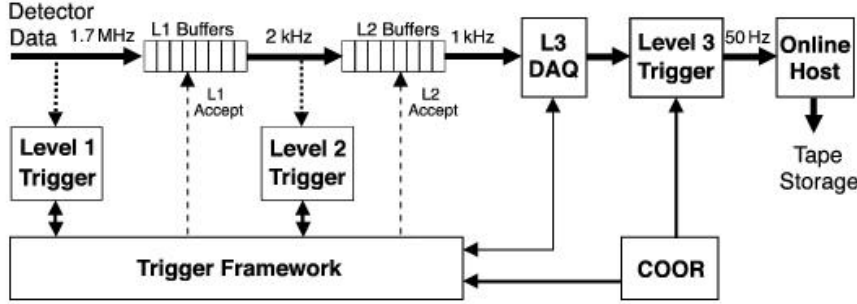
Figure 3.21: Simple layout of the DØ trigger system [113]

The level 1 trigger - Level 1 uses hardware to find tracks in the CFT/PS (called CTT trigger), transverse energy deposits and global missing energy in the calorimeter, and muon tracks in the muon system. The muon tracks can be required to be matched with CTT tracks, or trigger on the tracks independently. The level 1 trigger has only $4.2\mu s$ to make a decision and the rate should be reduced to 10 kHz, from an incoming rate of about 1.7 MHz.

The level 2 trigger - The Level 2 system is comprised of two stages, a preprocessor stage and a global trigger stage. The preprocessors identify objects such as tracks, electrons, jets and muons. The global stage allows the first opportunity to examine the correlation between objects, such as tracks and leptons. The Level 2 trigger has a time budget of 100 μs and must reduce the rate to 1 kHz.

The level 3 trigger - The Level 3 trigger is implemented entirely in software which performs an approximate reconstruction of the event and makes a trigger decision using the full event information. The Level 3 trigger has a time budget of 100 ms and must reduce the readout rate to 50 Hz.

The trigger system is closely integrated with the read out of data. Each event that satisfies the successive L1 and L2 triggers is fully digitized, and all of the data blocks for the event are transferred to a single commodity processor in the L3 farm. The L1 and L2 buffers play an important role in minimizing the experiment's deadtime by providing FIFO (First In First Out) storage to hold event data awaiting a Level 2 decision or awaiting transfer to Level 3.

3.4   Performance of the DØ Detector

The upgraded DØ detector started taking data in 2001. All subdetectors have been very stable and the data taking efficiency has always been 80-90%. Here we briefly discuss the efficiency of individual detectors and their combined effect on measuring different quantities.

At the Tevatron, some of the main particles of interest are the top quark, W and Z bosons. The top quark decays to a W and a b quark with the W decaying either to a charged lepton and a neutrino or to two jets. The b quark in this decay can be tagged by measuring the impact parameters of the decay products of the B particles. A typical distance between the primary and secondary vertex is $\sim 300\mu m$. The detector should be able to measure this distance. The resolution of the scintillating fiber doublet is ≈ 100 microns and the resolution of the silicon barrels is ≈ 10 microns. The transverse momentum
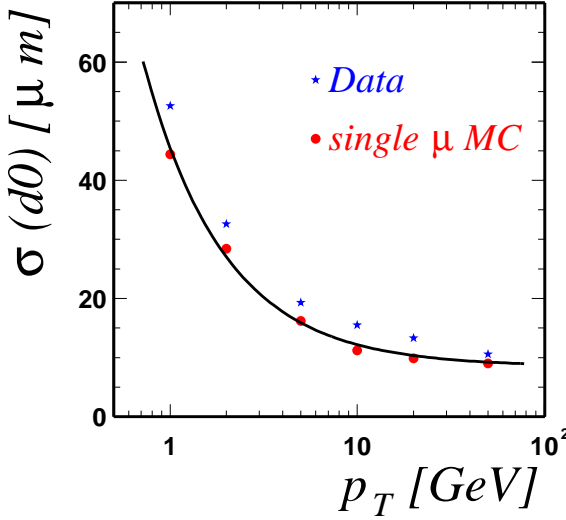
Figure 3.22: Impact parameter resolution measured in data (stars) and in simulated single muon events (dots). The line shows a fit to the MC.

resolution at pseudorapidity $\eta = 0$ may be parameterized as [114]:

$$\frac{\sigma p_T}{p_T} = \sqrt{0.015^2 + (0.0014.p_T)^2}$$

e.g. for a 50 GeV particle, the momentum resolution, σ_{p_T}, is about 3.5 GeV. The resolution of the impact parameter as a function of transverse momentum, using both of these detectors, is shown in Fig. 3.22.

The relative resolution at normal incidence of the calorimeter, as a function of energy, can be parameterized as:

$$\frac{\sigma_E}{E} = \sqrt{C^2 + \frac{S^2}{E} + \frac{N^2}{E^2}}$$

where the constants C , S and N represent calibration errors due to non-uniformities in the response, sampling fluctuations (intrinsic performance of the calorimeter), and noise contributions (e.g. from uranium, the readout

electronics, and, in collision data, the "underlying event"). Values of these parameters (from Run I test beam studies) are given in Table 3.3. The jet energy resolution for single electrons reconstructed only in the calorimeter is shown in Fig. 3.23. For Run II we did not have a test beam to study the resolution so Monte Carlo events have been used.
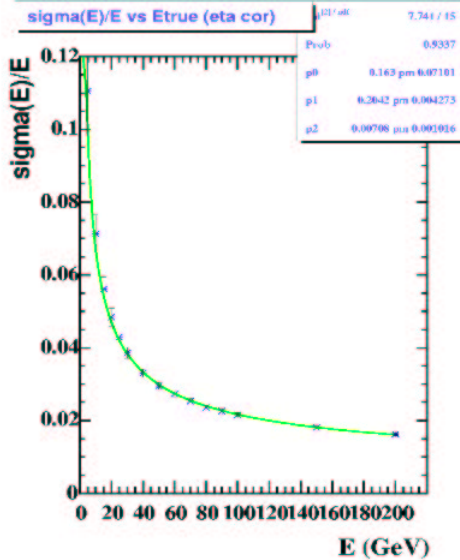
Figure 3.23: Jet energy resolution for single electrons [125].
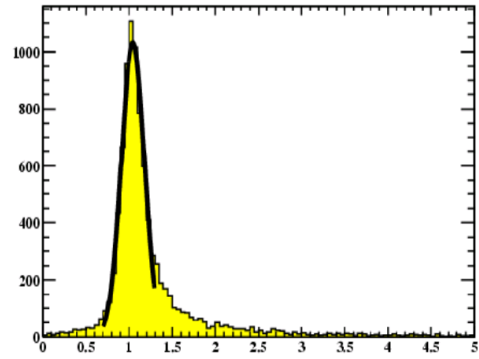
Figure 3.24: Ratio of energy deposited by an electron in the calorimeter and the p_T of the corresponding track [126].

The magnetic field also helps to calibrate the calorimeter energy scale, and enhances the electron identification by making it possible to compare the momentum of an electron with the energy it deposits in the calorimeter (E/p), as shown in Fig. 3.24.

The performance of the muon system combined with the central tracker is shown in Fig. 3.25 where the di-muon invariant mass is shown at the Z^0 mass.

The momentum resolution of the muon system has been studied using re-

Particle	C	S	N
e	0.014	$0.135\sqrt{\text{GeV}}$	0.14 GeV
π	0.032	$0.41\sqrt{\text{GeV}}$	1.3 GeV

Table 3.3: Test-beam results for calorimeter resolution parameters.
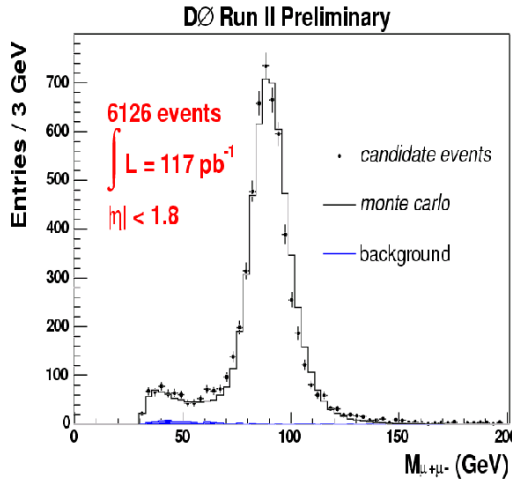
Figure 3.25: $Z \to \mu^+\mu^-$ events. [127].

constructed muons for which a central track was associated. The momentum resolution for muons as measured by the muon system, $\sigma(p_t)/p_t$, varies between 0.1 for low-momentum muons and 0.5 for muons with $p_t > 50$ GeV.

Chapter 4

Data Reconstruction and
Object Identification

You can't do it unless you organize.

Samuel Gompers

The detector collects and saves information in terms of hits on detecor elements, from these one finds tracks, charge, momenta, and energy. In order to know what types of particles were produced in a certain collision, starting from these end products, we trace our way back and reconstruct the whole event. First the base objects like leptons, jets, and missing energy are reconstructed using information from different parts of the detector and then from properties of these objects we construct massive particles like W, Z bosons and top quarks. In this chapter we will see how information from different detectors is used to reconstruct different objects.

Once data have been recorded, the offline reconstruction of the basic physics is done by processing events recorded during online data-taking through several steps of calculation using a software package called DØReco.

The first step: involves taking raw information from individual detectors and using it to either reconstruct hits (a spatial position where a particle deposits energy) or clusters (combination of close hits).

The second step: hits in the silicon detector and central fiber tracker detectors are used to reconstruct tracks.

The third step: is vertexing. First, primary vertex candidates are found. A primary vertex is the position where a $p\bar{p}$ interaction takes place and are used in the calculation of various kinematic quantities (e.g. transverse energy). Next, displaced secondary vertex candidates are identified. Such vertices are associated with the decays of long-lived particles.

The fourth step: information from each of the preceding reconstruction steps is combined and standard physics object candidates, such as electrons, photons, muons, neutrinos (in the form of missing transverse energy $\not{E}_T$), and jets are created. Candidates for heavy-quark and tau decays are identified next.

In all these steps of reconstruction two important things are kept in mind:
1) Maximization of the quality of measurements for required objects.
2) Minimization of misidentification from other objects which may mimic that object.
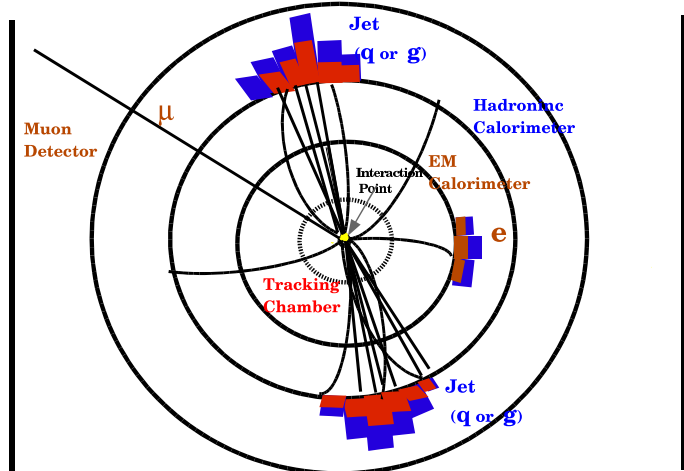
Since all the detectors have some limitations or inefficiencies, the final signals are corrected for these in efficiencies.

Now we will go through the details of these steps.

4.1   Track and Primary Vertex Reconstruction

When a charged particle passes through the tracker it deposits energy in various parts of the detector which is recorded in the form of raw signals in these

Bend angle coresponds to the momentum of the charged particle.
Unbalanced energy in the detector is a signature of neutrino (ν).

Figure 4.1: A cartoon showing behavior of different particles in different parts of the detector.

detectors (Fig. 4.1). One of the most challenging problems in hadron colliders is reconstruction of tracks from hits. It is challenging because at higher luminosities, like at the Tevatron, there may occur many events in every crossing and each event in turn can produce many charged particles in a small range of η. This high density of tracks makes it very difficult to recognize which hit is coming from which track.

The goal of the tracking algorithm [128, 129] is to find and fit the tracks in a D0 event using event data from the SMT and CFT. The input event data for tracking is a collection of hits from each sub-detector. The output is a collection of tracks where each track contains a list of hits and one or more kinematic fits based on this list. These are given to the vertexing package whose output is primary and/or secondary vertices.
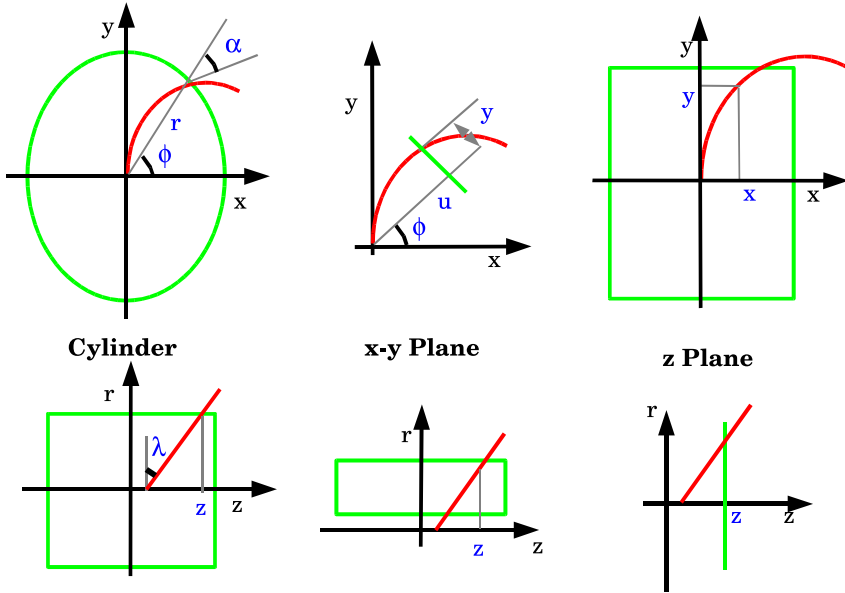
Figure 4.2: Track Parameters used in global tracking. The track is
shown in red, surfaces in green, and track parameters in blue [129]

4.1.1 Track Reconstruction

Particles passing through the inner tracking sub-detectors leave their marks
either in terms of light or current. Particles traversing the Silicon Microstrip
Tracker may deposit charge in a number of conducting micro strips. Depending
on its angle of incidence, a particle passing through a layer of the Central
Fiber Tracker will illuminate either one or two fibers. This raw data from
subdetectors is what makes hits, which are typically one or two-dimensional
measurements indicating where a track crossed a surface. The typical types of
surfaces needed to describe the DØ detector are cylinders, for the fiber tracker,
and $x - y$ and z planes for the silicon detector. Track parameters for these
surfaces are shown in Figure 4.2.

At every surface, a new cluster is added to the track. The track and cluster
errors are combined and fitted. If the χ^2 of the fit is too high the cluster is
rejected . When a new cluster is added to the track, the track parameters

and errors are updated and the track is "propagated" to the next surface. A track is propagated between the surfaces by solving the equation of motion for a track, including effects of the magnetic field. It is also important to update the track errors for the effects of multiple scattering and energy lost in different materials between different surfaces. When all the tracks are formed, a number of filters are applied to clean the list of candidate tracks. These filters reject tracks based on the overall χ^2, and number of missed surfaces. A track can be rejected if it shares clusters with another track. In this case, the track which has the lower fit χ^2 is kept.

Surface	Cylinder	$x - y$ Plane	z Plane
Fixed Parameters	radius, r	u, ϕ	z
Position Parameters	ϕ, z	v , z	x, y
Direction Parameters	α, $\tan\lambda$	$\mathrm{d}v/\mathrm{d}u$, $\mathrm{d}z/\mathrm{d}u$	$\mathrm{d}x/\mathrm{d}z$, $\mathrm{d}y/\mathrm{d}z$
Curvature	q/p_T	q/p	q/p

Table 4.1: Track parameters used in global tracking [?]. See Fig 4.2 for explanation of these parameters.

Finally, for each reconstructed track in the event a list of surfaces and track parameters at each surface is stored. Normally six parameters are needed to describe a track at a surface: 3 position coordinates, two direction parameters, and a curvature (or $\frac{q}{p_T}$). These parameters, for different surfaces, are shown in Table 4.1.

4.1.2 Cluster Finding Efficiency in the CFT

To measure the cluster finding efficiency we reconstruct the tracks in the tracker skipping one layer at a time. Then for the skipped layer we predict the cluster position by extrapolating the reconstructed track, and look for the CFT cluster within a certain window around the predicted position.

This efficiency is determined using clean tracks which have $p_t > 1.0$ GeV and more than 14 CFT hits. These hits are chosen to be isolated which means that there are no more than one hit within a certain region. We choose 11 $\sigma(tracking)$ for the isolation and 3 $\sigma(resolution)$ for the window size. The overall efficiency of the Central Fiber Tracker to find a cluster within the expected window is more than 98%, as shown in Fig. 4.3.
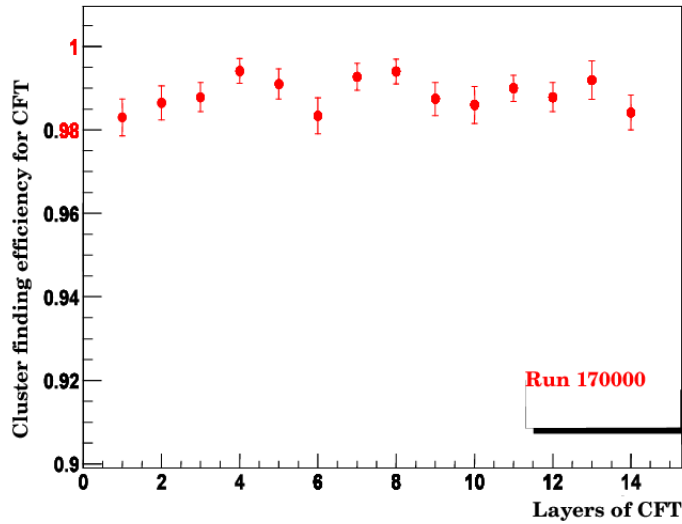
Figure 4.3: Cluster finding efficiency for the CFT [130].

4.1.3 Vertex Reconstruction

The vertex of an event is a point where almost all of the particles in the event were produced when the proton and antiproton collided (see Fig. 4.4). Having a precise position for the vertex is very important in the event reconstruction. The dimensions of the beam from the Tevatron are of the order of tens of microns in the transverse direction and tens of centimeters ($\sigma \approx 25$cm) along the beam direction. This limits the position of the vertex in the transverse plane
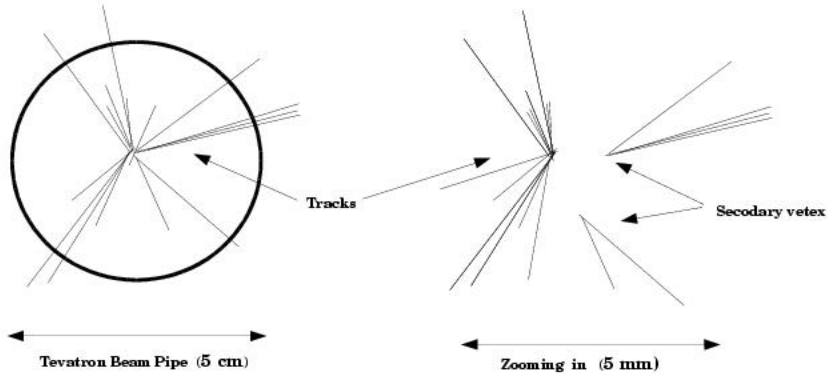
Figure 4.4: An illustration of primary and secondary vertices inside the detector.

by the size of the beam spot but there is little constraint in the longitudinal direction.

There are two main steps in vertex reconstruction:

Step one: The vertex is reconstructed by grouping tracks which approach each other near the beam axis. The fitting procedure begins with the highest p_T-track and forms clusters of tracks by adding new tracks less then 2 cm away from the center of the cluster in z.

Step two: For all of these reconstructed vertices, the probability for a vertex to originate from a minimum bias interaction is calculated. This calculation is based on the fact that tracks from a minimum bias interaction have smaller p_T than tracks from hard scatter interactions .

Tracks used in primary vertex reconstruction must have $p_T > 0.5$ GeV, at least two SMT hits, and a distance-of-closest-approach (DCA) significance from the beam spot less than four. In order to ensure the quality of the event reconstruction, the primary vertex is required to have at least three tracks. It

is also required to be within the volume of the silicon detector, $|z_0 < 60.0|$ cm. More detail on vertex reconstruction can be found in [131] and [132].

4.2 Identifying Electrons

When an electron passes through the detector, it is expected to make a track in the central tracking system and EM showers in the calorimeter. Its energy should be contained in a small group of cells in the calorimeter, as showin in Fig. 4.1. Electron identification can be divided into the following steps:

- Reconstruction of clusters

- Matching a track

- Constructing electron likelihood

- Measuring efficiencies

- Applying corrections

These steps are expalined in detail in the references [133]. Here we give a brief description of each one of these steps.

Reconstruction of Clusters in different regions of the calorimeter is done by defining an "electromagnetic" cluster as a set of towers in a cone of radius

$$\mathcal{R} = \sqrt{\Delta\eta^2 + \Delta\varphi^2} = 0.2$$

around an initial tower, selected on the basis of its energy. Clusters from real electrons are expected to deposit a large fraction of their energy in the EM calorimeter. Also, the longitudinal and lateral shower development is expected to be compatible with that of an electron. A χ^2 is attributed to each cluster based on the comparison of the values of the energy deposited in each layer of the EM calorimeter and the total energy of the shower with average distributions obtained from simulation. All of these considerations lead to the
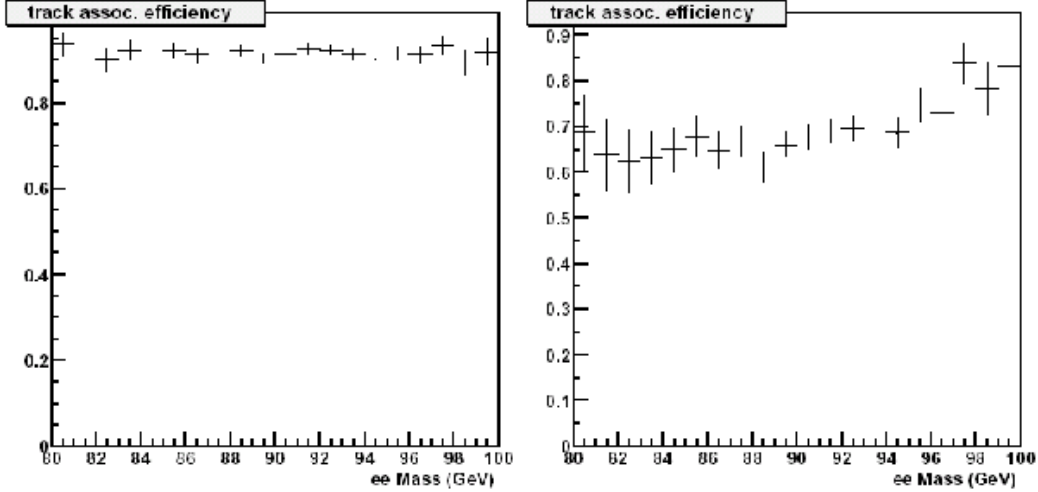
Figure 4.5: Efficiency to find a track associated with an EM cluster in CC (left) and EC (right) regions of calorimeter, as a function of di-electron invariant mass [131].

following criteria for EM cluster selection:

$$f_{\text{EM}} \equiv \frac{E_{\text{EM}}}{E_{\text{tot}}} > 0.9, \qquad \chi^2 < 20,$$

and

$$f_{\text{iso}} \equiv \frac{E_{\text{tot}}(\mathcal{R} < 0.4) - E_{\text{EM}}(\mathcal{R} < 0.2)}{E_{\text{EM}}(\mathcal{R} < 0.2)} < 0.15,$$

where, E_{tot} is total energy within the cone and E_{EM} is the energy in the electromagnetic calorimeter.

Matching a Track: Once the EM cluster in the calorimeter is well identified, we enhance this identification by using information from the tracking system. The electron is required to have an associated track which satisfies an initial selection:

$$|\Delta\phi_{EM,Track}| < 0.05, \qquad |\Delta\eta_{EM,Track}| < 0.05.$$

95

Electron Likelihood: This is a discriminant based on important variables that have different shapes for signal and backgrounds, [134]. It is defined as:

$$\mathcal{L}(x) = \frac{\mathcal{P}_{sig}(x)}{\mathcal{P}_{sig}(x) + \mathcal{P}_{bkg}(x)}$$

Where $P_{sig}(x)$ and $P_{bkg}(x)$ are the probabilities that a given EM object is from signal or background. Making use of this information from shapes of different distributions enables us to identify good electrons and separate them from backgrounds more efficiently than applying simple cuts on these variables. The suggested electron likelihood cuts are:

$\mathcal{L}_{CC} > 0.75$

$\mathcal{L}_{\mathcal{EC}} > 0.8$

Efficiencies: The efficiency of the selection cuts have been measured in $z \rightarrow ee$ data , using a tag and probe method, where all the cuts are applied on one of the electrons (called "tag") and efficiency is measured for the second electron (called "probe"). The efficiency to find a track associated with an EM cluster, in data, for the CC and EC regions of the calorimeter, is shown in Fig 4.5.

and overall efficiencies for these cuts are found to be [135]:

$$\epsilon_{lhood}^{CC} = 89.1 \pm 0.4[stat.] \pm 0.5[syst.]\%$$

$$\epsilon_{lhood}^{EC} = 86.3 \pm 0.7[stat.] \pm 0.8[syst.]\%$$

Corrections The energy measurements in the calorimeter are corrected for non-linearities in the readout electronics. Also, energy lost by electrons in the material in front of the calorimeter is parameterized as a function of η and electron energy. This parameterization is used to correct the data, using detailed simulations. The electron energy is also corrected for geometrical effects in the calorimeter [136].

4.3 Identifying Muons

Muons, being minimum ionizing particles, do not shower like electrons or hadrons inside the calorimeter. Thus the reconstruction of muons is done by using information from the muon system and the central tracker alone.

A local track in the muon system is the basis of the muon identification. The muon is required to have hits in all three layers A, B, and C. Tracks are constructed from segments in layers B and C by searching for matching segments in the A layer. An estimate of the muon's momentum is obtained from the bending angle through the toroid.

A signature in the calorimeter is used only for measuring identification efficiencies. A veto on cosmic muons is applied by requiring the time difference between scintillator hits in the B or C layer and the A layer to be consistent with a muon coming from the interaction region ($\delta t > -10$ns).

Like electrons, muons are also required to be isolated in the detector.

4.4 Hadronic Particles (a.k.a Jets)

All quarks and gluons (strongly interacting particles) are materialized, through fragmentation and hadronization, as jets of hadrons (π, K, p, etc.). Data on the mean number of charged particles emitted from colliding beams as a function of center-of-mass energy, $\sqrt{s}$, is shown in Fig. 4.6. It shows, to a first approximation, that the average number of charged particles $< N_{ch} >$ increases as $ln\sqrt{s}$. As you can see there is no entry for DØ on this plot, but we can roughly extrapolate and see that the average number of charged particles at $\sqrt{s} = 1.96$ TeV is about 40-50.

Since the emitted particles are mostly pions (π^0, π^+, π^-), the total emitted particles are expected to be, on average, 2/3 charged and 1/3 neutral. Neutral pions quickly decay into two photons. These photons then participate in the
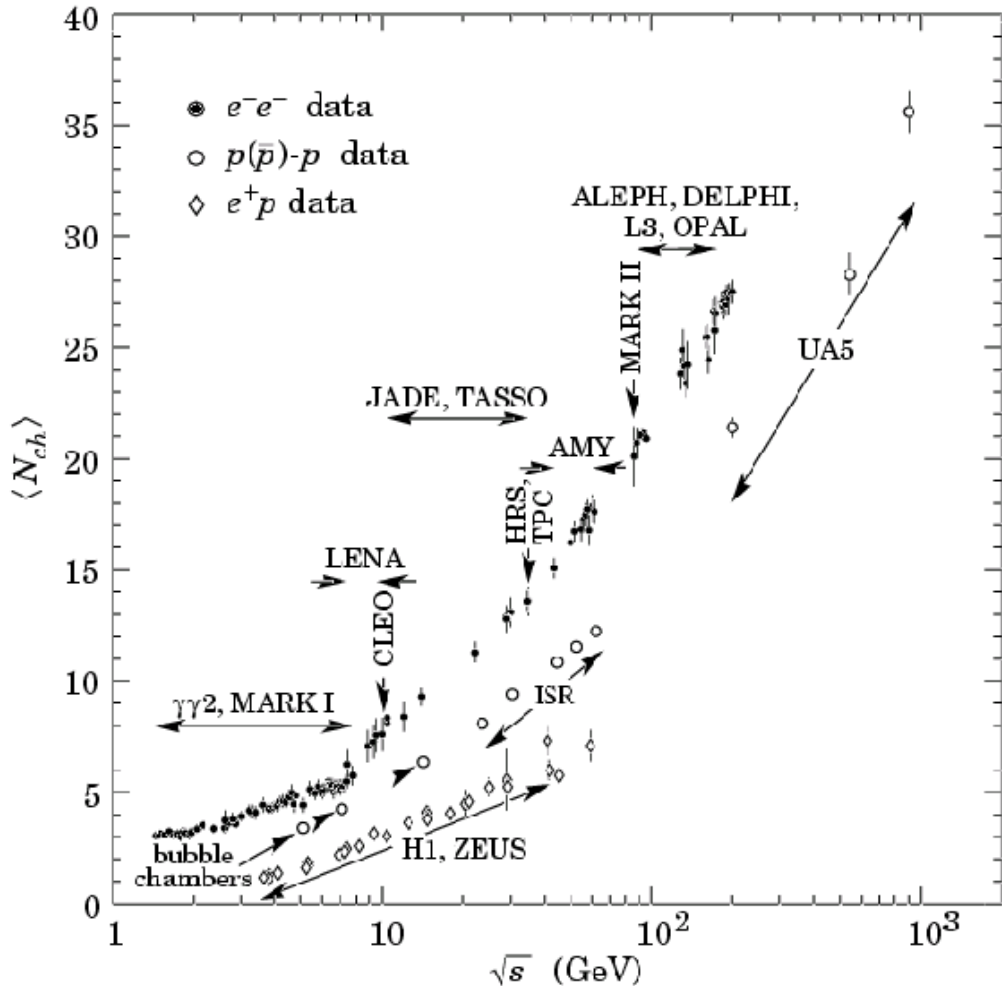
Figure 4.6: Mean number of charged particles as a function of the center of mass energy $\sqrt{s}$ [8].

hadronic cascade as an electromagnetic component.

The average number of particles in a jet $< N >$ versus $p_{T_{jet}}$ is similar to $< N >$ versus $\sqrt{s}$ in Fig. 4.6. High p_T jets are well collimated, hence easily recognizable [137].

Jet reconstruction starts with seed towers which are composed of the sum of all cells which share the same pseudorapidity (η) and azimuthal angle (ϕ). Only towers with positive energy are kept as seeds and a cone of radius $\mathcal{R} = \sqrt{\Delta\eta^2 + \Delta\varphi^2} = 0.5$ is chosen around the position of the seed [138, 139]. Once cells are clustered, further quality selection cuts are applied to each jet.

To remove isolated electromagnetic particles a cut on the fraction of energy deposited in the electromagnetic section of the calorimeter (EMF) is applied at $0.05 < EMF < 0.95$.

To remove jets which clustered around noise in the coarse hadronic section, a cut on the fraction of the jet energy deposited in the coarse hadroninc section (coarse hadroninfc fraction CHF) is applied at $CHF < 0.4$. Also, to remove those jets clustered from hot cells, a cut on the ratio of the highest to the next-to-highest transverse energy cell in the calorimeter ($HotF$) is applied at $HotF < 10$. To remove those jets clustered from a single hot tower, the number of towers containing 90% of the jet energy ($n90$) is required to be greater than 1.

Jet Energy Scale

Even though the calorimeter is very effective at absorbing the hadronic energy of the jet, because of non-linearities, dead material, noise and showering effects and because of the difference in calorimeter response to electrons and pions, the measured energy in a jet cone is not equal to the original particle energy and we need to correct for this difference.

The correction can be written as:

$$E_{jet}^{corrected} = \frac{E_{jet}^{uncorrected} - Off}{Show \times Resp},$$

where:

Off – $Energy\ Offset$ Is the correction for energy in the clustered cells which

is due to noise, underlying events, multiple interactions, energy pile-up and uranium noise and can provide an offset to the energy of the jet. Basically, this is energy not associated with the hard scattering. This term is determined using zero bias and minimum bias data.

Show – Showering Corrections The finite size of the cone used for clustering will certainly exclude a fraction of the jet energy. Showering corrections take into account the energy emitted outside of the jet cone because of detector, dead material, etc., but does not take into account physics showering outside the jet cone.

Resp –Calorimeter Response Hadronic showers may lose energy in ways which do not provide visible ionization. The response to electromagnetic and hadronic particles may therefore be unbalanced. This correction is obtained by using p_T balance in $\gamma+$ jet events, cross checked using $Z +$ jet events. The corrections for data jets are shown in Fig. 4.7.

Correction for a Tagging Muon and its Neutrino

When a heavy flavor hadron has a muon and neutrino in the decay chain, some energy is carried out of the calorimeter, leaving the calorimeter-only measurement of the particle energy lower than it should be. The momentum from the muon is added back to the jet momentum, along with some approximation to the neutrino momentum, andthe energy deposited in the calorimeter by the muon is properly account for so as not to double count it.

Jet-Electron separation

Jets which have a very large electromagnetic fraction may be reconstructed as electrons or photons. Or, conversely, electrons and photons, which over-
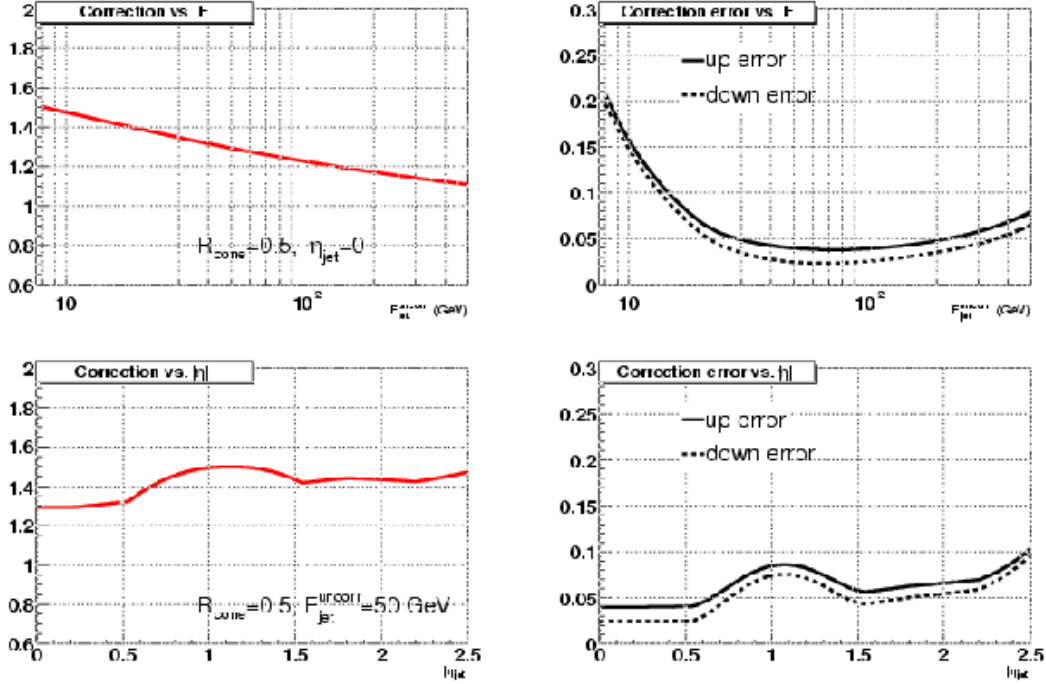
Figure 4.7: Correction to energies of jets in the data , as a function
of jet E_T (upper left) and η (lower left), with corresponding errors
in the correction (right) [141].

lap with hadronic activity, may be reconstructed as jets. All objects which
are reconstructed as electrons or photons are treated with the electromagnetic
energy corrections. Jets which do not overlap with any of the electromag-
netic options ($R = \sqrt{\Delta\phi^2 + \Delta\eta^2} > 0.5$) are treated with the jet corrections
described above.

Jet Energy Resolution

In order to measure the jet energy resolution, two different sets of data are
used: for high energy jets ($p_T \sim 50$ GeV), a dijet event sample is used; where

as for low p_T jets ($p_T < 50$ GeV), back-to-back photon-jet events are used.

In the case of high p_T jets, the distribution of the transverse momentum asymmetry variable, A, is studied. For a dijet sample, A is:

$$\mathcal{A} = \frac{|p_{T1} - p_{T2}|}{p_{T1} + p_{T2}}$$

The width of the distribution in A, σ_A, obtained from a Gaussian fit with a mean value set to zero, gives the jet p_T resolution.

In the case of low p_T jets, the asymmetry variable is defined as:

$$\mathcal{A} = \frac{p_T^{jet} - p_T^{\gamma}}{p_T^{\gamma}},$$

making use of the fact that the resolution for photons is much better known than for jets. For details see Ref. [131]. The resolutions from these two methods are combined and fitted using the formula:

$$\frac{\sigma_{p_T}}{p_T} = \sqrt{C^2 + \frac{S^2}{p_T} + \frac{N^2}{p_T^2}}$$

The energy resolutions for data jets are shown in Fig. 4.8.

4.5   Measuring Missing Energy

Among the particles we have encountered so far, the neutrino is the least interacting one. It does not leave any trace in the detector and the only way its presence can be inferred is the from imbalance of the energy of the event transverse to the beam direction. This missing transverse energy is reconstructed from the vector sum of the transverse energies in calorimeter cells with positive energies. The opposite of this vector sum is the measured missing E_T vector and its modulus is the raw missing transverse energy ($\not{E_T}^{raw}$).

In events with both electromagnetic objects and jets, this imbalance translates directly into missing transverse energy. As a jet energy scale (JES)
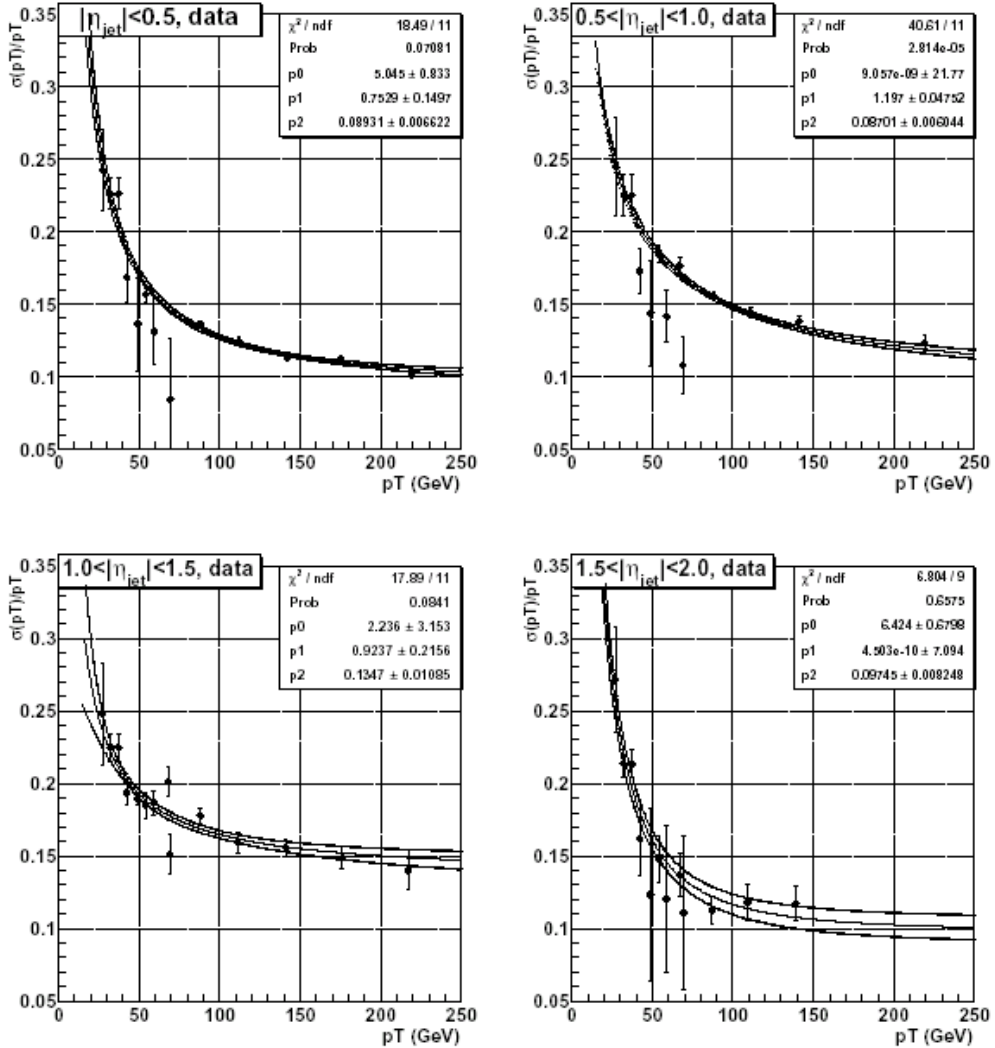
Figure 4.8: Jet p_T resolution in different regions of pseudorapidity (η) in data [131].

correction is derived for all good jets, it can also be applied to the missing transverse energy. In order to do so, the absolute JES correction applied to all good jets is subtracted from the $\not{E}_T$ vector. The resulting modulus is called the calorimeter missing transverse energy. This calorimeter-only missing transverse energy ($\not{E}_T^{\mathrm{cal}}$) is then corrected for the presence of electrons,

photons, jets, and muons in the event.

Electrons and photons: The calorimeter cluster energy for EM candidates is subtracted from $\not{E}_T^{\text{cal}}$ and then the EM-scale corrected energy is added.

Jets: The response part of the jet energy scale correction applied to good jets is also applied to the missing transverse energy. This quantity is called $\not{E}_T^{\text{JES}}$.

Muons: As a muon is a minimum ionizing particle throughout the entire detector, it will deposit only a small amount of energy in the calorimeter. Its presence can thus also fake missing transverse energy in the calorimeter. The momentum of track-matched muons is subtracted from the missing transverse energy vector, correcting for the energy deposited in the calorimeter by the muon. This correction is done for isolated muons.

A detailed description of the procedure can be found in Ref. [131].

4.6 Identifying Heavy Flavored Jets ("b/c tagging")

Hadrons containing b-quarks have sufficient lifetime that they travel some distance before decaying ($c\tau \approx$ a few mm). Identifying a jet with a b (or c) quark in it is very important. In particular, top quarks (almost always) decay to a b quark, and the Higgs boson, if light enough, is expected to decay into b quarks more than any other particle. Identifying b-quarks helps identify the decays of these particles.

Identifying a jet with a $b(c)$ quark in it is referred to as $b(c)$ tagging. b tagging is not an easy task. In DØ, a few different methods are used to identify b jets but none of these methods is more than $60 - 70\%$ efficient. A lot of effort is devoted to study b-tagging. The goal is not only to maximize the efficiency of how often a b jet is identified successfully but also to minimize the misidentification of other jets as b jets. The main taggers used at DØ are:

- Soft-Lepton Tagger "SLT," which looks for a muon associated with a jet. The muon is expected to come from a B hadron decay or the cascade charm decay.

- Secondary-Vertex Tagger, "SVT", a track-vertex reconstruction algorithm, looks for the secondary vertex in the event.

- Jet-Lifetime-Probability Tagger "JLIP," a track impact-parameter based algorithm.

- Counting Signed Impact Parameter (CSIP) method, which looks at the sign of the projection of the impact parameter onto the jet direction.

The secondary vertex tagger (SVT) relies completely on the tracks in the event. Since tracking efficiencies in high-activity environments like jets are higher in Monte Carlo than in data, we have to define procedures to calculate the proper tagging efficiencies and fake rates in Monte Carlo.

Since this analysis uses Secondary-Vertex tagging we will discuss SVT in some detail, for more details and for other tagging methods see Refs. [142, 143, 144, 145].

4.6.1 Secondary Vertex b-Tagging algorithm

The secondary vertex b-quark tagger (SVT) looks for track-vertices displaced from the primary vertex. For convenience, the probability for a jet to be tagged can be broken down into two components:

- *Taggability*, the probability for a jet to be taggable, is a jet-quality-sensitive component (ses Sec. 4.6.2). Taggability can also depend on the flavor of the jet.

- *Tagging efficiency*, the probability for a taggable jet to be tagged, which also depends on the flavor of the jet (ses Sec. 4.6.3).

The probability for a given jet of flavor α (b, c, light) to be tagged is the product of the taggability ($\varepsilon_{tagg(\alpha)}(p_T, \eta)$) and the tagging efficiency ($\varepsilon_\alpha(p_T, \eta)$):

$$\mathcal{P}_\alpha(p_T, \eta) = \varepsilon_{tagg(\alpha)}(p_T, \eta) \cdot \varepsilon_\alpha(p_T, \eta) , \tag{4.1}$$

Since the dead detector material and noise in the central tracking system are difficult to simulate, the straightforward MC-based calculation for tagging efficiency will overestimate tracking efficiency, in particular within jets. Thus the tagging algorithms are not applied directly to Monte Carlo events, instead the so called Tag Rate Functions (TRFs) are used to estimate the number of tagged events in Monte Carlo samples. These give the average probability that a taggable jet passes a tagging algorithm as a function of the jet's E_T and η. Flavor-Dependent TRFs are applied to Monte Carlo jets to determine their probability to be tagged. For each jet, one finds the Monte Carlo particle closest to that jet. Depending on the type of particle found, a bottom TRF, charm TRF, or light-quark TRF is applied to the jet as a function of its E_T and η. The *light-quark TRF* (which includes u, d, s, and gluons) is a *mistag rate* since there is no heavy flavor present. The bottom and light-quark TRFs are determined from data. The charm TRF is determined from a combination of data and Monte Carlo events.

The main steps of the SVT tagging algorithm are described here.

A simple V_0-removal algorithm (developed for the CSIP b-tagging algorithm) is applied to the tracks first. This removes most K_s's, Λ's, and photon-conversions.

Track quality cuts are then applied to the remaining tracks. Tracks are required to have two SMT hits, $p_T > 1.0$, impact parameter significance > 3.5, and a track $\chi^2 > 10$.

A simple cone jet-algorithm is used to cluster the tracks into *track-jets*, and then a Kalman filter algorithm is used to find vertices using the tracks

in each track-jet. The distance between the primary vertex and the found secondary vertex (known as the decay length, L_{xy}), along with its error ($\sigma_{L_{xy}}$), is calculated, taking into account the error on the primary vertex position.

If the decay length significance $L_{xy}/\sigma_{L_{xy}}$ is more than 7.0, then the found vertex is considered a tight tag. A calorimeter jet is considered tagged if $\Delta R < 0.5$, where ΔR is the separation between the jet axis and the line joining the primary vertex and the secondary vertex.

In order to characterize the performance of the tagger, three different versions of b-tags are defined on the basis of their efficiencies versus mistag rates.

- TIGHT

- MEDIUM

- LOOSE

4.6.2   Taggability

A jet is taggable if it is matched within $\Delta R \leq 0.5$ to a track-jet, where a track-jet is a good quality jet which also passes requirements on tracks and hits in the detector. A jet is required to be taggable before teh SVT algorithm is applied.

Taggability-Rate Functions (TRF) give the average probability that a jet is taggable as a function of the jet's E_T and η. Tracking and related variables are not well simulated by the Monte Carlo model, and so the taggability algorithm cannot be applied directly to Monte Carlo jets. These functions are measured using data and are applied to Monte Carlo before the flavor-dependent tag-rate functions are applied. The taggability distribution and the one-dimensional functional parameterizations are shown as a function of jet p_T and η in Fig. 4.9. $\not{E}_T$+jets (EM1TRK) data Sample, which requires low missing $E_T < 10$ GeV

107

along with two good jets, and QCD data sample, which requires two good jets is used to calculate this efficiency.
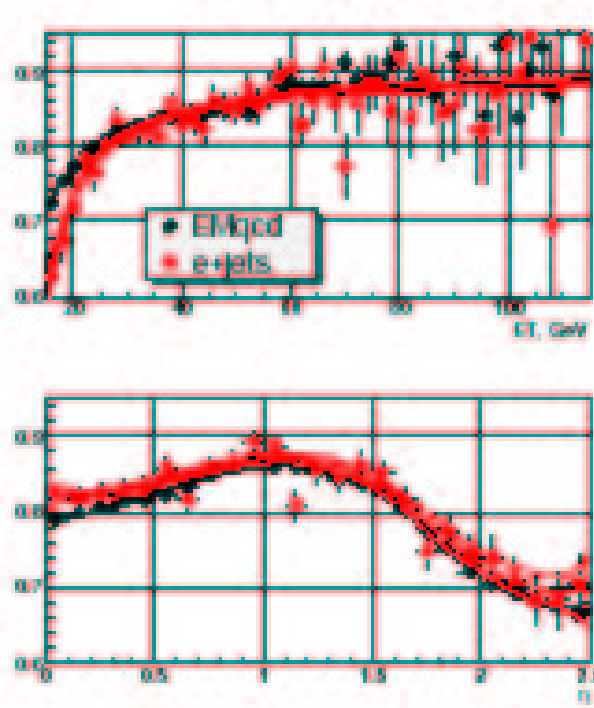
Figure 4.9: Jet taggability as a function of jet E_T (up) and η (down) for the e+jets data. Curves indicate the fit and its 1 σ error band.

The systematic uncertainty assigned to the taggability measurement, comprises the statistical uncertainty of the fit to derive the parameterizations and the sample dependence of the taggability. The dependence of the taggability on the description of the underlying event (Tune A [?]) is also used to assign a systematic uncertainty on the flavor dependent correction.

4.6.3 Tagging Efficiency

SVT b Jet Tagging

The SVT tag-rate function for b quarks is derived from a muon+jets data
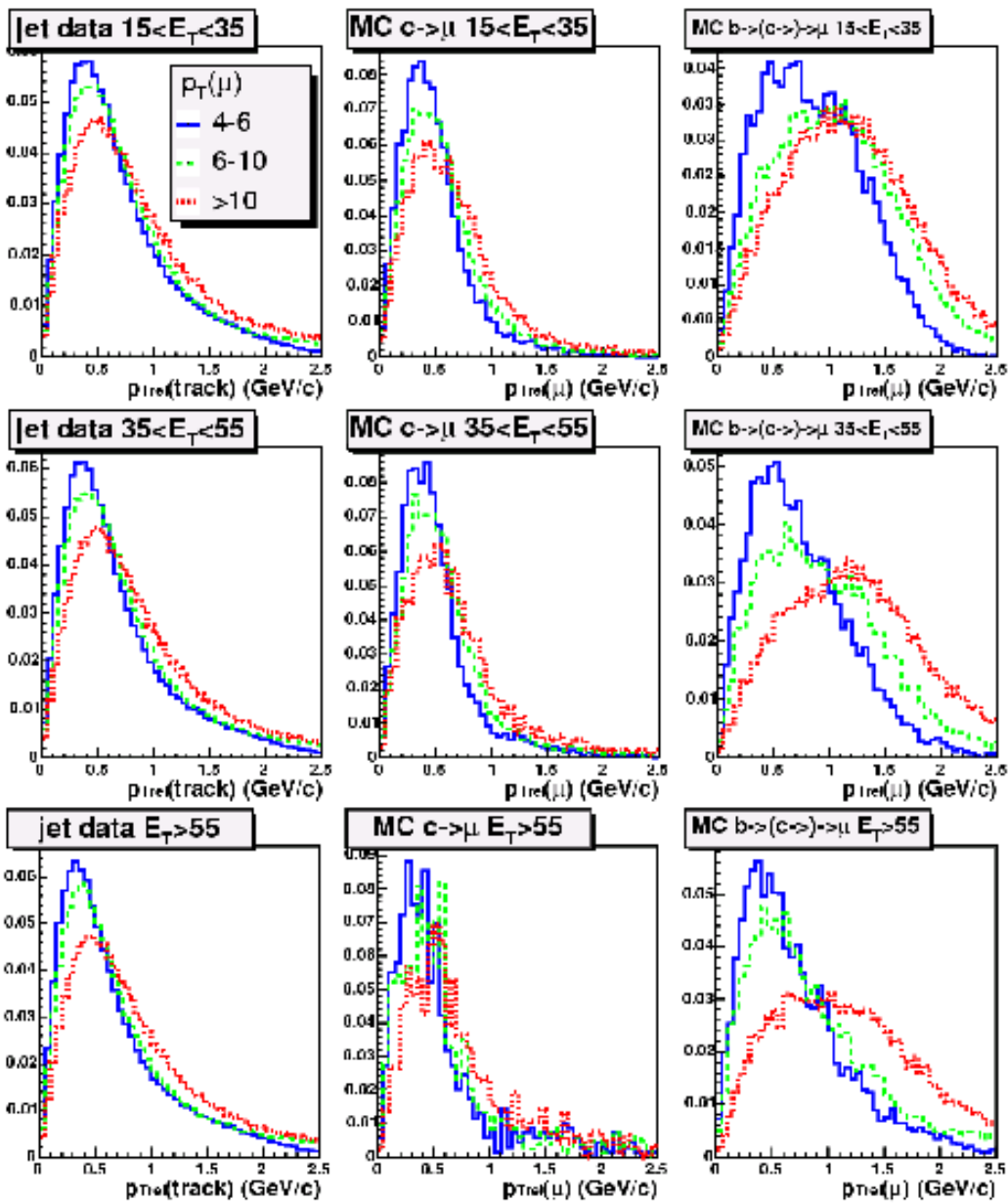
Figure 4.10: $p_T^{\rm rel}$ templates used to fit the muon-in-jet data. Left plots: light-quark templates; middle plots: c-quark templates; right plots: b-quark templates.

sample with $p_T(\mu) > 8$ GeV. Three methods are used to determine the heavy-flavor content and thus the tagging rate for b jets.

- *Muon p_T^{rel} Single-Tag Fit.* p_T^{rel} shapes for b-quarks, c-quarks and light quarks are determined from Monte Carlo samples. The b-quark content is determined using these fits and the SVT tag-rate of the away jet.

- *Muon p_T^{rel} Double-Tag Fit.* Similar to the previous method, but both the muon-jet and the away-jet are required to be tagged. Though statistics are lower, the p_T^{rel} fits are more stable.

- *System 8.* A set of eight nonlinear equations that play two independent tagging algorithms off each other (SLT and SVT).

The muon p_T^{rel} shapes in data are fitted to the Monte Carlo-generated shapes to determine the b-quark content. There are nine different shapes for light quark jets, charm quark jets, and b-quark jets — each flavor is split by both jet E_T and also jet η. Light-quark templates are approximated by using a tracks-in-jet trigger (or EMQCD) data, c-quark templates are approximated from $Z{\to}c\bar{c}{\to}\mu$ and $t\bar{t}$ Monte-Carlo simulations, and b-quark templates are approximated from $Z{\to}b\bar{b}{\to}\mu$ and $t\bar{t}$ Monte-Carlo simulations. For each flavor, the templates are subdivided according to the muon p_T and jet E_T range.Sample plots are shown in Fig. 4.10.

The left-hand plot in Figure 4.11 shows the performance of the SVT_Tight algorithm on b-jets as a function of the jet E_T for each method for all values of η. The final tag rate is the weighted average of the three methods. The systematic uncertainty on the TRF is taken to be the spread between the three results. The right-hand plot in Figure 4.11 shows the same thing, but as a function of jet η. This uncertainty is about 6.5% in the central region.

The tag rate derived above is for jets with a muon nearby. This is a side effect of the $p_T(\mu) > 8$ GeV cut discussed above. To determine the TRF for
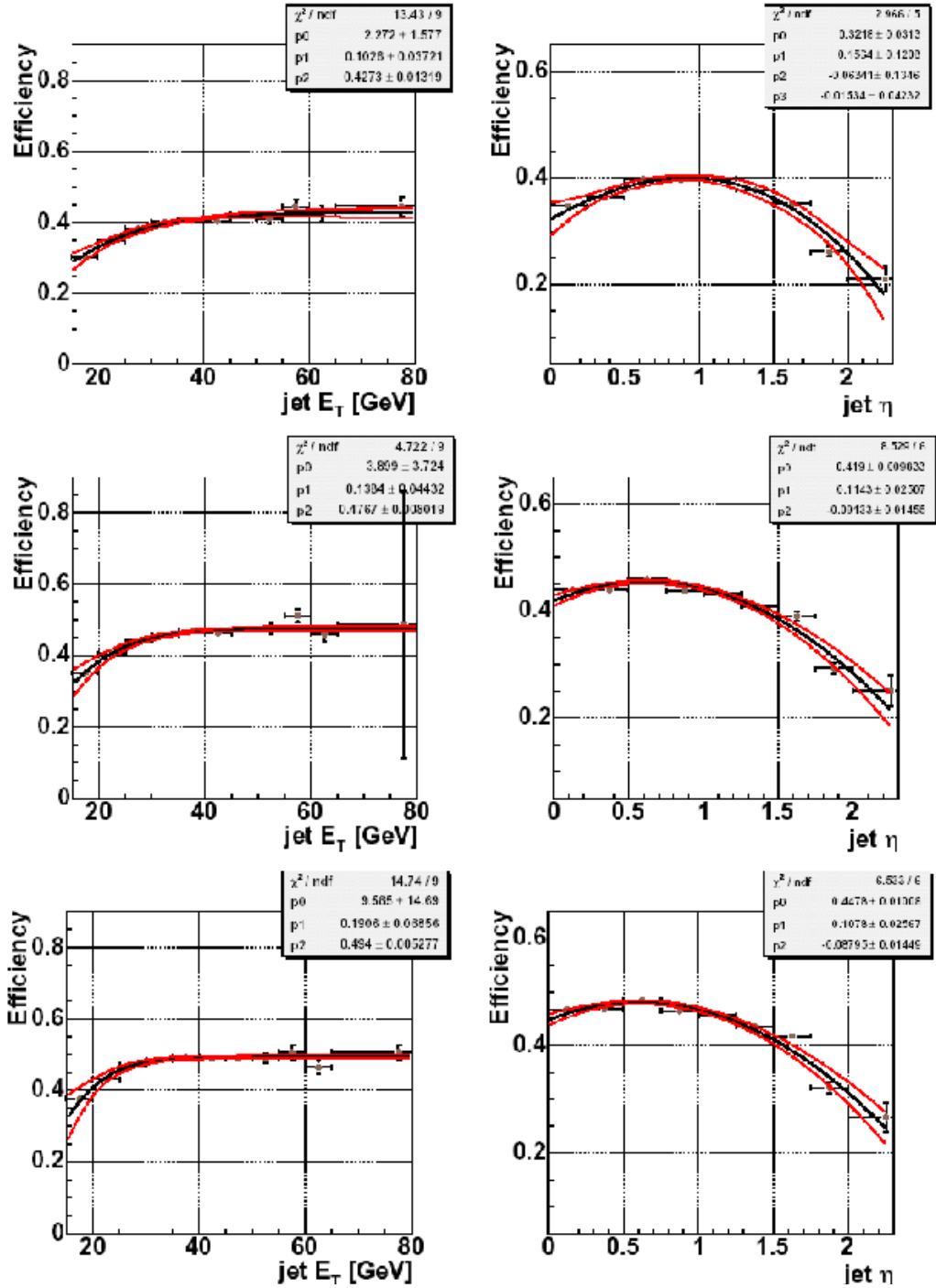
Figure 4.11: The b-quark tagging efficiency for the SVT Tight (upper plots), MEDIUM (middle plots) and LOOSE (lower plots) tagging algorithm as a function of jet E_T (left) and η (right) as measured on data [143].

111
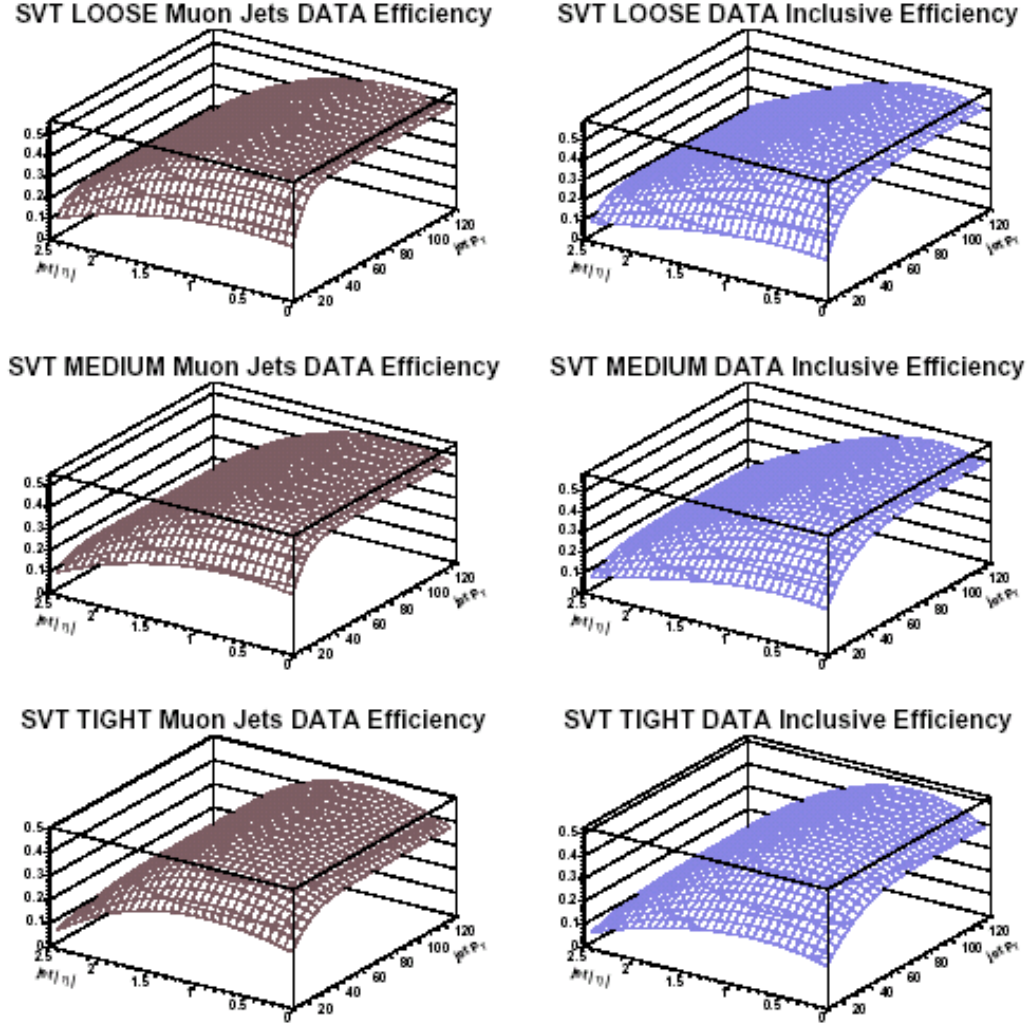
Figure 4.12: 2D parameterization of the tag rate functions for LOSSE, MEDIUM, and TIGHT tags [143].

hadronic jets without a nearby muon, a scale factor is derived from Monte Carlo. A TRF is derived for b-quark jets with and without a close by muon, and the ratio of these factors is used to scale the TRFs determined from data. The two dimensional parameterization of TRFs in η and p_T is showin

in Fig. 4.14.

The uncertainty on the scale factor is taken to be the uncertainty on the two Monte Carlo tag-rate functions that are input to the scale factor. The two are added in quadrature.

SVT Charm-Flavor Jet Tagging

An effective method of determining the charm quark tagging rate in data has not yet been found. To get around this, the charm and b-tagging ratio from Monte Carlo is used to scale the b-quark tag rate determined from data. The average ratio of b/c TRFs in Monte Carlo is 0.25. The ratio is calculated bin-by-bin (in jet E_T and η) when it is used to calculate the probability that a charm jet gets tagged.
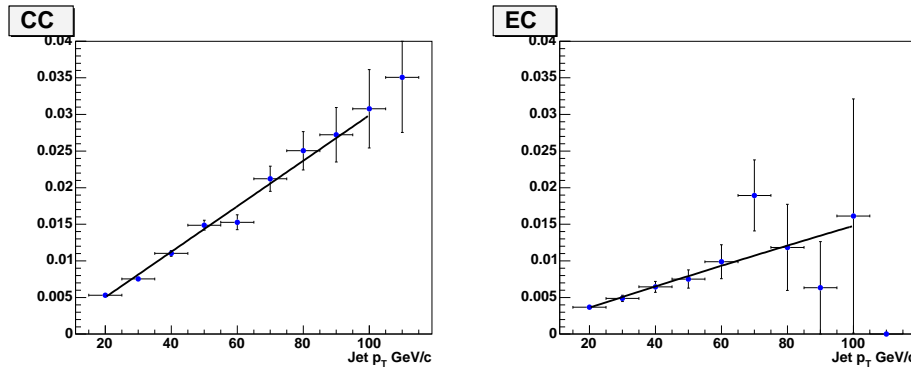
Figure 4.13: The negative tag rate in the CC and EC, as a function
of jet E_T for the SVT TIGHT tagging algorithm [143].

SVT Light-Flavor Jet Tagging

The light-quark tag-rate function is also calculated from data. Light-quark

tags are assumed to be mostly from tracking effects (resolution, reconstruction, etc.). The tagging algorithm normally requires a reconstructed secondary vertex to be in front of the primary vertex (along the jet axis). However, tags due to track mis-reconstruction and resolution will originate as often behind as in front of the primary vertex. Secondary vertices tagged and reconstructed behind the primary vertex are called *negative* tags, those in front are called *positive* tags. The light-quark tag-rate function is mostly a parametrization of the negative tags in the sample.
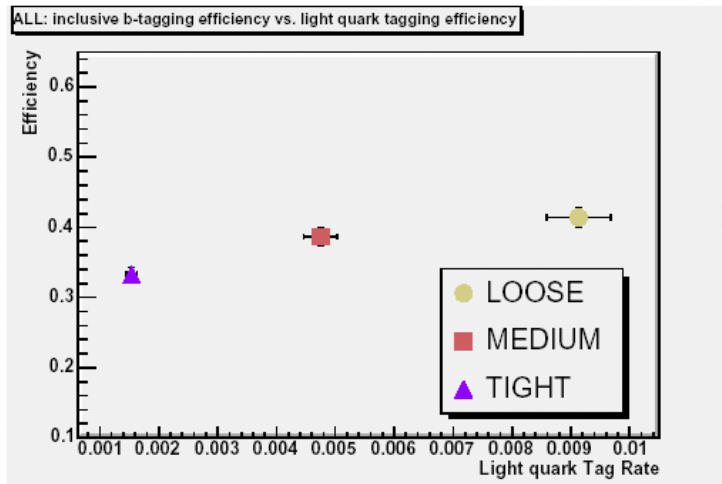
Figure 4.14: Inclusive SVT tagger efficiency versus light quark tag rate [143].

The light-flavor tag-rate function is parametrized in E_T only, but in three bins of η (CC, ICD, and EC). The efficiency of this method can be found in Ref. [142].

The negative tag rate is calculated on two data samples, an unbiased jet-trigger sample, and the multi-jet (EMQCD) sample. The average of the two is taken and the spread is used as an error. Figure 4.13 shows the negative tag-rate as a function of jet E_T in the CC and EC η regions. The inclusive

secondary vertex tagger efficiency for LOOSE, MEDIUM, and TIGHT tag, versus light quark tag rate is shown in Fig. 4.14.

Chapter 5

Monte Carlo Samples

In this chapter we describe the Monte Carlo (MC) event simulation and the Monte Carlo samples used for different backgrounds to single top.

5.1 Monte Carlo Simulation and Monte Carlo Samples

The generation of Monte Carlo events involves multiple stages. The first step is the simulation of a physical process, a $p\bar{p}$ collision producing a particular final state. The next step is to trace the particles through the detector and simulate their energy deposition and secondary interactions. For this step we use, DØG-STAR, a program based on the the CERN program GEANT (version 3.21) [146]. After the particles from the simulated reaction have been traced through the detector, the energy deposition is converted to the form that the real data takes when processed through the DØ electronics. Detector inefficiencies and noise (from the detector and electronic readout) must be taken into account. Monte Carlo data is then run through the same data reconstruction software to produce simulated events in the same format as the true events. Finally, the correction are applied to account for the differences in data and MC.

5.1.1 MC Simulation

To start with, the parton-level samples are processed with PYTHIA [147] for hadronization, particle decays, and modeling of the underlying event, using the CTEQ5L parton distribution functions. Tau leptons are decayed using TAUOLA [148] and B hadrons are decayed using EVTGEN [149]. The generated events are processed through a GEANT-based [146] simulation of the DØ detector.

5.1.2 Monte Carlo Samples

Signal

The CompHEP [151] matrix element generator has been used to model single top quark signal events. Each sample includes both top and antitop contributions, in equal parts. The top quarks decay to a W boson and a b quark. The W bosons decay to e and τ or to μ and τ. The τ's decay to either e or μ with branching fractions given in Ref. [152]. No parton-level cuts were applied when the events were generated. The CTEQ6M PDF set [153] was used. The scales for production were $Q^2 = M_{\text{top}}^2$ for the s-channel samples and $Q^2 = (M_{\text{top}}/2)^2$ for the t-channel samples. These choices correspond to where the leading oder (LO) and next-to-leading order (NLO) cross section calculations are equal. For these samples, $M_{\text{top}} = 175$ GeV and $\sqrt{s} = 1.96$ TeV.

We include not only the leading order Feynman diagrams in the event generation but also the additional gluon radiation NLO diagrams in order to reproduce NLO distributions. For the t-channel sample, we furthermore include both the leading order diagrams (Fig. 2.4) explicitly, generating W-

gluon fusion events for the region of phase space where the $\bar{b}$ quark from gluon splitting has $p_T\bar{b} > 17$ GeV. For the yield estimates, the sample of thus generated events is normalized to the NLO cross sections from Table 2.1. Both the s- and t-channel simulations include all spin information in the production and decay by generating all the 2→4 and 2→5 diagrams (i.e., including the decay for the t quark and W boson).

Fig. 2.12 shows the transverse momenta and pseudorapidities for the partons in our Monte Carlo models of the s-channel and t-channel single top processes, after decay of the top quark and W boson.

Figure 5.1 shows how the combination of the 2→2 process with the 2→3 process in the t-channel [154] produces the wide-but-central rapidity distribution of the low-p_T b quark shown in the last plot of Fig. 2.12. The combination is achieved by using the 2→2 process when $p_T(b) \le 10$ GeV, and using the 2→3 process when $p_T(b) > 10$ GeV. This creates NLO distributions for this process.
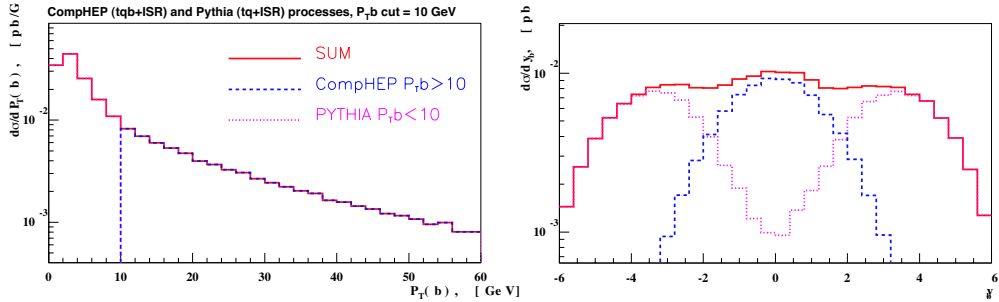
Figure 5.1: The transverse momentum and rapidity distributions of the low-p_T b quark produced with the top quark in the t-channel from the 2→2 and 2→3 processes and their combination.

	The Monte Carlo Event Sets			
Event Type	Cross Section [pb]	Branching Fraction	Number of Events	Int. Lum. [fb^{-1}]
Signals				
$tb \rightarrow e$+jets	0.88 ± 0.14	0.1309 ± 0.0026	32,500	278
$tqb \rightarrow e$+jets	1.98 ± 0.30	0.1309 ± 0.0026	33,000	125
Backgrounds				
$t\bar{t} \rightarrow l$+jets	6.77 ± 1.22	0.4444 ± 0.0089	191,300	64
$t\bar{t} \rightarrow ll$	6.77 ± 1.22	0.1111 ± 0.0089	97,750	131
Wbb	3.35 ± 0.60	0.1309 ± 0.0026	99,500	227
Wjj	287.0 ± 51.7	0.1309 ± 0.0026	189,500	5
$WW \rightarrow l\nu jj$	2.67 ± 0.06	0.3928 ± 0.0079	23,000	22
$WZ \rightarrow l\nu jj$	0.82 ± 0.73	0.3928 ± 0.0079	23,000	71

Table 5.1: The cross sections, branching fractions, initial numbers of events, and integrated luminosities of the Monte Carlo event samples.

Backgrounds

W +jets

These include Wjj and Wbb Monte Carlo samples. The Wjj sample includes Wcj and Wcc; the c is massless. The samples were generated with ALPGEN [102], a leading-order generator that includes the spins of the particles by using a full $2 \rightarrow 6$ calculation, at the parton level with the following parton-level cuts: $p_T(j, c, b) > 8$ GeV, $|\eta|(j, c, b) < 3$, and the jets should be apart by $\Delta R(j, j; j, c; c, c; b, b) > 0.4$. The events were then processed through PYTHIA for initial state radiation (ISR), final state radiation (FSR), addition of the underlying event, hadronization of the partons into jets, and decay of

119

the b's and c's. Pythia allowed gluons to split into $c\bar{c}$ and $b\bar{b}$, which filled in the low p_T and low ΔR regions not included at the Alpgen stage. The diboson samples ($WW \rightarrow l\nu jj$ and $WZ \rightarrow l\nu jj$) were produced in a similar manner.

Since the W+jets background is normalized to data (see section 7.1.2), it includes all sources of W+jets events with a similar flavor composition, in particular Z+jets events where one of the leptons from the Z decay was not identified.

$t\bar{t}$ Background

Top quark pair production contributes as a background both in the l+jets and in the dilepton decay channels. samples were generated with ALPGEN version 1.3.

We normalize these Monte Carlo backgrounds to the NNLO cross section [104].

Multijet Background

Part of the background comes from jets that are misidentified as isolated leptons. In the electron channel, this background is produced by jets that typically contain a leading π^0, which together with a randomly associated track is mis-reconstructed as an isolated electron.

This background is completely determined from data using a data sample dominated by multijet events (see section 7.1.1).

Table 5.1 summarizes the cross sections, branching fractions, initial numbers of events, and integrated luminosities of the Monte Carlo event samples for the single top analysis.

5.2 MC Correction Factors

The Monte Carlo simulation does not model the data well enough to be able to use acceptance calculations directly from the MC. We apply the following correction factors to each MC event so that the MC reconstruction efficiency matches that found in data:

- The efficiencies for reconstructing a primary vertex vary slightly between Monte Carlo events and data. We correct the Monte Carlo reconstruction efficiency to make it match data with the following factors: $\varepsilon_{\text{vertex}} = (100.8 \pm 0.6)\%$. Measurement of these factors is described in Ref. [150].

- The efficiencies for finding an EM cluster in data, and for it passing cluster identification, track match, and likelihood, as well as the methods used to evaluate them are given in Ref. [131]. All efficiencies are measured using $Z{\rightarrow}ee$ data. The electron-ID cuts are also applied to Monte Carlo electrons, but the corresponding efficiencies are mostly over-estimated. We therefore correct for this bias by applying a correction factor to Monte Carlo electrons:

$$
\begin{aligned}
\varepsilon_{e-\text{ID}} &= \frac{\varepsilon_{\text{Cluster}}^{\text{Data}}}{\varepsilon_{\text{Cluster}}^{\text{MonteCarlo}}} \times \frac{\varepsilon_{\text{EMF,Isol}}^{\text{Data}}}{\varepsilon_{\text{EMF,Isol}}^{\text{MonteCarlo}}} \times \frac{\varepsilon_{\text{Trackmatch}}^{\text{Data}}}{\varepsilon_{\text{Trackmatch}}^{\text{MonteCarlo}}} \times \frac{\varepsilon_{\text{Track}-\text{PV}}^{\text{Data}}}{\varepsilon_{\text{Track}-\text{PV}}^{\text{MonteCarlo}}} \times \frac{\varepsilon_{\text{Likelihood}}^{\text{Data}}}{\varepsilon_{\text{Likelihood}}^{\text{MonteCarlo}}} \\
&= \frac{0.960}{0.976} \times \frac{0.997}{0.984} \times \frac{0.913}{0.966} \times 0.991 \times \frac{0.891}{0.957} \\
&= 0.869 \pm 0.021
\end{aligned}
$$

$\varepsilon_{e-\text{ID}} = (86.9 \pm 2.1)\%$.

- The reconstructed fully-corrected energy of jets from the simulation of the detector performance does not match that seen in data. Specifically, the jet energy resolution is too good and there is a small offset not corrected
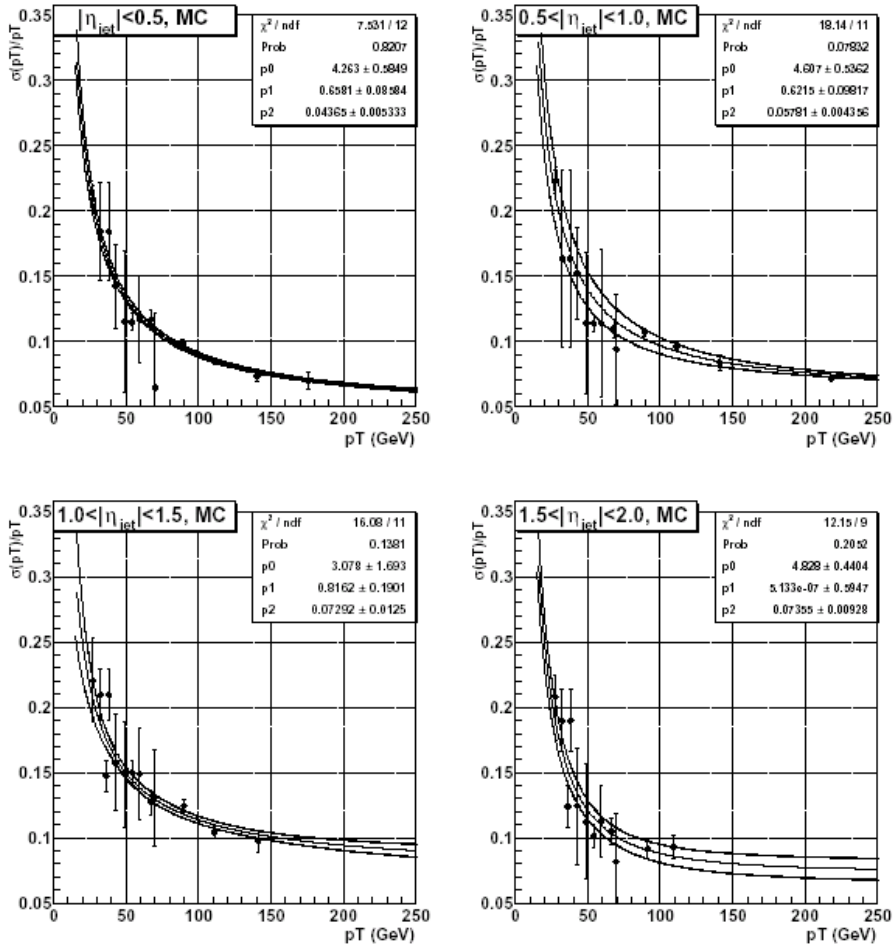
Figure 5.2: Jet p_T resolution in different regions of pseudorapidity
(η) in Monte Carlo [131].

by the jet energy scale. Therefore we smear the energies of the Monte
Carlo jets to make the resolution match the data. The jet p_T resolution in
different regions of pseudorapidity (η) in Monte Carlo is shown in Fig. 5.2
and correction to energies of jets in the Monte carlo, as a function of jet
E_T and η are shown in Fig. 5.3.
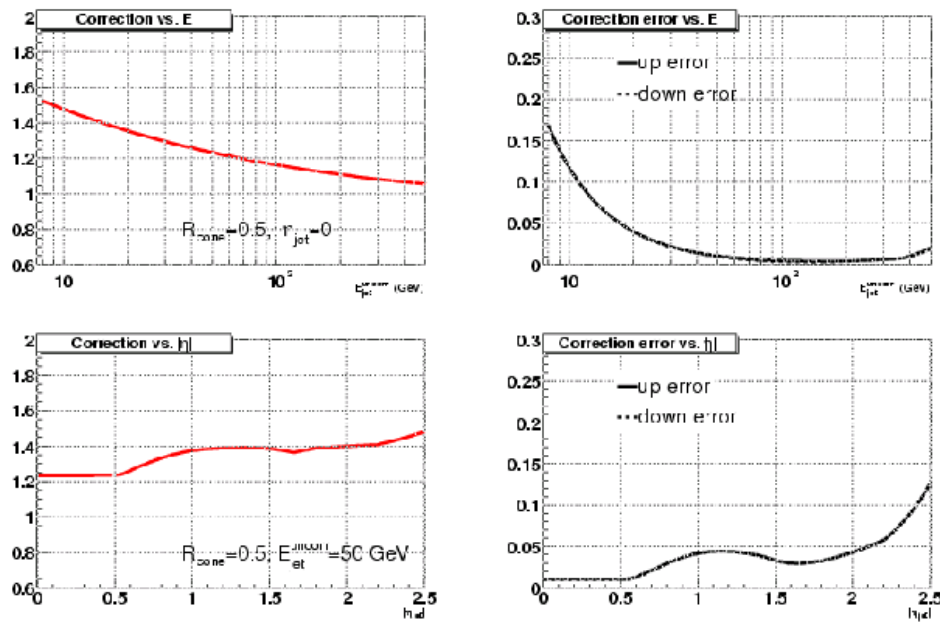
Figure 5.3: Correction to energies of jets in the Monte carlo, as a function of jet E_T (upper left) and η (lower left), with corresponding errors in the correction (right) [141].

Chapter 6

Event Selection

Survival of the fittest!

Anonymous

In this chapter we will describe the selection criteria for events. The selection cuts are designed to remove mis-reconstructed events and to keep only those that have the same final state objects in them as expected in the signal. The main goal is to get rid of as much background as we can while keeping signal acceptance as high as possible. This chapter is divided into three parts: trigger selection, selection before jet flavor tagging and selection of events which contain one or more b-tagged jets.

The data used for this analysis were taken between August 2002 and August 2004. Total delivered luminosity in this period was $\sim 480pb^{-1}$, out of which $\sim 430pb^{-1}$ was recorded by DØ. After rejecting events for which quality of any part of the detector was not satisfactory, the total good reconstructed luminosity is $366.3pb^{-1}$.

6.1 Data Quality and Trigger

The first step is to make sure that the data we are going to use for the analysis is of *good quality*, i.e. all the relevant detector parts were working well during the data taking process.

The second step is to separate out events that have at least one electromagnetic (EM) object, which can be an electron or a photon, and at least 2 jets with transverse momentum (E_T) greater than 15 GeV. The triggers used for this selection are summarized in Table 6.1. The event trigger for the e+jets channel requires an electron and a jet both at Level 1, 2 and 3 (apart from trigger list v12and v13). Details of these triggers can be found in [155, 156, 157, 158, 131].

Triggers used in the Single Top Analyses				
Trigger version	Trigger Name	Level 1	Level 2	Level 3
v13	E1_SHT15_2J25	CEM(1,11)	—	ELE_SHT(1,15)_
v12	E1_SHT15_2J20	CEM(1,11)	—	ELE_SHT(1,15)_ JET(2,20)
v8.2–v11	EM15_2JT15	CEM(1,10)_CJT(2,5)	EM(.85,10)_JET(2,10)	ELE_LOOSE_SH_ T(1,15)_JET(2,15)

Table 6.1: Summary of triggers used in trigger for the e+jets channel.

For data recorded using trigger list versions 8.2 to 11 during the period of August 2002 to July 2003, events are required to have fired the specific trigger EM15_2JT15. At Level 1, events must contain at least one electromagnetic trigger tower with energy greater than 10 GeV (CEM(1,10)) and two calorimeter jet trigger towers with energy above 5 GeV (CJT(2,5)). At Level 2, events must contain at least two jets with E_T >10 GeV (JET(2,10)) and

at least one electromagnetic object with $E_T > 10$ GeV and electromagnetic fraction greater than 0.85 (EM(.85,10)). One loose electron satisfying a transverse shower shape and with $E_T > 15$ GeV (ELE_LOOSE_SH_T(1,15)) must be present at Level 3 in addition to two jets with $E_T > 15$ GeV (JET(2,15)).

For trigger list versions 12 and v13, events must satisfy the specific trigger E1_SHT15_2J20. At Level 1, events must contain at least one electromagnetic trigger tower with transverse energy above 11 GeV (CEM(1,11)). There are no Level 2 requirements. At Level 3, events must contain at least one electron defined with a tight shower shape cut and $E_T > 15$ GeV (ELE_SHT(1,15)). In addition, at least two Level 3 jets with $E_T > 20$ GeV must be present in the event (JET(2,20)).

The break down of luminosity in different trigger versions is given in Table 6.2.

Trigger version	Luminosity (pb^{-1})
8.2– 11.0	110.6
12.0	209.8
13.0– 13.3	45.8

Table 6.2: Break down of this luminosity into different trigger versions for the e+jets channel.

6.1.1 Application of the Trigger Thresholds to Monte Carlo

Trigger efficiencies for our events are calculated using single-object (electron, muon, jet, etc.) trigger efficiency curves measured on data and applied to Monte Carlo events. Details of the method and its implementation can be found in Refs. [155, 158, 131].

The probability of a single object to satisfy a particular trigger requirement is measured using the following general procedure. The first step consists of identifying a sample of events unbiased with respect to the trigger requirement under study. Online reconstructed objects are then identified in the events. The efficiency is obtained by calculating the fraction of these online reconstructed objects that satisfy the trigger condition under study. Single object efficiencies are in general parameterized as a function of the kinematic variables p_T, η and ϕ of the online reconstructed objects.

The method used to combined single-object turn-on curves is summarized below. The total event probability for an event to pass level 1 (L1), level 2 (L2), and level 3 (L3) triggers, $P(L1, L2, L3)$, is calculated as the product of the probabilities for the event to satisfy the trigger conditions at each triggering level,

$$P(L1, L2, L3) = P(L1)P(L2|L1)P(L3|L1, L2)$$

where $P(L2|L1)$ and $P(L3|L1, L2)$ represent the conditional probability for an event to satisfy a set of criteria given it has already passed the requirements imposed at the previous triggering level(s). The total probability of an event to satisfy a set of trigger requirements is obtained assuming that the probability for a single object to satisfy a specific trigger condition is independent of the presence of other objects in the event. Under this assumption, the contributions from different types of objects to the total event probability can be factored out such that

127

$$P(object1, object2) = P(object1)P(object2)$$

Furthermore, under this assumption, the probability (P) for at least one object to satisfy a particular trigger condition, out of a total of N objects present in an event, is given by

$$P = 1 - \prod_{i=1}^{N}(1 - P_i)$$

where P_i represents the single object probability. It can be shown that the probability of at least two objects to satisfy a particular trigger condition, out of a total of N objects present in an event, is obtained using

$$P = 1 - \prod_{i=1}^{N}(1 - P_i) - \sum_{i=1}^{N} P_i \prod_{j=1, j\neq i}^{N}(1 - P_j)$$

The average efficiencies of the trigger for preselected $tb{\rightarrow}e$+jets and $tqb{\rightarrow}e$+jets events are 85.5% and 84.7% respectively.

6.2 Selection Before b-Tagging

Event selection begins after all corrections have been applied to the data. These corrections include the EM and the jet energy calibration. It is required that the primary vertex (z_{vertex}) for the event must be within the tracking fiducial region, $|z_{\text{vertex}}| < 60$ cm, which allows for a sufficient number of tracks, $N_{\text{tracks}} \geq 3$, associated with it to be properly reconstructed. Other main selection cuts are listed below:

- One isolated electron with $P_T \geq 15$ GeV.

  We require exactly one isolated electron in order to reduce the backgrounds from $t\bar{t}$, WW, WZ, and Z/γ decays to dileptons.

- Electron pseudorapidity $|\eta| < 1.1$ for Central Calorimeter.

128

- Electron track match.

- Electron track $p_T > 10$ GeV.

- $|Z(e, PV|) < 1$ cm.

- Electron likelihood $\mathcal{L} > 0.85$ for electron $P_T < 30$ GeV and > 0.4 for electron $P_T \geq 30$ GeV.

- Number of jets $2 \leq N_{jets} \leq 4$.

  We require 2 to 4 good jets with $E_T \geq 15 GeV$. The E_T cuts reduce the sensitivity of the analysis to the jet reconstruction turn-on differences between MC and data. Setting a maximum number of jets reduces the sensitivity of the analysis to the weaknesses of simulating multiple initial state radiation (ISR) and final state radiation (FSR) jets with PYTHIA. Jet pseudorapidity is $| \eta(jet) | \leq 3.2$. For Highest energy jet (leading jet) $E_T \geq 25.$ and $| \eta(jet) | \leq 2.5$.

- Missing Energy ($\not{E}_T$)≥ 15 GeV and $\not{E}_T < 200$ GeV . We cut on $\not{E}_T$ both with and without the muon corrections to reduce our sensitivity to mis-measured muon momentum in the backgrounds (in particular in misidentified-lepton multijet events).

  Sometimes an object's track is mis-reconstructed and as a consequence its transverse momentum is poorly measured. Particularly in the case of muons, this can lead to meaninglessly large values of missing transverse energy, which damage beyond repair the possibility to understand the kinematics of these events. To remove these problematic events from the analysis, we require: $\not{E}_T < 200$ GeV

- Triangle cuts: Often, a low-E_T electron is really a jet that happens to pass the electron ID criteria. The difference between the electron reconstruction and jet reconstruction algorithms leads to a small amount of missing transverse energy along the same direction as the electron. For

muons, sometimes the track momentum is measured too high or too low, and this also leads to a small amount of missing transverse energy along the direction of the muon or back-to-back with it. Jets can have their energy mis-measured or mis-calibrated, and this most often happens to attribute to the jet more energy than it really had, e.g. in a case where two close low-energy jets are merged into one with the cone algorithm. In this situation, a small amount of missing transverse energy is generated back-to-back with the jet.

These sources of mis-measurement are difficult to model in the background measurement, and since there is very little signal acceptance in these kinematic regions, we clean up the analysis significantly and efficiently by making so-called "triangle cuts" to reject events with mis-measured $\slashed{E}_T$. The triangle cuts remove these mis-measured events, which are difficult to model, but do not affect the signal because there is a small signal acceptance in these kinematic regions, as shown in Figs. 6.1, 6.2. In these figures rainbow color code has been used with red representing the heighest density density area. These cuts are listed below:
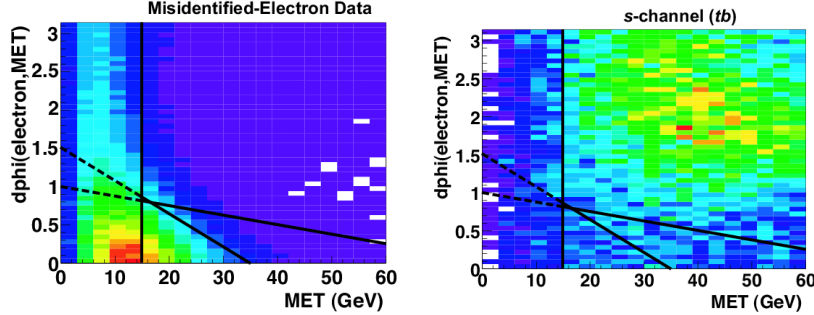
Figure 6.1: Distributions of the opening angle between the electron and $\slashed{E}_T$ versus $\slashed{E}_T$, for the misidentified-electron background data and for s-channel signal. The $\slashed{E}_T$ and triangle cuts are shown.

  $- |\Delta\phi(\text{electron}, \slashed{E}_T)|$ versus $\slashed{E}_T$: $|\Delta\phi|$ from 0.0 to 1.5 when $\slashed{E}_T = 0$ GeV,
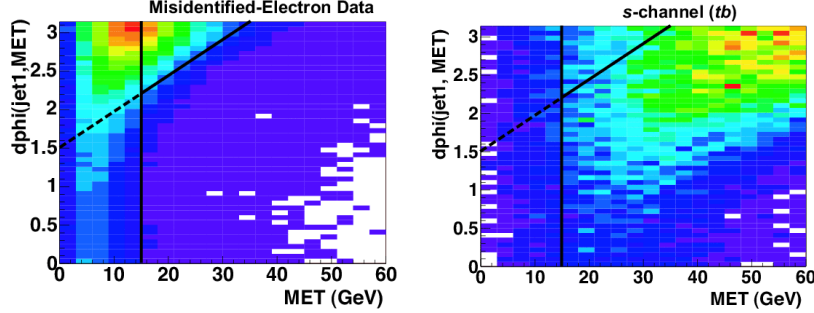
Figure 6.2: Distributions of the opening angle between the highest-E_T jet and $\not{E}_T$ versus $\not{E}_T$, for the misidentified-electron background data and for s-channel signal. The $\not{E}_T$ and triangle cuts are shown.

and $\not{E}_T$ from 0 to 35 GeV when $|\Delta\phi| = 0$

- $|\Delta\phi(\text{electron}, \not{E}_T)|$ versus $\not{E}_T$: $|\Delta\phi|$ from 0.0 to 1.0 when $\not{E}_T = 0$ GeV, and $\not{E}_T$ from 0 to 80 GeV when $|\Delta\phi| = 0$

- $|\Delta\phi(\text{leading jet}, \not{E}_T)|$ versus $\not{E}_T$: $|\Delta\phi|$ from 1.5 to π when $\not{E}_T = 0$ GeV, and $\not{E}_T$ from 0 to 35 GeV when $|\Delta\phi| = \pi$

- Isolated Muon Veto

The number of events in the data and the Monte Carlo samples after selection cuts, before b-tagging, are given in Table 6.3.

Table 6.4 shows efficiencies for single top s-channel MC events to pass all the cuts before tagging.

Some plots of basic variables, e.g. number of jets, leading jet p_T and η, electron p_T and η, and missing E_T are shown in Fig. 6.3. Each plot shows a summed histogram of all background contributions plus the expected single top signal, and the signal data. Here The individual contributions are (from the bottom up on each plot): misidentified-lepton multijet events in brown, W+jets (including Z+jets and dibosons) in green, $t\bar{t}{\rightarrow}l$+jets and $t\bar{t}{\rightarrow}ll$ in red, t-channel (tqb) single top in blue, and s-channel (tb) single top in cyan. The data is shown by black solid circles with error bars.

131

Samples	No. of Events after selection
Signal	
MC tb	8,945
Backgrounds	
MC tqb	9,107
MC $t\bar{t} \rightarrow l$+jets	23,728
MC $t\bar{t} \rightarrow ll$	13,725
MC wbb	6,929
MC wjj	12,640
MC $ww \rightarrow l\nu jj$	3,696
MC $wz \rightarrow l\nu jj$	3,822
Mis-ID'd l data	21,554
Signal data	7,232

Table 6.3: Numbers of events after preselection but before tagging.

6.3 Selection of Events With b-jets

One difference between single top and its backgrounds, except $t\bar{t}$ and Wbb, is the presence of a b jet. To take advantage of this fact, we use b-tagging - that is we look for a second vertex in the event that indicates the b jet came from a b quark.

Before applying the b-tagging algorithm to the events which have passed main selection of events, we make sure that all of our main backgrounds are well modeled and the data-versus-background comparison looks fine.

Once we have the main selection applied, events are then divided into subsets depending on the number of tagged jets found in the event and the number of total jets in the event. For this analysis we divide events in three sets: events

132

	Cut efficiencies for s-channel MC events		
	Number of Events	Exclusive cut Efficiency (%)	Cumulative Cut Efficiency (%)
Lumi,Xsection, Br	41.88	100	100
Acceptance & ID	22.92	54.73	54.81
Trigger	17.38	75.83	41.50
Primary vertex	16.83	98.52	40.19
Electron $P_T > 15$ GeV	16.33	97.63	38.99
$|\eta| < 1.1$	15.16	90.68	36.20
Electron Track Match	14.17	92.10	33.83
Electron Track $p_T > 10$ GeV	14.15	93.68	33.79
$|Z(e, PV)| < 1$ cm	14.14	90.86	33.76
Electron Likelihood> 0.4	13.60	88.59	32.47
Electron Lhood> 0.85 (for $P_T < 30$ GeV)	13.42	83.0	32.04
$2 \geq$ N Jets	10.59	77.19	25.29
N Jets ≥ 4	10.55	99.77	25.14
$\not{E}_T > 15$ GeV	9.79	93.21	23.38
$\not{E}_T < 200$ GeV	9.65	99.83	23.04
Jet1-$\not{E}_T$ Triangle	9.23	93.51	22.04
Elec-$\not{E}_T$ Triangle	9.14	96.00	21.82
Elec-$\not{E}_T$ Triangle	8.75	92.05	20.89
Isolated Muon Veto	8.63	96.61	20.61

Table 6.4: Cut efficiencies for s-channel MC events in the e+jets channel. The percentage cut efficiencies are with respect to yield after detector acceptance and trigger weights have been applied.

with exactly one tight and one loose tagged jet in them; events with more than one tight tagged jets and exactly two loose tagged jets. The reason of choosing one loose and one tight tag is to increase the acceptance but keeping the fake b-tag probability low (see Fig. 4.14).

In section 4.6, we saw how tagging is done in data and how MC TRF's are
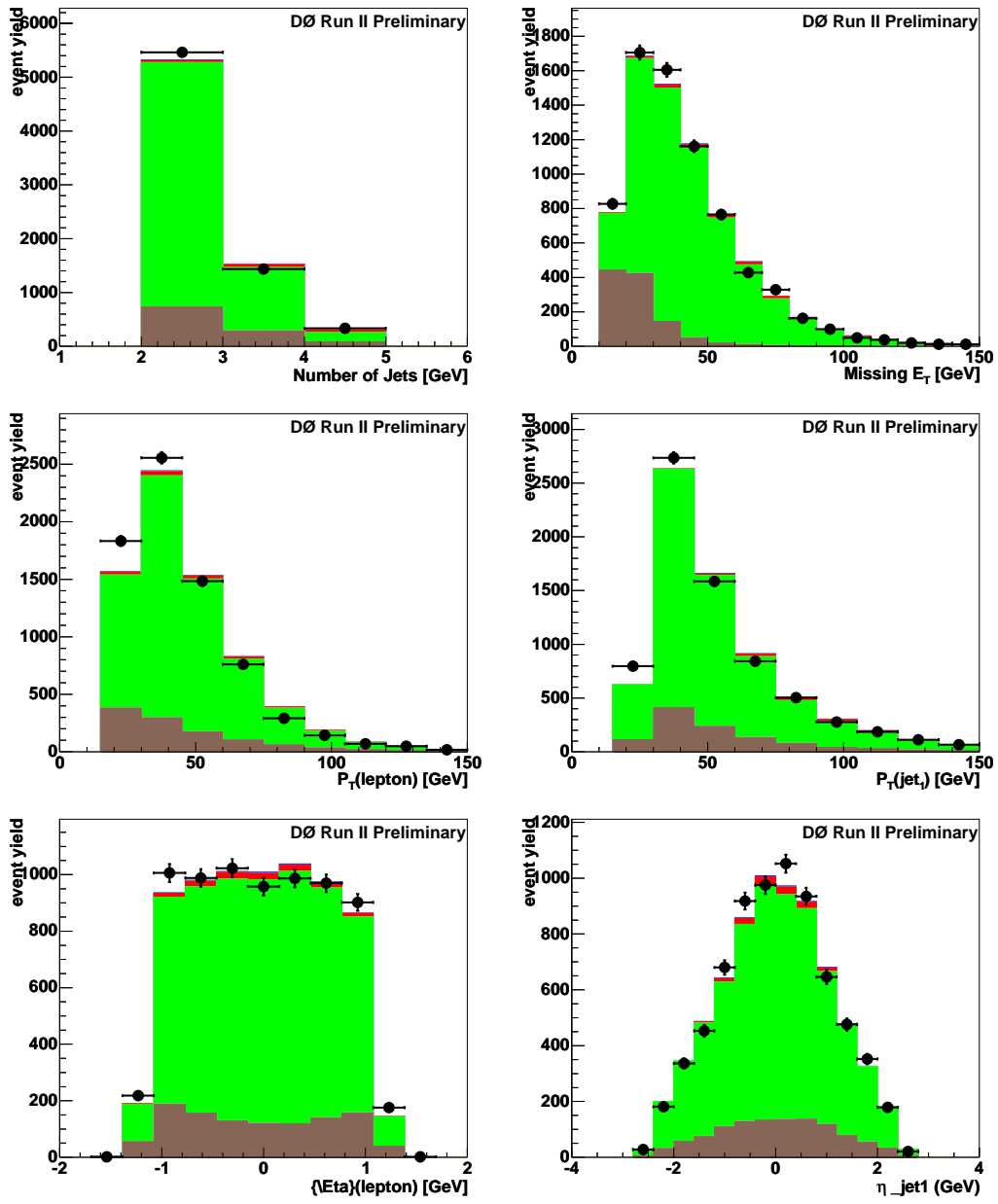
Figure 6.3: Data versus sum of all backgrounds before applyinh the tagging algorith.

derived. In this section we will see how to apply those TRFs to our different MC samples. The TRFs are applied to the single top and background Monte

Carlo samples as part of determining the acceptances. The procedure is given below:

First, for each jet in the event (with $E_T > 15$ GeV and $|\eta| < 3.4$) a taggability-rate function is applied.

Next, each jet's lineage is determined. If the jet contains a B meson within $\Delta R < 0.5$ of the jet axis it is labeled a b-quark jet. If a D meson is within $\Delta R < 0.5$ of the jet axis, it is labeled a c-quark jet. If neither of the two are close by, the jet is labeled a light-quark jet.

The probability determined from the appropriate TRF is then applied.

The taggability and tagging probability are multiplied together to determine the probability of the MC jet, j, being tagged (P_{j}).

The probability that no jet is tagged in the event is given by:

$$P_{=0\mathrm{tag}} = \prod_{\mathrm{j}=1}^{njets} \left(1 - P_{\mathrm{j}}\right)$$

Then the probability for at least one jet in the event to be tagged is one minus the probability of no jet being tagged:

$$P_{\geq 1\mathrm{tag}} = 1 - P_{=0\mathrm{tag}} = 1 - \prod_{\mathrm{j}}(1 - P_{\mathrm{j}})$$

and for exactly one jet tagged is:

$$P_{=1\mathrm{tag}} = \sum_{\mathrm{i}} P_{\mathrm{i}} \prod_{\mathrm{j}\neq\mathrm{i}}(1 - P_{\mathrm{j}})$$

and at least two jets tagged is:

$$P_{\geq 2\mathrm{tag}} = P_{\geq 1\mathrm{tag}} - P_{=1\mathrm{tag}}$$

In the case of an asymmetric tagger the total event probability is given by:

In case where a TIGHT tagged jet is also a LOOSE tagged, which is the case most of the time:

$$P_{event} = \sum_{perm} \prod_{\mathrm{T}} P_{\mathrm{T}} \prod_{\mathrm{L}} (P_{\mathrm{T}} - P_{\mathrm{L}}) \prod_{\neq \mathrm{T}, \neq \mathrm{L}} (1 - P_{\mathrm{L}}) \qquad (6.1)$$

But sometimes a TIGHT tagged jet may not be a LOOSE tagged jet and in that case:

$$P_{event} = \sum_{perm} \prod_{\mathrm{T}} P_{\mathrm{T}} \prod_{\mathrm{L}} \frac{(P_{\mathrm{T}} - P_{\mathrm{L}})}{P_{\mathrm{T}}} \prod_{\neq \mathrm{T}, \neq \mathrm{L}} (1 - P_{\mathrm{L}}) \qquad (6.2)$$

Here the sum is over all the possible permutations of the jets in an event. and the probability P is a function of p_T and η. The numbers obtained thus are used as part of the event weight for MC events. The advantage of calculating a weight for each event rather than just multiplying the total number of events by the average probability for an event to have at least one tagged jet is that the E_T turn-on curve and η fiducial region are properly modeled. Without the event weights, the shapes of distributions of variables such as H_T would be incorrect.

Another aspect of b-tagging is to identify which jet in the event is a b jet and which one is a light jet. This information is important and is needed to reconstruct various variables which we will use later in the analysis. For this, since for every permutation we know which jet is a b and which is not, every permutation is used separately. Each event is now considered many times with different weights (depending on the number of permutations or number of jets in other words). For every permutation, the value of the tag dependent variable may change but the weight of the event as a whole does not change and is given by the sum of all the permutations as given in the above equations.

Chapter 7

Analaysis: Search for Single Top

With regard to excellence, it is not enough to know,

but we must try to have and use it.

Aristotle

In the Standard Model, the top quark decays almost 100% of the time to a W boson and b quark. Therefore, in single top events, the final state is largely determined by the W boson decay modes. As we discussed earlier in Chapter 2, the event signatures, both for s- and t-channel production modes of single top, include a W boson and two b quarks. Experimentally, the most relevant channel is "lepton+jets", where the W boson decays to a lepton (electron or a muon) and a neutrino. In addition, two jets arising from the fragmentation of the b-quarks (b-jets) are expected in the final state. This analysis concentrates on the electron + jets channel i.e W decaying to an electron and a neutrino.

In order to observe single top quark production we will have to design selection cuts in such a way that we not only get rid of the overwhelming background but also keep the signal efficiency high.

Since, in the case of the electron+jets channel, the final state includes a high pT isolated electron, large $\not{E}_T$ indicating the presence of the neutrino and two high p_T b jets, the discrimination from the dominant background processes (W+jets and multi-jets production) can be achieved by making use of b-tagging to identify a b-jet in the event. For this analysis we will use the *Secondary Vertex Tagging (SVT)* method. SVT distinguishes heavy-flavor jet from a light-flavor jet by establishing the presence of a secondary vertex from the decay of long lived B- or D-meson. The tagging probabilities discussed in section 4.6 are applied to each background component to determine its contribution to the tagged sample.

Because of its small cross section and overwhelming background, single top is hard to find and b-tagging alone may not be enough to get a good signal-vs-background discrimination. For this reason we will use Neural Networks and Decision Trees, two sophisticated analysis tools, to get a better discrimination.

So, the main steps of the analysis are going to be as follows:

1. Before applying the secondary vertex tag, separate real and fake W contributions using the Matrix Method (see section 7.1.1). Here the fake W contribution comes from multi-jet events where one jet has been misidentified as an electron. The real W contribution includes W+jets, $t\bar{t}$ and dibosons as well as our single top signal. Here W+jets includes both Wbb and Wjj (jj being light quark, gluons, and charm quarks).

2. Determine the number of events coming from different backgrounds (W+jets, $t\bar{t}$, dibosons) in the untagged sample (see section 7.1.2).

3. Apply tagging probabilities, to each background component to determine its contribution to the tagged sample. In order to increase our sensitivity,

we will divide our tagged sample into events with exactly one tight tagged jet, and events with one or more tight tagged jet and exactly 2 loose tagged jets.

4. Find a list of discriminating variables to be used as input to Neural Networks (see section 7.4.1).

5. Apply Neural Networks separately to single and double tagged samples.

6. If an excess of events is seen, measure the cross-section, else set a limit. To get the most sensitivity, we will use a binned likelihood approach for limit setting(see section 7.5).

These steps are described in detail in the following sections:

7.1 Determining the Real and Fake W contributions

In this section we will describe how we model our different backgrounds. Background modeleing is a very important step because it summarizes how well we understand our backgrounds.

We can catagorize our background in two groups: $W + jets$ and $non - W + jets$ or events with real electrons making real W's and events with fake electrons making fake W's. There is a very small fraction of events where a real electron is not coming from from W (electron fron Z for instance). We get rid of most of these events at the selection level and the remaining very small fraction is taken care of when $W+jets$ is scaled to data (see section 7.1.2)

The $non - W + jets$ background comes from multijet events with a jet misidentified as an isolated electron, called fake-e in this analysis. This background is measured using data.

The $W + jets$ background is made up of individual backgrounds from $Wb\bar{b}$, Wjj, $t\bar{t}$, and diboson production. Here Wjj includes W + any flavor of jets but $b\bar{b}$. To detremine the $t\bar{t}$ and diboson background we completely rely on MC simulations. For $Wb\bar{b}$ and Wjj we use MC simulation and then scale the estimated backgrounds to data.

The first step in identifying our backgrounds is to estimate the $non - W + jets$ ("fake-e") content after we have applied all the selection cuts. The fake-e background is determined from data using a so-called "matrix method". The next section briefly describes matrix method.

7.1.1 Evaluation of Non-W Background

The background from multijet events with a jet misidentified as an isolated electron is measured using data. The steps to measure this background are as follows.

1. We determine the number of real and fake W events in the pretagged data sample (N_W and N_{fake-e}) using the "matrix method."

2. An independent pretagged, multijet, sample is selected that consists mainly of background events. This is known as the "orthogonal fake-e" sample

3. We normalize the orthogonal fake-e sample to the number of pretagged events N_{fake-e} found in step 1.

4. The b-tagging algorithm is applied to the normalized orthogonal sample to obtain the tagged fake-e background.

These steps are further explained below:

Pre-tag Misidentified-Electron Background Estimation

We use the matrix method to divide the pretagged signal data into two parts: events with a misidentified electron and those with a real electron. Misidentified electrons are from multijet events, while real electrons are mostly from W+jets events, with a very small fraction from $t\bar{t}$ and single top. The matrix method and its error calculation are explained in detail in Ref. [159].

Consider the following two equations:

$$N_{loose} = N_W + N_{fake-e}$$
$$N_{tight} = \varepsilon_W N_W + \varepsilon_{fake-e} N_{fake-e} \qquad (7.1)$$

Here N_{loose} and N_{tight} are the numbers of events in the loose and tight samples, where loose means all the selection cuts are applied except the electron likelihood cut and the tight sample is obtained by applying the electron likelihood cut to the loose sample. ε_W and ε_{fake-e} are the probabilities for the signal (real electrons) and fake-e background events to pass this cut respectively. Now, if we know these efficiencies, we can solve these two equations for N_W and N_{fake-e}. Solving these two simultaneous equations gives:

$$N_W = \frac{N_{tight} - \varepsilon_{fake-e}.N_{loose}}{\varepsilon_W - \varepsilon_{fake-e}}$$
$$N_{fake-e} = \frac{\varepsilon_W.N_{loose} - N_{tight}}{\varepsilon_W - \varepsilon_{fake-e}} \qquad (7.2)$$

Determination of ε_W

We determine ε_W using $Z \rightarrow ee$ events. Here we apply basic cuts to this sample and reconstruct the Z boson mass. All the cuts are applied to both electrons coming from Z, except the likelihood cut. This is our loose data set. We apply the likelihood cut to one of the electrons (called the "tag") and
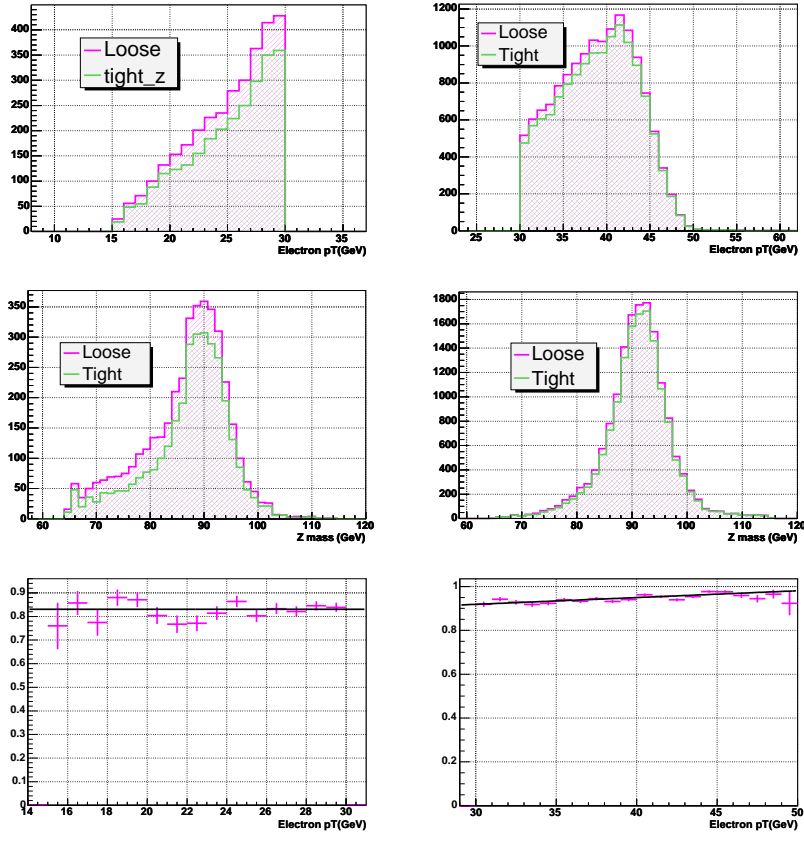
Figure 7.1: Evaluation of ε_W by reconstructing Z mass. The tag electron is required to be in the CC region of the calorimeter. Plots on left side are for electron $P_T < 30$ GeV and the ones on right are for $P_T > 30$ GeV. First row is electron P_T for loose and tight samples. Second row is reconstructed Z mass. Last row is the resulting efficiency of events to pass the likelihood cut versuselectron P_T.

then calculate the efficiency of the second electron (called the "probe") passing the likelihood cut. The plots in Fig. 7.1 show the resulting efficiencyies for electron $P_T < 30$ GeV and electron $P_T > 30$ GeV region. As you can see, in case of electron $P_T > 30$ GeV and $P_T < 45$ GeV, there is some dependence on electron P_T. For electron $P_T > 45$ we use a constant value. These efficiencies for different regions are given in Table 7.1
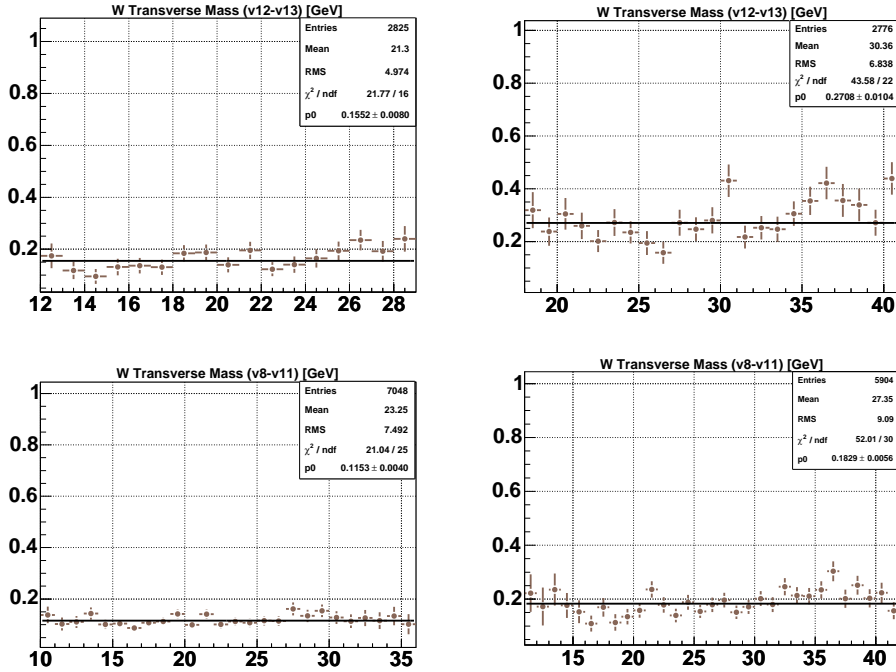
Figure 7.2: ε_{fake-e} versus W transverse mass for different trigger versions of data and two regions of electron P_T. Left: efficiency for electron $P_T < 30$, for trigger version v12-v13 (up) and for electron $P_T < 30$, for trigger version v8-v11 (down); right: efficiency for electron $P_T > 30$, for trigger version v12-v13 (up) and for electron $P_T > 30$, for trigger version v8-v11 (down). These efficiencies are for the central calorimeter region.

The probability $\varepsilon_{\text{fake}-e}$ that an EM object originating from a jet faked an electron (i.e., that it passed the electron likelihood cut) is determined from multujets data with low missing transverse energy (< 10 GeV), which is dominated by fake-e events. It was then assumed that the fake probability is the same in this region as in the signal region with high missing transverse energy

143

electron p_T	ε_W
$< 30 GeV$	0.83 ± 0.05
$\geq 30 GeV, < 45 GeV$	$(0.826 + 0.003 \times p_T) \pm 0.05$
$\geq 45 GeV$	0.980 ± 0.05

Table 7.1: ε_W values for different electron p_T regions.

electron p_T	Trigger version	ε_{fake-e}
$< 30 GeV$	v12	0.155 ± 0.008
$\geq 30 GeV$	v12	0.271 ± 0.010
$< 30 GeV$	v8-11	0.115 ± 0.004
$\geq 30 GeV$	v8-11	0.183 ± 0.006

Table 7.2: ε_{fake-e} values for different electron p_T and trigger versions.

$(> 15 \text{ GeV})$.

There are two things to note here: one, the fake-e background is mostly in the low electron P_T region. To suppress this background, we use a tighter electron likelihood cut for electron $P_T < 30$ GeV and a looser cut value for $P_T > 30$ GeV. Two, ε_{fake-e} has some dependence on the different trigger versions, so we calculate ε_{fake-e} separarely for the runs taken with v8-v11 trigger versions and the runs taken with v12-v13 trigger versions, as shown in Fig. 7.2. The ε_{fake-e} values for different P_T and trigger versions are given in Table 7.2.

Figure 7.3 shows a histogram of the transverse mass of the reconstructed W boson in the pre-tagged data sample, after applying the matrix method. Here you can see Data (black) divided into $W + jets$ (green) and $non - W$ (brown, we call it QCD) contribution from fake electrons. The different numbers from Matrix Method output are given in Table 7.3.

144
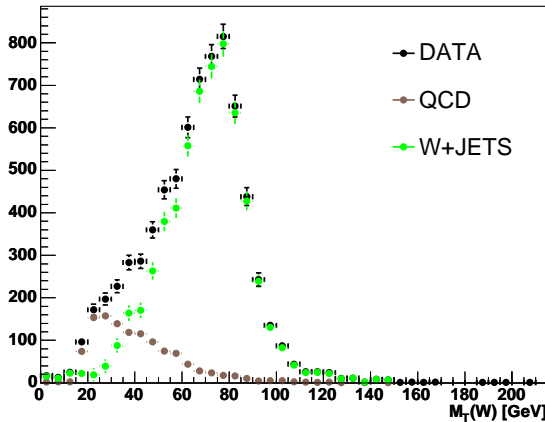
Figure 7.3: Plot showing the matrix method output for electrons recostrucetd in the central region of calorimeter.

		Matrix Method output			
N_{loose}	N_{tight}	$N_{W_{loose}}$	$N_{W_{tight}}$	$N_{fake-e_{loose}}$	$N_{fake-e_{tight}}$
12,736	7,232	6,539.68	6,066.16	6,196.31	1,165.84

Table 7.3: Matrix method normalization of the W+jets and misidentified electron backgrounds.

Tagged Misidentified-Electron Background Estimation

The matrix method works fine for determining the misidentified electron background before tagging, but after b-tagging, especially after double b-tagging , we are statistics limited, and cannot use this method directly on the data sample. So the following procedure has been adopted.

Starting from the main data sample (before any selection cuts), we create a sample consisting of mainly multijet events with a mis-reconstructed EM-object, and no good tight electrons in the sample. This sample passes all

preselection criteria except for the tight-electron criteria of a track match or a vertex cut. This sample is orthogonal to our signal sample in the respect that it is required to passes a tight inverted electron likelihood cut $\mathcal{L} < 0.05$.

The above orthogonal fake-e sample is normalized to the number of fake-e events that we evaluated using the matrix method for the pretagged sample. This normalized sample is then used to estimate the fake-e background after tagging. We apply the b-tagging algorithm directly to the orthogonal fake-e data sample and normalize it as described above to obtain the tagged misidentified isolated-electron background yields (Table 7.5).

7.1.2 Evaluation of Backgrounds with Real W's

Backgrounds with real W's (Wbb,Wjj, $t\bar{t}$ etc.) are evaluated using the Monte Carlo samples. Each MC event in the single top analysis is assigned a weight, a number between 0 and 1, which are summed to get the acceptances and yields. For MC, the weight includes all correction factors to make the MC look like data, including the probability for event to pass a certain trigger and the event to have one or more b-tagged jets.

The probability for each jet in the event to be tagged is determined from the taggability-rate functions and the tag-rate functions, as was discussed in Sec. 4.6, and the probability for a jet to have one or more b-tagged jets is given in Sec. 6.3. In the case of Wbb and Wjj, we normalize these MC samples to data using the following procedure. We apply all correction factors to the various MC samples and determine the yield Y for each sample before b tagging. We then find the total predicted MC yield Y^{MC}_{total} as:

$$Y^{MC}_{\text{total}} = C \times \left\{ Y^{Wjj} + Y^{Wbb} \right\} + Y^{t\bar{t}} + Y^{WW} + Y^{WZ}.$$

The normalization factor C is then found by requiring that the total MC

yield is equal to the real-lepton yield in data ($N_{W_{tight}}$):

$$C = \frac{N_{W_{tight}} - \left(Y^{t\bar{t}} + Y^{WW} + Y^{WZ}\right)}{Y^{Wjj} + Y^{Wbb}}.$$

The resulting normalization factor $C = 1.284$. Note that all yield estimates in this analysis for the Wjj and Wbb samples include the factor C.

7.2 Determining Acceptances and Yields for Signal and Background Samples

Not everything that can be counted counts,
and not everything that counts can be counted.

Albert Einstein

we have reconstructed our events, applied selection cuts and modeled different backgrounds. In this section we will get the yields and acceptances of our signal and background samples.

Yields are the actual number of signal or background events that are produced in our detector for the given luminosity, after all the corrections have been applied. Acceptances are needed to compute actual yields from measured yields. Signal acceptances tell us what percentage of signal events that were produced in the detector for the given luminosity, actually passed our selection cuts. We measure the signal and background acceptances in order to measure or set limits on the single top production cross sections.

In order to compare the observed event count in data with our expectation, and to set limits on the single top quark production cross section, we determine acceptances and event yields for the single top quark signal and the various Standard Model background contributions.

We apply all of the selections to the Monte Carlo except for the trigger and

b-tagging, which are taken account of with a weight applied to each event that represents the probability for it to pass the trigger and b-tagging requirements. The weight also includes a correction factor for particle identification efficiency differences between data and MC.

7.2.1 Acceptance Calculation

The signal acceptance is defined as:

$$\mathcal{A}^{\text{sigMC}} = \frac{\mathcal{B}}{N_{\text{initial}}} \sum_{N_{\text{preselect}}} \varepsilon_{\text{trigger}} \, \varepsilon_{\text{correction}} \, \varepsilon_{b-\text{tagging}}$$

where:

- $\mathcal{B}$ is the branching fraction for each MC sample, given in Table 5.1. The error on $\mathcal{B}$ is $\pm 2\%$.

- N_{initial} is the number of events in each MC sample before any cuts are applied. The numbers are given in Table 5.1.

- $\varepsilon_{\text{trigger}}$ is the trigger efficiency for each event, described in Section 6.1. The errors are between 4% and 10%, depending on the channel.

- $\varepsilon_{\text{correction}}$ is the product of the correction factors described in Section 5.1 that account for differences between MC events and data.

- $\varepsilon_{b-\text{tagging}}$ is the probability for each event to have at least one b-tagged jet. The errors are between 7% and 12%, depending on the channel.

The percentage acceptances for MC samples are given in Table 7.2.1.

7.2.2 Event Yields

The event yields then are given as:

$$\text{Yield} = \mathcal{Y}^{\text{MC}} = \mathcal{A}^{\text{MC}} \, \mathcal{L} \, \sigma$$

148

Percentage Acceptances for the MC Samples			
	Pretagged	=1 Tag	=2 Tags
tb	2.7	1.0	0.3
tqb	2.7	0.9	0.1
$t\bar{t}{\to}l+$jets	4.4	1.5	0.4
$t\bar{t}{\to}ll$	1.2	0.5	0.1
Wbb	6.0	2.0	0.5
Wjj	5.5	0.1	0.0
WW	2.1	0.1	0.0
WZ	2.2	0.3	0.1

Table 7.4: Acceptances for MC samples as percentage of the total cross sections.

where $\mathcal{L}$ is the integrated luminosity of the lepton channel signal data and σ is the theoretical cross section for each MC process.

Table 7.5 shows the numbers of events for each of the signals, combinations of signals, backgrounds, and data, after event selection and b-quark tagging. The background sum reproduces the data within uncertainties for all samples after b-quark tagging. This agreement is excellent in the pretagged sample as expected since the $W+$jets and QCD backgrounds are normalized using this sample. Here misidentified-lepton backgrounds are determined using an orthogonal data sample containing mis-measured leptons, which is normalized using the matrix method to the fraction of pretagged signal data that contains such mis-measured leptons, and afterwards, real tags are identified in the jets (no jet tag probability is needed). The details of this procedure are given in Section 7.1.1.

The tb, tqb, $t\bar{t}$, WW, and WZ samples are normalized using the theory cross sections, branching fractions, and numbers of events shown in Table 5.1,

| | Event Yields | | |
	Pretagged	=1 Tag	=2 Tags
Signal			
tb	8.63	3.17	0.95
Backgrounds			
tqb	19.21	6.35	0.69
$t\bar{t}{\rightarrow}l$+jets	108.03	37.73	10.89
$t\bar{t}{\rightarrow}ll$	29.95	11.04	3.22
Wbb	73.55	24.82	6.03
Wjj	5,785.59	102.5	3.54
WW	20.27	0.72	0.01
WZ	6.50	0.76	0.21
Mis-ID'd l	1,107.29	31.34	1.97
Sum bkgnds	7,150.38	215.25	26.52
Sum bkgnds+signal	7,159.0	218.42	27.51
Data	7,232	218	45

Table 7.5: Event yields after selection.

together with the integrated luminosities of the data sample.

The Wbb, Wjj, and misidentified-lepton samples are normalized to data; details about this calculation are given in Section 7.1.2. As part of the normalization procedure, we find that normalizing the Wbb and Wjj samples by cross section in the pretagged sample results in yields that are about 13% lower for CC electron than those found when normalizing to data.

Some plots of data versus sum background are are shown in Figs.[7.4,7.5], with different backgrounds summed and compared to data. Each plot shows a summed histogram of all background contributions plus the expected single top signal, and the signal data.Here The individual contributions are (from the bottom up on each plot): misidentified-lepton multijet events in brown,
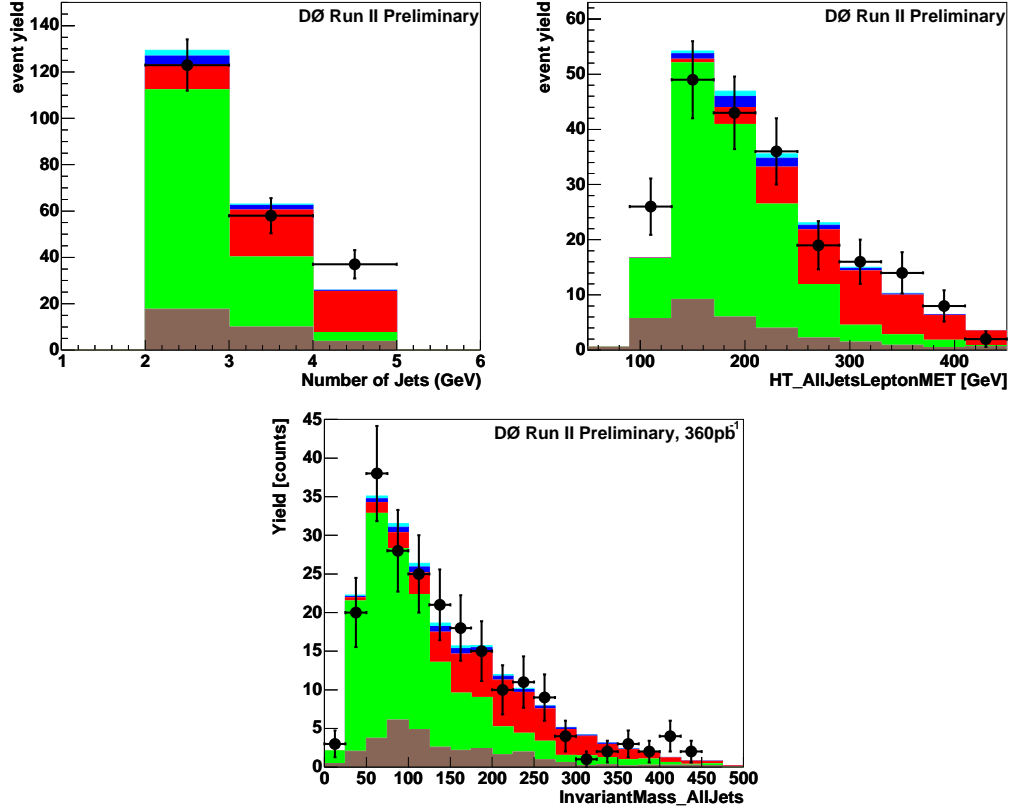
Figure 7.4: Data versus background comparison with exactly one b-tagged jet.

W+jets (including Z+jets and dibosons) in green, $t\bar{t} \rightarrow l$+jets in red, $t\bar{t} \rightarrow ll$ in pink, t-channel (tqb) single top in light blue, and s-channel (tb) single top in dark blue. The data is shown by black solid circles and/or black error bars. Additional plots are shown in Appendix A which also contains crosscheck plots, where we divided our samples into two: one predominantly Wjj events; the other predominantly $t\bar{t}$ events. We can see that after going through all the steps described in this chapter, we get a reasonable agreement between the data and the sum of all backgrounds.

Table 7.6 shows signal-to-background ratios for pretagged, and tagged samples. These ratios are not the best achievable, since that was not a goal of
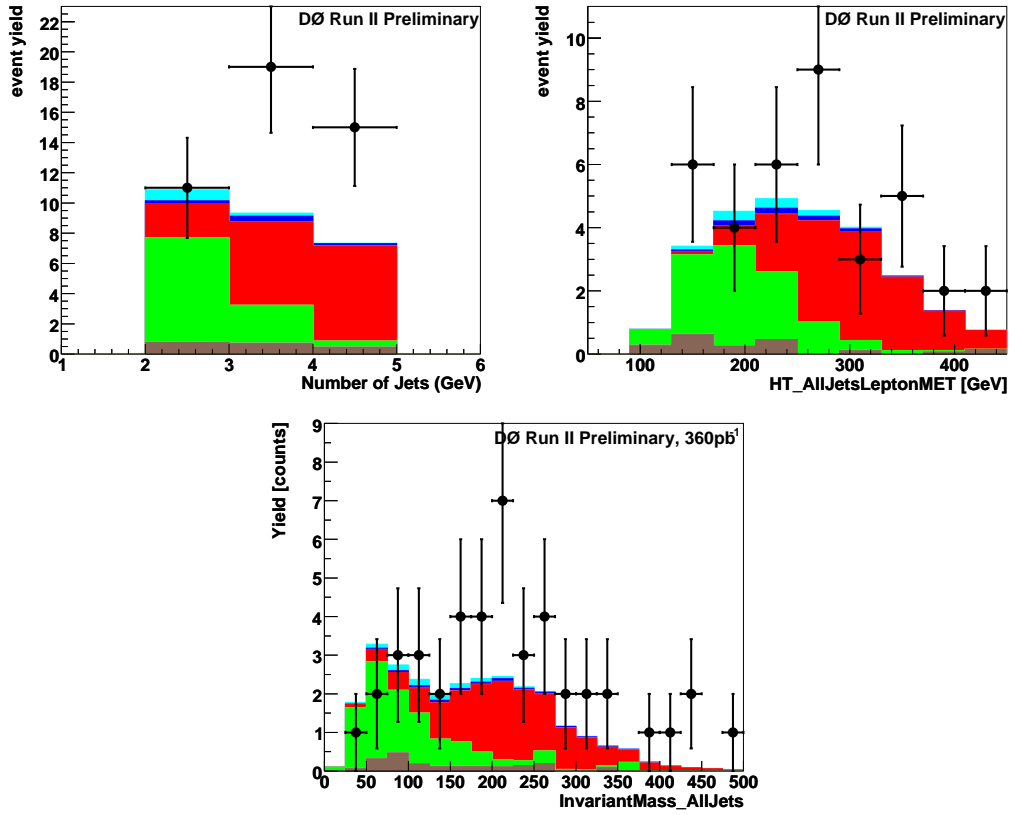
Figure 7.5: Data versus background comparison with more than one b-tagged jets.

this stage of the analysis. Our focus so far has been keeping the acceptance as large as possible.

	Signal:Background Ratios in the Main Samples		
	Pretagged	=1 Tag	=2 Tags
s-channel tb	1:829	1:75	1:28

Table 7.6: The ratio of the signal yield to the combined background yield for the main samples of selected events.

7.3   Systematic Uncertainties

Probable impossibilities are to be preferred to
improbable possibilities.

Aristotle

We consider several sources of systematic uncertainties in this analysis. Some of the uncertainties affect acceptance for Monte Carlo signals and backgrounds, others only affect background yield estimates. The luminosity, cross section, and branching fraction uncertainties, for exmple, are only needed for calculating MC yields, not acceptances.

Uncertainties from background modeling

The matrix method uncertainty term includes components for two parts of the calculation. One – determination of the number of real-lepton events in data is affected by the uncertainties associated with the determination of the probabilities for a loose lepton to be (mis)identified as a (fake) real lepton, $\varepsilon_{\text{fake-lepton}}$ and $\varepsilon_{\text{real-lepton}}$. It is also affected by the limited statistics of the data sample. Two – determination of the combined Wbb and Wjj yields is affected by the uncertainty on the theoretical cross sections for Wbb and Wjj used to estimate the yield before the matrix method normalization. We assign a relative uncertainty of 25% on the ratio of Wbb to Wjj cross sections before tagging. This uncertainty has been estimated conservatively to represent our current understanding of the flavor composition of the W+jets sample. It includes uncertainties on the NLO cross sections, factorization scale, and PDFs, as well as different jet-parton matching procedures. We propagate this uncertainty to the yield estimates after tagging, assigning the resulting uncertainty

equally to the Wbb and Wjj samples. Hence the uncertainty from the matrix method is larger in the two-tag samples where the Wbb fraction is larger than in the one-tag sample.

7.3.1 Acceptance Uncertainties

In addition to the uncertainties on $\mathcal{B}$, $\varepsilon_{\text{trigger}}$, $\varepsilon_{\text{correction}}$, and $\varepsilon_{b-\text{tagging}}$, the signal acceptance uncertainties also include the following components:

- $\varepsilon_{\text{jet}-\text{frag}} = \pm 5\%$ (tb, tqb, $t\bar{t}\rightarrow ll$, $Z\rightarrow\mu\mu$), $\pm 7\%(t\bar{t}\rightarrow l+\text{jets})$.

  The jet fragmentation uncertainty covers the uncertainty in modeling of initial and final state radiation as well as the difference in the fragmentation model between PYTHIA and HERWIG.

- $\varepsilon_{\text{JER}} = \pm$ between 2% and 19%, Correction for Jet Energy Resolution.

- $\varepsilon_{\text{JES}} = \pm$ between 2% and 20%, Correction for Jet Energy Scale.

  We measure the uncertainty from the jet energy scale for the Monte Carlo samples, to quantify how well the model matches the data.

7.3.2 Event Yield Uncertainties

The relative errors on the yield are calculated as:

$$\text{Yield statistical error} = \Delta\mathcal{Y}^{\text{MC}}_{\text{stat}} = \Delta\mathcal{A}^{\text{MC}}_{\text{stat}}$$

$$\text{Yield systematic error} = \Delta\mathcal{Y}^{\text{MC}}_{\text{syst}} = \sqrt{\left(\Delta\mathcal{A}^{\text{MC}}_{\text{syst}}\right)^2 + (\Delta\mathcal{L})^2 + (\Delta\sigma)^2}$$

Where $\Delta\mathcal{A}^{\text{MC}}_{\text{stat}}$ is the relative statistical error (relative error = dx/x) for the samples after preselection, $\Delta\mathcal{A}^{\text{MC}}_{\text{syst}}$ is the relative systematic error on the acceptance, $\Delta\mathcal{L}$ is the relative error on the integrated luminosity, $\Delta\sigma$ is the

relative error on the theoretical cross section.

Tables [7.7,7.8] show the systematic uncertainties on the signal and background samples for the single-tagged and double-tagged analyses.

These sytematics tables can be used to see the correlation between the various samples and analysis channels for each uncertainty. A systematic uncertainty is assumed to be fully correlated between all signal or background samples within a given row in each table, and for rows with the same name in different tables. The exceptions to this are the systematic uncertainties on the theoretical cross sections used to normalize the MC backgrounds (except for the two $t\bar{t}$ backgrounds), and the statistical uncertainty from the size of each MC sample.

Note that owing to the normalization to data before b tagging, the Wbb and Wjj tagged yield estimates are not affected by any of the systematic uncertainties that affect the overall yield. The exception to this is b tagging, which is applied after normalization. There is still an effect on the shapes of distributions from the uncertainty components that depend on event kinematics. For these shape-changing systematics (jet identification, jet energy scale, jet energy resolution, trigger, and tag-rate functions), we include the uncertainty in each bin of the binned likelihood calculation for the limit..

Note also that the normalization for Wbb and Wjj includes the other MC backgrounds and thus their uncertainties in principle also affect Wbb and Wjj. However, the other MC backgrounds only contribute about 3% to the pre-tagged yield, which means their uncertainties are negligible compared with the other matrix method uncertainties and thus we ignore them.

Table 7.9 shows the uncertainties on the signal yields and background components after selection. Table 7.10 shows the uncertainties on the acceptances and on the combined backgrounds. Some plots of basic variables, e.g. number

of jets, leading jetp_T, electron p_T, missing E_T, W transverse mass, invariant mass of all jets in the event and calar sum of the transverse momenta of all jets, the lepton, and the missing E_T are shown in Fig. 7.6, with different backgrounds summed and compared to data. Grey band shows the range of uncertainties. Solid blue line shows t-channel single top and solid cyan line shows s-channel single top signal multiplied by 10.

	Single-Tagged Electron Channel Percentage Errors								
	tb	tqb	$t\bar{t}lj$	$t\bar{t}ll$	Wbb	Wjj	WW	WZ	Mis-ID e
Components for Normalization									
Luminosity	6.5	6.5	6.5	6.5	—	—	6.5	6.5	—
Cross section	16.0	15.0	18.0	18.0	—	—	2.2	8.9	—
Branching fraction	2.0	2.0	2.0	2.0	—	—	2.0	2.0	—
Matrix method	—	—	—	—	4.2	4.2	—	—	4.2
Primary vertex	1.8	1.8	1.8	1.8	—	—	1.8	1.8	—
Electron ID	5.0	5.0	5.0	5.0	—	—	5.0	5.0	—
Jet fragmentation	5.0	5.0	7.0	5.0	—	—	5.0	5.0	—
Components for Normalization and Shape									
Jet ID	5.84	7.1	0.3	3.6	—	—	96.2	91.8	—
Jet energy scale	3.3	4.0	1.3	3.3	—	—	10.0	9.6	—
Jet energy resolution	1.9	1.9	0.9	0.5	—	—	81.9	78.1	—
Trigger	10.4	10.6	7.9	8.1	—	—	10.3	11.3	—
Flavor-dependent TRFs	2.7	3.9	3.0	3.0	—	—	8.8	3.0	—
Statistics	1.0	1.0	0.5	0.8	1.2	0.9	1.7	1.6	5.7

Table 7.7: Electron channel uncertainties for Central Calorimeter (CC) region, requiring exactly one tight and one loose tag in the event.

	Double-Tagged Electron Channel Percentage Errors								
	tb	tqb	$t\bar{t}lj$	$t\bar{t}ll$	Wbb	Wjj	WW	WZ	Mis-ID e
Components for Normalization									
Luminosity	6.5	6.5	6.5	6.5	—	—	6.5	6.5	—
Cross section	16.0	15.0	18.0	18.0	—	—	2.2	8.9	—
Branching fraction	2.0	2.0	2.0	2.0	—	—	2.0	2.0	—
Matrix method	—	—	—	—	13.3	13.3	—	—	13.3
Primary vertex	1.8	1.8	1.8	1.8	—	—	1.8	1.8	—
Electron ID	5.0	5.0	5.0	5.0	—	—	5.0	5.0	—
Jet fragmentation	5.0	5.0	7.0	5.0	—	—	5.0	5.0	—
Components for Normalization and Shape									
Jet ID	15.7	13.9	16.7	9.4	—	—	130	157	—
Jet energy scale	10.8	7.6	13.4	5.5	—	—	20.3	23.5	—
Jet energy resolution	4.5	12.3	1.9	3.0	—	—	104	117	—
Trigger	14.8	13.0	11.5	11.3	—	—	13.0	15.3	—
Flavor-dependent TRFs	10.8	11.9	10.0	9.2	11.6	17.1	21.1	11.6	—
Statistics	1.0	1.0	0.5	0.8	1.2	0.9	1.7	1.6	22.4

Table 7.8: Electron channel uncertainties for Central Calorimeter (CC) region, requiring at least one tight b-tag and exactly two loose tags in the event.

Signal and Background-Component Yields with Uncertainties		
	=1 Tag	=2 Tags
tb	$3.17 \pm 0.72 \ (23\%)$	$0.95 \pm 0.31 \ (33\%)$
tqb	$6.35 \pm 1.45 \ (23\%)$	$0.69 \pm 0.22 \ (32\%)$
$t\bar{t} \rightarrow l$+jets	$37.73 \pm 8.65 \ (23\%)$	$10.89 \pm 3.68 \ (34)$
$t\bar{t} \rightarrow ll$	$11.04 \pm 2.52 \ (23\%)$	$3.22 \pm 0.89 \ (28\%)$
Wbb	$24.82 \pm 1.58 \ (6\%)$	$6.03 \pm 1.19 \ (20\%)$
Wjj	$102.50 \pm 9.27 \ (9\ \%)$	$3.54 \pm 0.83 \ (23\%)$
WW	$0.72 \pm 0.92 \ (127\ \%)$	$0.01 \pm 0.02 \ (169\%)$
WZ	$0.76 \pm 0.93 \ (122\ \%)$	$0.21 \pm 0.42 \ (199\ \%)$
Mis-ID'd l	$31.34 \pm 4.82 \ (15\%)$	$1.97 \pm 0.52 \ (27\%)$

Table 7.9: Signal and background-component yields after selection with total uncertainties.

Signal Acceptances and Background Yields with Uncertainties		
	=1 Tag	=2 Tags
Signal Acceptances	$0.00983 \pm 0.0015 \ (15\%)$	$0.0029 \pm 0.0008 \ (28\%)$
Background Yields	$215.25 \pm 17.44 \ (8\%)$	$26.56 \pm 5.61 \ (25\%)$

Table 7.10: Signal acceptances and combined background yields with total uncertainties for s-channel.
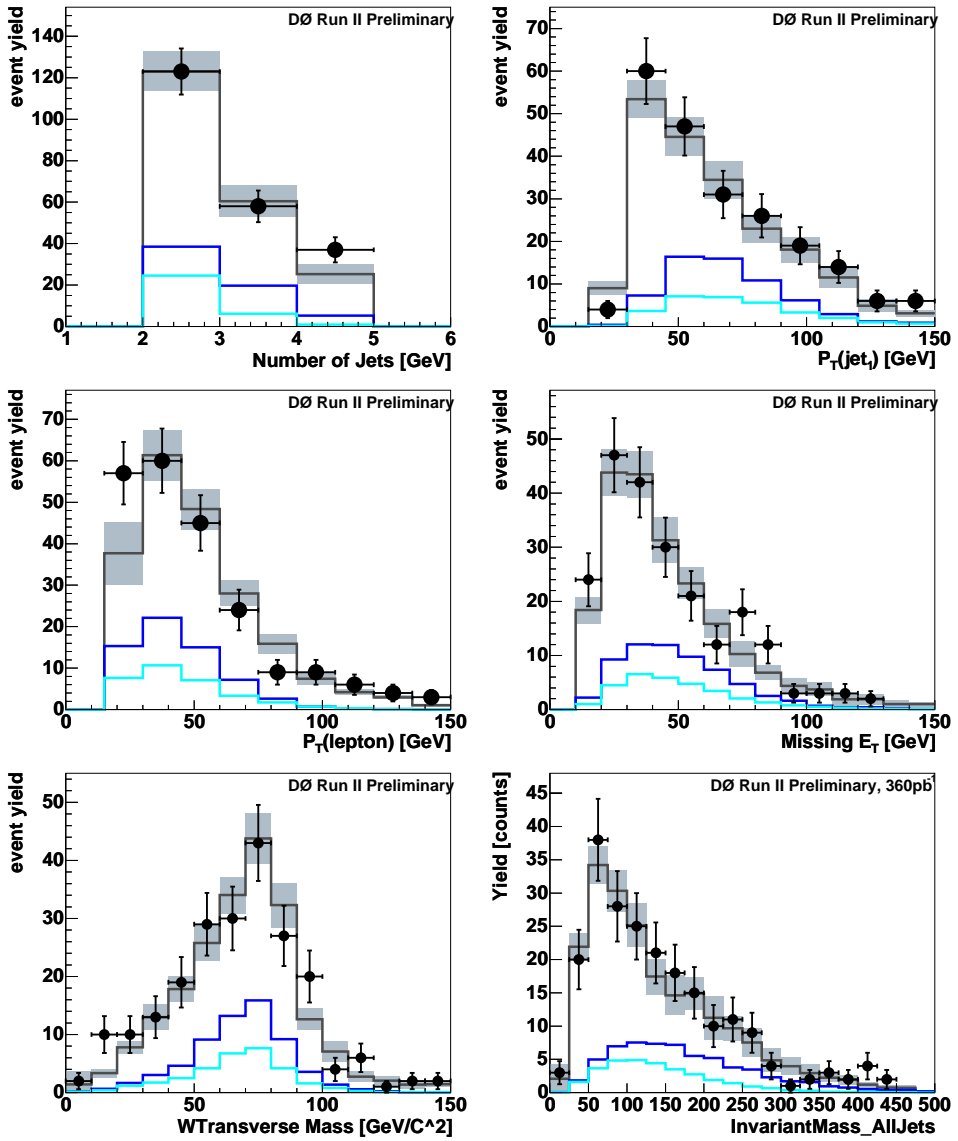
Figure 7.6: Data versus background sum with uncertainties shown as grey band.

7.4   Neural Networks

The important thing in science

is not so much to obtain new facts

159

as to discover new ways of thinking about them.

Sir William Bragg

The single top analysis is difficult in the sense that not only is the production cross-section small but the background is huge and very difficult to separate from signal. So far we have used the best Monte Carlo samples available for signal and background, and we have tried to be conservative in our cuts, but still, as Table 7.6 shows, the signal to background ratio is very small. In this situation, the limits we can set on single top production cross sections from the numbers of events after selection are not going to be very interesting. In order to improve the sensitivity of the search, we must either remove some of the background while keeping enough of the signal, or separate the signal from the background using carefully chosen variables which show discrimination between signal and background. If we perform a binned likelihood fit in the shape of one or more variables to set the cross section limits, we gain a second improvement in sensitivity over just calculating limits by counting events. If one cuts on the variables first to improve the signal:background ratio, the limits from fitting are not improved, and so we have focused our efforts on developing the best possible variables and multivariate methods using these variables for signal-background separation. There are many analysis techniques that can be used for signal-background searation, for example, neural networks, decision trees, likelihood etc. The method that we have decided to explore for this analysis is the use of neural networks, with a little help from decision trees. Our strategy would be to train the neural networks for all the major backgrounds, Wjj, Wbb, $t\bar{t}$, and misidentified leptons.

The steps in our neural network analysis are as follows:

- Find a large set of variables that each:
    - have good signal-background separation
    - are as uncorrelated as possible

- – have distributions in the data that are well reproduced by the background model

- Use the neural network to combine the variables in a way that maximizes signal-background separation.

- Choose the best subset of the variables.

  - – Get the preliminary list of good variables by using "decision trees".

  - – Choose a set of variables for which we get the best separation possible with the minimum number of variables. For this we will use a figure of merit based on the efficiency of the neural network output.

- Optimize each network for number of epochs, and number of hidden nodes.

- Apply resulting filter functions to all the samples.

- Feed the outputs of the above step to another neural network, for which the input variables are now the neural network distributions from the Wjj, Wbb, $t\bar{t}$, etc. neural networks.

- Optimize the second neural network.

- Produce final-variable distributions with maximal signal-background separation.

- Optimize the binning of these variables for maximal sensitivity in the likelihood calculation.

- Perform a binned likelihood calculation of the background and signal final-variable distributions to the data to set upper limits on the signal cross sections.

In the following sections, we describe these steps in more detail.

7.4.1 The Sensitive Variables

We start with an exhaustive list of variables which show discrimination against one or more backgrounds. These variables must be reconstructed from information on the final state objects in the event, from the basic objects like electron and jets, reconstructed from the information collected by the detector, as depicted in Fig. 7.7. In some case we need to know which jet in the event is the b coming from top decay.

Final State Object Reconstruction
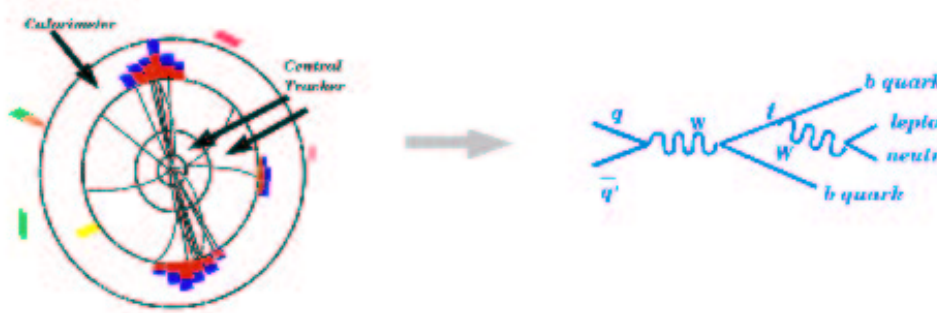
Figure 7.7: When a single top event is produced in the detector, the information that we get from the detector is tracks and deposited energy in the calorimeter. From this information the final state objects in the event, like a W and a b coming from top decay are reconstructed.

Single top quarks are produced together with either a b quark (s-channel) or a light quark (t-channel); in the t-channel, there is sometimes an additional low-p_T b quark. The final state products also include a lepton and a neutrino from the W boson and a further b quark from the top quark decay. Reconstructing the top quark requires reconstruction of the neutrino and identifying the correct jet to combine with the W.

The transverse components of the neutrino momentum are reconstructed from the missing transverse energy in the event. The z component of the neutrino momentum is obtained from a W boson mass constraint, choosing the smaller $|p_z(\nu)|$ solution of the two possible solutions. This procedure identifies the correct $p_z(\nu)$ in about 70% of the events.

The b-quark jets are chosen using different procedures for the s-channel and the t-channel. In the t-channel the highest-p_T b-tagged jet is chosen as the b from top. This procedure identifies the proper b jet about 90% of the time. In the s-channel, the situation is not as clear because there are two high-p_T b-quark jets in the final state. Thus, choosing the highest p_T b-tagged jet as the b from top would be the correct choice only about 50% of the time. To improve the fraction of properly reconstructed s-channel events, we therefore choose the "best jet" as the b from top. The best jet is defined as the one for which the invariant mass $M(W, \text{jet})$ is closest to 175 GeV. This algorithm identifies the correct jet also about 90% of the time. It was used in DØ's second search for single top quark production in Run I [161].

A list of sensitive variables is given in Appendix B. The variables that show discrimination between signal and background can be divided into three basic categories:

- *Single-object kinematics:* Transverse momenta of the jets

- *Event kinematics:* Properties such as transverse momentum, transverse mass, invariant mass, total transverse energy, and total energy of composite final state objects such as the W boson or the top quark, and total event energy

- *Angular variables:* Angles between objects that take account of whether their origin is from a polarized top quark

Selection of the variables, listed in Appendix B, was based on an analysis of the

signal and background Feynman diagrams [162] and on a study of single-top quark production at next-to-leading order [163].

7.4.2 Neural Network Analysis
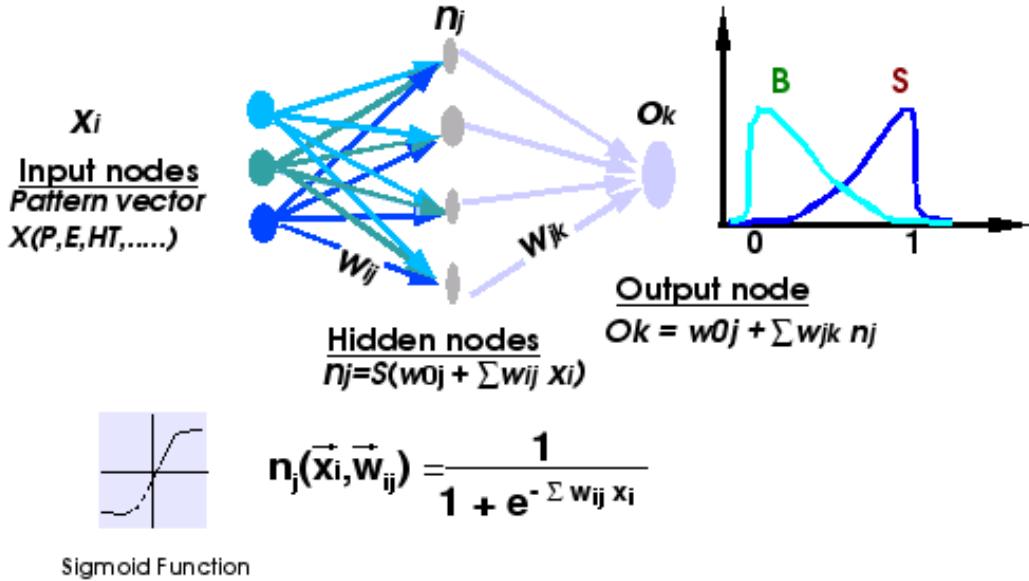
Figure 7.8: A simple layout of the neurl network used in the analysis. see text for explanation.

Neural network has been effectively used previously in the Run I and the Run II analyses [161, 164]. For the present analysis we are using the Multi-Layer Perceptron (MLP) neural network. For the details of MLP see [165, 166, 167]. A simple layout of the network is shown in Fig. 7.8. Here X_i are the input nodes, n_j are called *hidden nodes* and W_{ij} is the weight that is applied to the ith input when it is collected at jth hidden node. For every network that we train, inputs are the variables that show dicrimination between signal and corresponding background. Every network has one hidden layer and one output layer. At every hidden node, a sigmoid function is calculated from the

164

sum of weighted input variables. The linear sum of these sigmoid functions appears at the output node. During the training process weights are adjusted such that signal is moved towards 1 and background toward 0. We keep training until the maximal separation is achieved. The number of iterations used are termed as epochs

We will use this network twice in the analysis. First we will train for every background separately. The outputs of these networks will then be used as inputs to another, similar, neural network, as shown in Fig. 7.9.
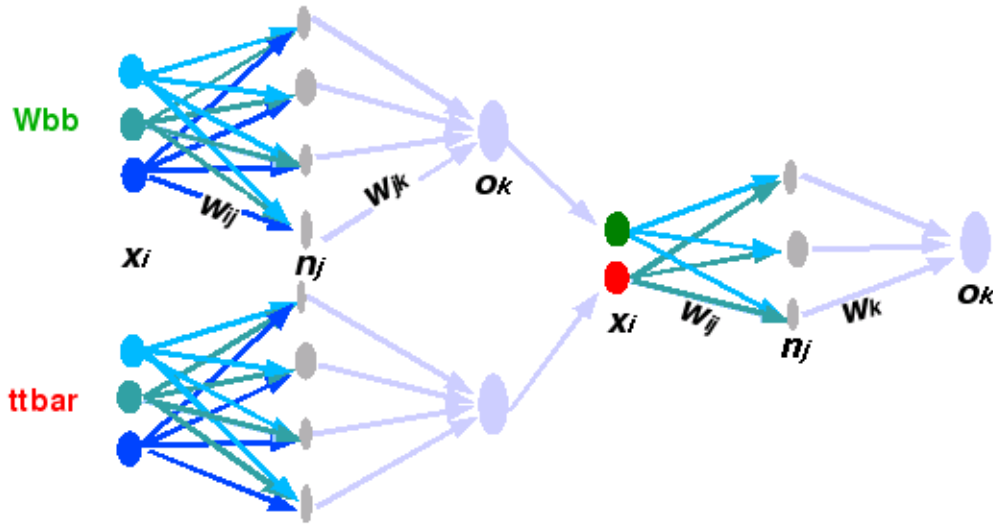
Figure 7.9: A simple layout of two layers of neural networks used in the analysis. Here Wbb and $t\bar{t}$ are examples of the networks we train in this analysis.

We optimize our networks in following steps:

- Number of networks: making a decision about which backgrounds we want to train using neural networks, and sample percentages to be used for training and testing of these networks.

- Input variables: Selection and optimization of input variables.

- Network parameters: Optimize for parameters involving the neural network's training and testing.

- Repeat above two steps for the second neural network.

These steps are described in the following sections.

Choice of Signal-Background Pairs

Fig. 7.10 show contributions from different backgrounds for single and double tagged events. You can see that for single and double tagged events, the most important backgrounds are Wjj, Wbb, $t\bar{t}$ and background from fake leptons. In case of single tagged events, Wjj is the largest background, whereas, in cas of double tagged events, $t\bar{t}$ becomes the largest background. The signal-background pairs for neural network analysis are:

$tb\text{-}Wbb$

$tb\text{-}Wjj$

$tb\text{-}t\bar{t} \rightarrow lj$

$tb\text{-}t\bar{t} \rightarrow ll$

$tb\text{-}fake\text{-}e$

So we optimized a total of 5 background networks for single and double tagged samples. We label these networks as $t\bar{t}$, Wbb, etc. Network training and optimization is done separately for each one of these networks.

To make sure that we are not being biased in any way, we divide the available background and signal samples into two parts: one half is used for the teting and training of the neural network and the other one is used for yields and limit calculations.

Choice of Input Variables

Perhaps the most important part of the optimization of the neural networks is choosing the sets of input variables. We began with a list of about 50

166
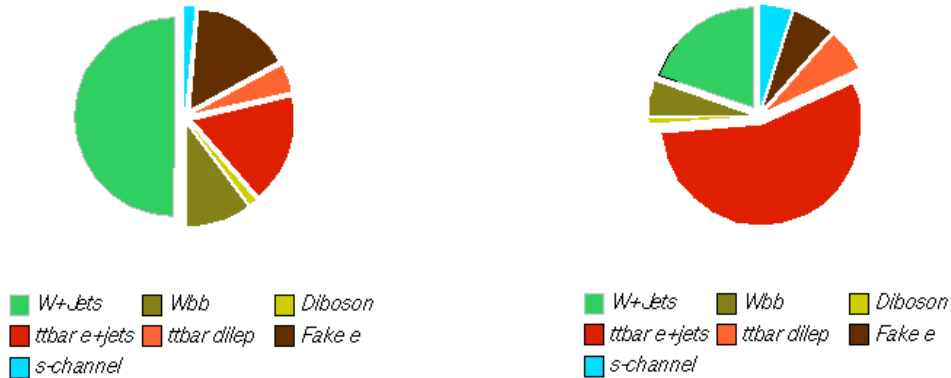
Figure 7.10: Pie charts showing the relative proportion of main backgrounds and singnal after selection for Central Calorimeter electrons. For single tagged eventsleft and double tagged events(right).

variables, listed and explained in Appendix B, and selected a final subset of variables for each network. This set of variables is selected based on the ranking provided by the *decision tree*. This is a multivariate analysis technique that uses a training procedure to create estimator functions called "decision trees"[168]. The input is a set of variables completely analogous to the neural network analysis, Basically, the training procdure attempts to partition the multidimensional variable space into regions for which the purity, or fraction of signal events, is either close to one or to zero. The resulting decision tree function applied to a given event then determines which region the event lies in, and returns the associated purity from the training sample. Since the number of such regions is finite, the function can only take on a discrete number of values.

A byproduct of this procedure is that it provides a quantitative measure of the effectiveness of a particular variable. Thus, using the ranking provided by decision trees, we can select a smaller list of the most important variables

167

and remove those which are never chosen, or which contribute very little to the resulting tree.

The final set of variables was obtained by using the following procedure:

The optimization starts by training the neural network with the first two highest ranked variables. After the network is trained, a figure-of-merit is calculated for how well this network separates signal and background. The figure-of-merit is based on the integral of the area above the signal vs. background efficiency curve for the neural network output distribution - the smaller this figure, the better. After the figure of merit has been calculated, the third highest ranked variable is added to the training, and steps are repeated. This process continues until all variables from the preliminary list have been added to the network for training. After the optimization has been completed for a network, the set of variables is chosen, for which the best figure of merit was obtained. The final sets of variables thus obtained are listed in Table 7.11. Figs **??** show normalized plots for these variables along with data versus sum of all backgrounds. The color code for these figures is the same as used for the ones in A. ,

7.4.3   Optimizing the Network Parameters

We optimize the number of hidden nodes in each final network by training with hidden nodes between n and 2n, where n is the number of variables used for training. The number of hidden nodes which give the smallest training error are then selected. Note that often there are several different numbers of nodes that have training errors within 1% of each other, and so no significance should be read into having widely different numbers for two similar networks, it is a result of the choice of hidden-node selection algorithm. Networks with the same training error as each other produce the same amount of signal-background separation, although the shapes of the signal and background

	Final Input Variables to the Neural Networks				
	$tb\text{-}Wbb$	$tb\text{-}Wjj$	$tb\text{-}t\bar{t} \to lj$	$tb\text{-}t\bar{t} \to ll$	$tb\text{-}fake\text{-}e$
Equal One Tag					
1. p_T(jet2)	✓	✓	—	—	✓
2. p_T(jet1,jet2)	✓	—	—	✓	—
3. MET	✓	—	—	✓	✓
4. H(alljets-lepton-met)	—	✓	—	—	—
5. H_T(alljets)	—	—	✓	—	—
6. H_T(alljets-lepton-met)	—	—	✓	—	—
7. H_T(jet1,jet2)	✓	✓	✓	—	—
8. TopMass(best)	✓	—	—	—	—
9. M(alljets-best)	—	—	✓	✓	✓
10. M(jet1,jet2)	✓	—	✓	—	—
11. WTransverseMass	—	—	—	✓	✓
12. cos(bestjet, lepton)$_\text{besttop}$	✓	—	—	—	—
13. cos(lepton, Q(lepton)$\times z$)$_\text{besttop}$	—	✓	—	—	—
14. cos(notbest, lepton)$_\text{besttop}$	✓	—	—	—	—
Equal Two Tags					
1. p_T(jet1)	—	—	✓	—	—
2. p_T(jet2)	—	—	✓	—	✓
3. p_T(notbest1)	—	—	✓	—	—
4. p_T(jet1,jet2)	✓	—	—	—	—
5. MET	—	—	—	✓	✓
6.. WTransverseMass	—	—	—	✓	✓
7. H_T(jet1,jet2)	✓	✓	—	—	—
8. TopMass(best)	✓	—	—	—	—
9. M(alljets$-$best)	✓	✓	✓	✓	✓
10. M(jet1,jet2)	✓	—	—	—	—
11. $\Delta R(jet1, jet2)$	—	—	✓	—	—

Table 7.11: The input variables for each neural network. For each variable, "—" means a variable was not used for a network.

	Configuration of the Neural Networks					
	Single Tag			Double Tag		
Network	Hidden Nodes	Best Epoch	Minimum Error	Hidden Nodes	Best Epoch	Minimum Error
$tb\text{-}t\bar{t}\ell j$	9	199	2.1×10^{-6}	6	148	1.7×10^{-6}
$tb\text{-}t\bar{t}ll$	10	199	3.4×10^{-6}	5	192	3.4×10^{-6}
$tb\text{-}Wbb$	11	187	3.6×10^{-6}	9	107	3.7×10^{-6}
$tb\text{-}Wjj$	6	133	3.8×10^{-6}	3	3	4.5×10^{-6}
$tb\text{-}fake\_e$	4	142	2.1×10^{-6}	8	139	0.6×10^{-6}

Table 7.12: Values of the number of hidden nodes and epochs where the most efficient configuration of the neural net was obtained. The minimum training error evaluated at the minimum testing error is also given.

output distributions need not be the same between the networks.

We split the input samples such that 75% of the events were used for training and the remaining 25% for testing. Training was done with weighted Monte Carlo events, and the logarithm of all non-angular variables. The method used for minimization of the network output error function is called the MLPfit hybrid method 6 [165]. Our previously published analysis [101] used method 7 but because methods 6 and 7 show almost the same performance with method 6 having much smaller training time, we decided to use method 6 for this analysis. Table 7.12 shows values of the number of hidden nodes and epochs where the most efficient configuration of the neural net was obtained. The minimum training error evaluated at the minimum testing error is also given.

Network Performance

The figure of merit plots, for $=1$ tag and $=2$ tag samples, and efficiency curves for the best sets of variables are shown in Fig. 7.21 through Fig. 7.30. They also

show the neural network output distributions and a comparison of the summed backgrounds to data for these networks for single-tagged, and double-tagged samples. . All the curves on these plots are normalized to have equal area so that the separation between signal and background can be best seen.

These distributions show that the background model reproduces the data reasonably well. They also show that separation of the single top quark signal from background is not yet powerful enough since the background dominates even in the regions where the signal peaks.

It should be noted that the output variable from MLPfit networks is a linear combination of sigmoid functions, and thus is not restricted to lie between zero and one, as can be seen in these plots [1].

The neural network output distributions are used as input variables to the second neural network. This second network is then optimized for number of hidden nodes and epochs. The output distributions and comparison of the summed backgrounds to data from the second network are shown in Fig. 7.32. These output distributions are what we are going to use for the binned lekelihood limit calculation, as explained in the next chapter. Table 7.13 showes the signal to background ratios before and after the application of second neural network. As you can see that neural network gives us almost two times better signal to background ratio, compared to simple b-tagging analysis. Situation in the double tag analysis is especially encouraging.

---

[1] Some other network packages, for example JETNET (used in the Run I $t\bar{t}$ analysis), do produce output only in this range
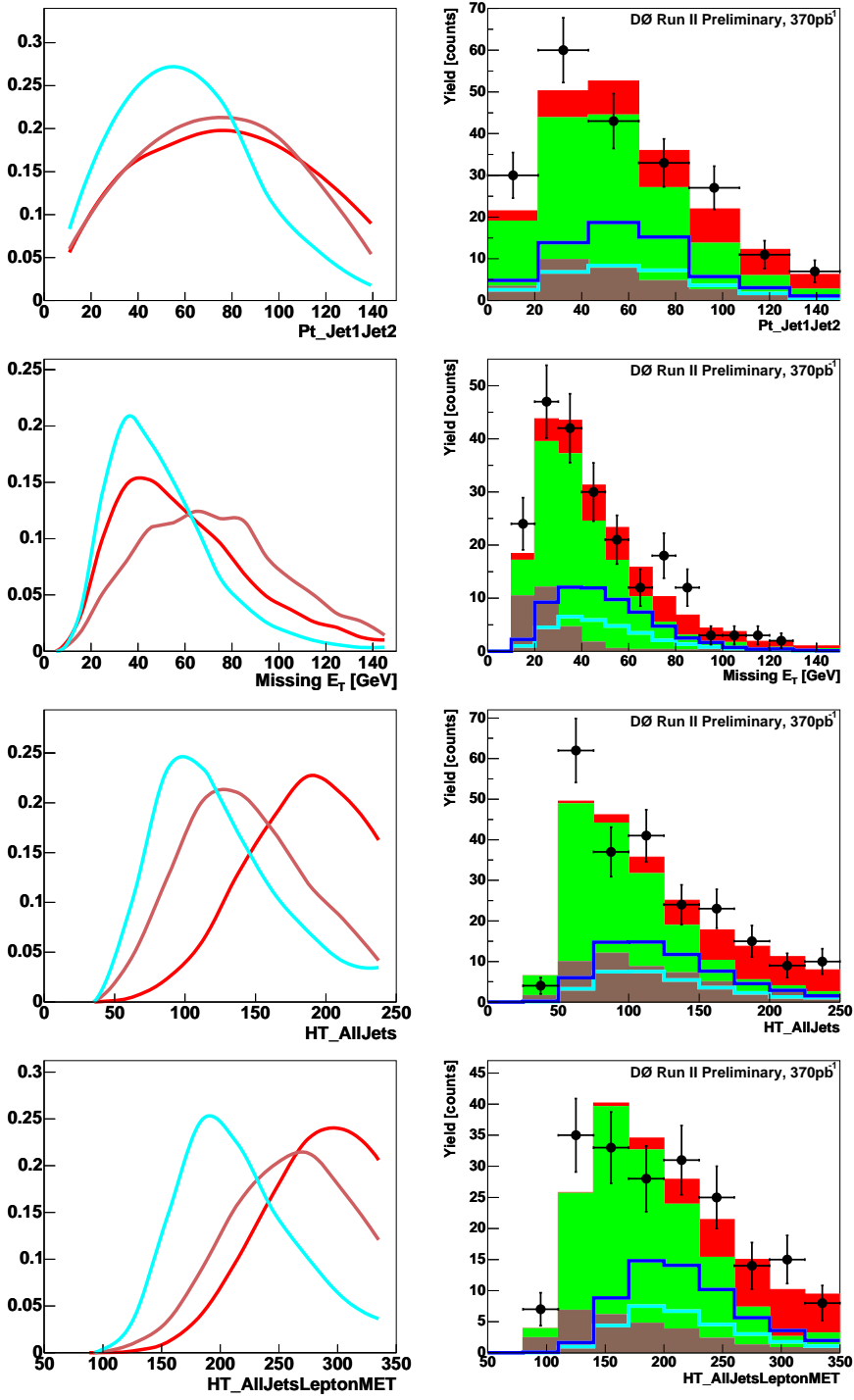
Figure 7.11: Discriminating variables for $t\bar{t} \rightarrow lepton + jets$ and $t\bar{t} \rightarrow dileptons$ for single tagged samples.
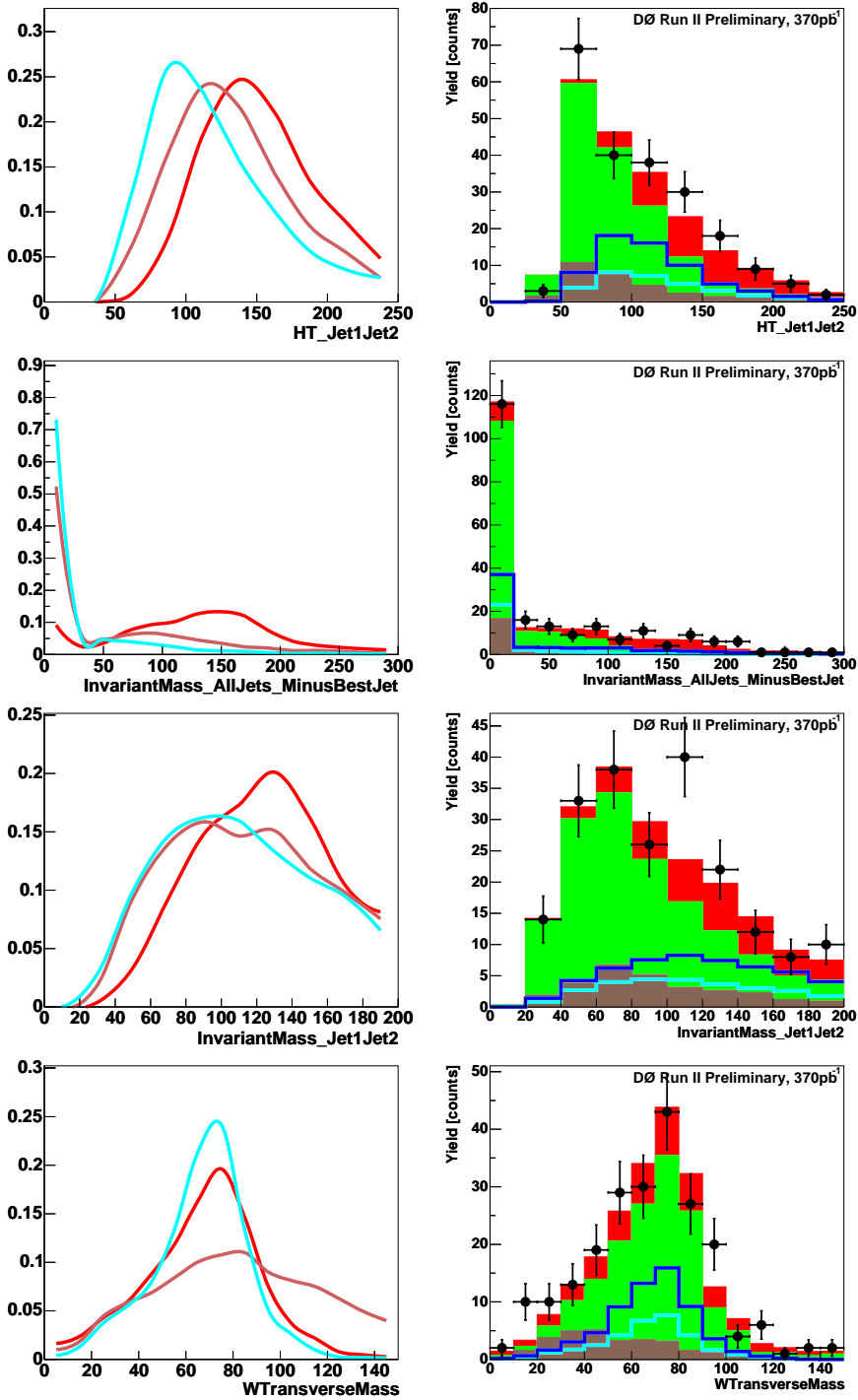
Figure 7.12: Discriminating variables for $t\bar{t} \to lepton + jets$ and $t\bar{t} \to dileptons$ for single tagged samples.
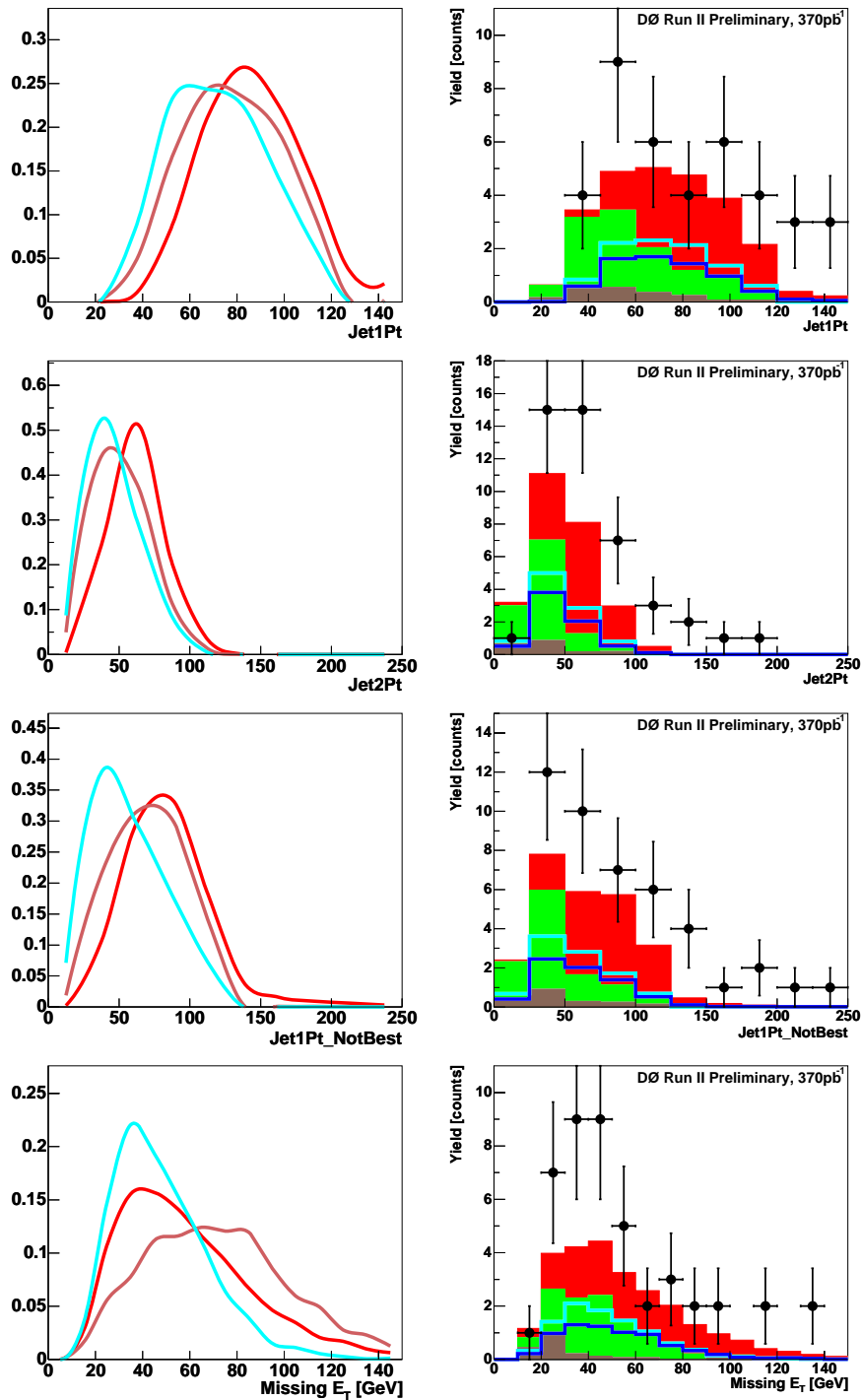
Figure 7.13: Discriminating variables for $t\bar{t} \rightarrow lepton + jets$ and $t\bar{t} \rightarrow dileptons$ for double tagged samples.
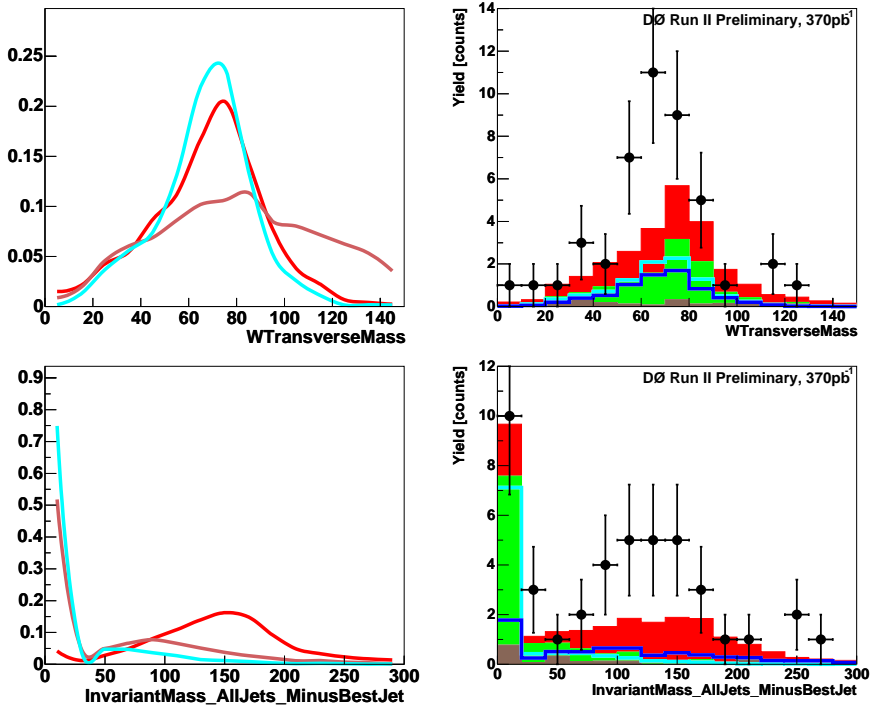
Figure 7.14: Discriminating variables for $t\bar{t} \rightarrow lepton + jets$ and $t\bar{t} \rightarrow dileptons$ for double tagged samples.
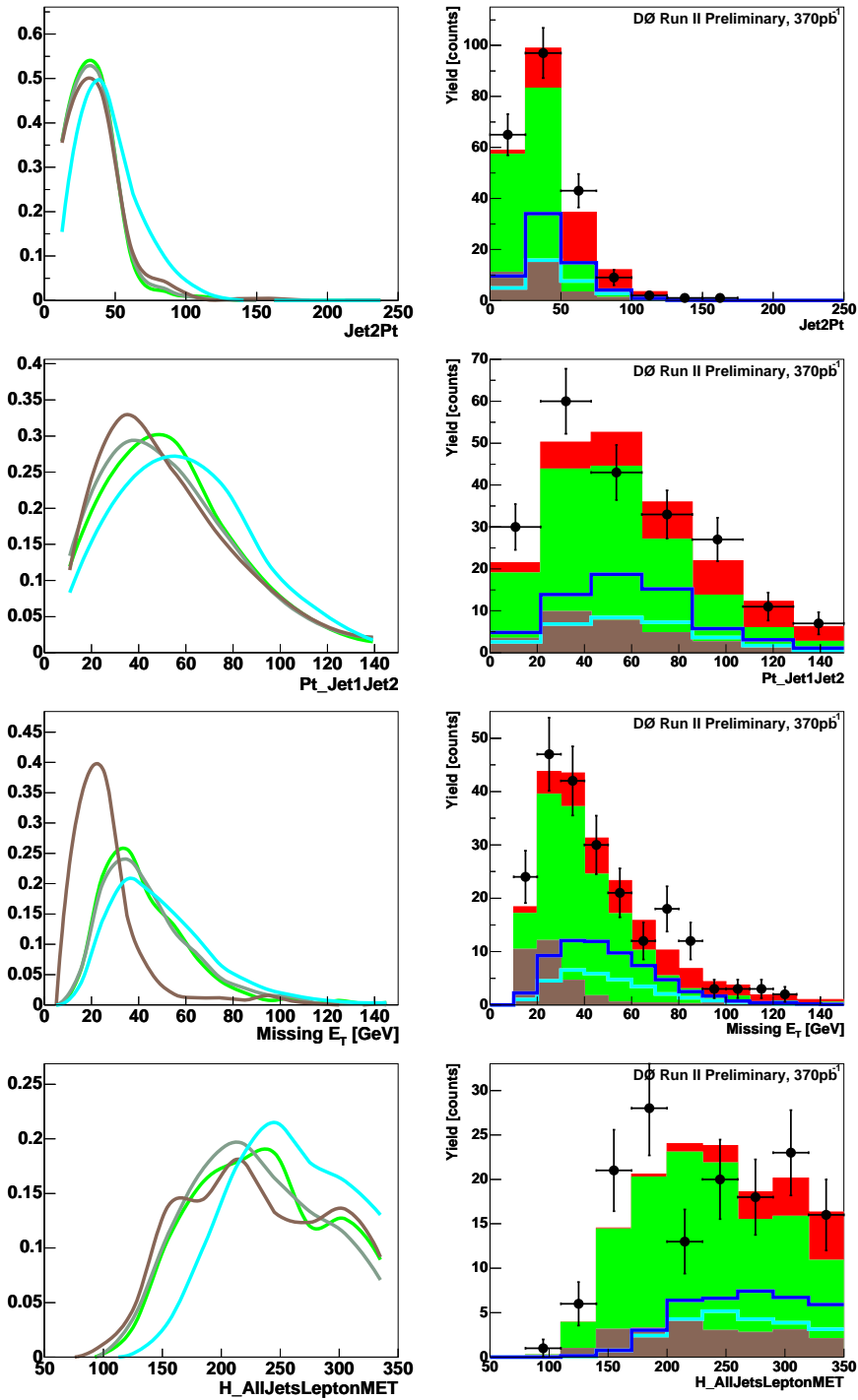
Figure 7.15: Discriminating variables for Wbb, W+jets and $fake_e$ for single tagged samples.
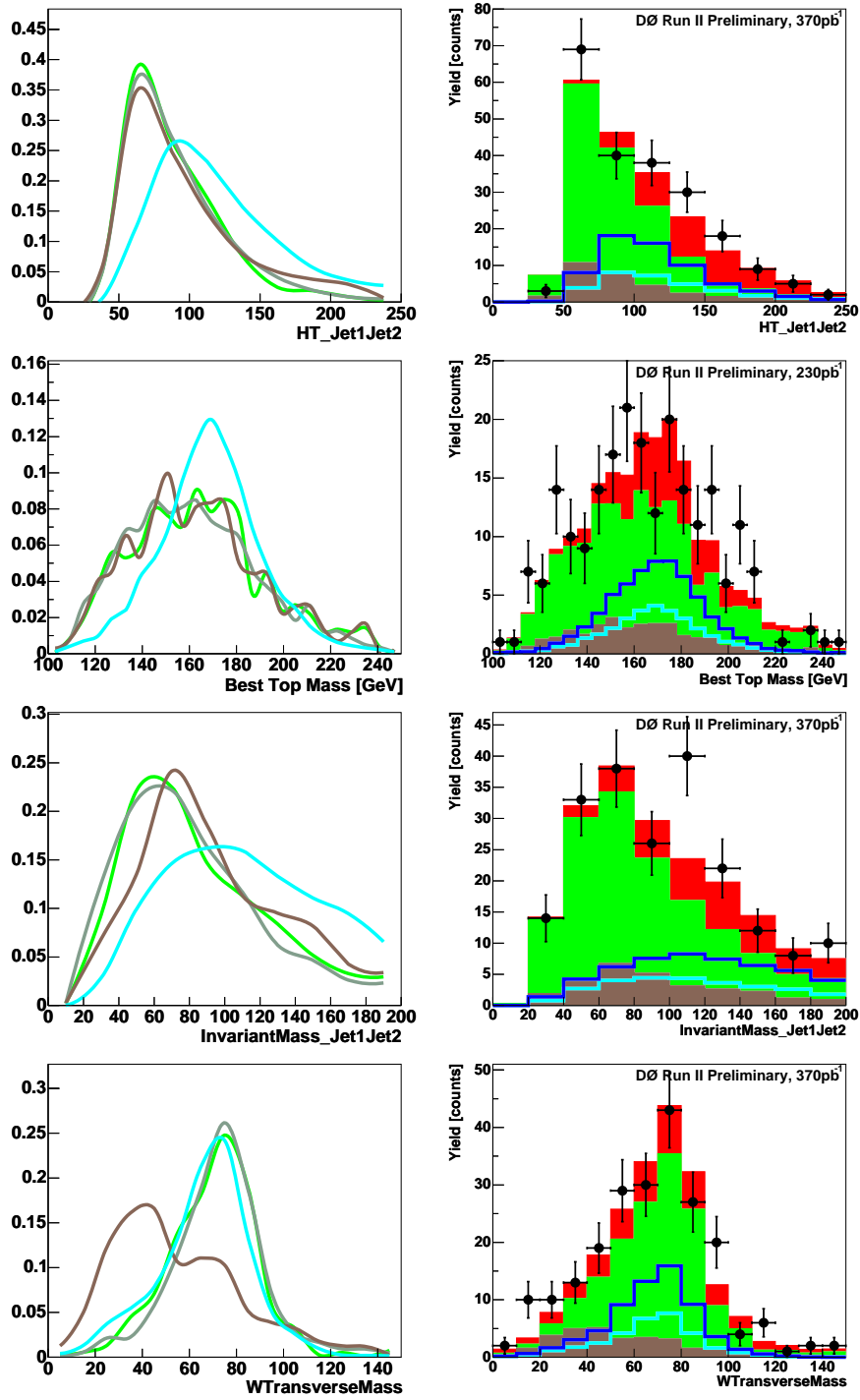
Figure 7.16: Discriminating variables for Wbb, W+jets and $fake_e$ for single tagged samples.
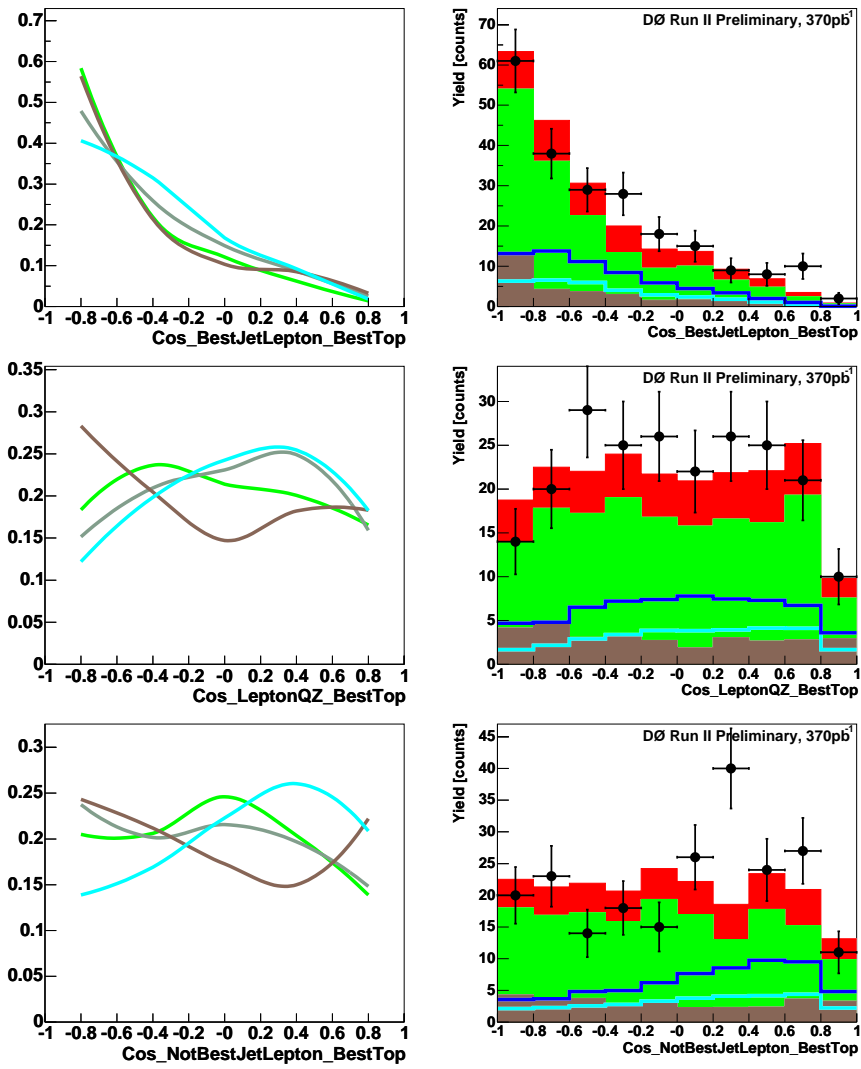
Figure 7.17: Discriminating variables for Wbb, W+jets and $fake_e$ for single tagged samples.
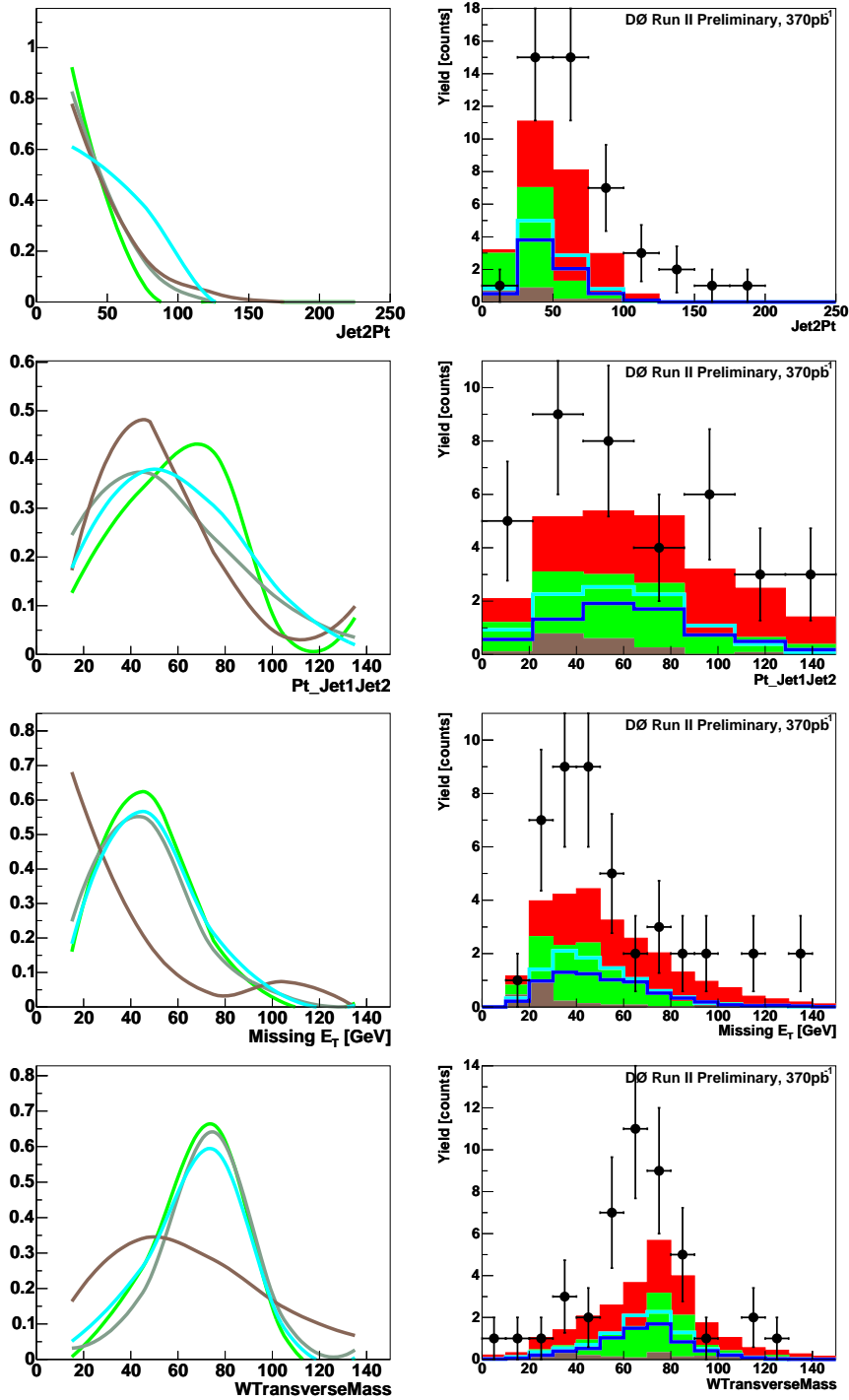
Figure 7.18: Discriminating variables for Wbb, W+jets and $fake_e$ for double tagged samples.

179
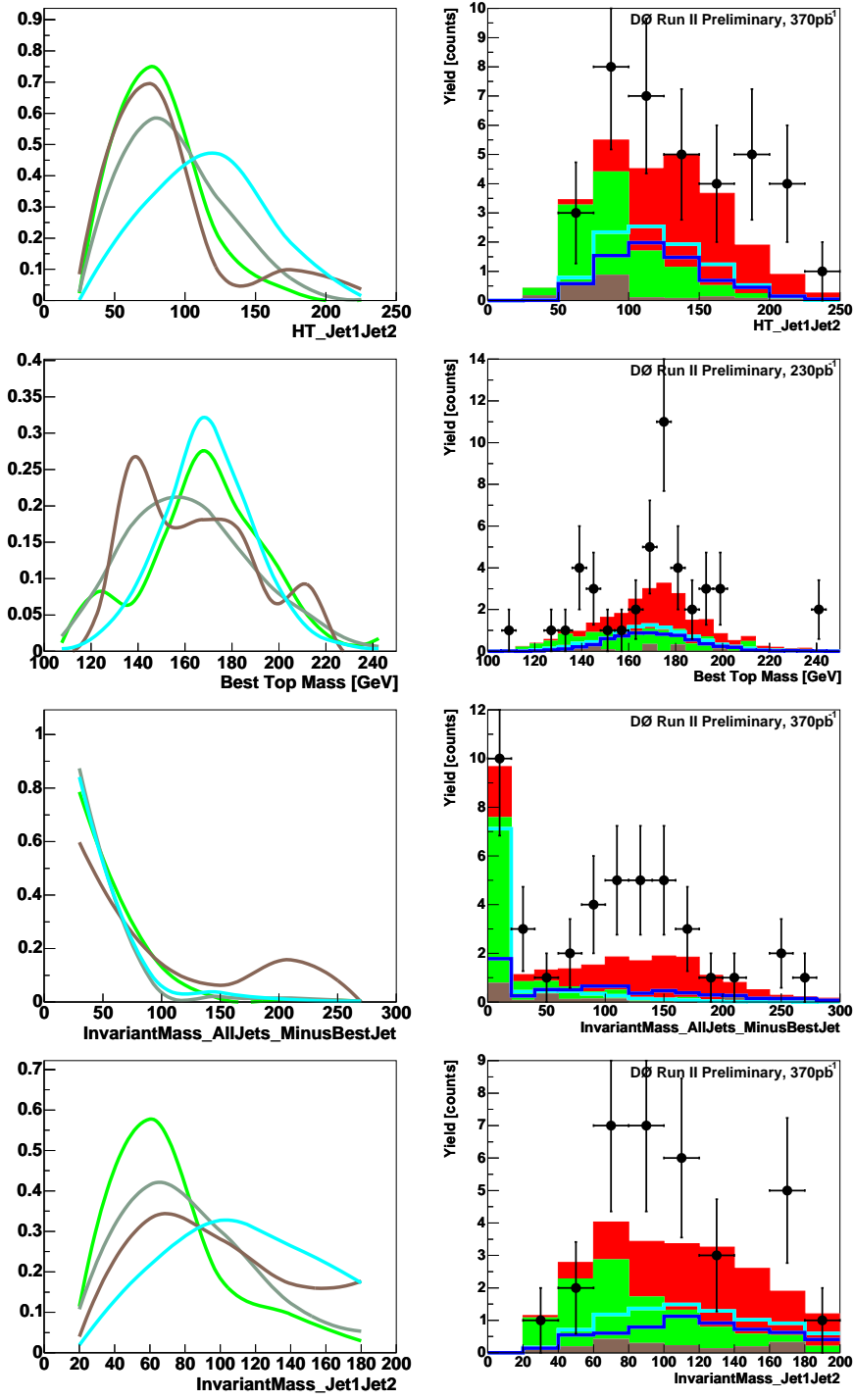
Figure 7.19: Discriminating variables for Wbb, W+jets and $fake_e$ for double tagged samples.
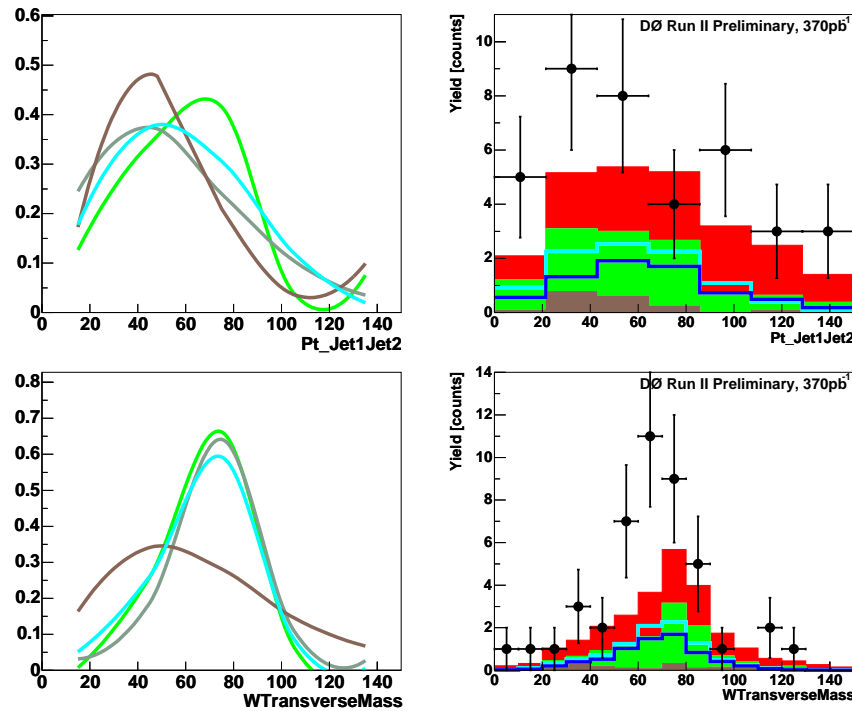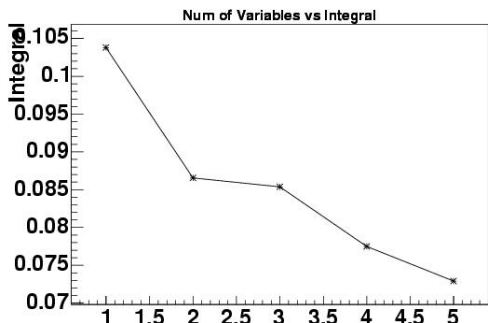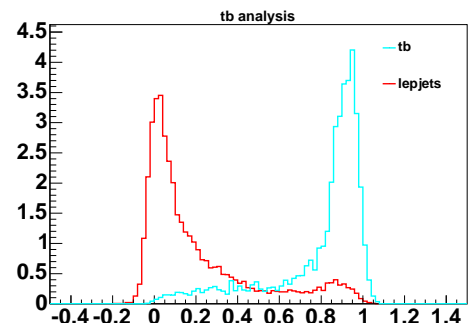
Figure 7.20: Discriminating variables for Wbb, W+jets and $fake_e$ for double tagged samples.
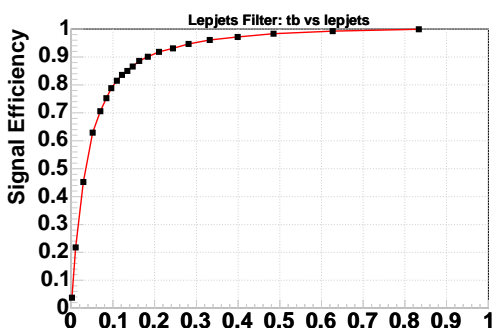
Figure of Merit

NN output

NN Efficiency

Data vs. Sum of Backgrounds
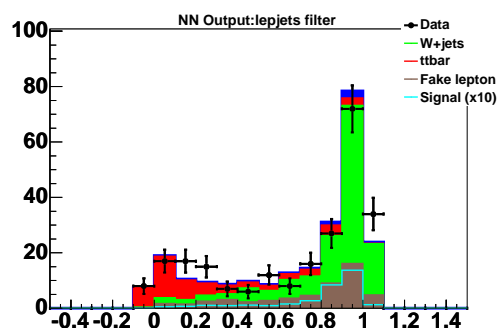
Figure 7.21: Performance of tb-$t\bar{t} \rightarrow lj$ neural network for single tagged samples.

Figure of Merit

NN output

NN Efficiency

Data vs. Sum of Backgrounds
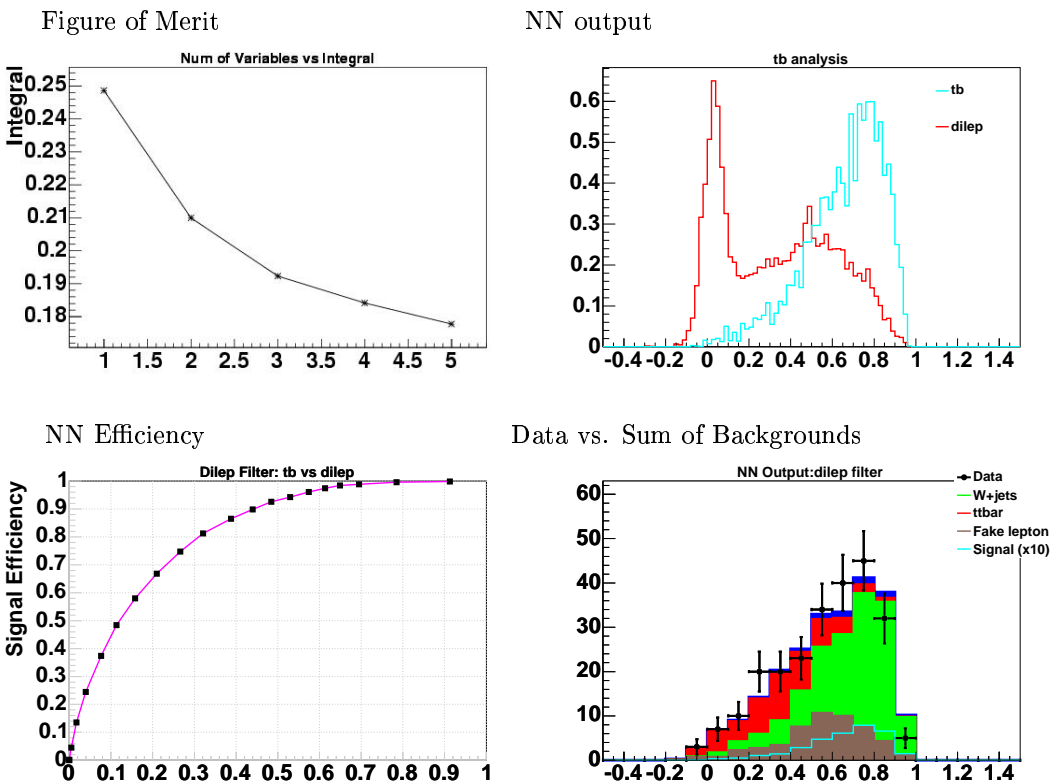
Figure 7.22: Performance of tb-$t\bar{t} \to ll$ neural network for single tagged samples.

Figure of Merit

NN output

NN Efficiency

Data vs. Sum of Backgrounds
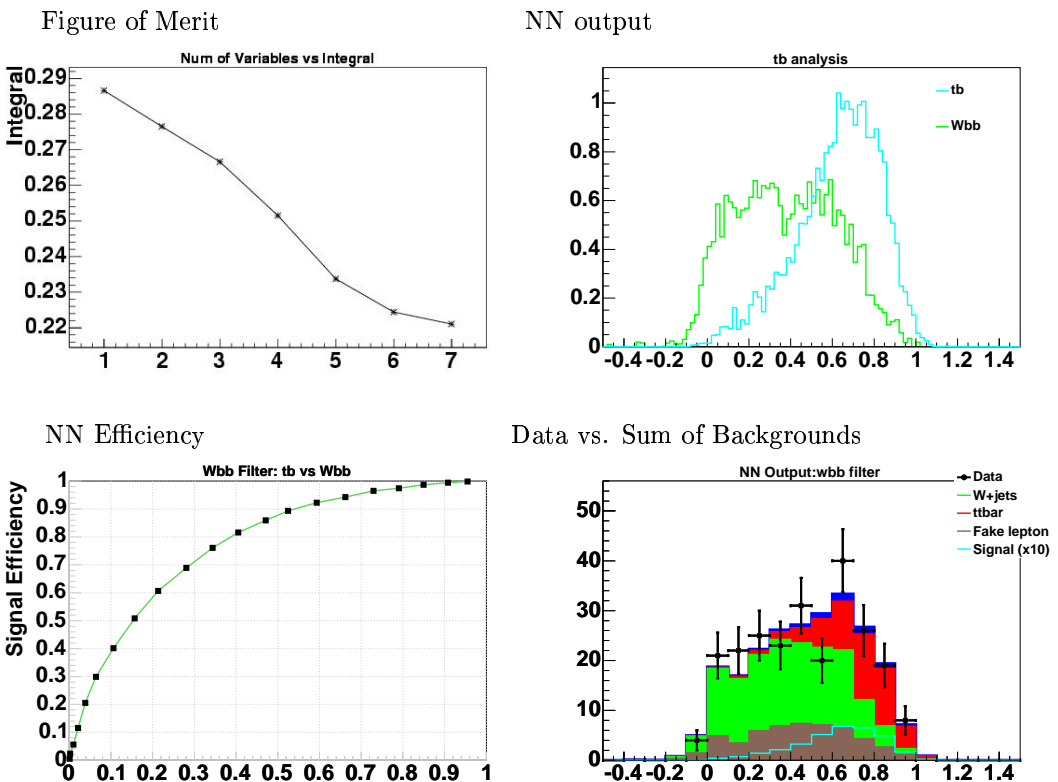
Figure 7.23: Performance of *tb-Wbb* neural network for single tagged samples.

Figure of Merit

NN output

NN Efficiency

Data vs. Sum of Backgrounds
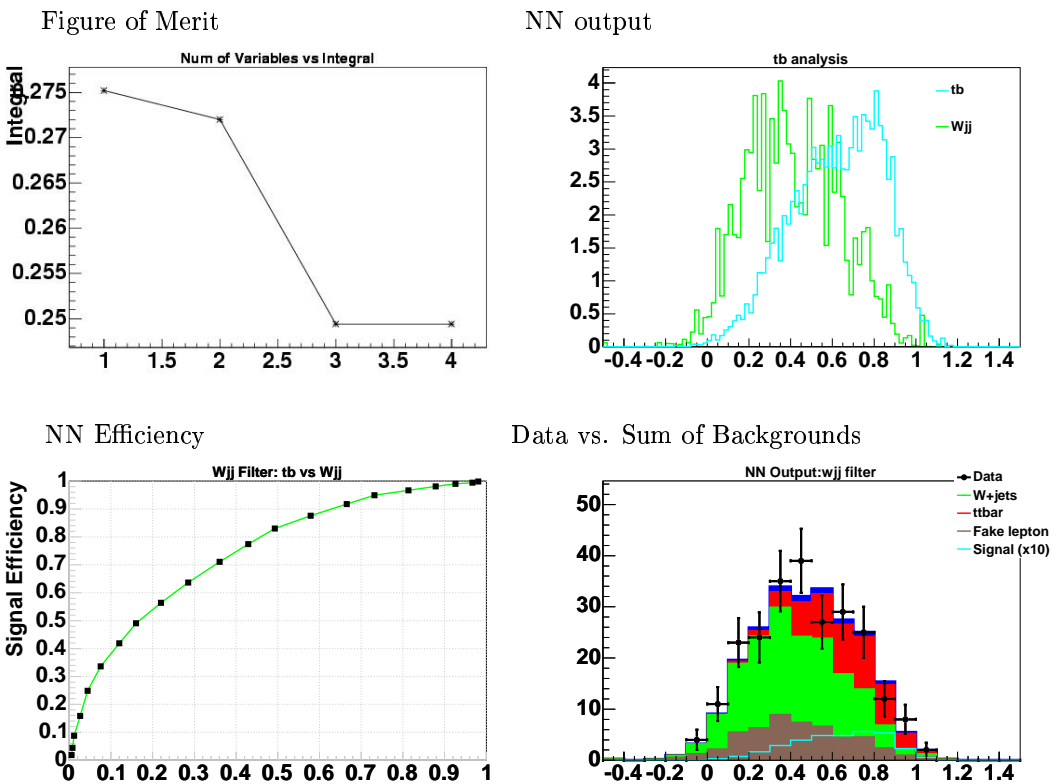
Figure 7.24: Performance of tb-Wjj neural network for single tagged samples.

Figure of Merit

NN output

NN Efficiency

Data vs. Sum of Backgrounds
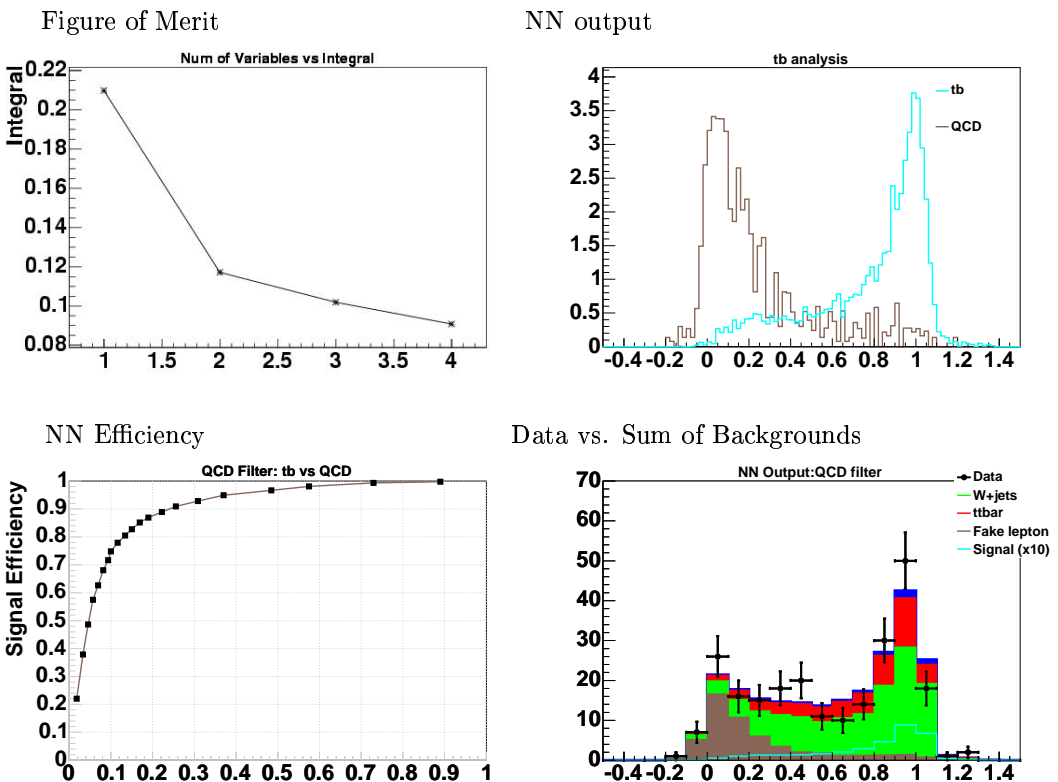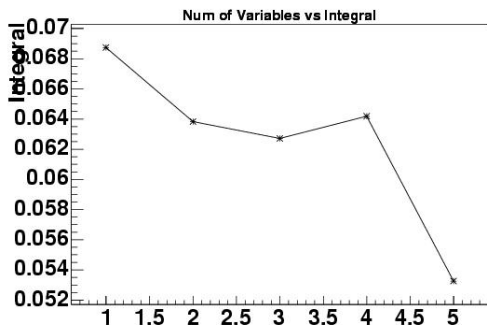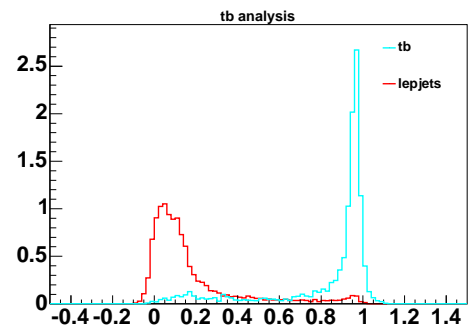
Figure 7.25: Performance of *tb-fake-e* neural network for single tagged samples.
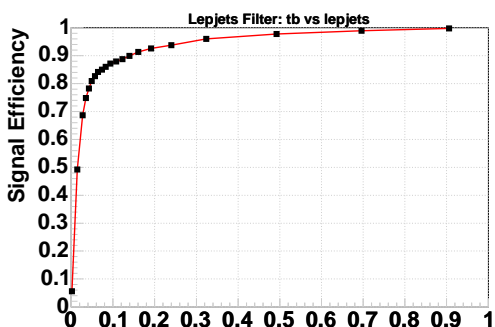
Figure of Merit

NN output

NN Efficiency

Data vs. Sum of Backgrounds
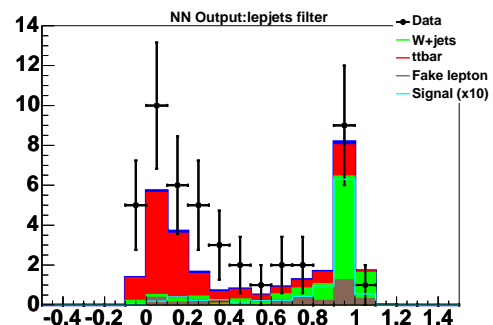
Figure 7.26: Performance of tb-$t\bar{t} \rightarrow lj$ neural network for double tagged samples.

Figure of Merit

NN output

NN Efficiency

Data vs. Sum of Backgrounds
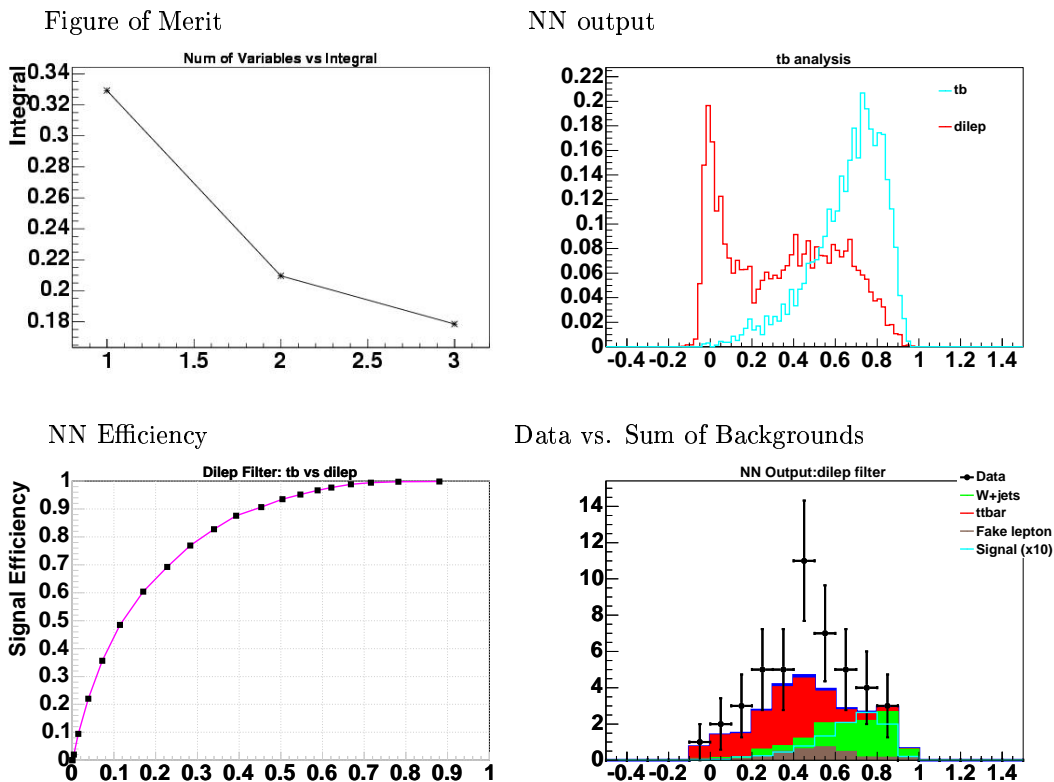
Figure 7.27: Performance of tb-$t\bar{t} \rightarrow ll$ neural network for double tagged samples.

Figure of Merit

NN output

NN Efficiency

Data vs. Sum of Backgrounds
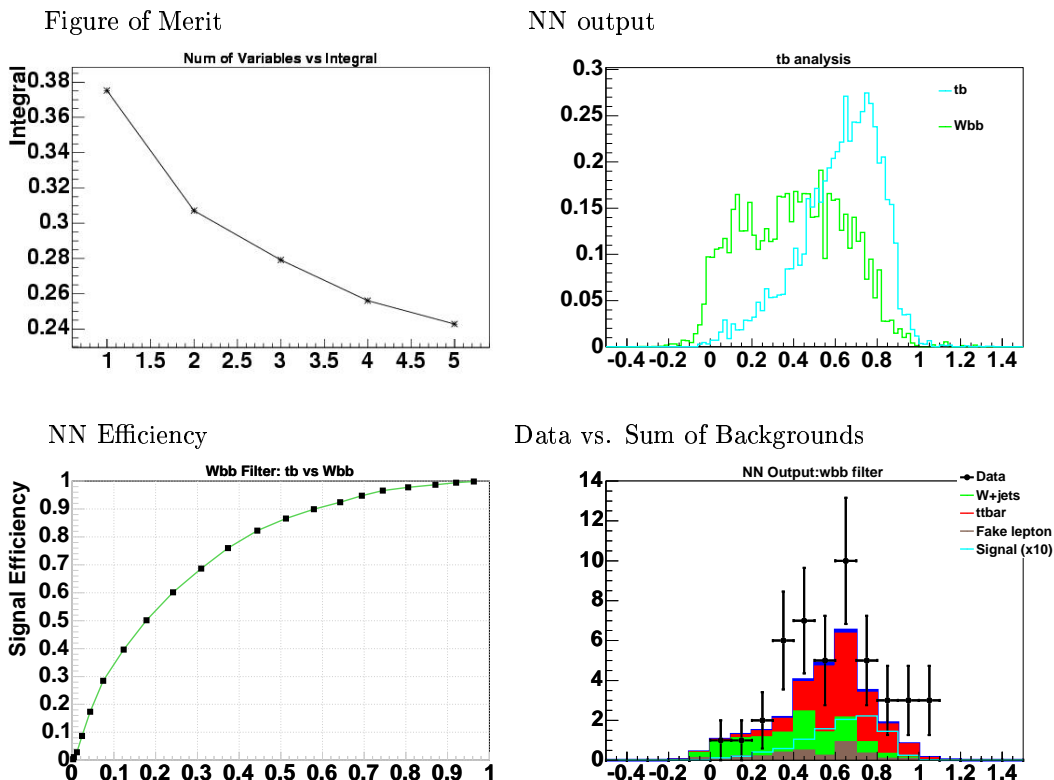
Figure 7.28: Performance of *tb-Wbb* neural network for double tagged samples.
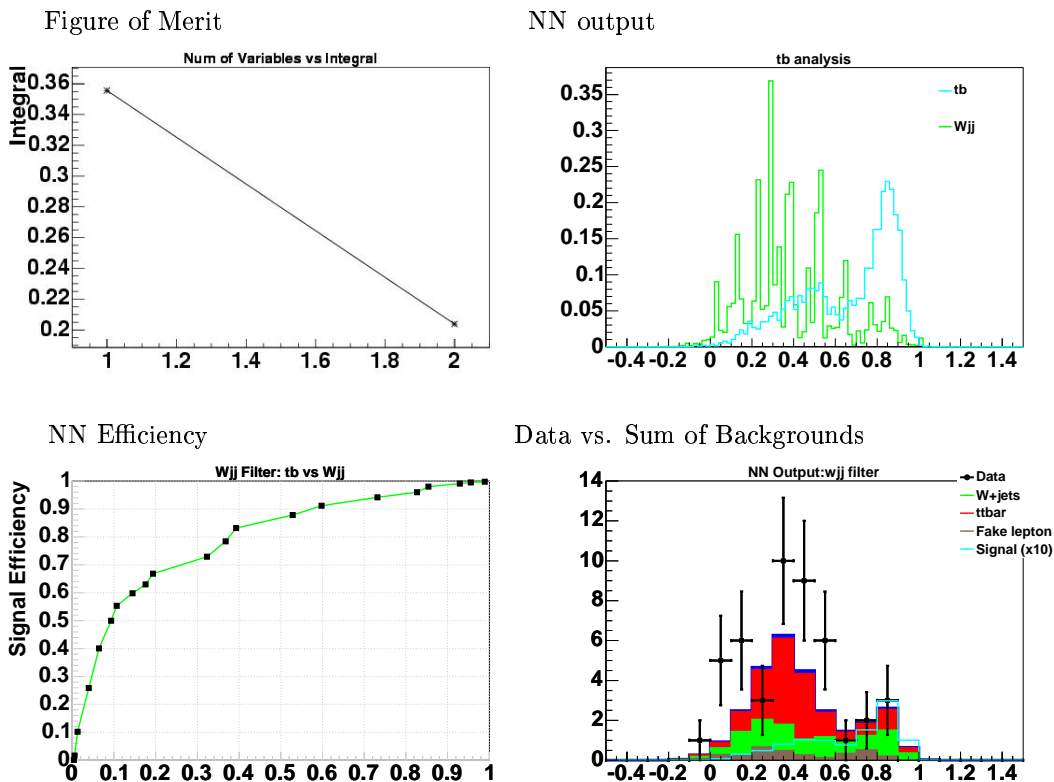
Figure 7.29: Performance of tb-Wjj neural network for double tagged samples.

Figure of Merit

NN output

NN Efficiency

Data vs. Sum of Backgrounds
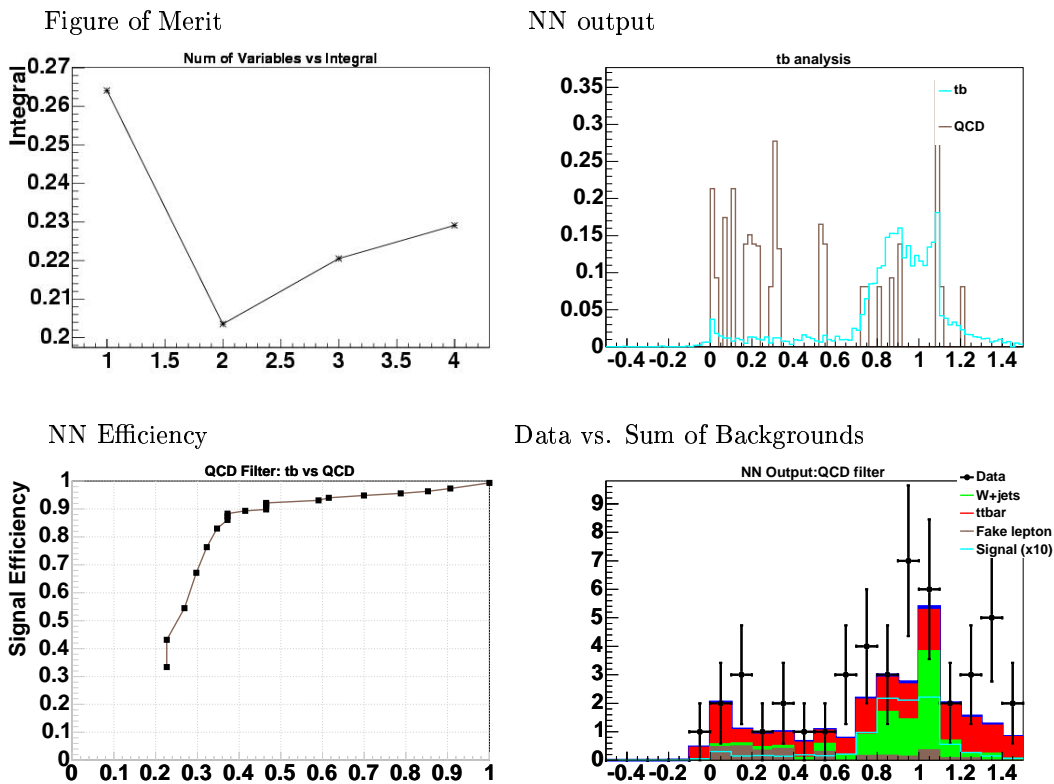
Figure 7.30: Performance of *tb-fake-e* neural network for double tagged samples.
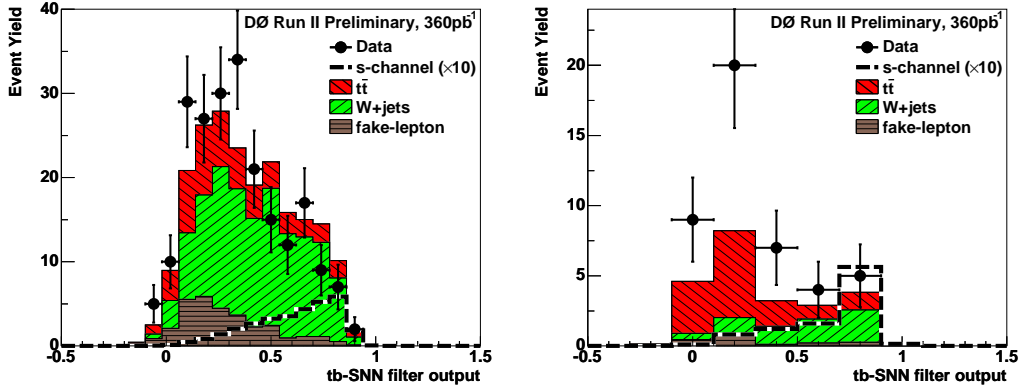
Figure 7.31: Data vs. sum of backgrounds after applying second neural network, for single tagged events (left), and for double tagged events (right).

	Signal:Background Ratios		
	Pretagged	=1 Tag	=2 Tags
After Selection	1:829	1:75	1:28
After NN (cut = 0.5)	—	1:32	1:11

Table 7.13: The ratio of the signal yield to the combined background yield for selected events.

7.5 Setting the Limit

We are setting the limit on our search not on our imagination.

Me

(Inspired by Bertrand Russell)

As is evident from the results of the previous chapter, we do not have a clear signal above the background. In this situation the only thing we can do is to set an upper limit on the production cross-section. We use a Bayesian approach [169] to calculate limits on the cross section for single top quark

production in the s-channel. The limits are derived from a likelihood function that is proportional to the probability to obtain the number of observed counts. In the case of the neural network analysis, we use the one-dimensional distributions of the final neural network output for single tagged analysis and for double tagged analysis.

We assume that the probability to observe an event count D, given the mean count is d (which is our expected total yield), is given by the Poisson distribution:

$$P(D|d) = \frac{\exp(-d)\, d^D}{\Gamma(D+1)}.$$ (7.3)

Here mean count d is a sum of the predicted contributions from the signal and N background sources ($s = 1$ to N) and can be written in terms of the signal acceptance A, the integrated luminosity l, the mean count b_s for background source s, and signal cross section σ:

$$d = A\, l\, \sigma + \sum_{s=1}^{N} b_s \equiv a\sigma + \sum_{s=1}^{N} b_s.$$ (7.4)

Here σ is the quantity of interest, and $a \equiv A\, l$ is the effective luminosity for the signal. For the s-channel the background b_s includes the t-channel process.

The likelihood function $L(D|d)$ is then,

$$L(D|d) \equiv L(D|\sigma) \propto P(D|d)$$

.

We use Bayes theorem to invert the likelihood function, and integrate over the parameters a and b to obtain the posterior probability density for the signal cross section:

$$P(\sigma|D) = \frac{1}{\mathcal{N}} \int \int L(D|\sigma, a, b)\pi(\sigma, a, b)\, da\, db.$$ (7.5)

Here $\mathcal{N}$ is an overall normalization that is obtained from the requirement $\int \mathrm{P}(\sigma|\mathrm{D})d\sigma = 1$; $\pi(\sigma, a, b)$ is the prior probability that contains any prior

knowledge that we may have about the parameters σ, a and b. We assume that any prior knowledge of a and b is independent of the cross section σ, and therefore factorize the prior probability as follows:

$$\pi(\sigma, a, b) = \pi(a, b)\,\pi(\sigma). \tag{7.6}$$

Conventionally, we use a flat prior for σ: $\pi(\sigma) = 1/\sigma_{max}$, where σ_{max} is any sufficiently high upper bound on the cross section. The posterior probability density for the signal cross section is therefore:

$$P(\sigma|D) = \frac{1}{\mathcal{N}} \int \int L(D|\sigma, a, b)\pi(a, b)\,da\,db. \tag{7.7}$$

A Bayesian upper limit σ_{CL} at confidence level CL is the solution of:

$$\int_0^{\sigma_{CL}} P(\sigma|D) = CL. \tag{7.8}$$

The prior $\pi(a, b)$ encodes our knowledge of the effective signal luminosities and the background yields: we have estimates of the parameters and the associated uncertainties from the different systematic effects discussed in Sec. 7.3. In our case, since we consider distributions, we separate the uncertainties into two classes: those that alter the overall *normalization*, such as the luminosity measurement and Monte Carlo cross sections, and those that alter the *shapes* of distributions, such as the trigger modeling, jet energy calibration, jet energy resolution, jet identification, and $b-$tag modeling. Note: for the $Wb\bar{b}$ and Wjj Monte Carlo samples, since the overall yields are normalized to the data before b-tagging, the total tagged yield estimates are affected by only (i) an uncertainty from the normalization to data, and (ii) b tag modeling, since this is applied after the normalization. Nevertheless, the effect on the *shapes* of distributions from the uncertainty components that depend on event kinematics are taken into account in each bin.

The final limits on the production cross sections of single top quarks are given in Table **??**, where the limits are calculated from the signal acceptances

194

and background yields after selection and after using neural networks, with and without systematics. Here expected limit is calculated by putting observed number of events equal to the expected number of events. Here the final output distributions of the second neural network are used as input distributions for the limit calculations.
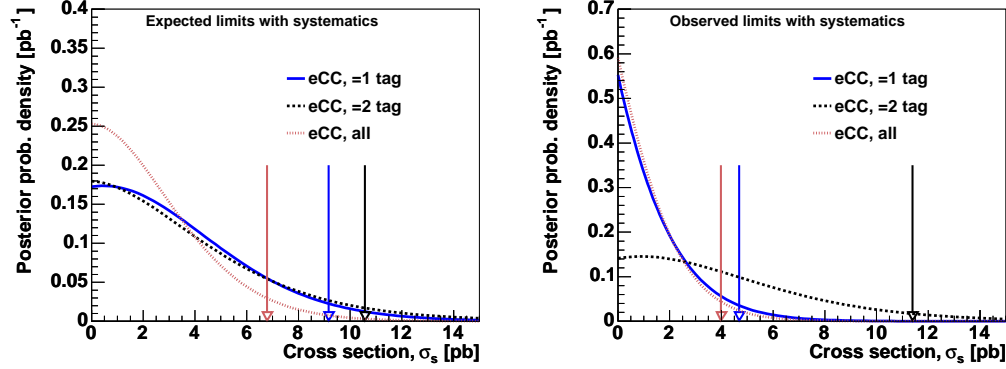
Figure 7.32: s-channel Bayesian posterior density distributions for =1 tag (blue), =2 tags (black) and combined (red). Left: expected densities; Right: measured densities.

Chapter 8

Conclusions

As I mentioned in the first chapter, theory and experiment, like two active children, are trying to help one another in understanding the fascinating universe around us. This thesis is, however infinitesimal it may be, another step forward in this direction.

As challenging as it is, the single top search is important. The predictions of the Standard Model and the possibility of new physics in the top quark sector make this search even more attractive and interesting.

The 95% CL upper limit on the s-channel production cross-section at the Tevatron, in the e+jets channel, with 360 pb^{-1} of data, is found to be 4.0 pb. This limit is far better than the previous CDF limit [110] of 13.6 pb. Our previously published limit [101] on the s-channel was 6.4 pb, and is the world's best published limit so far. That limit was for 230 pb^{-1} of data, with e+jets and μ+jets channels combined and one layer of neural networks with two networks, $tb - t\bar{t} + lj$ and $tb - Wb\bar{b}$. Extrapolating our published results to 360 pb^{-1} of data, the limit comes out to be about 5.0 pb [170] (with e+jets and μ+jets channels combined). Comparison with this extrapolated limit gives us an idea how much the second layer of neural network imparts to our limit of 4.0 pb (which is in the e+jets channel alone). Of course, in order to get a

quantitative estimate, we will need to repeat the present analysis with a single layer of neural networks, with two networks only.

As you can see from Fig. 2.19, with the limit presented here, we are approaching the region of sensitivity for some of the theoretical models of new physics. Also, the signal:background ratio after applying neural networks (Table 7.13), especially after requiring two tagged jets in the event, indicates that our method is sophisticated enough to reduce the signal:background ratio to about 1:10, and now it is just a matter of more statistics that we observe single top. A brief study [171] estimated the amount of data needed for the 3 sigma discovery of single top to be about 2 fb^{-1}. This study was done for the previous neural network analysis with 230 pb^{-1} of data. Based on this estimate we can say that, with the present analysis, we might be able to observe single top with less than 2 fb^{-1} of data.

I have been working on this analysis for a few years now and still I feel (like all the others working with me) that we have just started. We have faced many difficulties, technnical issues and limitations [1] during this search, some of which we were able to solve or simplify and some are still waiting to be solved. We have done a lot, we gave the world's most stringent limit on the single top production cross section but still there is a lot of work to be done, there are a lots of collisions to be recorded, there are lots of analysis techniques that exist and need to be looked at, there could be more techniques we might discover soon..... . In short, the story has just begun. It may hold many surprises and I hope it does.

---

[1] e.g., trigger efficiency for Monte Carlo is about $80 - 90\%$, our b-tagging eficiency is less than 50%, and we had to drop e+jets analysis for electrons in the End Cap region of the calorimeter because our electron reconstruction in that region was not well enough understood to give reasonabale data vs. background comparisons.

Appendix A

Data vs Background Sum

The figures in this section show distributions of various basic variables for initial samples before tagging, after tagging and cross-check data samples with ≥ 1 tag.

The cross-check samples are obtained by making the following cuts along with the usual selection cuts before tagging:

For W+jets dominated sample:
Exactly 2 jets, $HTJet1Jet2 - Lepton - Met < 200$ GeV.

For $t\bar{t}$ dominated sample:
Exactly 4 jets, HTAllJets > 250 GeV.

Each plot shows a summed histogram of all background contributions plus the expected single top signal, and the signal data. The individual contributions are (from the bottom up on each plot): misidentified-lepton multijet events in brown, W+jets (including Z+jets and dibosons) in green, $t\bar{t}{\rightarrow}l$+jets in red, $t\bar{t}{\rightarrow}ll$ in pink, t-channel (tqb) single top in light blue, and s-channel (tb) single top in dark blue. The data are shown by black solid circles with

black error bars.
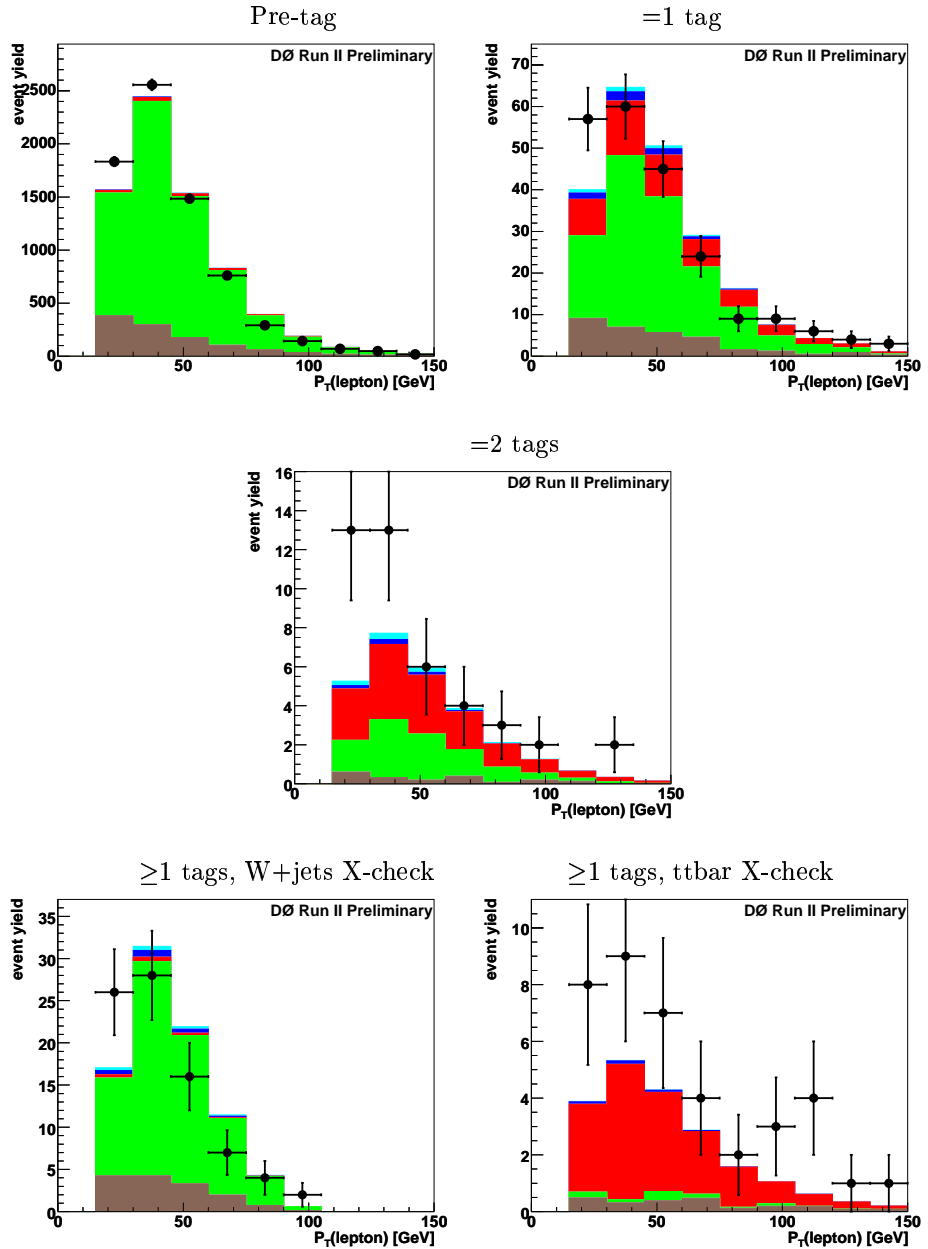
Figure A.1: Electron transverse energy (E_T).
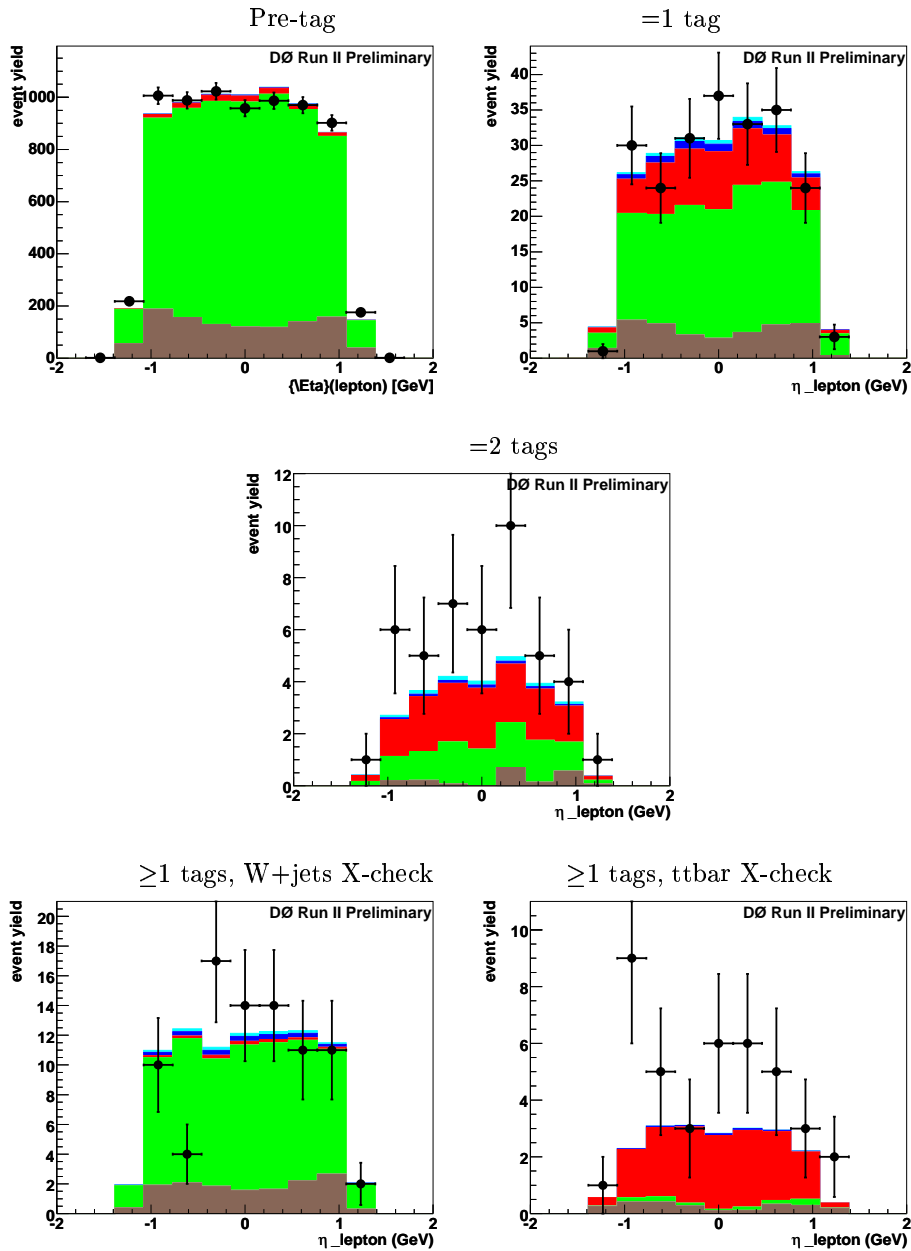
Figure A.2: Electron pseudorapidity (η).
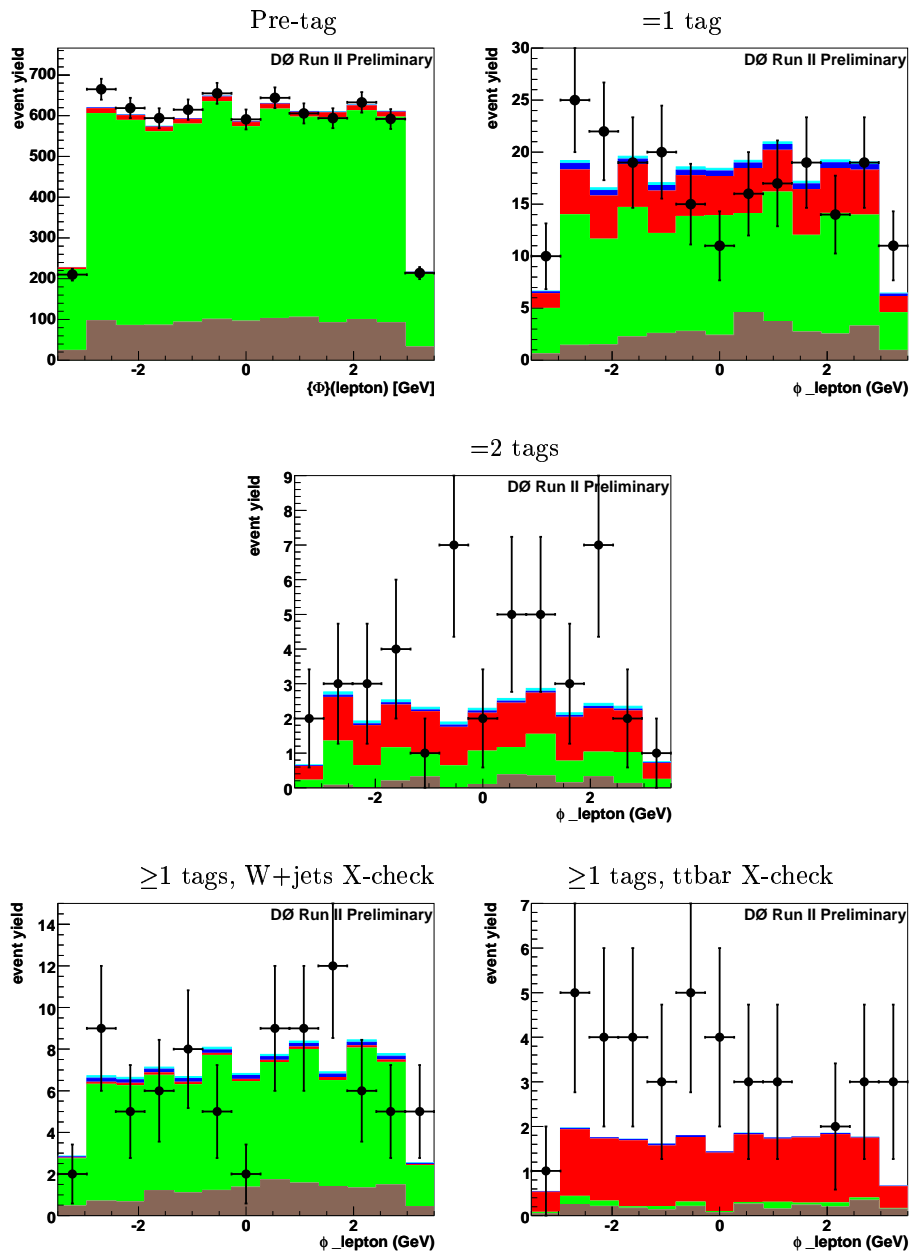
Figure A.3: Electron azimuthal angle (ϕ).
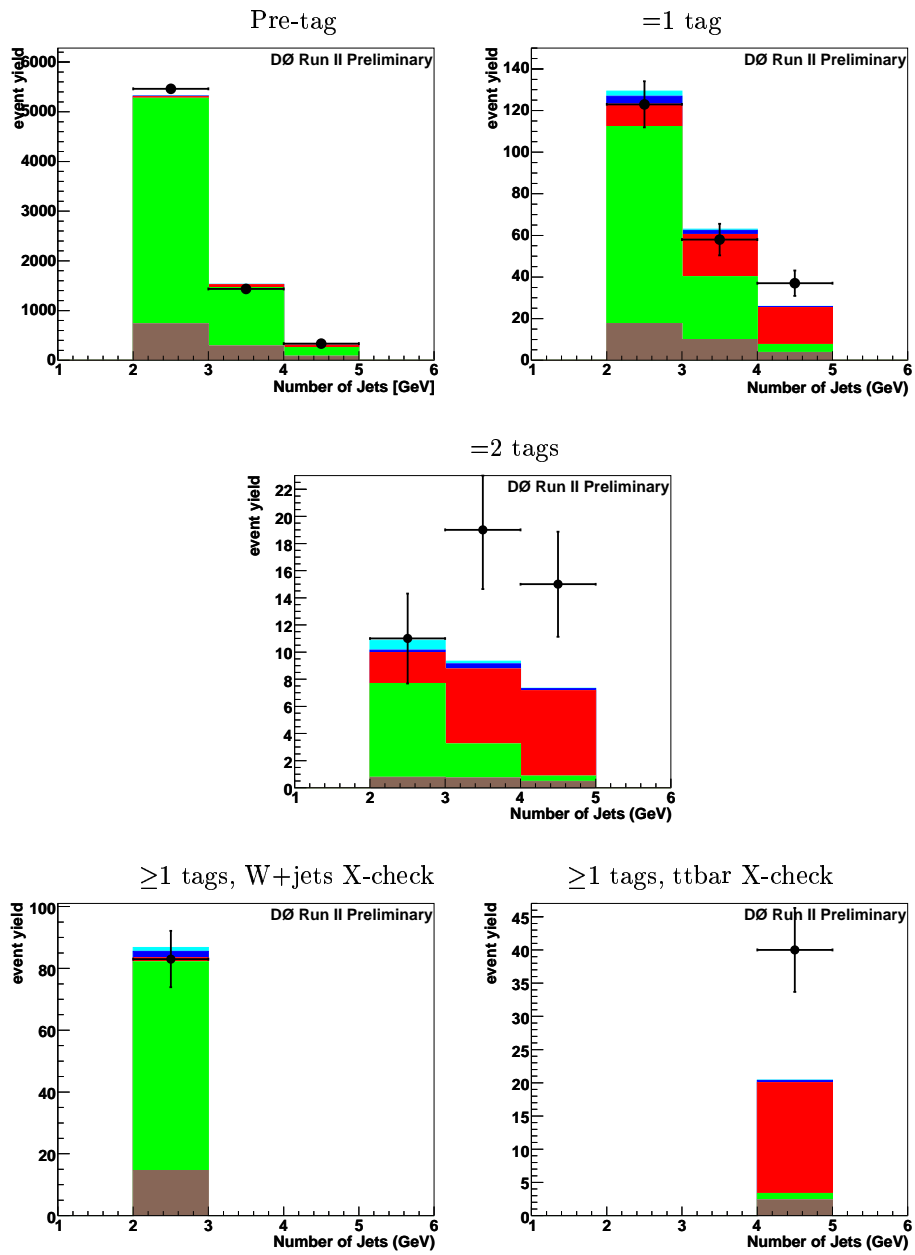
Figure A.4: Jet Multiplicity.
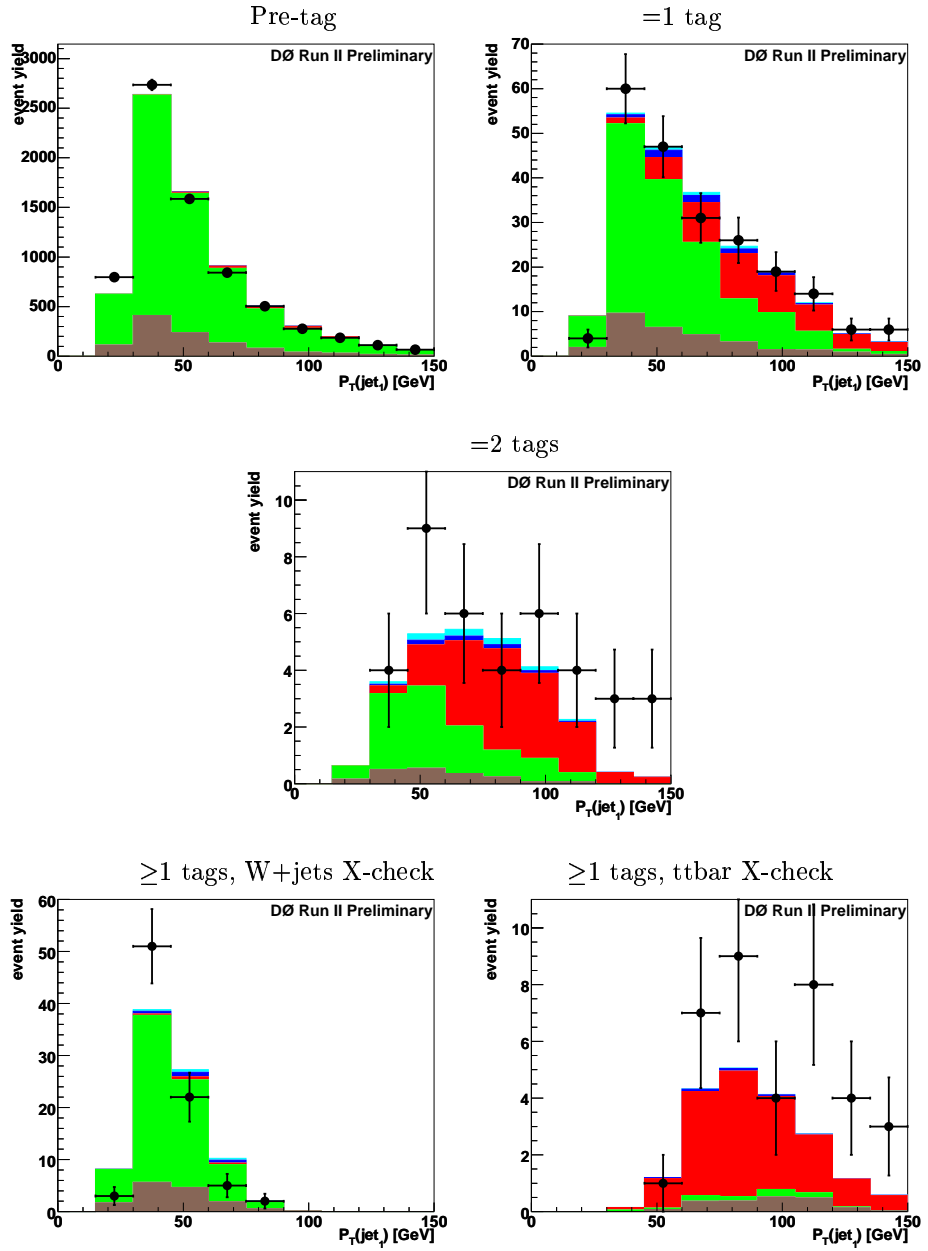
Figure A.5: Leading jet transverse energy (E_T).
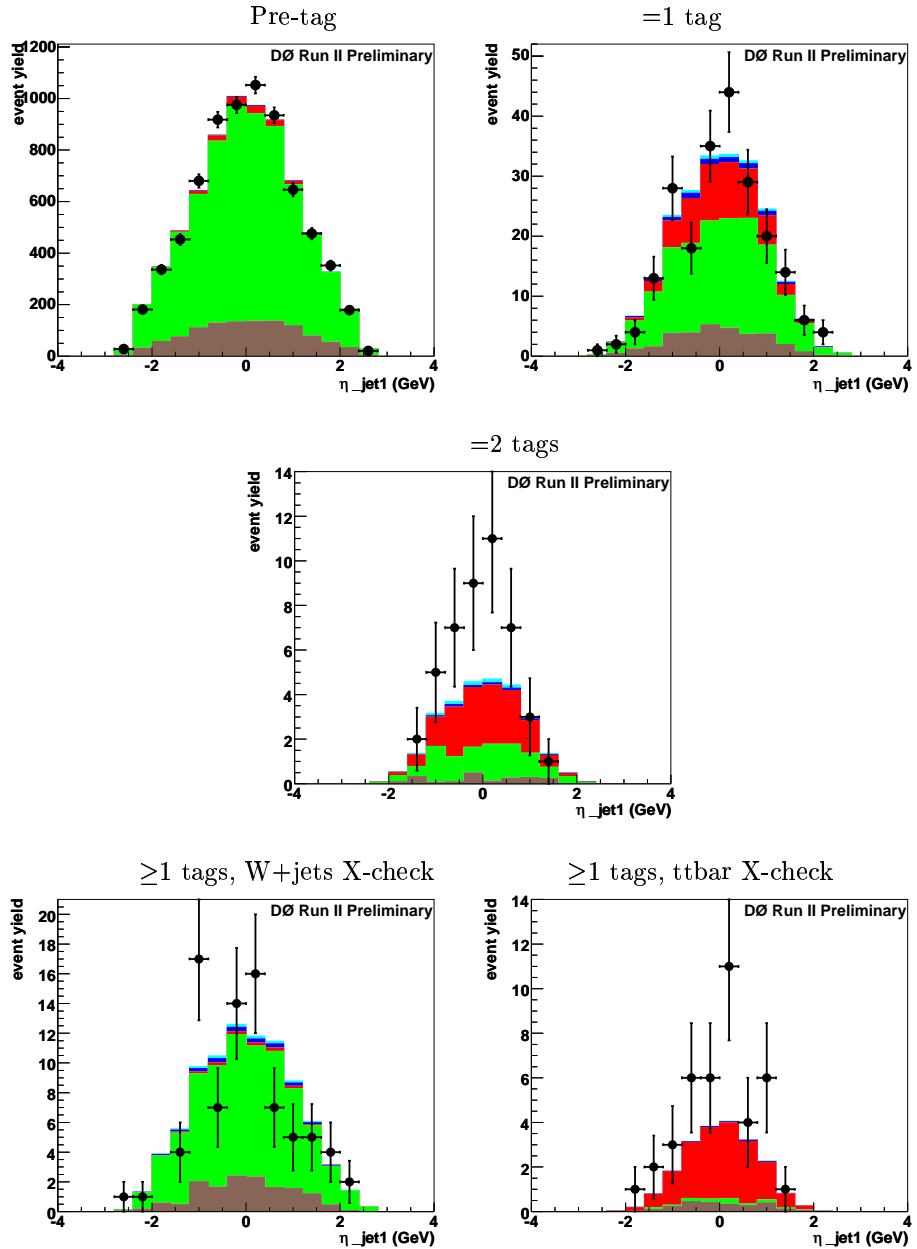
Figure A.6: Leading jet pseudorapidity (η).
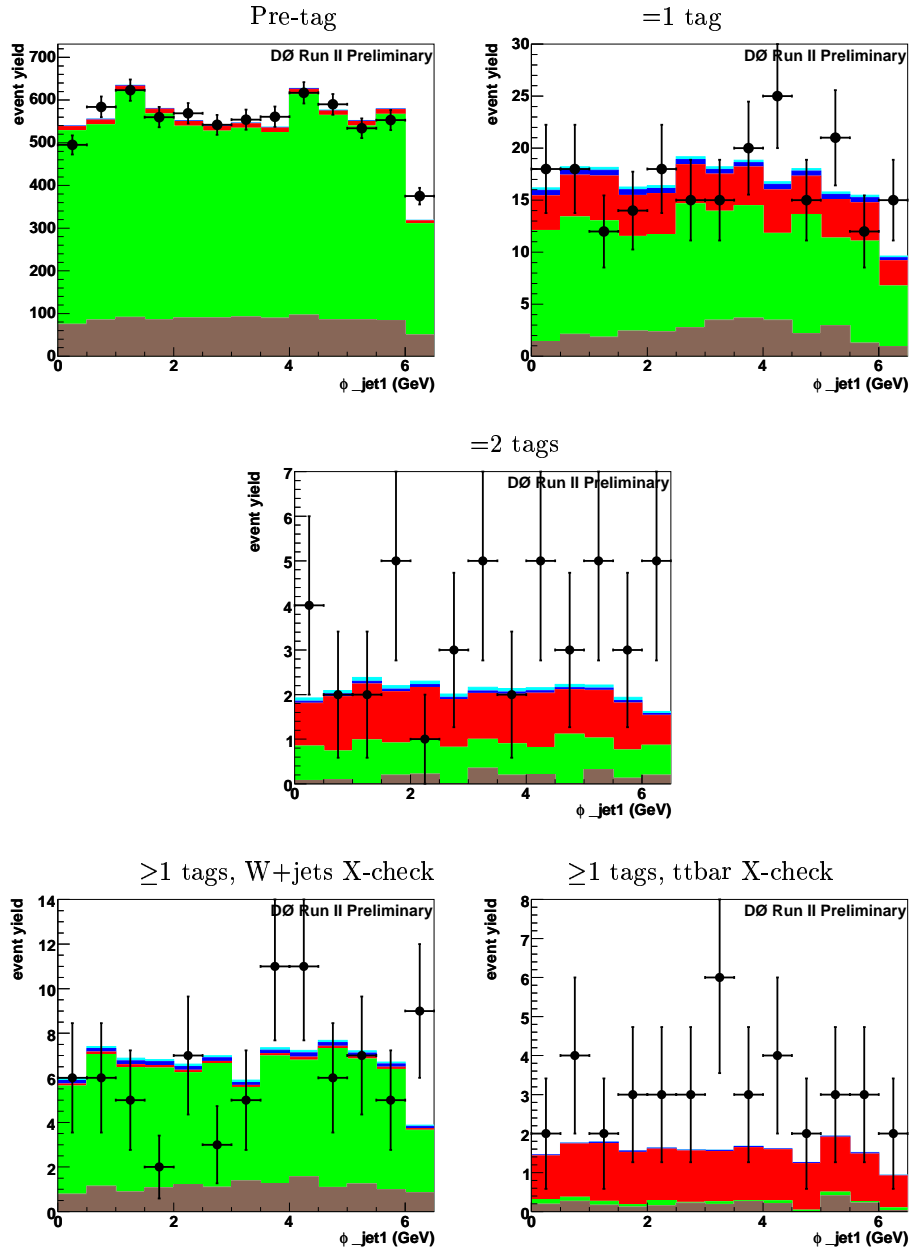
Figure A.7: Leading jet azimuthal angle (ϕ).
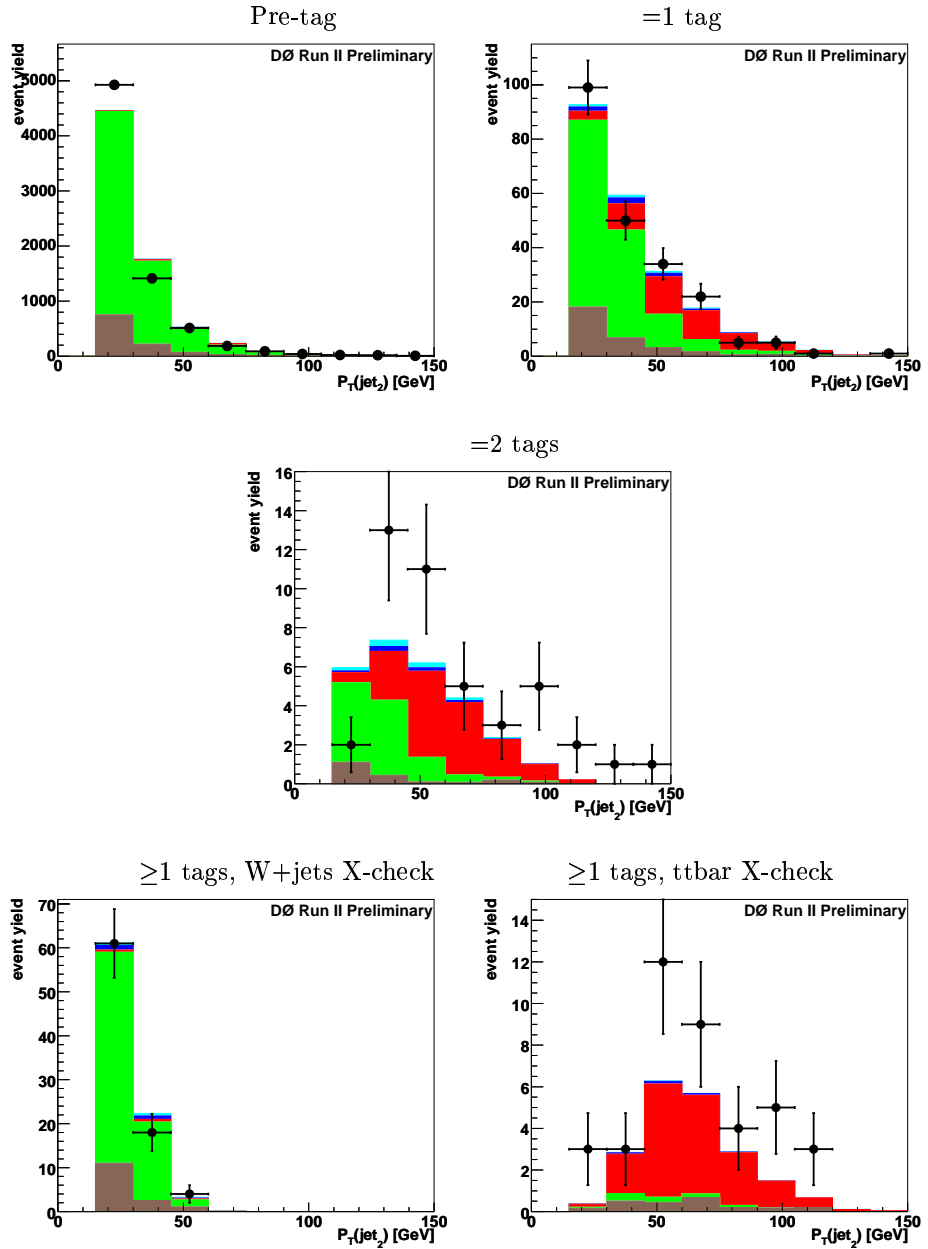
Figure A.8: Second leading jet transverse energy (E_T).
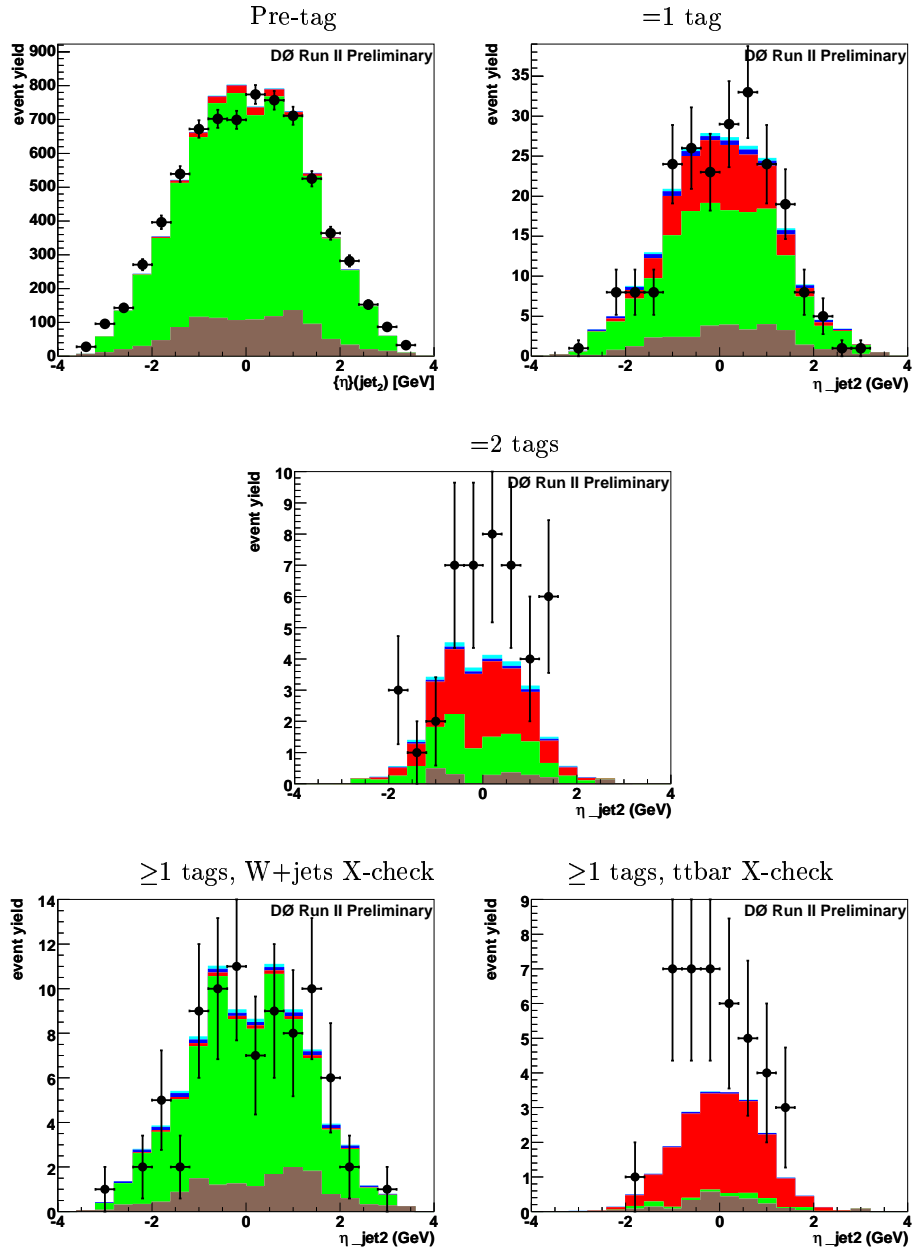
Figure A.9: Second leading jet pseudorapidity (η).
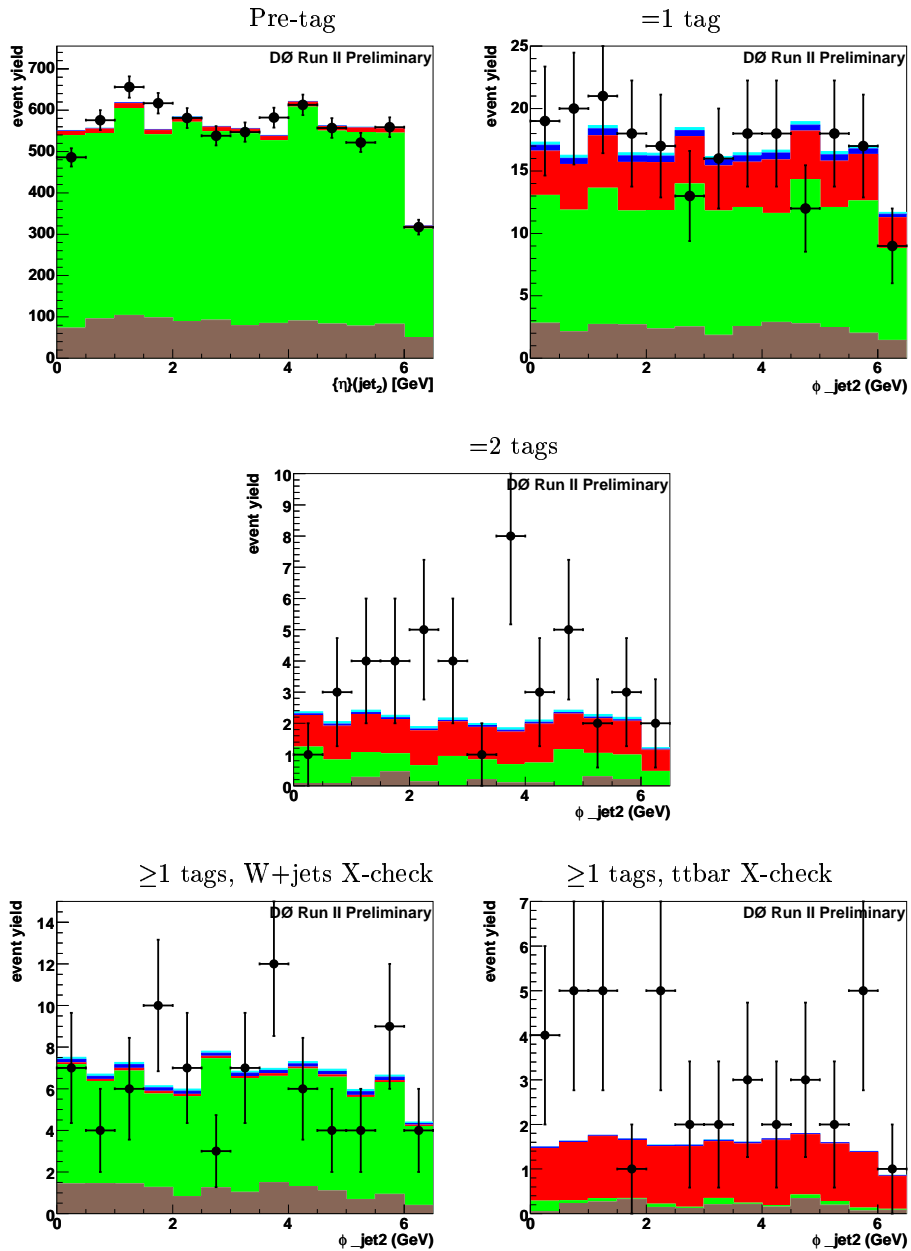
Figure A.10: Second leading jet azimuthal angle (ϕ).
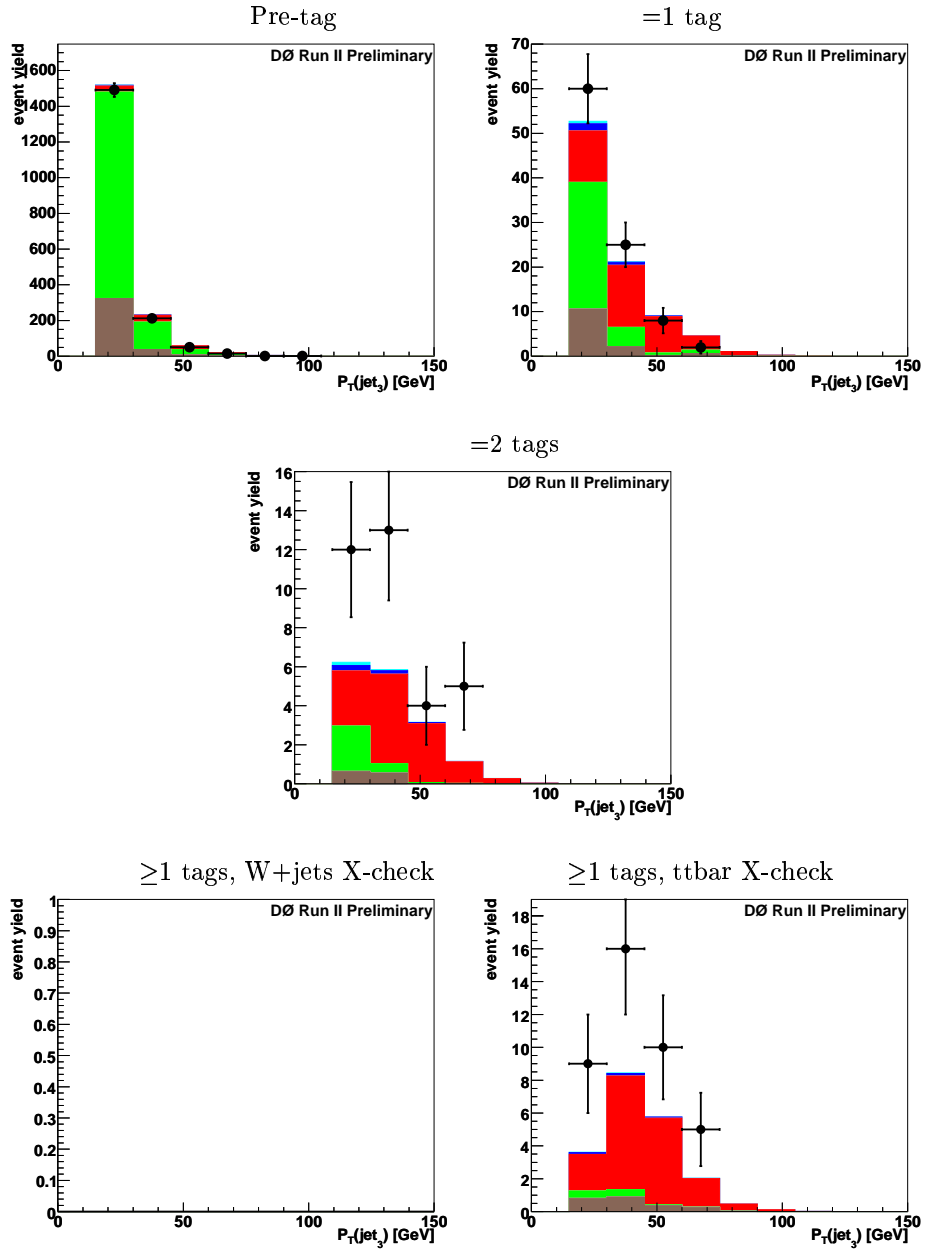
Figure A.11: Third leading jet transverse energy (E_T).
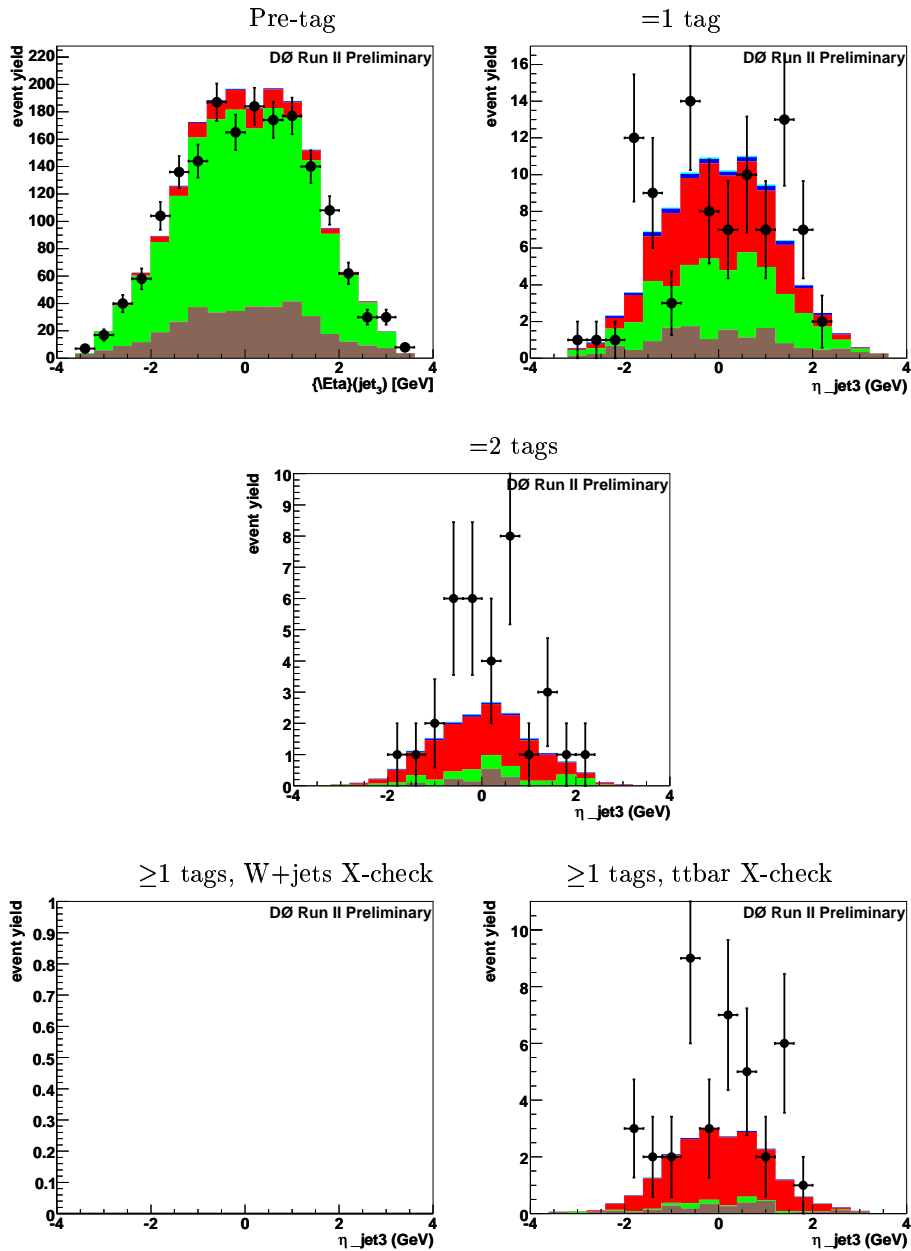
Figure A.12: Third leading jet pseudorapidity (η).
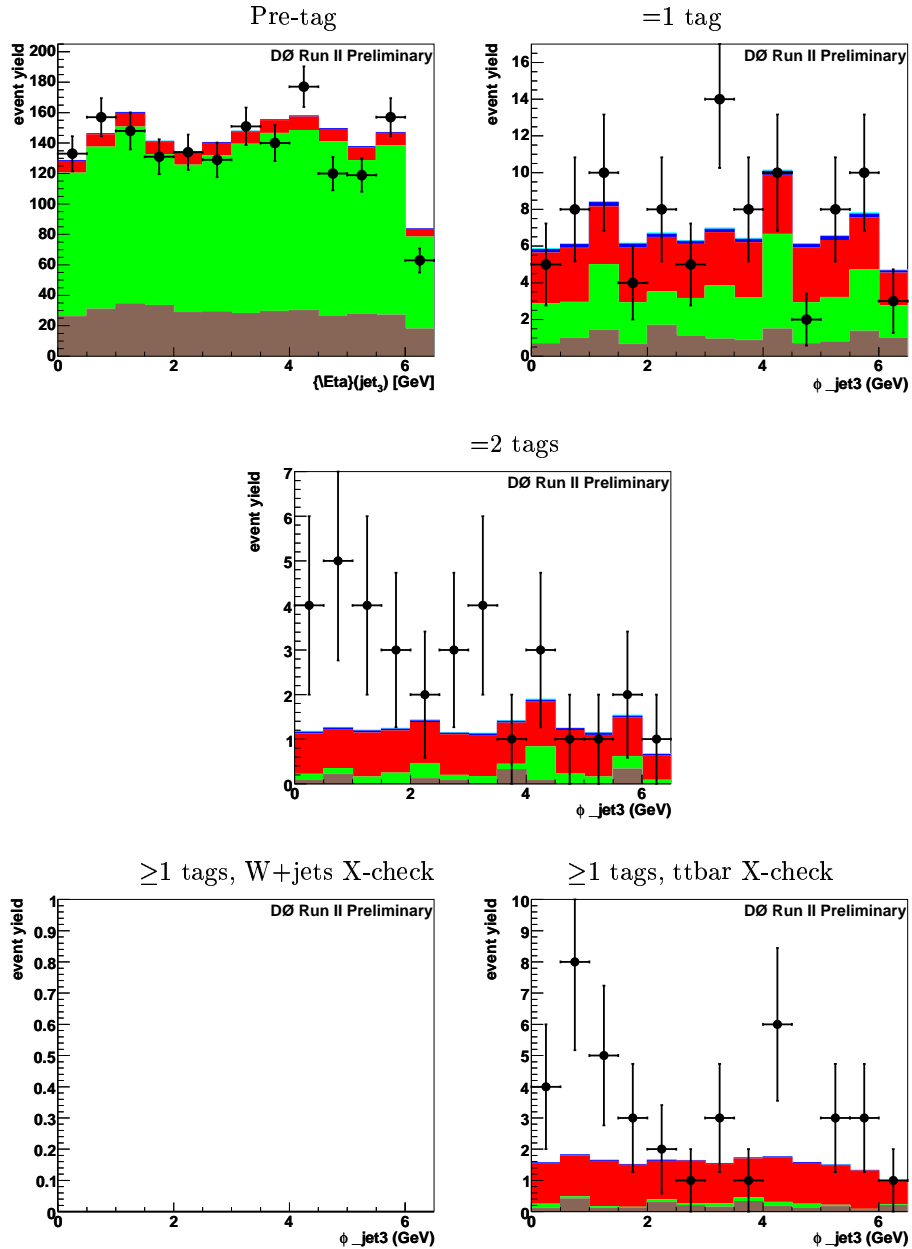
Figure A.13: Third leading jet azimuthal angle (ϕ).
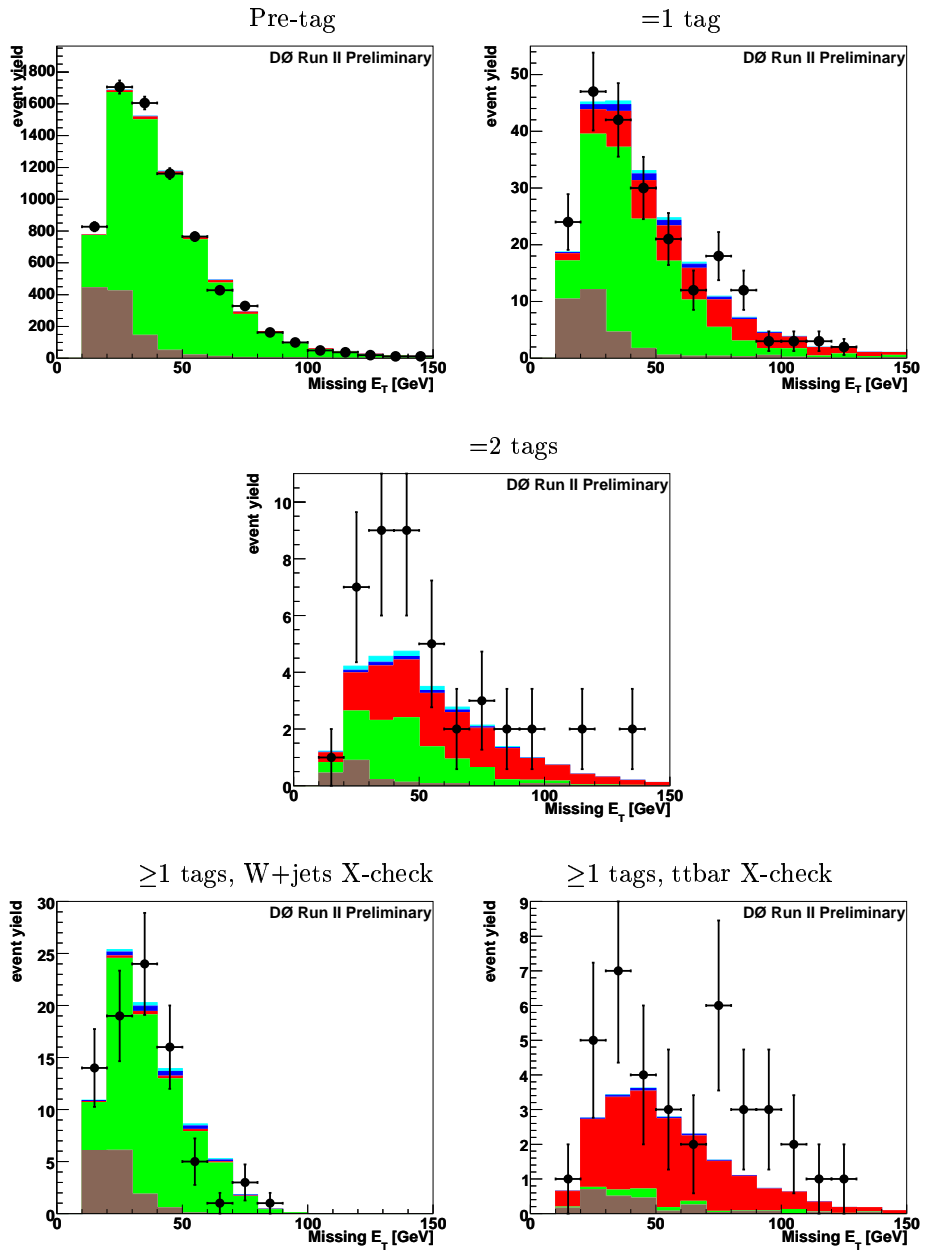
Figure A.14: Missing transverse energy.
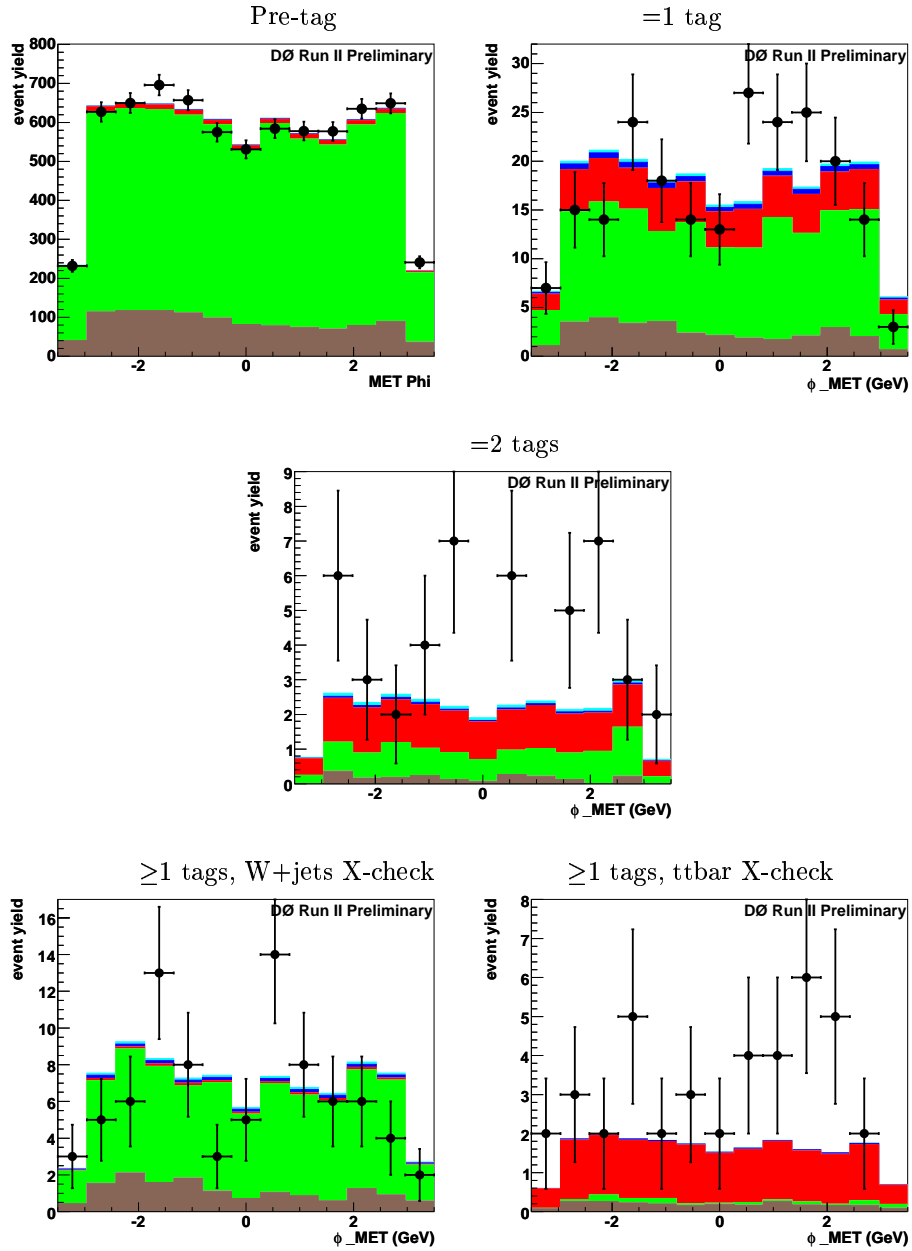
Figure A.15: MET azimuthal angle.
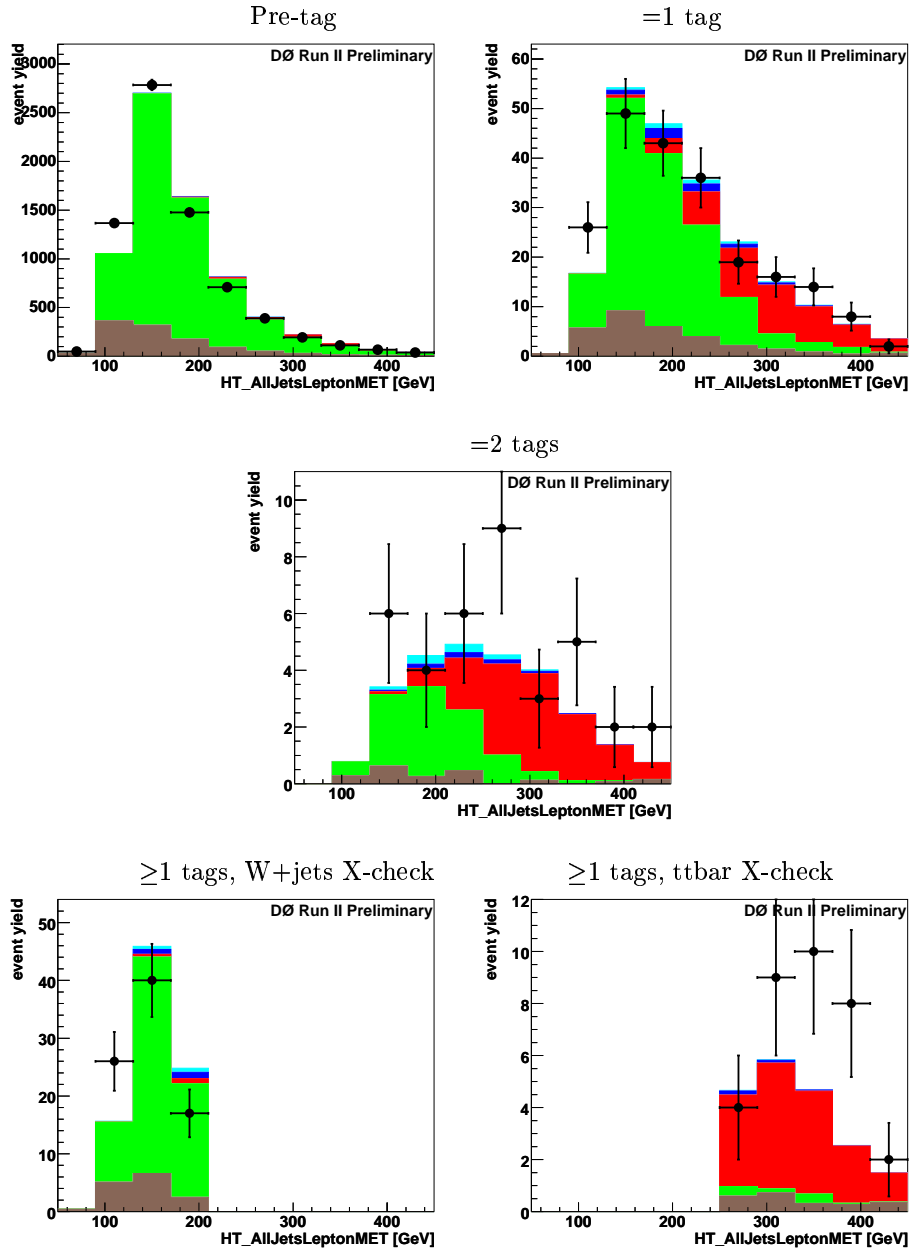
Figure A.16: Sum of all jets, lepton, and met transverse energies.
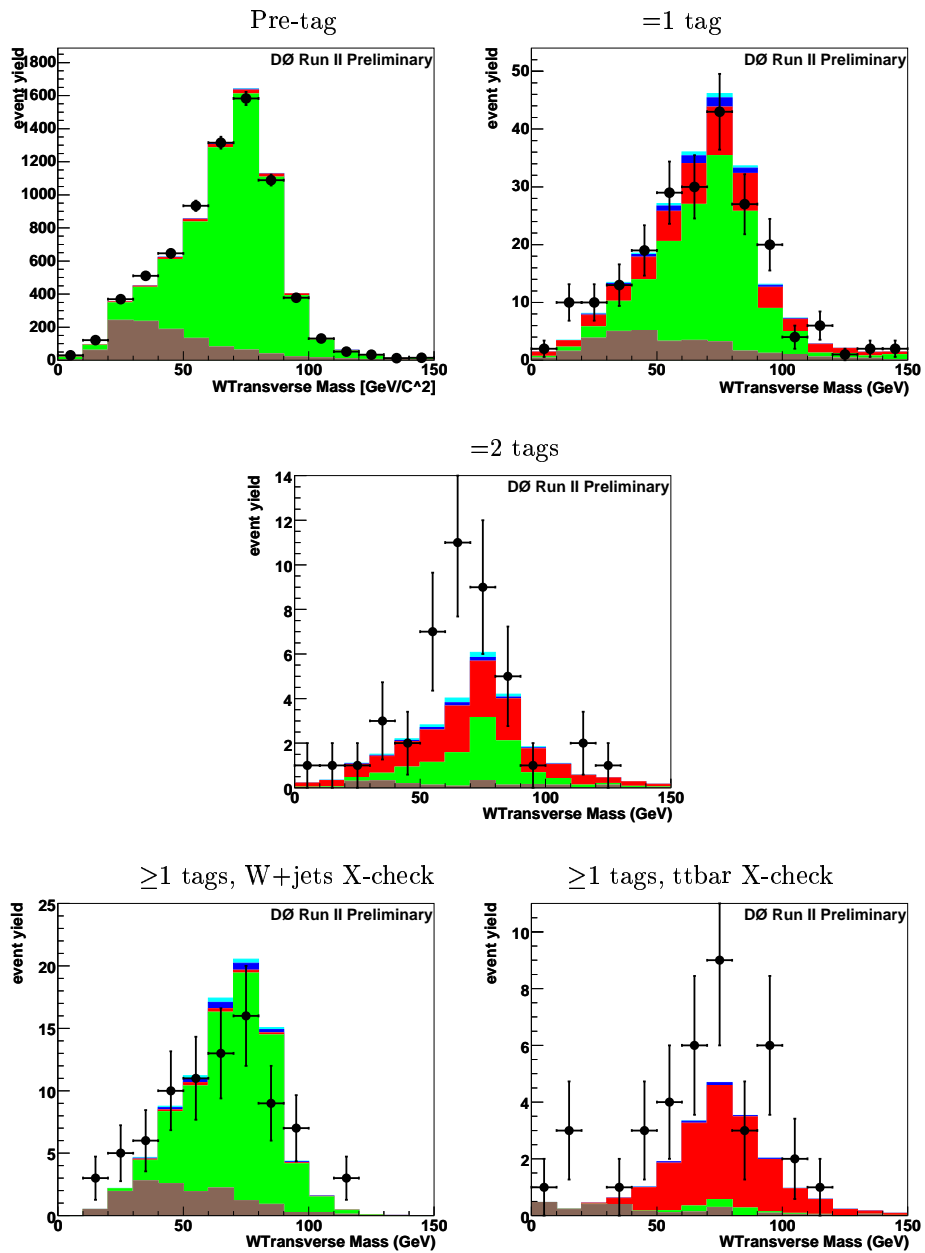
Figure A.17: W boson transverse mass.
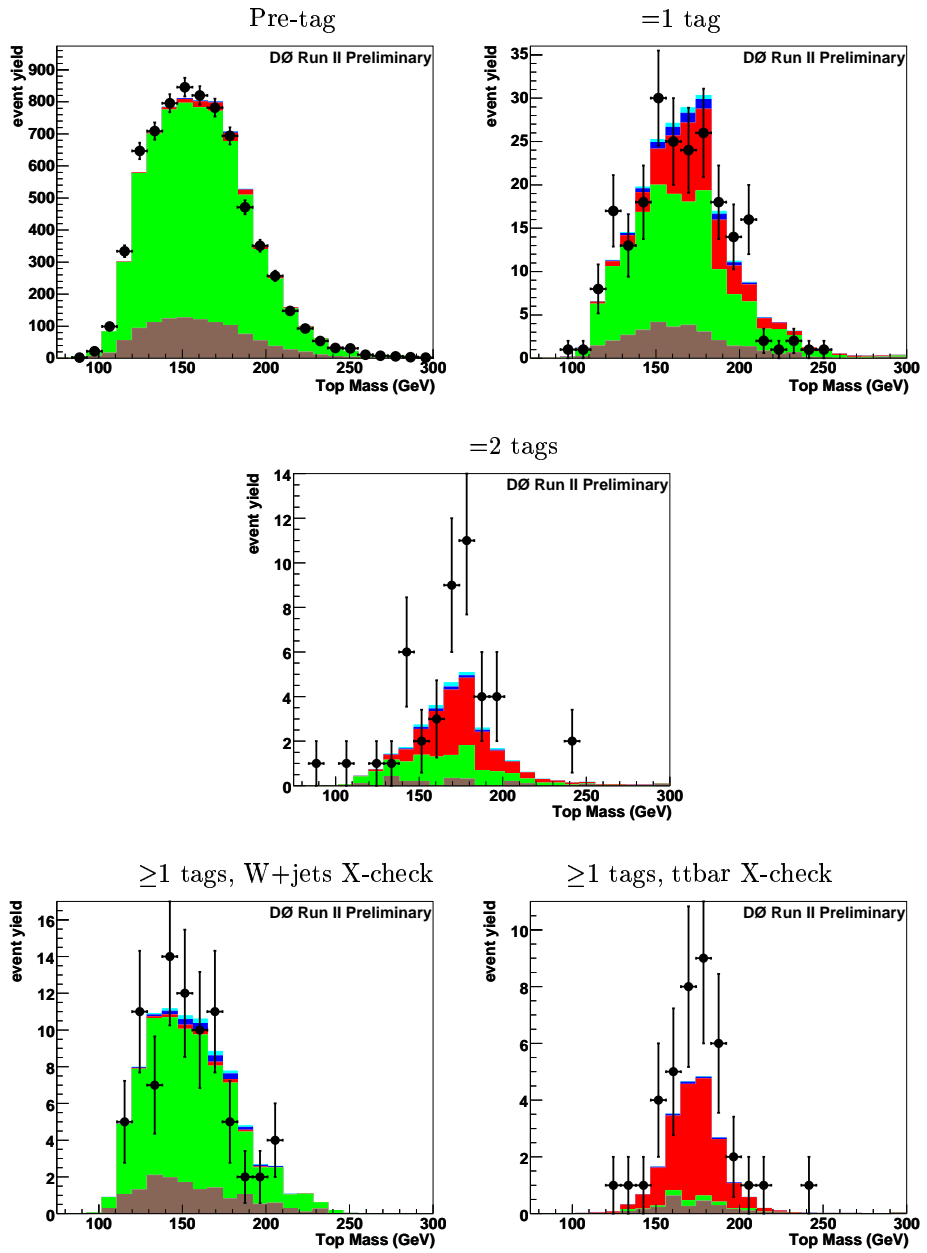
Figure A.18: Top mass.

Appendix B

Variables

In this section discriminating variables used in the neural network analysis are described.

Single-Object Kinematics

1. **p_T(jet1):** Transverse momentum of the leading jet. The leading jet is the jet with hieghest transverse energy.

2. **p_T(jet2):** Transverse momentum of the second leading jet.

3. **p_T(tag1):** Transverse momentum of the leading tagged jet.

4. **p_T(untag1):** Transverse momentum of the leading untagged jet. This is the leading jet that is not b-tagged.

5. **p_T(notbest1):** Transverse momentum of the leading jet that is not the best jet. The best jet is the one for which invariant mass of the system of the W boson and the jet is closest to the top mass (taken to be 175 GeV).

6. **p_T(MET):** Transverse momentum of the the missing energy in the event.

Event Kinematics

7. $p_T(\textbf{jet1}, \textbf{jet2})$: Transverse momentum of the system of the leading two jets, i.e., the four-vector sum of the leading two jets.

8. $p_T(\textbf{alljets} - \textbf{tag1})$: Transverse momentum of the system of all jets except the leading tagged jet.

9. $p_T(\textbf{alljets} - \textbf{best})$: Transverse momentum of the system of all jets except the best jet.

10. $H_T(\textbf{alljets})$: Scalar sum of the transverse momenta of all jets in the event.

11. $H_T(\textbf{alljets} - \textbf{tag1})$: Scalar sum of the transverse momenta of all jets except the leading tagged jet.

12. $H_T(\textbf{alljets} - \textbf{best})$: Scalar sum of the transverse momenta of all jets except the best jet.

13. $H_T(\textbf{alljets}, \textbf{lepton}, \textbf{MET})$: Scalar sum of the transverse momenta of all jets, the lepton, and the MET.

14. $H_T(\textbf{jet1}, \textbf{jet2})$: Scalar sum of the transverse momenta of the leading and second leading jets.

15. $H_T(\textbf{jet1}, \textbf{jet2}, \textbf{lepton}, \textbf{MET})$: Scalar sum of the transverse momenta of the leading jet, second leading jet, lepton, and MET.

16. $H(\textbf{alljets})$: Scalar sum of the energy of all jets in the event.

17. $H(\textbf{alljets} - \textbf{tag1})$: Scalar sum of the energy of all jets except the leading tagged jet.

18. $H(\textbf{alljets} - \textbf{best})$: Scalar sum of the energy of all jets except the best jet.

19. **H(alljets, lepton, MET):** Scalar sum of the energy of all jets, lepton, and MET.

20. **H(jet1, jet2):** Scalar sum of the energy of the leading and second leading jets.

21. **H(jet1, jet2, lepton, MET):** Scalar sum of the energy of the leading jet, second leading jet, lepton, and MET.

22. **M_T(jet1, jet2):** Transverse mass $\left(= \sqrt{(E_1 + E_2)^2 - (p_{x,1} + p_{x,2})^2 - (p_{y,1} + p_{y,2})^2}\right)$ of the system of the leading two jets.

23. **M(alljets):** Invariant mass of the system of all jets, i.e., the four-vector sum of all jets in the event.

24. **M(alljets − tag1):** Invariant mass of the system of all the jets except the leading tagged jet.

25. **M(alljets − best):** Invariant mass of the system of all the jets except the best jet.

26. **M(alljets, lepton, MET):** Invariant mass of the system of all jets, lepton, and MET.

27. **M(jet1, jet2):** Invariant mass of the system of the leading and second leading jets.

28. **M(jet1, jet2, lepton, MET):** Invariant mass of the system of the leading and second leading jets, lepton, and MET.

29. **M(W, tag1):** Invariant mass of the system of the W boson and the leading tagged jet (the reconstructed tagged top quark mass).

30. **M(W, best):** Invariant mass of the system of the W boson and the best jet (the reconstructed best top quark mass).

31. $\sqrt{\hat{s}}$: Invariant mass of the system of all objects in the event, $\sqrt{(\sum E_i)^2 - (\sum \vec{p}_i)^2}$, where the sums go over the objects in the event.

32. *Aplanarity*: a variable used to describe the momentum flow of jets in the event. It is based on the smallest of the three eigenvalues of the momentum tensor M_{ab} of the jets in the event. Planar events would have: $Q_1 = Q_2 = 0$ and $Q_3 = 1$. $\mathcal{A} = \frac{3}{2}Q_1$

33. *Sphericity*: a variable used to describe the momentum flow of jets in the event. It is based on the smaller two eigenvalues of the momentum tensor M_{ab} of the jets in the event. Spherical events would have $Q_1 = Q_2 = Q_3 = \frac{1}{3}$. $\mathcal{S} = \frac{3}{2}(Q_1 + Q_2)$

Angular Variables

34. $\Delta R(\mathbf{jet1}, \mathbf{jet2})$: Angular separation in η, ϕ between the leading two jets.

35. $Q(\mathbf{lepton}) \times \eta(\mathbf{untag1})$: Pseudorapidity of the leading untagged jet, multiplied by the charge of the lepton. In the t-channel, the final state d quark produced with the top quark tends to go along the incoming proton direction. Similarly, the $\bar{d}$ quark produced with the anti-top quark goes along the anti-proton direction. We take this CP symmetry into account through multiplying the η distribution by the charge of the lepton, which reflects the charge of the top quark.

36. $\cos(\mathbf{jet1}, \mathbf{lepton})_{\mathrm{lab}}$: Cosine of the angle between the leading jet and the lepton in the laboratory rest frame.

37. $\cos(\mathbf{jet2}, \mathbf{lepton})_{\mathrm{lab}}$: Cosine of the angle between the second leading jet and the lepton in the laboratory rest frame.

38. $\cos(\mathbf{tag1}, \mathbf{lepton})_{\mathrm{lab}}$: Cosine of the angle between the leading tagged jet and the lepton in the laboratory rest frame.

39. **cos(best, lepton)$_{\text{lab}}$:** Cosine of the angle between the best jet and the lepton in the laboratory rest frame.

40. **cos(jet1, alljets)$_{\text{alljets}}$:** Cosine of the angle between the leading jet and the alljets system in the alljets reference frame.

41. **cos(jet2, alljets)$_{\text{alljets}}$:** Cosine of the angle between the second leading jet and the alljets system in the alljets reference frame.

42. **cos(tag1, alljets)$_{\text{alljets}}$:** Cosine of the angle between the leading tagged jet and the alljets system in the alljets rest frame.

43. **cos(untag1, alljets)$_{\text{alljets}}$:** Cosine of the angle between the leading untagged jet and the alljets system in the alljets reference frame.

44. **cos(notbest, alljets)$_{\text{alljets}}$:** Cosine of the angle between the leading non-best jet and the alljets system in the alljets reference frame.

45. **cos(jet1, lepton)$_{\text{tag1top}}$:** Cosine of the angle between the leading jet and the lepton in the rest frame of the top quark reconstructed with the leading tagged jet.

46. **cos(jet2, lepton)$_{\text{tag1top}}$:** Cosine of the angle between the second leading jet and the lepton in the rest frame of the top quark reconstructed with the leading tagged jet.

47. **cos(tag1, lepton)$_{\text{tag1top}}$:** Cosine of the angle between the leading tagged jet and the lepton in the rest frame of the top quark reconstructed with the leading tagged jet.

48. **cos(untag1, lepton)$_{\text{tag1top}}$:** Cosine of the angle between the leading untagged jet and the lepton in the rest frame of the top quark reconstructed with the leading tagged jet.

49. **cos(best, lepton)$_\textbf{besttop}$:** Cosine of the angle between the best jet and the lepton in the rest frame of the top quark reconstructed with the best jet.

50. **cos(lepton, Q(lepton) $\times$ z)$_\textbf{besttop}$:** Cosine of the angle between the lepton and the z-axis, in the rest frame of the top quark reconstructed with the best jet.

51. **cos(notbest, lepton)$_\textbf{besttop}$:** Cosine of the angle between the leading non-best jet and the lepton in the rest frame of the top quark reconstructed with the best jet.

Bibliography

[1] D.J. Griffiths, *Introduction to Elementary Particles*, John Wiley & Sons, Inc., 1987.

[2] F. Halzen and A.D. Martin, *Quarks and Leptons: An Introductory Course in Modern Particle Physics*, John Wiley & Sons, Inc., 1984.

[3] F. Mandl and G. Shaw, *Quantum Field Theory*, John Wiley & Sons, Inc., 1984.

[4] P. Renton, *Electroweak Interactions: An Introduction to the Physics of Quarks and Leptons*, Cambridge University Press, 1990.

[5] P.D.B.Collins, A.D.Martin and E.J.Squires, *Particle Physics And Cosmology*, John Wiley & Sons, Inc., 1989.

[6] Abraham Pais, Inward bounds: OF MATTER AND FORCES IN THE PHYSICAL WORLD, Oxford (Oxfordshire); Clarendon Press, Oxford University Press, 1986

[7] 'QCD and collider physics', R.K.Ellis, W.J.Stirling and B.R.Webber, cambridge University Press (1996).

[8] The Particle Data Group, Review of Particle Physics, Phys. Rev. D 66 (2002) 1.

[9] The standard Model of Particale physics. Reviews of Modern Physics

[10] E.Fermi, Nuovo Cimento 11(1934)1; Z.Phys.88(1934)161.

[11] C.S.Wu et al., Phys.Rev.105(1957)1413.

[12] T.D.Lee and C.N.Yang, Phys. Rev.104(1956)254.

[13] T.D.Lee, M.Rosenbluth and C.N.Yang, Phys.Rev.75(1949)9905;
     T.D.Lee, CERN Report 61-30(1961).

[14] S.L.Glashow, Nucl.Phys.22(1961)579.

[15] F.J.Hasert, et al., Phys.Lett.B**46**(1973)138.

[16] S.L.Glashow, Nucl.Phys.22(1961),579;
     S.Weinberg, Phys.Rev.Lett.19(1967),1264;
     A.Salam in Elementary Particle Physics (Nobel Symp. N.8), Ed.
     N.Svartholm, Almquist and Wiksells, Stockholm (1968), p.367

[17] P.W.Higgs, Phys.Lett.12(1964),132;
     F.Englert and R.Brout, Phys.Rev.Lett.(1964),321;
     G.S.Guralnik, C.R.Hagen and T.W.B.Kibble,
     Phys.Rev.Lett.13(1964)585;
     P.W.Higgs, Phys.Rev.145(1966),1156;
     T.W.B.Kibble, Phys.Rev.155(1967),1554.

[18] G. 't Hooft, Nucl.Phys.B33(1971),173; B35(1971)167.

[19] The ALEPH, DELPHI, L3, OPAL, SLD Collaborations and the LEP
     Electroweak Working Group, A Combination of Preliminary Electroweak
     Measurements and Constraints on the Standard Model, hep-ex/0312023.

[20] Guido Altarelli and Martin W. Grunewald, Precision Electroweak Tests
     of the Standard Model, hep-ph/0404165.

[21] UA1 Collaboration, G.Arnison et al., Phys.Lett.B122(1983)103;
     UA2 Collaboration, M.Banner et al., Phys.Lett.B122(1983)476

225

[22] The CDF Collaboration, the DØ Collaboration, and the Tevatron Electroweak Working Group, Combination of CDF and DØ Results on the Top-Quark Mass, hep-ex/0404010.

[23] H. Burkhardt, B. Pietrzyk, Update of the Hadronic Contribution to the QED Vacuum Polarization, Phys. Lett. B 513 (2001) 46.

[24] CDF Collaboration: F. Abe et al., Phys. Rev. Lett.73(1994), 225; Phys. Rev.D50 (1994), 2966;
CDF Collaboration: F.Abe et al., Phys.Rev.Lett.74(1995)2626;
DØ Collaboration: S.Abachi et al., Phys.Rev.Lett.74(1995)2632

[25] K.G. Chetyrkin, R. Harlander, T. Seindensticker, and M. Steinhauser, Phys. Rev. D60, 114015, (1999).

[26] A. Denner and T. Sack, Nucl. Phys. B238, 46 (1991).

[27] I.I. Bigi, Y.L. Dokshitzer, V. Khoze, J. Kuehn, and P. Zerwas, Phys. Lett. B181, 157 (1986).

[28] M. Beneke *et al.*, "Top Quark Physics," in *Standard Model Physics (and more) at the LHC*, arXiv:hep-ph/0003033, (March 2000).

[29] D. Chakraborty, J. Konigsberg, and D. Rainwater, "Review of Top Quark Physics," to appear in Ann.Rev.Nucl.Part.Sci., arXiv:hep-ph/0303092, (March 2003).

[30] A. Belyaev, E. Boos, and L. Dudko, Phys. Rev. D **59**, 075001 (1999); T. Tait, Phys. Rev. D **61**, 034001 (2000); A. Belyaev and E. Boos, Phys. Rev. D **63**, 034012 (2001); S. Zhu, Phys. Lett. **B524**, 283 (2002), [Erratum-ibid. **B537**, 351 (2002)]; E.E. Boos and A.V. Sherstnev, Phys. Lett. **B534**, 97 (2002); B.W. Harris, E. Laenen, L. Phaf, Z. Sullivan, and

S. Weinzierl, Phys. Rev. D **66**, 054024 (2002). D. Dicus and S. Willenbrock, Phys. Rev. D **34**, 155 (1986); C.-P. Yuan, Phys. Rev. D **41**, 42 (1990); G. V. Jikia and S. R. Slabospitsky, Phys. Lett. **B295**, 136 (1992); R. K. Ellis and S. Parke, Phys. Rev. D **46**, 3785 (1992); G. Bordes and B. van Eijk, Z. Phys. **C57**, 81 (1993); D. O. Carlson and C.-P. Yuan, Phys. Lett. **B306**, 386 (1993); G. Bordes and B. van Eijk, Nucl. Phys. **B435**, 23 (1995); S. Cortese and R. Petronzio, Phys. Lett. **B253**, 494 (1991); D.O. Carlson, E. Malkawi, and C.-P. Yuan, Phys. Lett. **B337**, 145 (1994); T. Stelzer and S. Willenbrock, Phys. Lett. **B357**, 125 (1995); R. Pittau, Phys. Lett. **B386**, 397 (1996); M. Smith and S. Willenbrock, Phys. Rev. D **54**, 6696 (1996); D. Atwood, S. Bar-Shalom, G. Eilam, and A. Soni, Phys. Rev. D **54**, 5412 (1996); C.S. Li, R.J. Oakes, and J. M. Yang, Phys. Rev. D **55**, 1672 (1997); C.S. Li, R. J. Oakes, and J. M. Yang, Phys. Rev. D **55**, 5780 (1997); G. Mahlon, S. Parke, Phys. Rev. D **55**, 7249 (1997); A.P. Heinson, A.S. Belyaev, and E.E. Boos, Phys. Rev. D **56**, 3114 (1997); T. Stelzer, Z. Sullivan, and S. Willenbrock, Phys. Rev. D **56**, 5919 (1997);

[31] A.P. Heinson, A.S. Belyaev and E.E. Boos, "Single Top Quarks at the Fermilab Tevatron," Phys. Rev. D **56**, 3114 (1997).

[32] M. C. Smith and S. Willenbrock, Phys. Rev. **D 54**, 6696 (1996).

[33] T. Stelzer and S. Willenbrock, Phys. Lett. **B357**, 125 (1995).

[34] A. P. Heinson, A. S. Belyaev, and E. E. Boos, Phys. Rev. **D 56**, 3114 (1997).

[35] D. Carlson, Ph.D. thesis, Michigan State University, MSUHEP-050727, August 1995.

[36] S. Mrenna and C.–P. Yuan, "Effects of QCD Resummation on W^+h and $t\bar{b}$ Production at the Tevatron", hep-ph/9703224 (1997).

[37] T. Tait and C. P. Yuan, hep-ph/9710372.

[38] T. Stelzer, Z. Sullivan, and S. Willenbrock, "Single-Top Production via W-Gluon Fusion at Next-to-Leading Order", hep-ph/9705398 (1997).

[39] C.–P. Yuan, "Top Quark Physics at Hadron Colliders", published in CCAST Symposium 1993, 259 (1993); hep-ph/9308240.
D. O. Carlson and C.–P. Yuan, "Probing New Physics from the Single Top Production", Particle Phys. & Phen. 1995, 172 (1995); hep-ph/9509208.
C.–P. Yuan, "Top Quark Physics", published in Valencia Elem. Part. Phys. 1995, 148 (1995); hep-ph/9509209.
C.–P. Yuan, "Physics of Top Quark at the Tevatron", talk given at 5th Mexican Workshop of Particles and Fields, Puebla, Mexico, Oct. 30 - Nov 3, 1995; hep-ph/9604434.

[40] T. Stelzer, Z. Sullivan and S. Willenbrock, "Single-Top-Quark Production via W-gluon Fusion at Next-to-Leading Order," Phys. Rev. D **56**, 5919 (1997).

[41] R.N. Cahn and S. Dawson, *Phys. Lett.* **B136**, 196 (1984), **B138**, 464(E) (1984);
M.S. Chanowitz and M.K. Gaillard, *Phys. Lett.* **B142**, 85 (1984);
G.L. Kane, W.W. Repko and W.R. Rolnick, *Phys. Lett.* **B148**, 367 (1984);
S. Dawson, *Nucl. Phys.* **B249**, 427 (1985);
J. Lindfors, *Z. Phys.* **C28**, 427 (1985);

W.B. Rolnick, *Nucl. Phys.* **B274**, 171 (1986);

P.W. Johnson, F.I. Olness and W.-K. Tung, *Phys. Rev.* **D36**, 291 (1987);

Z. Kunszt and D.E. Soper, *Nucl. Phys.* **B296**, 253 (1988);

A. Abbasabadi, W.W. Repko, D.A. Dicus and R. Vega, *Phys. Rev.* **D38**, 2770 (1988); S. Dawson, *Phys. Lett.* **B217**, 347 (1989);

S. Cortese and R. Petronzio, *Phys. Lett.* **B276**, 203 (1992);

I. Kuss and H. Spiesberger, *Phys. Rev.* **D53**, 6078 (1996).

[42] T. Affolder *et al.* [CDF Collaboration], "First measurement of the ratio $\frac{B(t\rightarrow Wb)}{B(t\rightarrow Wq)}$ and Associated Limit on the CKM Element V_{tb}, " Phys. Rev. Lett. 86, 3233 (2001).

[43] E.L. Berger and H. Contopanagos, "Perturbative Gluon Resummation of the Top Quark Production Cross Section," Phys. Lett. **B361**, 115 (1995); "The Perturbative Resummed Series for Top Quark Production in Hadron Reactions," Phys. Rev. D **54**, 3085 (1996).

[44] Agelou, Andrieu, Baringer, Bean, Bloch, Boos, Bunichev, Busato, Christofek, Clement, Dudko, Gadfort, Garcia-Bellido, Gaudio, Gele, Gutierrez, Heinson, Jabeen, S.Jain, Juste, Kau, Kopal, Mitrevski, Parsons, Perea, Perez, Prosper, Quadt, Rud, Schwienhorst, Strauss, Vachon, Warsinsky, Watts,
Search for Single Top Quark Production at DZero in Run II, *DØ Note* 4398.

[45] M.C. Smith and S. Willenbrock, "QCD and Yukawa Corrections to Single-Top-Quark Production via $q\bar{q}\rightarrow tb$," Phys. Rev. D **54**, 6696 (1996).

[46] B.W. Harris, E. Laenen, L. Phaf, Z. Sullivan and S. Weinzierl, "The Fully Differential Single Top Quark Cross Section in Next-to-Leading Order QCD," Phys. Rev. D **66**, 054024 (2002).

[47] T. Stelzer, Z. Sullivan, and S. Willenbrock, Phys. Rev. D **58**, 094021 (1998).

[48] T. Tait and C. P. Yuan, Phys. Rev. D **63**, 014018 (2001);

[49] T. Stelzer, Z. Sullivan, and S. Willenbrock, Phys. Rev. D **56**, 5919 (1997).

[50] M.C. Smith and S. Willenbrock, "QCD and Yukawa Corrections to Single-Top-Quark Production via $q\bar{q} \to tb$," Phys. Rev. D **54**, 6696 (1996).

[51] T. Stelzer, Z. Sullivan and S. Willenbrock, "Single-Top-Quark Production via W-gluon Fusion at Next-to-Leading Order," Phys. Rev. D **56**, 5919 (1997).

[52] B.W. Harris, E. Laenen, L. Phaf, Z. Sullivan and S. Weinzierl, "The Fully Differential Single Top Quark Cross Section in Next-to-Leading Order QCD," Phys. Rev. D **66**, 054024 (2002).

[53] Dan Amidei and Chip Brock, "Report of the $TeV2000$ Study Group on Future ElectroWeak Physics at the Tevatron", 1995.

[54] K. Hagiwara *et al.*, (Particle Data Group Collaboration), "Review Of Particle Physics," Phys. Rev. D **66**, 010001 (2002).

[55] G. Mahlon and S.J. Parke, "Improved Spin Basis for Angular Correlation Studies in Single Top Quark Production at the Tevatron," Phys. Rev. D **55**, 7249 (1997); G. Mahlon and S.J. Parke, "Single Top Quark Production at the LHC: Understanding Spin," Phys. Lett. B **476**, 323 (2000).

[56] E.E. Boos and A.V. Sherstnev, "Spin Effects in Processes of Single Top Quark Production at Hadron Colliders," Phys. Lett. **B534**, 97 (2002).

[57] A. Czarnecki and M. Jezabek, "Distributions of Leptons in Decays of Polarized Heavy Quarks," Nucl. Phys. **B427**, 3 (1994).

[58] A. Czarnecki, M. Jezabek and J.H. Kuhn, "Lepton Spectra From Decays Of Polarized Top Quarks," Nucl. Phys. **B351**, 70 (1991).

[59] A. Brandenburg, Z.G. Si and P. Uwer, "QCD-Corrected Spin Analyzing Power of Jets in Decays of Polarized Top Quarks," Phys. Lett. **B539**, 235 (2002).

[60] LHC/LC Study Group Working Document. In preparation.

[61] D. Atwood, S. Bar-Shalom, G. Eilam, and A. Soni, Phys. Rev. D **54**, 5412 (1996).

[62] S. Bar-Shalom, D. Atwood, and A. Soni, Phys. Rev. D **57**, 1495 (1998).

[63] C. S. Li, R. J. Oakes, and J. M. Yang, Phys. Rev. D **55**, 1672 (1997);

[64] A. Datta, J. M. Yang, B. L. Young, and X. Zhang, Phys. Rev. D **56**, 3107 (1997).

[65] E. Christova, S. Fichtinger, S. Kraml, and W. Majerotto, Phys. Rev. D **65**, 094002 (2002).

[66] R. J. Oakes, K. Whisnant, J. M. Yang, B. L. Young, and X. Zhang, Phys. Rev. D **57**, 534 (1998).

[67] K. i. Hikasa, J. M. Yang, and B. L. Young, Phys. Rev. D **60**, 114041 (1999).

[68] P. Chiappetta, A. Deandrea, E. Nagy, S. Negroni, G. Polesello, and J. M. Virey, Phys. Rev. D **61**, 115008 (2000).

[69] *R*-parity Working Group Collaboration, B. Allanach *et al.*, in *Physics at Run II: the Supersymmetry/Higgs Workshop*, Fermilab, 1998, edited by M. Carena and J. Lykken (Fermilab, Batavia, 2002), p. 299, hep-ph/9906224.

[70] Higgs Working Group Collaboration, M. Carena *et al.*, in *Physics at Run II: the Supersymmetry/Higgs Workshop*, Fermilab, 1998, edited by M. Carena and J. Lykken (Fermilab, Batavia, 2002), p. 424, hep-ph/0010338.

[71] SUGRA Working Group Collaboration, S. Abel *et al.*, in *Physics at Run II: the Supersymmetry/Higgs Workshop*, Fermilab, 1998, edited by M. Carena and J. Lykken (Fermilab, Batavia, 2002), p. 70, hep-ph/0003154.

[72] E. L. Berger, B. W. Harris, and Z. Sullivan, Phys. Rev. Lett. **83**, 4472 (1999); Phys. Rev. D **63**, 115001 (2001).

[73] D. O. Carlson, E. Malkawi, and C. P. Yuan, Phys. Lett. B **337**, 145 (1994).

[74] G. L. Kane, G. A. Ladinsky, and C. P. Yuan, Phys. Rev. D **45**, 124 (1992).

[75] T. G. Rizzo, Phys. Rev. D **53**, 6218 (1996).

[76] T. Tait and C. P. Yuan, Phys. Rev. D **55**, 7300 (1997).

[77] A. Datta and X. Zhang, Phys. Rev. D **55**, 2530 (1997).

[78] K. Whisnant, J. M. Yang, B. L. Young, and X. Zhang, Phys. Rev. D **56**, 467 (1997).

[79] E. Boos, L. Dudko, and T. Ohl, Eur. Phys. J. C **11**, 473 (1999).

[80] D. Espriu and J. Manzano, Phys. Rev. D **65**, 073005 (2002).

[81] T. Han, M. Hosch, K. Whisnant, B. L. Young, and X. Zhang, Phys. Rev. D **58**, 073008 (1998).

[82] E. H. Simmons, Phys. Rev. D **55**, 5494 (1997).

[83] G. Lu, Y. Cao, J. Huang, J. Zhang, and Z. Xiao, hep-ph/9701406.

[84] P. Baringer, P. Jain, D. W. McKay, and L. L. Smith, Phys. Rev. D **56**, 2914 (1997).

[85] C. X. Yue and G. R. Lu, Chin. Phys. Lett. **15**, 631 (1998).

[86] H. J. He and C. P. Yuan, Phys. Rev. Lett. **83**, 28 (1999).

[87] J. j. Cao, Z. h. Xiong, and J. M. Yang, Phys. Rev. D **67**, 071701 (2003).

[88] A. Datta, P. J. O'Donnell, Z. H. Lin, X. Zhang, and T. Huang, Phys. Lett. B **483**, 203 (2000).

[89] X. Li and E. Ma, Phys. Rev. Lett. **47**, 1788 (1981).

[90] E. Malkawi, T. Tait, and C. P. Yuan, Phys. Lett. B **385**, 304 (1996).

[91] D. J. Muller and S. Nandi, Phys. Lett. B **383**, 345 (1996).

[92] Z. Sullivan, Phys. Rev. D **66**, 075011 (2002).

[93] CDF Collaboration, D. Acosta *et al.*, Phys. Rev. Lett. **90**, 081802 (2003).

[94] Zack Sullivan, "How to rule out Little Higgs (and constrain many other models) at the LHC," to be published in *Proceedings of the XXXVIIIth Rencontres de Moriond: QCD and High Energy Hadronic Interactions*, Les Arcs, Savoie, France, March 22–29, 2003, hep-ph/0306266.

[95] D. Carlson and C.–P. Yuan, Phys. Lett. **B306**, 386 (1993).
D. Carlson, E. Malkawi and C.–P. Yuan, Phys. Lett. **B337** 145 (1994).
F. Larios and C.–P. Yuan, Phys. Rev. **D 55**, 7218 (1997).
F. Larios, T. Tait, and C.–P. Yuan, hep-ph/9709316 (1997).

[96] T. Han, R.D. Peccei, and X. Zhang, Nucl. Phys. **B454**, 527 (1995).

[97] T. Han, K. Whisnant, B.-L. Young, X. Zhang, Phys. Rev. **D 55**, 7241 (1997).

K. J. Abraham, K. Whisnant, B.-L. Young, hep-ph/9707476 (1997).

[98] E. Malkawi and T. Tait, Phys. Rev. **D 54**, 5758 (1996).

T. Han, K. Whisnant, B.-L. Young, X. Zhang, Phys. Lett. **B 385**, 311 (1996).

T. Tait and C.-P. Yuan, Phys. Rev. **D 55**, 7300 (1997).

[99] A. Datta and X. Zhang, Phys. Rev. **D 55**, 2530 (1997).

[100] C.–P. Yuan, Phys. Rev. **D 41**, 42 (1990).

[101] The DØ Collaboration, "Search for Single Top Quark Production in ppbar Collisions at sqrt(s) = 1.96 TeV,"

[102] M.L. Mangano, M. Moretti, F. Piccinini, R. Pittau, and A.D. Polosa, "ALPGEN, a Generator for Hard Multiparton Processes in Hadronic Collisions," J. High Energy Physics **0307**, 001 (2003).

[103] S. Mrenna and P. Richardson, "Matching Matrix Elements and Parton Showers with HERWIG and PYTHIA," arXiv:hep-ph/0312274.

[104] R. Bonciani *et al.*, Nucl. Phys. B **529**, 424 (1998); M. Cacciari *et al.*, JHEP **0404**, 068 (2004); N. Kidonakis and R. Vogt, Phys. Rev. D **68**, 114014 (2003).

[105] R. Bonciani, S. Catani, M.L. Mangano, and P. Nason, "NLL Resummation of the Heavy-Quark Hadroproduction Cross-Section," Nucl. Phys. **B529**, 424 (1998).

[106] B. Abbott *et al.*, (dzero Collaboration), "Search for Electroweak Production of Single Top Quarks in $p\bar{p}$ Collisions," Phys. Rev. D **63**, 031101 (2001).

[107] V.M. Abazov *et al.*, (DØ Collaboration), "Search for Single Top Quark Production at DØ Using Neural Networks," Phys. Lett. **B517**, 282 (2001).

[108] D. Acosta *et al.*, (CDF Collaboration), "Search for Single Top Quark Production in $p\bar{p}$ Collisions at $\sqrt{s} = 1.8$ TeV," Phys. Rev. D **65**, 091102 (2002).

Phys. Lett. **B 622**, 265-276 (2005)

[109] Search for single top quark production in $p\bar{p}$ collisions at $\sqrt{s} = 1.96$ TeV, paper to be submitted to PRD, by the DØ collaboration.

[110] The CDF Collaboration, Phys. Rev. **D 71**, 012005 (2005)

[111] Tevatron RunII Handbook.

[112] DØ Upgrade for RUN II. hep-ex/9910028

[113] The Upgraded DØ Detector hep-physics/0507191; Fermilab-Pub-05/341-E . Submitted to Nucl. Instr. and Methods.

[114] D. Adams et al, The DØ Upgrade: Central Fiber Tracker, Technical Design Report,
DØ Note 004164.
E. Haggard, A. Bross, V. Buescher, G. Davis, J. Estrada, T. Gasteyer, G. Ginther, K. Gray, S. Gruenendahl, C. Lindemeyer, M. Matulik, D. Olis, R. Rucinski, D. E. Smith,
DØ Central Fiber Tracker 1024 Channel VLPC Cassette Technical Design Report, Specifications and Fabrication Procedures,
DØ Note 004766.

[115] A. Gordeev, J. Kotcher, M. Xiong Liu, P. Yamin, M. Bhattacharjee, D. Chakraborty, P. Grannis, A. Lucotte, A. Patwa, M. Rijssenbeek, D.

Shpakov, J. Steffens, A. Talalaevskii, and M. Chung,

Technical Design Report of the Forward Preshower Detector for the DØ Upgrade,

DØ Note 003445.

[116] Technical Design Report for the DØ Forward Muon Tracking Detector Based on Mini-drift Tubes, DØ Note 003366.

[117] Lo A., Miao C., Partridge R, Luminosity Monitor Technical Design Report,

DØ Note 003320.

[118] L. Sawyer, K. De, P. Draper, E. Gallas, J. Li, M. Sosebee, R.W. Stephens, A. White,

Technical Design Report for the Upgrade of the ICD for DØ Run 2,

DØ Note 002686.

[119] H.Evans, U.Heintz, T.Heuring, J.Hobbs, M.Johnson, S.Mani, M.Narain, F.Stichelbaut, H.Wahl,

A Silicon Track Trigger for the DØ Experiment in Run II - Technical Design Report,

DØ Note 003510.

[120] CTT Design Group, Technical Design Report for the Upgrade L1/L2 Tracking Trigger - TDR for the CTT,

DØ Note 003551.

[121] Ann Heinson, UC, Riverside.

[122] Ph.D Thesis, Kenichi, Hatakeyama, 2003

[123] http://d0server1.fnal.gov/projects/Silicon/www/silicon.html

[124] http://d0server1.fnal.gov/projects/SciFi/cft_home.html

[125] Talk by Tim Andeen, Jan Stark, and Matt Wetstein, Calorimeter Workshop, September 26th, 2005

[126] Electron and Photon Identification, talk given by Jan Stark, Winter Physics Workshop, February 22nd, 2004.

[127] Emily Nurse and Paul Telford, Measurement of σ.Br for $Z \to \mu^+ \mu^-$ in $p\bar{p}$ collisions at $\sqrt{s} = 1.96$ TeV, DØ note 4284.

[128] H. Greenlee, Motion of a Charged Particle in a Magnetic Field , DØ note 4180 ;
H. Greenlee, The DØ Interacting Propagator, DØ note 4293;
H. Greenlee, The DØ Kalman Track Fit, DØ note 4303;

HTF track finding algorithm (DØ note 3778, DØ note 3845),
AA track finding algorithm (Feb. 28, 2003 ADM Meeting).

[129] G. Hesketh, Central Track Extrapolation Through the D0 Detector, DØ note 4079.

[130] S. Jabeen, M. Zdrazil, S. Kulik, A. Kharchilava, A. Alton,
Cluster finding Efficiency for Central Fiber Tracker, DØ note 004518.

[131] DØ Top Physics Working Group, DØ Top Analysis and Data Sample for the Winter Conferences 2004, by DØ Note 4419,

[132] S. Grinstein, C. Gerber, R. Piegaia, Topological Vertex Reconstruction at DØ, DØ note 3866.

[133] Junjie Zhu, EM Certification Tools, DØ Note 004171.

[134] Joseph Kozminski, Robert Kehoe, Harry Weerts, Su-Jung Park, Arnulf Quadt, John Gardner, Shabnam Jabeen, Electron Likelihood in p14, DØ Note 004449.

[135] Doug Chapin, Harald Fox, John Gardner, Robert Illingworth, Adam Lyon, Junjie Zhu,
Measurement of $Z \rightarrow ee$ and $We \rightarrow \nu$ Production Cross Sections with $|\eta| < 2.3$

[136] Sabine Crepe-Renaudin, Energy corrections for geometry effects for electrons in Run II, DØ note 4023.

[137] The physics of particle detectors by Dan Green, cambridge University Press, 2000

[138] E. Busato, B. Andrieu, Jet Algorithms in D0 RunII Software: Description and User's Guide, DØ Note 4457.

[139] Run II Jet Physics, G.C. blazey *et al*,DØ note 003750.

[140] Jochen Cammin, Subhendu Chakrabarti, Yann Coadou, Dag Gillberg, Kazu Hanagaki, Jeroen Hegeman, Alexander Kupco, Vivian O'Dell, Dugan O'Neil, Nirmalya Parua, Jyothsna Rani, Christophe Royon, Mikko Voutilainen,
Jet Energy Scale v6.0 for PASS2 Data, DØ note 004762.

[141] http://www-d0.fnal.gov/phys_id/jes/d0_private/certified/v5.3/links.html

[142] L. Feligioni, M. Narain, P. Schieferdecker, and A. Schwartzman,
Update on *b*-Quark Jet Identification with Secondary Vertex Reconstruction using DØReco version p14, DØ Note 4414, (March 2004).

[143] D.Boline, L. Feligioni, M. Narain,
Update on *b*-Quark Jet Identification with Secondary Vertex Reconstruc-

tion using DØReco version p14-Pass2 Samples, by DØ Note 4796, (October 2005).

[144] D. Bloch, B. Clement, D. Gele, S. Greder, and I. Ripp-Baudot, "Performance of the JLIP *b*-Tagger in p14", DØ Note 4348, (February 2004).

[145] R. Demina, A. Khanov, and F. Rizatdinova, and E. Shabalina, "Measurement of *b*-Tagging Efficiency and Mistagging Rates with the Counting Signed Impact Parameter Method," DØ Note 4432, (April 2004).

tuneA http://www.phys.ufl.edu/ rfield/cdf/tunes/rdf_tunes.html

[146] R. Brun *et al.*, CERN Program Library Long Writeup **W 5013** (1994).

[147] T. Sjöstrand *et al.*, Comput. Phys. Commun. **135**, 238 (2001).

[148] S. Jadach, J. H. Kuhn and Z. Was, Comput. Phys. Commun. **64**, 275 (1990).

[149] D. J. Lange, Nucl. Instrum. Meth. A **462**, 152 (2001).

[150] S. Lager, "Primary Vertex Cut Efficiencies and Scale Factors," DØ Note xxxx, (January 2004),
http://www-clued0.fnal.gov/~lager/pv_eff.ps.

[151] CompHEP Collaboration, E. Boos *et al.*, Nucl. Instrum. Meth. A **534**, 250 (2004).

[152] K. Hagiwara *et al.*, "The Review of Particle Physics", Phys. Rev. D **66**, 010001 (2002) and 2003 off-year partial update for the 2004 edition available on the PDG WWW pages (http://pdg.lbl.gov).

[153] Jonathan Pumplin et al, New Generation of Parton Distributions with Uncertainties from Global QCD Analysis,
2002 J. High Energy Phys. JHEP07(2002)012.

[154] E.E. Boos, L.V. Dudko, V.I. Savrin, and A.E. Sherstnev, NLO Generator SingleTop, in preparation, (June 2004).

[155] Leonard Christofek, "Measurement of Select L3 Electron Tool Trigger Turn-on Curves for Trigger List Versions 8-12", DØ Note 4515, (July 2004).

[156] Micheal Begel, Freya Blekman, Leonard Christofek, Thomas Gadfort, Nils Gollub, Miroslav Kopal, Reinhard Schwienhorst, The Top Trigger Package: Including Version 13 Triggers and Other Improvements, DØ Note 004883.

[157] M.Angelou, S.Anderson, B.Andrieu, S.Banerjee, F.Blekman, E.Busato, L.Christofek, B.Clement, C.Clement, T.Golling, S.Jabeen, S.Jain, A.Juste, J.Kozminski, J.Leveque, P.Mal, E.Perez, A.Quadt, R.Schwienhorst, J.Stark, B.Vachon, G.Watts, Top Trigger Efficiency Measurements and the top_trigger package, DØ Note 004512.

[158] Reinhard Schwienhorst, Top Trigger Selection and Application of Turn On Curves to the Monte Carlo, DØ Note 004508.

[159] E. Barberis, T. Golling, I. Iashvili, A. Juste, A. Quadt, and P. Schieferdecker, The Matrix Method and its Error Calculation, DØ Note xxxx, (January 2004),
http://www-d0.fnal.gov/Run2Physics/top/private/winter04/matrix.ps.

[160] C. Clement, R. Demina, T. Golling, A. Juste, A. Khanov, S. Lager, F. Rizatdinova, E. Shabalina, and J. Strandberg, "Measurement of the $t\bar{t}$ Production Cross-Section at $\sqrt{s} = 1.96$ TeV using Lifetime Tagging," DØ Note 4682 (January 2005).

[161] V.M. Abazov *et al.*, (DØ Collaboration), "Search for Single Top Quark Production at DØ Using Neural Networks," Phys. Lett. **B517**, 282 (2001).

[162] L. Dudko, for the DØ Collaboration, "Use of Neural Networks in a Search for Single Top Quark Production at DØ," in the proceedings of the 7th International Workshop on Advanced Computing and Analysis Techniques in Physics Research, Fermilab, Batavia, IL, (October 2000);
E. Boos and L. Dudko, "Optimized Neural Networks to Search for Higgs Boson Production at the Tevatron," Nucl. Instrum. Methods **A 502**, 486 (2003).

[163] Q.-H. Cao, R. Schwienhorst, and C.-P. Yuan, "Next-to-Leading Order Corrections to Single Top Quark Production and Decay at the Tevatron: 1: s-channel process," to appear in *Phys. Rev.* D, hep-ph/0409040.

[164] DØ Note Number: 004722 Improved Search for Single Top Quark Production

[165] D.W. Ruck *et al.*, "The Multilayer Perceptron as an Approximation to a Bayes Optimal Discriminant Function," IEEE Trans. Neural Networks **1 (4)**, 296 (1990);
E.A. Wan, "Neural Network Classification: a Bayesian interpretation," IEEE Trans. Neural Networks **1 (4)**, 303 (1990);
H.B. Prosper, "Some Mathematical Comments on Feed-Forward Neural Networks," DØ Note 1606 (1993).

[166] Christopher M. Bishop "Neural Networks for Pattern Recognition" Oxford University Press (November, 1995)

[167] http://schwind.home.cern.ch/schwind/MLPfit.html

[168] L. Breiman, J. Friedman, R. Olshen, and C. Stone, "Classification and Regression Trees," Wadsworth (1984).

[169] I. Bertram et al., FERMILAB-TM-2104 (2000).

[170] Benoit Clement, Denis Gele, Search for Single Top Quark Production using Likelihood Discriminants, DØ note 004825.

[171] Supriya Jain, Collaboration Comments on the Single Top Paper, All DØ meeting.